PH.D.DISSERTATION/TESIS DOCTORAL

AFRICAN DESERT DUST EVENTS IMPACT OVER SOUTHEASTERN SPAIN (2005-2010): AEROSOL RADIATIVE PROPERTIES AND FORCING

Author:

ANTONIO VALENZUELA GUTIÉRREZ

UNIVERSIDAD DE GRANADA

Programa oficial de Doctorado en Física y Ciencias del Espacio

Grupo Física de la Atmósfera   Centro Andaluz de Medio Ambiente

UNIVERSIDAD DE GRANADA

DEPARTAMENTO DE FÍSICA APLICADA

GRUPO DE FÍSICA DE LA ATMÓSFERA

TESIS DOCTORAL

AFRICAN DESERT DUST EVENTS IMPACT OVER SOUTHEASTERN SPAIN (2005-2010): AEROSOL RADIATIVE PROPERTIES AND FORCING

Tesis presentada por ANTONIO VALENZUELA GUTIÉRREZ para optar al grado de Doctor:

Director de Tesis:

Dr. Francisco José Olmo Reyes

Catedrático de la Universidad de Granada

Departamento de Física Aplicada

Universidad de Granada

Granada, Junio de 2013

El trabajo de investigación que se expone en la presente memoria, titulada:

AFRICAN DESERT DUST EVENTS IMPACT OVER SOUTHEASTERN SPAIN (2005-2010): AEROSOL RADIATIVE PROPERTIES AND FORCING, que para aspirar al grado de Doctor, ha sido realizado en la Universidad de Granada gracias a la beca de Excelencia concedida por la Junta de Andalucía "Personal investigador en formación asociado a proyecto de excelencia" (Consejería de innovación, ciencia y empresa, convocatoria 2008), bajo la dirección de:

El director

Dr. Francisco José Olmo Reyes

Aspirante al grado de doctor

Ldo. ANTONIO VALENZUELA GUTIÉRREZ

El doctorando **Antonio Valenzuela Gutiérrez** y el director de la tesis **Francisco José Olmo Reyes**, garantizamos, al firmar esta tesis doctoral, que el trabajo ha sido realizado por el doctorando bajo la dirección del director de la tesis y hasta donde nuestro conocimiento alcanza, en la realización del trabajo, se han respetado los derechos de otros autores a ser citados, cuando se han utilizado sus resultados o publicaciones.

Granada, Junio de 2013

Director de la Tesis   Doctorando

Fdo.: Francisco José Olmo Reyes   Fdo.: Antonio Valenzuela Gutiérrez

A mi madre,

a mi hermana,

AGRADECIMIENTOS

Y llegados a este punto hay tantas cosas que me gustaría decir y trasmitir… Espero que la defensa de esta Tesis sea un punto y seguido y no un punto y final. Escribir estas líneas resulta más complicado de lo que parece pues son tantas las personas que han contribuido a que esta Tesis sea una realidad que es difícil plasmarlo en unas pocas palabras.

En primer lugar mi más sincero agradecimiento a mi director de Tesis, el Catedrático D. Francisco José Olmo Reyes. Gracias a su ayuda incansable y permanente, así como a su cercanía como persona esta Tesis ha sido una realidad. Su apoyo ha sido de vital importancia en mi formación durante estos cuatro años.

Quiero dar las gracias también al Catedrático D. Lucas Alados Arboledas por haber confiado en mí desde el primer día. Todavía recuerdo ese primer momento en el que me presenté en el CEAMA y le comenté que me gustaría trabajar en el grupo de Física de la Atmósfera. Me fascinaba el campo relacionado con la meteorología y la radiación solar. Él me abrió las puertas del grupo. Durante estos años, me ha mostrado su cariño, apoyo y confianza.

Agradecimiento también al resto de profesores del grupo que me han acompañado a lo largo de estos cuatro años de Tesis. A Inmaculada Foyo por su disponibilidad en todo momento, por sus aportaciones y por su trato siempre agradable y comprensivo. A Inma Alados, por esos momentos compartidos en los seminarios del grupo y en las visitas a Málaga para revisar el CIMEL. No puedo olvidarme de Andy,

estando siempre disponible para realizar correcciones desinteresadas de inglés, así como por los buenos momentos compartidos en esas barbacoas del grupo.

Y cómo no agradecer a todos los compañeros del Grupo de Física de la Atmósfera que durante todo este tiempo me han acompañado en esta andadura, compartiendo unas veces momentos entrañables y en otras ocasiones momentos más difíciles. A Juan Antonio, por esa colaboración y ayuda desinteresada, siempre dispuesto a resolver cualquier duda que le planteaba; gracias a él mi trabajo en el grupo ha resultado mucho más fácil. A María José y Gloria, por su carácter afable y divertido. A Fran por su carácter extrovertido y por su compañerismo, siempre dispuesto a lo que surja. A Jesús, Juanlu, Enrique y Alberto por su amistad, y también a Alba que acaba de incorporarse al grupo. Cómo no agradecer a Penélope con su sonrisa incansable que hace todo más fácil en el CEAMA.

Este párrafo lo quiero dedicar exclusivamente a Hassan. Sin su incansable ayuda esta Tesis no hubiera sido nunca una realidad. Tengo que agradecerle su paciencia, su saber estar, su colaboración, su comprensión y sus ánimos en los momentos más difíciles.

No puedo olvidarme de Manuel Antón, pues gracias a su coraje, ánimos y arrojo mi trabajo ha resultado mucho más llevadero.

Mi agradecimiento al Profesor Helmuth Horvath que me acogió en la Universidad de Viena durante mi estancia de tres meses.

Por último, quiero dedicar este trabajo a las personas que más quiero por su apoyo constante en los momentos más difíciles. A mi madre, por estar siempre ahí para lo que hiciese falta sin esperar nada a cambio. A mi abuela Gracia que ha sido un ejemplo de coraje y valentía para afrontar las dificultades que se plantean en la vida. A

mis hermanos, Moisés, Loreto, y Chevis por haber depositado siempre su confianza en mí; a mi cuñado Jesús por su bondad, y a mis sobrinos Lorenzo y Pedro que son lo mejor del mundo. A Coral por su comprensión, humildad y apoyo constante; siempre me ha acogido en su casa. Estas líneas van dedicadas a mi novia Sofía, que ha tenido que soportarme en los momentos más complicados, y que sin su apoyo y confianza esta Tesis nuca hubiera sido posible. Por último quiero dedicar esta Tesis a mi hermana Gracia; justo cuando comencé mi camino en el mundo de la investigación ella dejo de estar entre nosotros. No ha pasado ni un solo día desde que te fuiste que no haya pensado en ti, y seguro que me estarás viendo con tu alegría contagiable desde alguna parte.

Contents

ABSTRACT

The aim of this PhD thesis is to analyze the radiative properties of the atmospheric aerosol during the African dust events registered at Granada from 2005 to 2010, as well as their influence on radiative forcing both at the surface and at the top of the atmosphere (TOA). To accomplish this goal we have used mainly the measurements made with a sun-photometer. In contrast to measurements performed by in-situ or chemical analysis, the advantage of this remote sensing technique is the no modification of the aerosol properties during the measurement process. The sun-photometer used is included in the AERONET network (AErosol RObotic NETwork), sponsored by NASA, and operated continuously in radiometric station located at CEAMA (Andalusian Center of Environment) as part of the instrumentation used by the Atmospheric Physic Group of the University of Granada (GFAT).

Major advances presented in this work are related to the implementation and application of a new methodology for deriving optical and microphysical properties of the aerosol in the atmospheric column using sky radiance in the principal plane configuration, and considering, from a methodological point of view, that the particles are not spherical. The following paragraphs summarize briefly the main specific objectives discussed in this work.

ABSTRACT

After the introduction, where we show the relevance of the PhD thesis; in next chapters, the radiometric magnitudes and the procedure for deriving the Radiative Transfer Equation (ETR) used in the Earth's atmosphere studies are defined. In addition, the atmospheric aerosol and its possible classification by sources, the chemical composition and size distribution are described in detail. From instrumental point of view, the sun-photometer CIMEL, the methodology for measurements and its calibration processes are also detailed. Finally, other instruments used in this PhD thesis are also briefly described.

In the Methodology Section, a detailed description of the procedure to derive the aerosol optical depth is included, besides the algorithm used for ETR inversion using the sky radiance measurements in principal plane configuration and taking into account the non sphericity of particles. Also, we analyzed the sensitivity of the inversion algorithm and the atmospheric aerosol properties obtained with those provided by the AERONET network. Additionally, the quality control procedure of the experimental data, the criteria used for the selection of days with African dust events affecting our radiometric station, and the methodology used to derive the radiative forcing at surface and TOA are also described in detail.

The analysis of the optical and microphysical aerosol properties during African dust events is carried out far away from the source regions. In this sense, it may produce efficient mixing of mineral particles with other particles from sources in the air masses path. Also, the aerosol properties may change depending on the African dust source regions. To account for these effects, we classified the optical and microphysical properties according to potential origin sources and also applying a cluster analysis.

ABSTRACT

Moreover, it is interesting to analyze the atmospheric aerosol properties at some distance of its source regions before mixing with particles originated in other regions. In this sense, the Alborán Island, located in between the North African coast and the Southern Iberian Peninsula, offers an appropriate place to perform such studies. The GFAT have installed in spring-summer-autumn a sun-photometer instrument at the remote place of the Alborán Island. Therefore, taking into account these sun-photometer measurements, we have analyzed the properties of atmospheric aerosol transported from North Africa before contacting air masses from other regions.

The atmospheric aerosol radiative forcing computed at surface and TOA, at daily and seasonal temporal scales, is estimated using aerosol properties according to the classification of the origin sources. To carry out this objective, we have used the radiative transfer model SBDART in spectral range 310-2800 nm, using as input parameters the aerosol optical depth and the inversion parameters: single scattering albedo and asymmetry parameter. In addition, the aerosol radiative forcing efficiency (aerosol radiative forcing per unit of aerosol optical depth) has been computed and analyzed.

Taking into account that our atmospheric station includes in-situ instrumentation for estimating atmospheric aerosol properties on the surface, we have compared the aerosol properties derived in the atmospheric column and at surface for African dust events and dust free days. This is performed using measurements made with a PSAP (Particle Soot Absorption Photometer) and an integral nephelometer. These measurements enable to evaluate if the aerosol properties retrieval in the atmospheric column are reproduced at surface.

ABSTRACT

Furthermore, in the literature, there are few studies that analyze the effects of atmospheric aerosol on UV spectral range during African dust events. In this sense, the results shown UVER transmittance (erythemal) as well as the results of applying an aerosol absorption post-correction method to the UVER algorithm employed in the OMI (Ozone Monitoring Instrument) sensor.

RESUMEN

Esta Tesis doctoral tiene como objetivo general el estudio de las propiedades radiativas del aerosol atmosférico durante los eventos de masas de aire con origen Africano que llegaron a Granada entre los años 2005 y 2010, así como su influencia sobre el forzamiento radiativo tanto en la superficie como en el tope de la atmósfera (TOA). Para llevar a cabo este objetivo hemos utilizado, fundamentalmente, las medidas realizadas con un fotómetro solar. En contraste con las medidas que se realizan in-situ o los análisis químicos, la ventaja de esta técnica fotométrica es, entre otras, la no modificación de las propiedades del aerosol atmosférico durante el proceso de medida. El fotómetro solar utilizado está incluido en la red AERONET (AErosol RObotic NETwork), auspiciada por NASA, y opera de forma continua en la estación radiométrica situada en el CEAMA (Centro Andaluz de Medio Ambiente), como parte de la instrumentación utilizada por el Grupo de Física de la atmósfera de la Universidad de Granada (GFAT).

Los principales avances presentados en este trabajo están relacionados con la implementación y aplicación de una novedosa metodología para la obtención de las propiedades ópticas y microfísicas del aerosol en la columna atmosférica utilizando la radiancia del cielo en la configuración del plano principal, y considerando, desde un punto de vista metodológico, que las partículas no son esféricas. Los siguientes párrafos resumen brevemente los principales objetivos específicos discutidos en esta Tesis.

Tras una introducción, donde ponemos de manifiesto la importancia de este tipo de trabajos, en los siguientes capítulos se definen las principales magnitudes

RESUMEN

radiométricas utilizadas, así como el procedimiento para obtener la Ecuación de Transporte Radiativo (ETR) que se utiliza en los estudios de la atmósfera de la Tierra. También se define el aerosol atmosférico y su posible clasificación atendiendo a las fuentes, a la composición química y a su distribución de tamaño. Desde el punto de vista instrumental, se describe con detalle el fotómetro solar CIMEL, su procedimiento de medida y los procesos de calibración. También se describen brevemente otros instrumentos empleados en esta tesis.

En cuanto a la metodología, se incluye una detallada descripción del procedimiento para obtener la profundidad óptica del aerosol atmosférico y el algoritmo utilizado para la inversión de la ETR a partir de las medidas de radiancia del cielo en la configuración de plano principal teniendo en cuenta la no esfericidad de las partículas. También se realiza un test de sensibilidad del algoritmo de inversión. A continuación se comparan las propiedades del aerosol atmosférico obtenidas con las proporcionadas por la red AERONET. Además, se describe el procedimiento de control de calidad de los datos experimentales, el criterio utilizado para la selección de días con eventos de masas de aire con origen africano que afectaron a nuestra estación radiométrica y, finalmente, la metodología empleada para la estimación del forzamiento radiativo en la superficie y en el TOA.

El análisis de las propiedades ópticas y microfísicas del aerosol atmosférico durante los eventos de masas de aire con origen africano se realiza lejos de las regiones fuente. En este sentido, puede producirse una mezcla eficiente de las partículas minerales asociadas a las masas de aire con origen africano con otro tipo de partículas procedentes de fuentes localizadas en el camino recorrido por las masas de aire. Así mismo, las propiedades de las partículas minerales podrían cambiar dependiendo de las regiones fuente. Para tener en cuenta estos efectos, clasificamos las propiedades ópticas

RESUMEN

y microfísicas de acuerdo con las potenciales fuentes de origen y, también, aplicando un análisis de clúster. Además, es interesante estudiar las propiedades del aerosol atmosférico a cierta distancia de sus regiones fuente antes de mezclarse con partículas procedentes de otras regiones. En este sentido, la isla de Alborán, localizada entre la costa Norte de África y el Sureste de la Península Ibérica ofrece un lugar apropiado para realizar tales estudios. A partir de las medidas realizadas por un fotómetro solar que el GFAT tiene instalado durante la primavera, verano y otoño en la mencionada isla, analizaremos las propiedades del aerosol atmosférico transportado desde el Norte de África antes de entrar en contacto con las masas de aire procedentes de otras regiones.

El forzamiento radiativo producido por el aerosol atmosférico en la superficie y en el TOA se ha estimado en escalas temporales diaria y estacional utilizando las propiedades del aerosol de acuerdo con la clasificación de las fuentes de origen. Para llevar a cabo este objetivo se ha utilizado el modelo de transferencia radiativa SBDART en el rango espectral 310-2800 nm, usando como parámetros de entrada la profundidad óptica del aerosol atmosférico y los parámetros obtenidos con la metodología de inversión: albedo de dispersión simple y parámetro de asimetría. Además, también se ha calculado la eficiencia del forzamiento radiativo (forzamiento radiativo por unidad de espesor óptico).

Teniendo en cuenta que nuestra estación incluye instrumentación in-situ para la estimación de las propiedades del aerosol atmosférico en la superficie, se comparan las propiedades obtenidas en la columna y en la superficie, tanto para los eventos de masas de aire con origen africano como para días con masas de aire procedentes de otras regiones. Para ello, se emplean medidas realizadas con un PSAP (Particle Soot Absorption Photometer) y un nefelómetro integrante. Esta comparación permite evaluar

RESUMEN

si las propiedades del aerosol obtenidas en la columna atmosférica se reproducen en la superficie.

Además, en la literatura científica, existen pocos estudios donde se analizan los efectos del aerosol atmosférico en la irradiancia espectral UV durante eventos de masas de aire con origen africano. En este sentido, se muestran los resultados de la transmitancia UVER (eritemática), así como los resultados de aplicar un método de post-corrección de la absorción del aerosol atmosférico al algoritmo UVER empleado en el instrumento satelital OMI (Ozone Monitoring Instrument).

CHAPTER 1

INTRODUCTION

1. Introduction

1. Introduction

1.1 The atmospheric aerosol

The atmospheric aerosol is defined as the ensemble of solid and liquid particles suspended in the atmosphere. The effect of atmospheric aerosols on climate remains one of the largest radiative forcing uncertainties according to the latest IPCC report (Solomon et al., 2007). The large temporal variability and the characterization of horizontal and vertical distributions, aerosol mixtures and absorptive properties constitute difficulties in the evaluation of the aerosol direct radiative forcing (e.g. Myhre, 2009; Eck et al., 2010).

Desert dust is one the major aerosol components in the global atmosphere that affects the Earth's climate through interacting with both solar and thermal infrared radiation. The North Africa dust is the most important source of mineral dust in North Hemisphere (Goudie and Middleton, 2001). The continuous measurements recorded during the SAMUM campaign (May/June 2006, Morocco) provided an excellent opportunity to analyse the height that can reach the dust particles when they are injected to the atmosphere from the potential sources of emission (e.g. Knippertz at al., 2009; Tesche et al, 2009). The results of this campaign revealed that the depth of the dust layer usually reaches a height of 4-6 km above sea level, even sometimes up to 7 km. Dust is then transported in a wide range of different altitudes (up to 5 km) to other areas (e.g. Escudero et al., 2005; Escudero et al., 2011). Papayannis et al. (2008) reported during the period May 2000 to December 2002 more than 130 observation days of the horizontal and vertical extent of Saharan dust intrusions over Europe by means of a

1. Introduction

coordinated lidar network in the frame of the European Aerosol Research Lidar Network (EARLINET). They found that Saharan dust source regions play a key role in dust transport to Europe for the height layer between 3 and 5 km. The Iberian Peninsula is frequently affected by North African dust episodes with large aerosol load that can modulate the aerosol climatology in different areas, especially in Southern Spain (e.g. Lyamani et al., 2005; Toledano et al., 2007a; Cachorro et al., 2008; Valenzuela et al., 2012a) and Portugal (Wagner et al., 2009). Lidar observations have been utilized to characterize the vertical layering structure during desert dust events over Granada (Guerrero-Rascado et al., 2009; Cordoba et al. 2011). These authors have shown that the dust layers are transported between 2.5 and 4.5 km heights and peaking about at 3.2 km.

On a global average, mineral dust is responsible for approximately one third of global extinction optical depth (Tegen et al., 1997) in the mid-visible wavelengths, and absorbs significantly in the blue and ultraviolet wavelengths due to iron oxide impurities (Sokolik and Toon, 1999). Close to the source region mostly pure dust is found, but after a long range transport the aging of the dust and mixing with other aerosol types modify the optical properties of the desert dust (e.g. Bauer et al., 2011; Hand et al., 2010). Therefore, the measured aerosol optical properties could be different than the original ones at the emission sources. A possibility in order to minimize the effect of the local aerosol is placing the measuring stations in remote locations far from the potential influence of local aerosol sources. Measurements taking at small islands are valuable because local sources are generally negligible, and medium and long-range transport, together with aerosol aging processes, play a relevant role, thus providing information on aerosol properties over a relatively large scale (e.g. Di Biaggio et al., 2009). In this sense, several authors have monitored aerosol optical and microphysical

1. Introduction

properties in remote places (e.g. Dubovik et al., 2002 and Toledano et al., 2011 in Cape Verde; Pace et al., 2006 and Meloni et al., 2006 in Lampedusa; Valenzuela et al., 2013 in Alborán Island).

The mixing of desert dust with anthropogenic particles may prompt changes in the physical properties and chemical composition of the desert dust and this may have important consequences in processes affecting climate (e.g. Rodriguez et al., 2011; Gu et al., 2010). The sign and magnitude of the aerosol radiative forcing (ARF) associated with these intrusions depend on dust scattering and absorbing properties that are controlled by a number of properties such as dust size distribution, chemical composition, particle mixing state and shapes (e.g. Otto et al. 2009). Recently, Rodríguez et al. (2011) showed that anthropogenic emissions from crude oil refineries and power plants, located on Northern African coasts, contribute to desert dust mixing with particulate pollutants. Hence, the contribution of anthropogenic particles emitted from such regions can be relevant during African dust outbreaks over Mediterranean sites. This fact is suggested by the relatively high Angström exponent (α) values - measured after medium-long range dust transport in comparison with those obtained in source areas - and confirmed by analyses of chemical composition of ground-collected particles (e.g. Bellantone et al., 2008; Carofalo et al., 2008). Thus, several authors have pointed out the importance of taking into account the influence of anthropogenic particles on the direct radiative forcing associated with African desert dust intrusions over the Mediterranean basin and continental Europe (e.g. Gerasopoulos et al., 2003; Perrone and Bergamo, 2011).

The Mediterranean basin is a place of special interest for the study of the atmospheric aerosol due to its geographic location surrounded by continents with

1. Introduction

different surface characteristics and where local winds, complex coastlines and orography have strong influence on the atmospheric flow. In this sense, studies have been conducted over its Western area, over the Iberian Peninsula (e.g. Silva et al., 2002 and Pereira et al., 2011 in Portugal; Lyamani et al., 2006a; Toledano et al., 2007a; Estellés et al., 2007; Cachorro et al., 2008; Prats et al., 2008; Valenzuela et al., 2012b in Spain), in the central Mediterranean (e.g. Pace et al., 2006; Tafuro et al., 2006; Meloni et al., 2006, 2008; Di Biagio et al., 2009; Perrone and Bergamo, 2011 in Italy) and in the Eastern Mediterranean (e.g. Gerasopoulos et al., 2003; Gerasopoulos et al., 2006; Gerasopoulos et al., 2009; Kaskaoutis et al., 2010 in Greece). The Mediterranean basin is a reception's place of primarily two aerosol types: anthropogenic aerosol arriving from the most industrialized areas in Europe and desert dust arriving from the African continent. These aerosol types have been continuously characterized in numerous studies. On the one hand, the anthropogenic aerosol contribution mainly from central Europe has been characterized in some studies (e.g. Lyamani et al., 2006b; Perrone and Bergamo, 2011). On the other hand, others studies have focused their research on desert dust (e.g. Meloni et al., 2005; Lyamani et al., 2005; Tafuro et al., 2006; Toledano et al., 2007a; Meloni et al., 2008; Papayannis et al., 2008, 2009; Papayannis et al., 2012; Pavese et al., 2009; Escudero et al., 2011; Córdoba-Jabonero et al., 2011; Valenzuela et al., 2012a). However, there are relatively few studies analysing effects of dust intrusions on shortwave solar radiation reaching the Earth's surface. (e.g. Díaz et al., 2001; Lyamani et al., 2006b; Santos et al., 2008; Cachorro et al., 2008; Antón et al., 2012a). To our knowledge, only Díaz et al. (2007) and Antón et al. (2012b) have analysed the atmospheric aerosol effects on spectral ultraviolet (UV) irradiance during two Saharan dust events in South Spain. In general, there are only a few works about this subject in

1. Introduction

literature (e.g. di Sarra et al., 2002; Meloni et al., 2003; Kalashnikova et al., 2007; García et al., 2009) due to the scarcity of routinely operational ground-based stations with high-quality instrumentation to measure simultaneously UV irradiance and aerosol data during desert dust intrusions.

The analysis of air mass back-trajectories is a powerful tool commonly used to study the atmospheric aerosol and aerosol transport from an origin source to receptor sites. Previous studies (e.g. Estellés et al., 2007; Toledano et al., 2009) identified the air-mass origin sector by considering the time spent over the source. Other works have taken into account the altitude of the air masses and the possible interactions with the boundary layer (e.g. Pace et al., 2006). Although the dust injection height can reach up to 7 km in the sources, the authors used as reference minimum height (1000 m a.s.l.) of air masses trajectories which interact with the mixed layer (e.g. Petzold et al., 2009). Other relevant method of the air masses classification is the cluster analysis (e.g. Dorling et al., 1992; Mattis I. et al., 2000, Rozwadowska et al., 2010; Bösenberg et al., 2003). Using this methodology, Toledano et al. (2009) established as representative of Saharan air masses trajectories the 1500 and 3000 m height levels reaching the Iberian Peninsula.

On the other hand, the shapes of dust particles are irregular (e.g. Koren et al., 2001; Muñoz et al., 2001). Theoretical studies of dust optical properties based on a spheroid polydispersion model have shown that dust properties can be substantially different to those obtained with Lorenz-Mie theory adopting spherical models (e.g. Mishchenko et al., 1997). Certain spheroidal shape parameterizations can substantially diminish the differences between experimental and modeled values of the atmospheric aerosol radiative forcing (e.g. Otto et al. 2009). Yang et al. (2007) estimated the

1. Introduction

influence of prolate spheroidal model particles on the radiation field and stated that the non-sphericity of particles affects short-wave radiation significantly, but has no impact on long-wave radiation. Pilinis and Li (1998) estimated the radiative forcing of prolate spheroidal model particles and found that assuming such shapes can result in a radiative forcing up to three times larger than for spherical shapes when the solar zenith angle near is zero. These authors found that the assumption of particle shape is important for the upwelling scattered radiation, especially for small solar zenith angles and super-micron particles, and that the upward scattered radiation is underestimated when assuming spherical particles.

During recent years different inversion methods have been proposed to retrieve aerosol microphysical properties using sun and sky radiance measurements in the almucantar or principal plane configurations (e.g. Nakajima et al., 1996; Vermeulen et al., 2000; Dubovik and King, 2000; Dubovik et al., 2002a, 2006; Olmo et al., 2006, 2008). Applying such methods to sun-photometric sky radiance measurements in the almucantar configuration, many authors have presented results of columnar aerosol optical and microphysical properties (e.g. Dubovik et al., 2002b; Kubilay et al., 2003; Lyamani et al., 2006b; Tafuro et al., 2006; Olmo et al., 2006; Cachorro et al., 2008; Pinker et al., 2010; Eck et al., 2010; Garcia et al., 2011). However, only a few authors have presented optical properties retrieved using sky radiance measurements in the principal plane configuration (e.g. Li et al., 2004; Dubovik et al., 2006; Olmo et al., 2008; Valenzuela et al., 2012a,b,c). Sky radiance measurements in the solar principal plane have received less attention than almucantar sky radiance measurements due to the difficulties in data quality assurance. In fact, the AERONET network routinely distributes only almucantar retrievals. One of the major difficulties for retrieving aerosol

1. Introduction

properties from sky radiance in principal plane is the screening of partially cloud-contaminated data. Using almucantar measurements, these cloud-affected data can be detected by checking the symmetry of left and right almucantar scans. However, the symmetry criteria cannot be applied for principal plane observations and therefore screening partially cloudy principal plane data is more difficult. The sky radiance measurements in the principal plane allow us to obtain columnar optical and microphysical aerosol properties throughout the day, not just for large solar zenith angles as in the almucantar configuration. In this study we used the aerosol optical properties retrieved by the principal plane inversion method described by Olmo et al. (2008). This inversion method uses a spheroid particle model similar to that used in AERONET (Dubovik et al., 2006) to account for particle nonsphericity in modeling aerosol properties. A similar spheroid model was used by Kobayashi et al. (2010) to retrieval optical properties of non-spherical aerosols using SKYRAD.pack code (Nakajima et al., 1996) in the almucantar configuration.

1.2 Objectives

A better understanding of the effects of aerosols during desert dust outbreaks on regional climate is important in predicting global climate changes in the future. The aim of this study is to investigate the aerosol optical and microphysical properties during desert dust outbreaks that occurred over Southeastern of the Iberian Peninsula from 2005 to 2010. The results reported on this thesis will aid in understanding of possible ways to minimize the observational errors in estimates of aerosol optical and

1. Introduction

microphysical properties as well as aerosol radiative forcing during desert dust outbreaks.

The specific objectives of this Thesis are summarizes in the following sentences;

1. The analysis of the aerosol optical and microphysical properties using sun-photometric sky radiance measurements in the principal plane configuration during desert dust outbreaks over southeaster of Iberian Peninsula from 2005 to 2010 period.

2. Assessments of these properties following two air masses classification methods:

    - Classification according to desert dust origin sources.

    - Classification according to cluster analysis.

3. Comparison of the columnar and in-situ ground based aerosol optical properties during desert dust outbreaks and free-dust days over monitoring station.

4. Influence of desert dust aerosol on the UV erythemally weighted surface irradiance (UVER) measured at Granada. This study also evaluates the differences between the UVER measurements and the satellite retrievals from Ozone Monitoring Instrument (OMI) on NASA EOS Aura satellite.

5. Estimation of the aerosol radiative forcing during desert dust outbreaks and comparison of the aerosol radiative forcing according to the desert dust origin sources.

6. General description of the aerosol optical properties for air masses transported from different areas arriving over Alborán Island. We will pay special attention

in air masses transported from North Africa. Characterization of the aerosol optical and microphysical properties will be performed during desert dust events over the Alborán Island.

1.3 Outline

This thesis is structured in seven chapters:

Chapter 2 describes the background regarding the Earth's atmosphere. We also present a description of the radiometric magnitudes, procedures to derive the radiative transfer equation, atmospheric aerosol and its classification according to sources, chemical composition and size distribution. Finally, we introduce the optical and microphysical atmospheric aerosol properties used in this Thesis.

Chapter 3 carries out a detailed description of the instruments used in this work. In particular, we pay special attention to the sun-photometer CE318, its measurement procedure and calibration processes. Others instruments also used in this thesis will be briefly explained.

Chapter 4 describes the procedures to obtain the aerosol optical depth. Afterwards, we explain the sky radiance principal plane inversion method. A sensibility analysis of the inversion method is performed. The atmospheric aerosol properties obtained with this methodology will be compared with those obtained by AERONET network. Later, quality control data procedure is explained as well as the criteria for select of desert dust days. The methodology to obtain the aerosol radiative forcing during desert dust events is developed. After, the methodology to compare column and in-situ aerosol optical properties will be explained. Finally we propose, taking into

account the quality assured ground-based measurements, the application of aerosol absorption post-correction method of the OMI UVER algorithm.

Chapter 5 shows the two methodologies of classification air masses transported from North Africa. Air masses arriving to the Alborán Island are also classified according with one of these methodologies.

Chapter 6 presents the main results. Firstly we analyze the atmospheric aerosol optical and microphysical properties during desert dust events over Granada from 2005 to 2010. This work is focused in those desert dust events which reached the surface (CALIMA.ws). Therefore, in the next section will be assessment the aerosol optical properties during desert dust events and dust-free conditions at atmospheric column and at surface. For this purpose, measurements of a passive remote sensing (sun-photometer CIMEL) and ground-based "in situ" instruments (integrating nephelometer and Particle Soot Absorption Photometer, PSAP) will be used. On the other hand, there are relatively few studies analyzing analyzed the atmospheric aerosol effects on spectral UV irradiance during Saharan dust events in South Spain. In this sense, the UVER transmittance will be calculated for the desert dust dataset obtained in this thesis, in addition to the analysis of their effects on the estimation of UV irradiance from OMI satellite instrument. In this work, the analysis of the aerosol properties was performed away from the desert dust source region, giving sufficient time for efficient mixing of the mineral particles with other aerosol types. On the other hand, the mineral optical properties could change depending on the desert dust source region. In this sense, the aerosol optical and microphysical properties will be classified according to the potential origin sources and also applying cluster analysis. The desert dust, among the different aerosol types present over the South-eastern Spain, produces larger radiative

perturbation at the surface and at the top of the atmosphere (TOA). Later, aerosol radiative forcing will be compute according to the origin sources classification. Therefore, in this study photometric measurements are combined with a radiative transfer model (SBDART) to quantify the aerosol radiative forcing in (310-2800 nm) spectral range both at the surface and at TOA during desert dust events. Finally, it is interesting to study the atmospheric aerosol transported from North Africa to Europe before its mixing with antropogenic aerosol originated in Europe. In this sense, Alborán Island, located in between the North African coast and the Southern Iberian Peninsula offers a strategy place to perform this study. The small Island, is located in the Western Mediterranean Basin around 90 km North of Africa coast and 60 km South of the Iberian Peninsula. The analysis of the aerosol properties over Alborán Island will be performed in detail. We pay special attention in aerosol optical and microphysical properties during desert dust events over this Island.

Chapter 7 presents the main concluding remarks. Finally, to conclude the work, some suggestions for future research are offered.

Finally, we present the references, a list of symbol used and the list of publications related to this thesis in different journals and scientific congresses.

1. Introduction

CHAPTER 2

FUNDAMENTALS

2. Fundamentals

2. Fundamentals

Chapter 2 describes the background regarding the Earth's atmosphere. We also present a description of the radiometric magnitudes, procedures to derive the radiative transfer equation, atmospheric aerosol and its classification according to sources, chemical composition and size distribution. Finally, we introduce the optical and microphysical atmospheric aerosol properties used in this Thesis.

2. Fundamentals

2.1 The SUN

The Sun and Earth are intimately related. Since long time ago, the Sun has been acknowledged to be the primary source of energy, and without that source life could neither have appeared nor be sustained on Earth. The Sun is the star at the centre of the Solar System. It is almost perfectly spherical and consists of hot plasma. It has a diameter of about 1392684 km, about 109 times that of Earth, and its approximately mass is of $1.99 \cdot 10^{30}$ Kg. The temperature decreases from its centre (around $5 \cdot 10^6$ K) until its surface (around 5888 K). The density in the Sun's centre is around 150 g/cm^3, while in its surface reaches a 10^{-7} g/cm^3 value. Its mean density is around 1.4 g/cm^3 (Liou, 2002). Chemically, about three quarters of the Sun's mass consists of hydrogen, while the rest is mostly helium. The remainder (1.69%, which nonetheless equals 5.628 times the mass of Earth) consists of heavier elements, including oxygen, carbon, neon and iron, among others. The Sun is a typical star that generates energy via nuclear fusion reactions deep in its interior. The Sun is, ultimately, the source of energy responsible for most life on Earth (Liou, 2002).

The mean distance Earth-Sun, r_0, is of $1.5 \cdot 10^8$ km which in astronomy is equivalent to an astronomic unit, *AU*. The earth's orbit around the sun is not a circle, is slightly elliptical. Therefore, the distance between the Earth and the Sun varies throughout the year. At its nearest point on the ellipse the Earth is 147166462 km from the Sun. This point in the Earth's orbit is known as perihelion and it occurs on January 3. The Earth is farthest away from the sun on July 4, when it is 152171522 km from the sun. This point in the Earth's orbit is called aphelion. Taking into account that d_n is

Julian day, corresponding to $d_n=1$, January 1, and to $d_n=365$, December 31, the Earth-Sun distance, r, can be approximately by the following equation (Iqbal, 1983):

$$\left(\frac{r}{r_0}\right)^2 = 1 + 0.033 \cdot \cos\left(\frac{2\pi d_n}{365}\right)$$ (2.1)

2.2 Earth's Atmosphere

The atmosphere of Earth is a layer of gases surrounding the planet that is retained by Earth's gravity. The atmosphere protects life on Earth by absorbing ultraviolet solar radiation, warming the surface through heat retention (greenhouse effect), and reducing temperature extremes between day and night (the diurnal temperature variations).

2.2.1 Thermal Vertical structure of Earth's Atmosphere

It is difficult to define an absolute depth of the atmosphere, although the most of the atmosphere is confined to a narrow layer around the planet, with the pressure and density of air decreasing rapidly with altitude. Fifty percent of the mass of the atmosphere is confined within 5.5 kilometers of sea level; 90 percent is confined within about 16 kilometers of sea level, and 99.9 percent is below 49 kilometers. Since the mean radius of the Earth is 6,370 kilometers, the atmosphere is a very thin coating around our planet. At altitudes of 500 to 600 kilometers it is still possible to detect air, although the density of gases there is less than 10^{-12} (one trillionth) of that at sea level (Liou, 2002). In Figure 2.1, we first present the vertical temperature profile for the standard atmosphere. This profile represents typical conditions in the midlatitude

regions. According to the standard nomenclature defined by the International Union of Geodesy and Geophysics (IUGG) in 1960, the vertical profile is structured into four different layers as displayed in Fig. 2.1. These are the troposphere, stratosphere, mesosphere, and thermosphere. The tops of these layers are called the tropopause, stratopause, mesopause, and thermopause, respectively. The troposphere is characterized by a decrease in temperature with respect to height (around 6.5 K km^{-1}) from a mean surface temperature of about 288 K to a temperature of about 220 K. The temperature structure in this layer is produced by the radiative balance and the convective transport of energy between the surface and the atmosphere. In general, all water vapor, aerosol particles, clouds, and precipitation are confined in this layer. The stratosphere is characterized by an isothermal layer from the tropopause to about 20 km, above which the temperature increases to the stratopause with a temperature of about 270 K. Ozone is contained mainly in the stratosphere. In addition, aerosol is observed to persist for a long period of time within certain altitude ranges of the stratosphere. The processes of energetic exchange in the stratosphere are primarily determined by the absorption of solar fluxes by ozone and through the emission of infrared fluxes by carbon dioxide. The temperatures in the mesosphere decrease with height from about 50 to 85 km. The thermosphere lies above this height and extending until an altitude of several hundred kilometers where temperatures can range from 500 K to 2000 K. The region of the atmosphere above the thermosphere is called the exosphere (Liou, 2002).
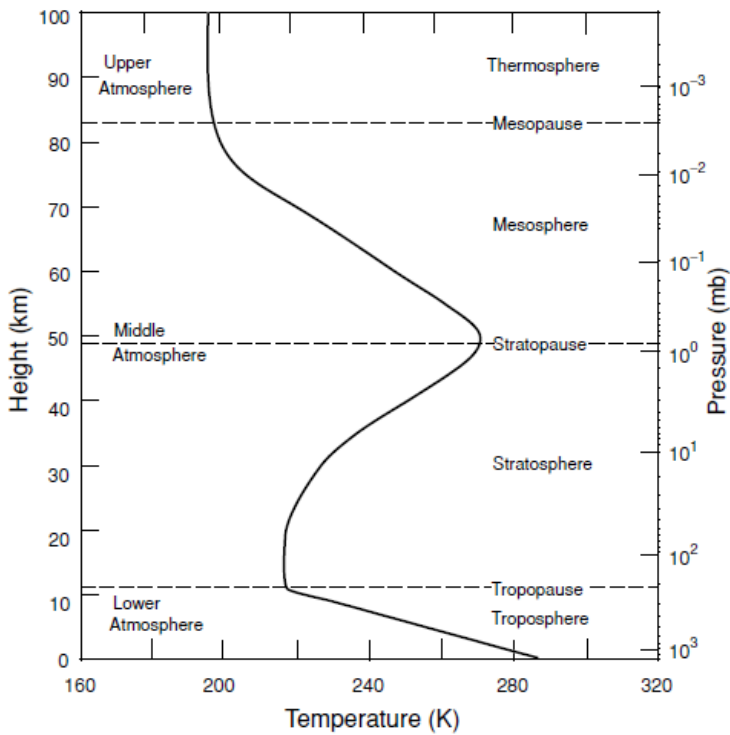
Figure 2.1: Vertical temperature profile after the U.S. Standard Atmosphere and definitions of atmospheric nomenclature (Figure obtain from Liou, 2002).

2.2.2 Atmospheric components

The Earth's atmosphere is mainly constituted of two groups of gases, one with nearly permanent concentrations and another with variable concentrations. The atmosphere also contains different types of particles, clouds and precipitation, which are highly variable in space and time. Table 2.1 lists the chemical formulas and volume ratio for the concentrations of permanent and variable gases. Nitrogen, oxygen, and argon account for more than 99.96% of the atmosphere by volume. The permanent gases have constant volume ratios up to an altitude of about 60 km. The carbon dioxide is listed as a permanent constituent, although its concentration has been increasing by

about 0.4% per year as a result of the combustion of fossil fuels, absorption and release

by the oceans, and photosynthesis (Liou, 2002).

Permanent constituents		Variable constituents	
Constituent	% by volume	Constituent	% by volume
Nitrogen	78.084	Water vapor	0 - 0.04
Oxigen	20.948	Ozone	$0 - 12 \cdot 10^{-4}$
Argon	0.934	Sulfur dioxide	$0.001 \cdot 10^{-4}$
Carbon dioxide	0.036	Nitrogen dioxide	$0.001 \cdot 10^{-4}$
Neon	$18.18 \cdot 10^{-4}$	Ammonia	$0.004 \cdot 10^{-4}$
Helium	$5.24 \cdot 10^{-4}$	Nitric oxide	$0.0005 \cdot 10^{-4}$
Krypton	$1.14 \cdot 10^{-4}$	Hydrogen sulfide	$0.00005 \cdot 10^{-4}$
Xenon	$0.089 \cdot 10^{-4}$	Nitric acid vapor	Trace
Hydrogen	$0.5 \cdot 10^{-4}$	Chlorofluorocarbons	Trace
Methane	$1.7 \cdot 10^{-4}$	(CFCl3, CF2Cl2	
Nitrous oxide	$0.3 \cdot 10^{-4}$	CH3CCl3, CCl4,	
Carbon monoxide	$0.08 \cdot 10^{-4}$	etc..)	

Table 2.1: The Composition of the Atmosphere (Table obtained from Liou, 2002).

The concentrations of variable gases listed in Table 2.1 are small, but they have

important implications in the radiation budget of the atmosphere. The variable gas,

water vapour (H_2O) is the most important component from point of view of its radiative

effect in the Earth's atmosphere. The H_2O concentration varies of important way spatially and temporally. The spatial distribution of H_2O in the tropospheric is determinate by evaporation, condensation and precipitation processes, and also by large-scale transport processes. Specific humidity decreases rapidly with pressure, almost following an exponential function. Specific humidity also decreases with latitude. More than 50% of water vapour is concentrated below ~850 mb, while more than 90% is confined to the layers below ~500 mb.

The ozone concentration also varies significantly with space and time, but it is produced mainly at altitudes from~15 to 30 km. The ozone concentration peak is produced at ~20–25 km, conditioned by latitude and season. Atmospheric ozone is continually produced and removed by photochemical processes associated with solar ultraviolet radiation. The absorption of the most energetic solar ultraviolet radiation by the ozone layer enables the life on earth (Foster el al., 2007). Many photochemical reactions associated with O_3 involve H_2O, CH_4, and CO (Liou, 2002).

Nitrogen oxides (NO_x=NO, NO_2) appear to be important in the determination of both tropospheric and stratospheric O_3 concentrations. Atmospheric NO_x are emitted mainly by combustion processes at the surface and by flying aircraft in large height. In the stratosphere, the major source of NO_x is the dissociation of N_2O by excited oxygen atoms. In the lower atmosphere, the major source of NO_x appears to be the anthropogenic combustion of fossil fuels and biomass burning. Sulphur dioxide in the stratosphere is mainly produced by volcanic eruptions. SO_2 and other sulphur-based gases are believed to be the primary precursors of stratospheric aerosols. Emissions of SO_2 from the surface may be important in the formation of tropospheric aerosols (Liou,

2002). Figure 2.2 shows representative vertical profiles of the gases listed in Table 2.1 for mean midlatitude conditions.
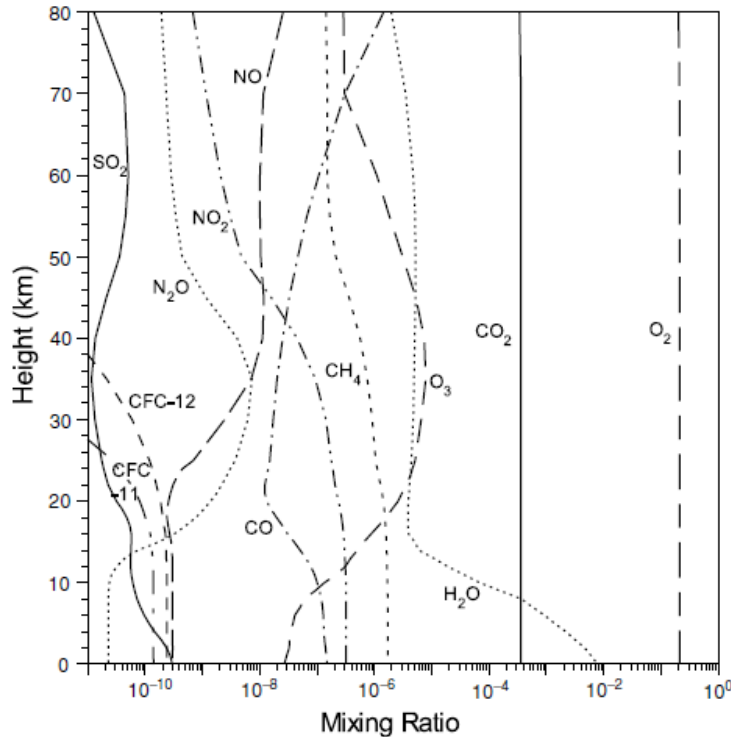
Figure 2.2: Representative vertical profiles of mixing ratios of gases for midlatitude conditions (Figure obtain from Liou, 2002).

2.3 Basic radiometric parameters

The most important process responsible for energy transfer in the atmosphere is electromagnetic radiation. Electromagnetic radiation travels in wave form, and all electromagnetic waves travel at the speed of light. This is $2.99793 \pm 1 \times 10^8$ m sec^{-1} in a vacuum and very nearly the same speed in air. The electromagnetic spectrum is constituted by visible light, gamma rays, x-rays, ultraviolet light, infrared radiation, microwaves, television signals, and radio waves (Liou, 2002).

Let us to consider an amount of radiant energy confined to an element of solid angle. A solid angle is defined as the ratio of the area σ of a spherical surface intercepted at the core to the square of the radius, r (Fig. 2.3). It is defined as:

$$\Omega = \frac{\sigma}{r^2} \qquad (2.2)$$

Units of solid angle are expressed in terms of the steradian (sr). For a sphere whose surface area is $4\pi r^2$, its solid angle is $4\pi sr$. To obtain a differential elemental solid angle, we construct a sphere whose central point is denoted as O. Assuming a line through point O moving in space and intersecting an arbitrary surface located at a distance r from point O, then as is evident from Fig. 2.4, the differential area in polar coordinates is given by:

$$d\sigma = (rd\theta)(rsen\theta d\phi) \qquad (2.3)$$
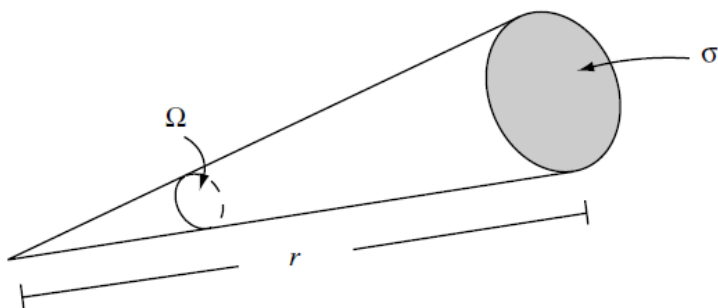
Figure 2.3: Definition of a solid angle Ω, where σ denotes the area and r is the distance (Figure obtained from Liou, 2002).
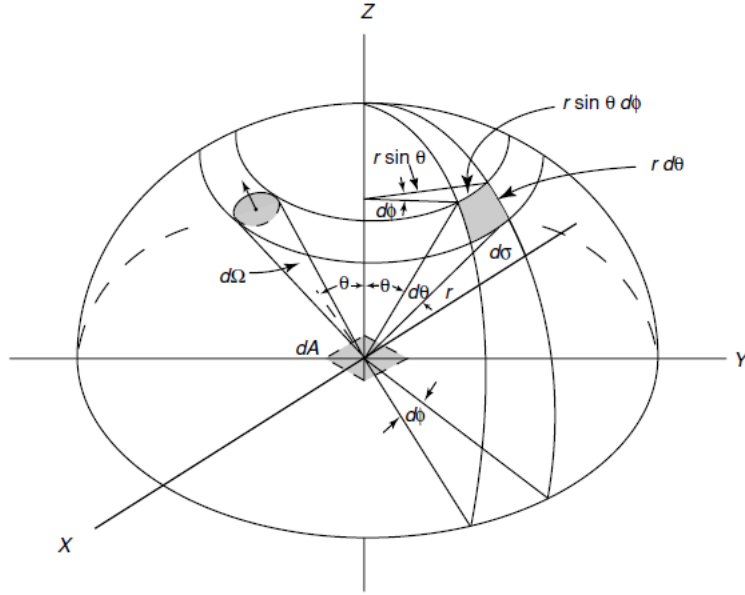
Figure 2.4: Schematic illustration of a differential solid angle and its representation in polar coordinates. Also shown for demonstrative purposes is a pencil of radiation through an element of area dA in directions confined to an element of solid angle $d\Omega$ (Figure obtained from Liou, 2002).

Therefore, the differential solid angle is

$$d\Omega = \frac{d\sigma}{r^2} = sen\,\theta d\theta d\phi \tag{2.4}$$

where θ and $\varPhi$ denote the zenith and azimuthal angles, respectively, in polar coordinates.

Let us to consider the differential amount of radiant energy dE_λ in a time interval dt in the wavelength range, (λ, $\lambda + d\lambda$), which go through an element of area dA displayed in Fig. 2.4, in directions confined to a differential solid angle, which is oriented at an angle θ to the normal of dA. This energy is expressed in terms of the specific intensity I_λ by:

$$dE_\lambda = I_\lambda \cos\theta dAd\Omega d\lambda dt \tag{2.5}$$

representing *cosθdA* the effective area at which the energy is being intercepted. Equation (2.5) defines the monochromatic intensity (or radiance) as follows:

$$I_\lambda = \frac{dE_\lambda}{\cos\theta dAd\Omega d\lambda dt} \tag{2.6}$$

expressed in units of energy per area per time per wavelength and per steradian. It is evident that the intensity implies directionality in the radiation stream. Commonly, the intensity is said to be confined in a pencil of radiation.

The monochromatic irradiance of radiant energy is defined by the normal component of I_λ integrated over the entire hemispheric solid angle and is written as:

$$F_\lambda = \int_\Omega I_\lambda \cos\theta d\Omega \tag{2.7}$$

being in polar coordinates

$$F_\lambda = \int_0^{2\pi}\int_0^\pi I_\lambda(\theta,\phi)\cos\theta sen\theta d\theta d\phi \tag{2.8}$$

If the radiation is isotropic (independient of direction) then we obtained

$$F_\lambda = \pi I_\lambda \tag{2.9}$$

Integrating for entire electromagnetic spectrum we obtained the total monochromatic irradiance of radiant energy (energy per area per time):

$$F = \int_0^\infty F_\lambda d\lambda \tag{2.10}$$

Moreover, the radiant power f, in W (energy per time), is defined by:

$$f = \int_A F dA \qquad\qquad (2.11)$$

Table 2.2 shows a summary of the radiometric parameters with its units.

Radiometric quantity	Symbol	Unit
Radiant energy	E	J
Radiant flux	f	W (Joule per second)
Radiant flux density (Irradiance)	F	Wm^{-2}
Radiant intensity	I	Wsr^{-1}
Radiance	L	$W\,m^{-2}sr^{-1}$

Table 2.2: Radiaometric symbol and units (Table obtained from Liou, 2002).

2.4 Scattering and absorption processes in the atmosphere

In order to research the attenuation affecting to solar electromagnetic radiation which go through the Earth's atmosphere, is important to know the absorption and scattering processes produced by atmospheric components as gases and particles.

The attenuation of solar radiation caused by solid and/or liquid particles is mainly the result of a two processes combination (absorption and scattering). i) Absorption: the energy becomes part of the internal energy of the particle. As a

2. Fundamentals

consequence the radiation that reaches the Earth's surface without a change in its direction (direct radiation) suffers attenuation. ii) Elastic scattering: in this process the energy transported by an electromagnetic wave is scattered in every direction as a consequence of the interaction of this wave with the particles in the medium. Part of the scattered radiation comes back to the space and another part reaches the Earth's surface. Thus, in this process the incident energy does not form part of the internal energy of the particle. In this process the scattered radiation has the same wavelength that incident radiation. iii) Inelastic scattering: in this process the energy transported by an electromagnetic wave is scattered in every direction as a consequence of the interaction of this wave with the particles in the medium. However, in this case the radiation scattered has different wavelength that incident radiation.

The medium's capacity to absorb and scatter radiation is quantify using absorption and scattering coefficients, $\sigma_{a\lambda}$ and $\sigma_{s\lambda}$. The extinction coefficient, $\sigma_{e\lambda}$, which is defined as the sum of the $\sigma_{a\lambda} + \sigma_{s\lambda}$, represents the radiant flux fraction per unit of extinction thickness of a radiation beam in a given direction. Gustav Mie (1908) solved the Maxwell equations for the problem of the interaction of an electromagnetic wave with a sphere, assuming that the sphere is homogeneous and isotropic. Mie reached to an expression for the extinction coefficient, $\sigma_{e\lambda}$, for a suspension of spherical particles of different radii (between r_1 and r_2):

$$\sigma_{e\lambda} = \int_{r_1}^{r_2} \pi r^2 Q_e(r,\lambda) n(r) dr \qquad (2.12)$$

where Q_e is the extinction efficiency factor and can be understood as the effectiveness with which the particle interacts with radiant flux, and n(r) is the size distribution of those spherical particles.

The scattering processes depend on the size parameter, x, defined as a relation between the radius of the particles and the wavelength of the incident wave, and also on the complex refractive index, m, which depends on the chemical composition of the particle. The spherical size parameter is;

$$x = \frac{2\pi r}{\lambda} \qquad (2.13)$$

i) If $x < 0.6/n$, with n the real part of the complex refractive index of the particles. In this case, assuming that the scattering nuclei are small compared to the wavelength, the spectral distribution of sky radiance is describe by Rayleigh theory. The solution presents a dependency of the intensity of the scattering proportional to λ^{-4} and a little dependency of the scattering angle.

ii) If $0.6/n < x < 5$, the scattering is explained by Mie theory. It is applied when the size of the particles is comparable to the incident wavelength ($x \sim 1$), producing interference patterns with the partial waves emitted by multipoles of the particles having phase differences. For this reason there is a strong angular dependency, increasing in the forward scattering (compared to Rayleigh pattern) and the chromatic dependency of the scattering is smaller.

iii) If $x > 5$, the scattering is mainly a process the diffuse reflexion that usually doesn't happen in the Earth's atmosphere. In this case is used the geometric optic.

The angle between the incident and scattering directions is known as scattering angle, Θ. If $\Theta = 0°$ the scattering is fully produced in the direction of the wave propagation. For $\Theta > 90°$ it is produced backscattering. Figure 2.5 shows the differences in the scattering for Rayleigh and Mie theories. Rayleigh is symmetric respect to the plane perpendicular to the propagation direction and find its minimum at $\Theta = \pm 90°$, being its maximums at $\Theta = 0°$ and $\Theta = 180°$. On the other hand, Mie scattering presents an asymmetry pattern, with a strong forward scattering.
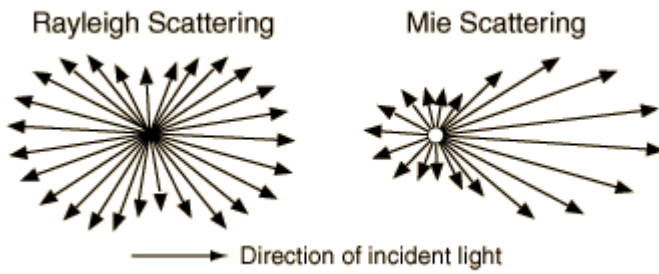
Figure 2.5: Left, Rayleigh scattering. Right, Mie scattering.

On the other hand, solar radiation is also partially absorbed by the atmospheric components increasing their internal energy and therefore their temperature. The main molecules absorbers are H_2O (water vapour), CO_2, O_3, N_2O, O_2, CH_4, N_2; hydrocarbon combinations C_2H_4, C_2H_6, C_3H_8; and sulphurous gas H_2S. Mostly of these absorbers are active mainly in the near-and far-infrared wavelengths regions (from 0.7 to 100 um). Atomic gases as O and N, on the contrary, absorb mainly the maximum

UV and shorter wavelengths. Figure 2.6 shows the solar spectrum outside of the Earth's atmosphere and solar spectrum that reaches the Earth's surface.
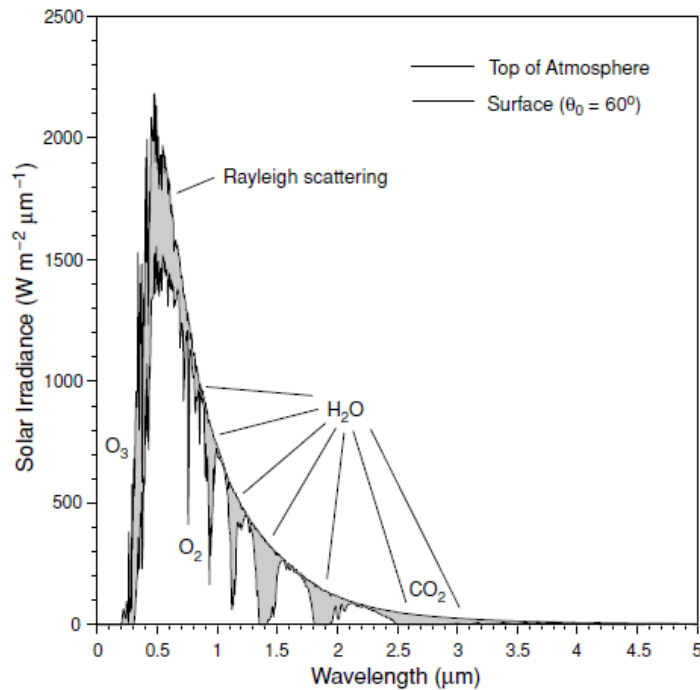
Figure 2.6: Solar irradiance outside atmosphere and at the surface for a solar zenith angle of 60° in an atmosphere without aerosols or clouds. Absorption and scattering regions are indicated. (Figure obtained from Liou, 2002).

2.5 Radiative Transfer Equation

A radiation beam traveling through a medium will be attenuated by its interaction with this medium. If the intensity of incident radiation is I_λ after it travels thought a thickness ds in the direction of its propagation becomes $I_\lambda + d I_\lambda$, then:

$$dI_\lambda^1 = -\sigma_e I_\lambda ds \tag{2.14}$$

representing σ_e the extinction coefficient for radiation of wavelength λ. As discussed in Section 2.4, the extinction coefficient is the sum of the absorption and scattering coefficients. Thus, the reduction in intensity is due to absorption by the material as well as to scattering by this.

On the other hand, the radiation's intensity can be increased by emission from the material plus multiple scattering from all other directions (Fig. 2.7). We define the source function coefficient (J_λ) as the increase in intensity due to emission and multiple scattering is given:

$$dI_\lambda{}^2 = \sigma_e J_\lambda ds \qquad (2.15)$$

where the source function coefficient J_λ has the same physical meaning as I_λ. If we combine the equations (2.14) and (2.15):

$$dI_\lambda = -\sigma_e I_\lambda ds + \sigma_e J_\lambda ds \qquad (2.16)$$

If we divide this expression by $\sigma_e ds$, the result is the general radiative transfer equation:

$$\frac{dI_\lambda}{\sigma_e ds} = -I_\lambda + J_\lambda \qquad (2.17)$$

which is fundamental to the discussion of any radiative transfer process.
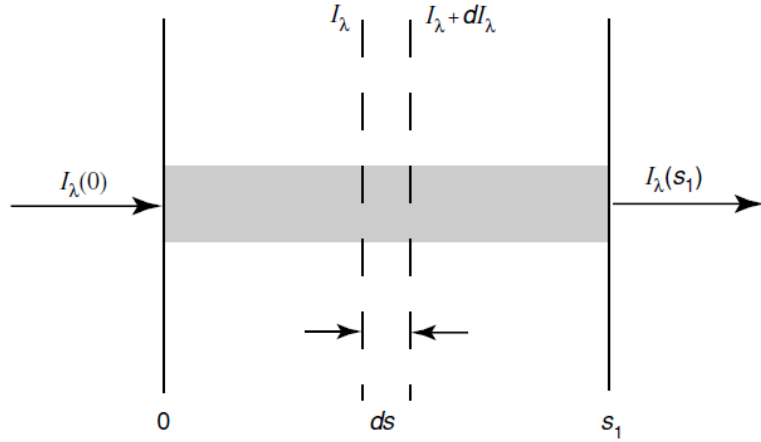
Figure 2.7: Attenuation of a radiation beam which travel thought of the thickness *ds* (Figure obtained from Liou, 2002).

This equation is the "***Radiative transfer general equation***", and it is the main expression in the radiative transfer processes. There are two components, the first one by attenuation because scattering and absorption, and second one by gain because emission by the medium and scattering multiple in all directions.

Beer-Bouguer-Lambert Law: Consider a direct light beam from the sun, which covers the wavelengths from about 0.2 to 5 μm. Emission contributions from the Earth–atmosphere system can be generally neglected. Therefore, if the diffuse radiation produced by multiple scattering can be neglected, then Eq. (2.17) reduces to the following form:

$$\frac{dI_\lambda}{\sigma_e \, ds} = -I_\lambda \qquad (2.18)$$

Let us considered that intensity in *s*=0 is $I_\lambda(0)$. Then the outgoing intensity at a distances *s* will be obtained integrating the equation (2.18):

$$I_\lambda = I_\lambda(0)e^{-\int_0^s \sigma_e ds} \tag{2.19}$$

Let us to consider a non-scattering medium in local thermodynamic equilibrium. A beam of intensity I_λ travels through it will modify by absorption and emission processes simultaneously. This situation is given in the Earth and the atmosphere which emitted thermal infrared radiation. The source function, J_λ, is given by the Planck function, and can be expressed as:

$$J_\lambda = B(T) \tag{2.20}$$

Therefore, according to the before expression the equation of radiative transfer can be written as:

$$\frac{dI_\lambda}{\sigma_e ds} = -I_\lambda + B(T) \tag{2.21}$$

where the first term in the right-hand side of Eq. (2.21) indicates the reduction of the radiant intensity due to absorption, while that the second term represents the increase in the radiant intensity arising from blackbody emission of the material. To solve this equation, we define the monochromatic optical thickness of the medium between two points, s and s_1 (Figure 2.8) as:

$$\tau_\lambda^*(s_1, s) = \int_s^{s_1} \sigma_e ds' \tag{2.22}$$

Considering that

$$d\tau_\lambda^*(s_1, s) = -\sigma_e ds \tag{2.23}$$

The equation 2.21 can be written as:

$$-\frac{dI_\lambda}{d\tau_\lambda^*(s_1,s)} = -I_\lambda + B[T(s)]$$ (2.24)
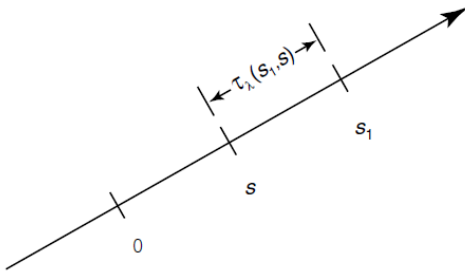
Figure 2.8: Attenuation of a radiation beam which travel thought of the thickness *ds* (Figure obtained from Liou, 2002).

If multiplying Eq. (2.24) by a factor $e^{-\tau^*(s_1,s)}$, and integrating the thickness *ds* from 0 to s_1, we obtain

$$I_\lambda(s_1) = I_\lambda(0)e^{-\tau_\lambda^*(s_1,0)} + \int_0^{s_1} B_\lambda[T(s)]e^{-\tau_\lambda^*(s_1,s)}\sigma_e ds$$ (2.25)

where the first term in Eq. (2.25) represents the attenuation of the radiant intensity by absorption of the medium. The second term represents the emission contribution from the medium along the path from 0 to s_1.

Thus, the problem consists in to solve the equation 2.17 for a medium equivalent to the atmosphere as real as possible. The simplest geometry is a layer limited by two parallel and infinite planes, where the properties are constant and the incident radiation is also constant. This is the case of the plane-parallel atmospheres that constitute a good

approximation for the real atmosphere, where the vertical variations are faster than the horizontal variations for all the magnitudes. In this situation is convenient measuring the distance over the vertical direction z, normal to the stratification plane (Figure 2.9).
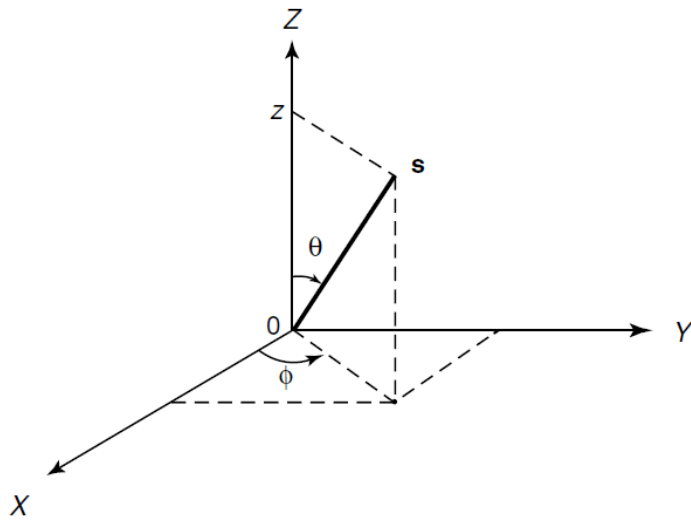
Figure 2.9: Coordinates defining a point in plane-parallel atmosphere. θ is the zenith angle while Φ is the azimuthal angle, and s represents the position vector (Figure obtained from Liou, 2002).

According to the geometry in figure 2.9 it is defined the relative optic mass as:

$$m_r = \frac{\int_0^s \rho\, ds}{\int_0^z \rho\, dz} \tag{2.26}$$

where ρ is the density of medium. θ is the solar zenithal angle defined as the angle between the zenith (the vertical direction) and the direct solar irradiance path. In the real atmosphere, the expression to the relative optic mass as function of the zenithal angle was given by Kasten and Young (1989) as:

$$m_r = (\cos\theta + 0.15(93.885 - \theta)^{-1.253})^{-1} \tag{2.27}$$

However, in the case the plane-parallel atmosphere, this expression can be approximated as (Iqbal, 1983):

$$m_r = \sec\theta = \frac{1}{\cos\theta} = \frac{1}{\mu} \tag{2.28}$$

Equation 2.28 considers a uniform atmosphere with refractive index equal to one. This approximation can be applied for θ smaller than 80º. Applying the variable change $dz=\mu ds$ in equation 2.22, we obtain the optical depth as:

$$\tau_\lambda = \int_0^\infty \sigma_e dz \tag{2.29}$$

The relationship between optical thickness and optical depth is:

$$\tau_\lambda^* = \tau_\lambda m_r \tag{2.30}$$

Thus, taking into account this relationship, the general equation of radiative transfer defined in Equation (2.17) is written as:

$$\mu\frac{dI(\lambda,\tau_\lambda,\mu,\phi)}{d\tau_\lambda} = -I(\lambda,\tau_\lambda,\mu,\phi) + J(\lambda,\tau_\lambda,\mu,\phi) \tag{2.31}$$

Let us assume that the input radiance does not vary with time, does not present horizontal gradients and that the atmosphere is isotropic. Multiplying the equation 2.31 by $e^{-\tau_\lambda/\mu}$ and integrating between $\tau_o = 0$ (top of the atmosphere) and τ_λ, we obtain the solution for outgoing radiance through the atmosphere from level τ_λ:

$$I(\lambda,\tau_\lambda,\mu,\phi) = I(\lambda,\tau_\lambda,\mu,\phi)e^{\frac{-(\tau_\lambda-\tau_{0\lambda})}{\mu}} + \frac{1}{\mu}\int_{\tau_\lambda}^{\tau_0} J(\lambda,\tau_\lambda',\mu,\phi)e^{\frac{-(\tau_\lambda-\tau'_{0\lambda})}{\mu}} d\tau_\lambda' \tag{2.32}$$

In case of the solar direct irradiance, where the contributions for emission and scattering in directions other than the direct flux can be neglible, the solution to the radiative transfer equation can be reduced to the Beer-Bouguer-Lambert Law:

$$I_\lambda(\tau_\lambda, \mu, \phi) = I_\lambda(\tau_0, \mu, \phi)e^{\frac{-(\tau_0 - \tau_\lambda)}{\mu}} \qquad (2.33)$$

This equation indicates that the attenuation of the monochromatic direct irradiance by the plane-parallel atmosphere follows an exponential function.

2.6 The atmospheric aerosol

Atmospheric aerosol can be considered as the system composed by a gas and solid or liquid particles suspended on the atmosphere at least several minutes. The atmospheric aerosol is a trace component in the atmosphere (1 a 100 ppb of the air mass) that presents a large variability in the space and time, as well as in its size, shape and chemistry composition. The atmosphere contains particles ranging in size from a few nanometers to tens of micrometers in diameter, and shows also large vertical variability (e.g. Escudero et al., 2005, 2011; Guerrero-Rascado et al., 2009; Cordoba et al. 2011; Tesche et al., 2011). These particles show highly variable densities.

2.6.1 Aerosol classification

The atmospheric aerosol can be classified from sources (natural or anthropogenic), formation mechanics (primary or secondary), chemistry composition (inorganic, mineral, marine …), or its size (nucleation, accumulation or coarse modes) (e.g.Seinfeld and Pandis, 2006; Eck et al., 2010).

Classification from sources

The atmospheric aerosol can be emitted to the atmosphere as natural processes or as anthropogenic processes. The atmospheric aerosol which has natural origin is constituted by particles generates in mechanical processes which conduct to the direct injection of particles into the atmosphere (mineral dust, marine, etc.). There is also occasionally important emission from volcanic eruptions, fires, sea spray and other natural processes. On the other hand, the anthropogenic particles are injected to the atmosphere in human activities processes as industrial activities or carbon particles produces in combustion processes. We can also include mineral particles emitted in human activities.

Classification from formation processes

The particles can be injected to the atmosphere in primary processes or in secondary processes. The primary particles are emitted directly to the atmosphere. Their origin are mostly in natural sources (deserts, ocean), while in local scales the anthropogenic emissions can be determinant (e.g. road traffic, industrial processes). The secondary particles are produced by gas-to-particle conversion. Gas-to-particles conversion includes the production of solid and liquid particles from substances in gas form. This production is due to the formation of new particles (homogeneous condensation) or the condensation on existing particles (heterogenic condensation).

2. Fundamentals

Classification from chemistry composition

According to their chemistry composition the atmospheric aerosol is classified in the follows group: mineral aerosol, marine aerosol, organic aerosol and elemental carbon.

Mineral aerosol: Deserts are a large source of airborne particles. On a global scale the desert aerosol contributes 60–1800 Tg/year of the total yearly production of 2900–4000 Tg (Jaenicke, 1988). Wind blown dust is the major contributor to atmospheric particles. The desert dust particles are generated by mechanical processes and thus are not spherical, many electron micrographs have shown this (e.g. Iwasaka et al., 2003). The mechanical production of particles results in particle sizes usually larger than 1 µm. Electron microscopic analysis of individual particles of the Sahara aerosol gave a maximum in the mass size distribution of 5 µm (Falkovich et al., 2001). The life time of the particles in the atmosphere is limited to 1–10 days (Jaenicke, 1988). For example, a 0.3 µm particle has a residence time of 8 days, a 10 µm particle resides 1 day, for 1 and 5 µm the residence times are 5 and 2 days.

Besides natural dust particles, we may consider the anthropogenic mineral dust. They are emitted in human activities as building, miner, etc. The road traffic can also be other mineral particles source (e.g. Querol et al., 2001).

Marine aerosol: Sea-salt aerosols are the leading contributors to the global-mean clear-sky radiative balance directly over oceans (Haywood et al., 1999) and indirectly (O'Dowd et al., 1999). Due to that two-thirds of the surfaces of the Earth are oceans the marine aerosol is very important. This particles type are generated in maritime-ocean environments because the wind hit the water surface injecting small water drops which

are transporting by air masses. These drops in suspension evaporate part of the water until to reach the saline saturation, and in thermodynamic favourable conditions appear the crystallization. The size ranges between 0.1 and 100 µm.

Carbonaceous substances: Light-absorbing carbon particles are the most abundant and efficient light-absorbing components in the atmosphere in the visible spectrum. These particles are a product of incomplete combustion of carbon-based fuels such as from industrial processes, motor vehicles, and biomass burning (Lewis et al., 2008). Combustion-produced particles are predominately fine mode particles (typically radius < ~1 mm) (Eck et al., 2010). In combustion produced aerosols the principal absorber is soot or black carbon, which exhibits absorption throughout the entire solar spectrum due to a relatively spectrally constant imaginary index of refraction (Bergstrom et al., 2002).

Sulphates: The sulphates in the atmosphere are usually particles of secondary origin. They are generated as a result of oxidation of gaseous precursors (mainly SO_2) (Penner et al., 2001). The diameter of these types of particles usually is below 1 µm. There are also natural and anthropogenic sources of primary sulphates such as industrial processes for the production of sulphuric acid. The anthropogenic sulphates are around in half of total (regions with dense population and industrialized), and they are produced in general in processes with fossil fuels, mainly carbon (Coal combustion involves a 60% of anthropogenic sulphate emissions and oil implies for 28%) (Warneck, 1988). Natural sulphates are mainly by marine phytoplankton (around 19%) and volcanic emission (around 7%).

Nitrates: The elemental composition of this particles type is nitrogen. The most of these particles are secondary origin, formed from precursor natural or anthropogenic gases. These compounds represent approximately 2-5% of global emissions at ground level. The diameter of the resulting atmospheric particles is usually $< 1\mu m$. Nitrated compounds of natural origin usually originate from the biomass burning and biogenic emissions (e.g.Seinfeld and Pandis, 2006).

Volcanic sources: The volcanic eruption emitted an aerosol type which has a large radiative effect. Therefore, it has a large important due to its climatic effect. It is injected sporadically, but in a very intense reaching the stratosphere, where it can stay up to more one year. Once the particles reach the stratosphere, are redistributed along around the planet through global circulation. The large eruption of the Pinatube volcano in 1991 provided an unprecedented opportunity to study the dispersion of dense volcanic aerosol plumes across world (Alados-Arboledas et al., 1997; Olmo et al., 1999) and the impact of these volcanic aerosol layers on atmospheric processes. The particles emitted in the volcanic eruptions are mainly constituted by ash particles with diameters above 1 μm and H_2SO_4 drops with radii in the range 0.001 and $1\mu m$.

Classification from their size range

According to the classification of Whitby (1980), are identified the nucleation, accumulation and coarse modes (Figure 2.10).

Nuclei mode: This mode is constituted by particles with diameter from 0.005 to $0.1\mu m$, which are emitted to the atmosphere by combustion and conversion process of gas to particle. Due to small size the particles which constituted this mode are a mass

minimum fraction of the total aerosol. They are lost mainly by coagulation with larger particles.
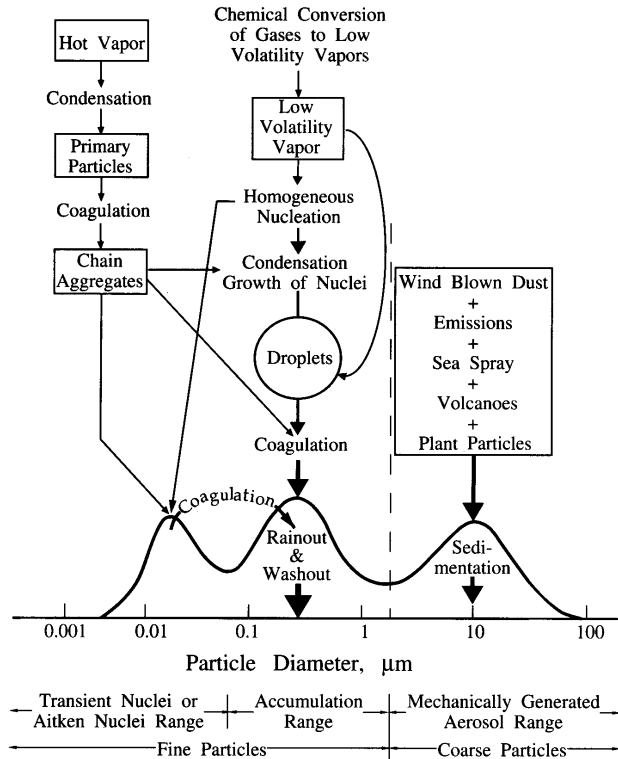
Figure 2.10: Distribution of particle surface area of atmospheric aerosol. Formation process, sources, particle modes and removal mechanisms (Whitby and Cantrell, 1976).

Accumulation mode: This mode contains particles extending from 0.1 to 2.5 μm diameter formed from coagulation of particles in the nuclei mode and from condensation of vapours onto existing particles, causing them to grow into this size range. The accumulation mode is so named because particle removal mechanisms are least efficient in this regime, causing particles to accumulate there.

Coarse mode: This mode is constituted by particles with diameter from 2.5 to 100 μm. These particles usually are primary origin (marine aerosol and mineral

aerosol). In a global scale are mainly natural but in urban areas can have anthropogenic origin. On the other hand, coarse particles can have also secondary origin as some nitrates and sulphates species. The coarse particles are easily deposited and their time of residence in the atmosphere is short, ranging between a few hours until a few days.

2.7 Radiative properties of the atmospheric aerosol particles

The modeling of the atmospheric aerosol radiative effect is performed solving the radiative transfer equation (e.g. Thomas and Stammes, 1999) and it need as input the follows aerosol optical properties: aerosol optical depth ($\tau_{a\lambda}$), which indicate the aerosol load, phase function ($P(\Theta,\lambda)$), which is a normalized function and describes the angular distribution of scattered radiation produced by the aerosol and, therefore, depends on the aerosol type and single scattering albedo (ω_λ), which represents the ratio between the scattered light and the extinction (scattered plus absorbed light). For the Rayleigh scattering, this magnitude is 1.

Microphysical properties

Size distribution: The size of particles ranges approximately between 0.001 and 100 µm in radius, and is described by the size numeric distribution *n(r)* as:

$$n(r) = \frac{dN}{d \ln r} \tag{2.34}$$

representing the number of particles with radius in the logarithmic interval ($\ln r$, $\ln r + d\ln r$). The use the logarithmic scale is useful due to the large range in size of aerosol particles. We can also define the size surface distribution as:

$$s(r) = \frac{dS}{d\ln r} = 4\pi r^2 \frac{dN}{d\ln r} = 4\pi r^2 n(r) \qquad (2.35)$$

representing the surface of particles per unity of air volume for particles with radius in the logarithmic interval ($\ln r$, $\ln r + d\ln r$). We can define the total surface S of the aerosol particles as:

$$S = \int_0^\infty s(r)\,d\ln r \qquad (2.36)$$

In the same way, volume size distribution is defined as:

$$v(r) = \frac{dV}{d\ln r} \qquad (2.37)$$

representing the aerosol volume in an air column of unity cross section per logarithmic particle radius unit. The total number of particles is obtained integrating in total column as:

$$N = \int_0^\infty n(r)\,d\ln r \qquad (2.38)$$

2. Fundamentals

Considering spherical particles, volume and number distributions can be related using the following expression:

$$v(r) = \frac{dV}{d \ln r} = \frac{4\pi}{3} r^3 \frac{dN}{d \ln r}$$

(2.39)

On the other hand, is also important to define the *effective radius* of the distribution as (Van de Hulst, 1957):

$$r_{eff} = \frac{\displaystyle\int_0^\infty r^3 n(r) d \ln r}{\displaystyle\int_0^\infty r^2 n(r) d \ln r} = \frac{3V}{S}$$

(2.40)

representing the relation between the volume and total surface.

It has been observed that the measured size distributions present certain characteristics, and this allows their modeling. The general approach is to represent these size distributions using a mathematical expression with some fitting parameters retrieved by the measurements. Hegg (1993) adopted a log-normal distribution as a good representation of volume size distributions. In our case, we have used the following expression:

$$\frac{dV(r)}{d \ln r} = \sum_{i=1}^2 \frac{V_i}{\sqrt{2\pi}\sigma_i r} \exp\left[-\frac{(\ln r - \ln r_i)^2}{2\sigma_i^2} \right]$$

(2.41)

where *dV(r)/dlnr* is the particle volume size distribution, r is the particle radius, *i* denotes fine or coarse modes, V_i is the volume concentrations, and σ_i the standard deviations. In this work we used mainly the volume size distribution to distinguish clearly the fine and coarse modes.

2. Fundamentals

Optical properties

Aerosol optical depth: The aerosol optical depth ($\tau_{a\lambda}$) is the simplest magnitude to characterize the columnar atmospheric aerosol load (e.g. Holben et al., 2001). The equation 2.24 in section 2.5 is *the Beer-Bouguer-Lambert law*, which represents the attenuation of the monochromatic direct solar flux density as it travels through the atmosphere and reaches the Earth's surface. This attenuation is determined by the optical depth (equation 2.29) which represents the extinction due to the sum of scattering and absorption processes. Thus, the total optical depth, τ_λ, is the sum of scattering and absorption processes of the different atmospheric components. Therefore, the optical depth is expressed as (Pedrós et al., 2003):

$$\tau_\lambda = \tau_{g\lambda} + \tau_{w\lambda} + \tau_{NO_2\lambda} + \tau_{O_3\lambda} + \tau_{R\lambda} + \tau_{a\lambda} \qquad (2.42)$$

where the different subscripts refers the relevant attenuation processes in the solar spectrum: *g* refers to the uniformly mixed gases absorption, NO_2 is the nitrogen dioxide absorption, *w* refers to the water vapor absorption, O_3 to the ozone absorption, *R* refers to the Rayleigh scattering component, and the subscript *a* refers to the aerosol attenuation (scattering an absorption). In Chapter 4 we will discuss about the optical depth computations using the spectral direct irradiance measurements.

On the other hand, the spectral dependence of the optical depth is usually parameterized using the Angström law (Angström, 1964):

$$\tau_{a\lambda} = \beta\lambda^{-\alpha} \qquad (2.43)$$

where α and β are the Angström coefficients. The Angström coefficient, α, characterizes the spectral features of aerosols and is related to the size of the particles (Shifrin, 1995),

while the β coefficient is related to particle concentration and represents the $\tau_{a\lambda}$ at 1µm. Large values of α indicate the prevalence of fine particles from urban-industrial and biomass burning sources, while low values of α are related with the presence of coarse particles such as desert dust and marine aerosols (Dubovik et al., 2002b).

Single scattering albedo: The aerosol optical depth indicates the atmospheric extinction of the incident irradiance due to the scattering or absorption processes. However, when the radiation interacts with particles, part of this radiation is absorbed and another one part is scattered. The Mie theory defines the efficiency factors of scattering ($Q_s(x,m)$) and absorption ($Q_a(x,m)$), where x is the size parameter and m the refractive index. Therefore, for a beam of N particles, we can calculate the scattering and absorption coefficients as (Goody y Yung, 1989):

$$\sigma_s(x,m) = \pi r^2 Q_s(x,m)N \tag{2.44}$$

$$\sigma_a(x,m) = \pi r^2 Q_a(x,m)N \tag{2.45}$$

representing r the radius of particles. The extinction coefficient $\sigma_e(x, m)$ will be the sum of scattering and absorption coefficients $\sigma_e(x, m) = \sigma_s(x, m) + \sigma_a(x, m)$. Taking into account these two definitions it is define the single scattering albedo as:

$$\omega(x,m) = \frac{\sigma_s(x,m)}{\sigma_e(x,m)} = \frac{\sigma_s(x,m)}{\sigma_s(x,m) + \sigma_a(x,m)} \tag{2.46}$$

The single scattering albedo shows the relative importance of the absorption respect to the extinction process. It depends on the relative source strengths of the various aerosol substances and on aging during transport. Absorption of solar radiation by atmospheric aerosols results mainly from elemental carbon originating from biomass

burning and fuel combustion, and from mineral dust. On the other hand, in section 2.5 we showed:

$$\tau_{a\lambda} = \int_0^\infty \sigma_e(z)dz \qquad (2.47)$$

where σ_e depends on the height. Using the equation 2.47 and taking into account the equations 2.44 and 2.45, we can obtain the relation between optical depth and the size distribution, $n(r)$, as:

$$\tau_{a\lambda} = \int_{r_{min}}^{r_{max}} \pi r^2 Q_e(x,m)v(r)d\ln r \qquad (2.48)$$

where r_{min} and r_{max} are the minimum and maximum radius of the particles considered.

Phase function: To describe the angular distribution of scattered energy we define a non-dimensional parameter called the phase function, $P(\Theta)$. It is defined as the fraction of the scattering energy by aerosol in a direction respect to the ratio of the total scattering energy in all directions. According to Mie theory, the phase function, $P(\Theta)$, is defined as:

$$P(x,\Theta) = \frac{\lambda^2}{\sigma_s(x,m)\pi} \int_{r_1}^{r_2} \left(\frac{i_1 + i_2}{2}\right)v(r)d\ln r \qquad (2.49)$$

where i_1 and i_2 are the intensity functions for parallel and perpendicular components of the scattered radiation (Goody y Yung, 1989).

The phase function is normalized in the space being the sum of the energy in all directions equal to solid angle 4π:

$$\int\limits_{0}^{2\pi}\int\limits_{0}^{\pi} P(x,\Theta)sen\Theta d\Theta d\Phi = 4\pi \tag{2.50}$$

In terms of Legendre polynomials P_l, the phase function may be written in the form

$$P(\cos\Theta) = \sum_{l=0}^{N}\varpi_l P_l(\cos\Theta) \tag{2.51}$$

where the expansion coefficient, based on the orthogonal property, is given by to the

$$\varpi_l = \frac{2l+1}{2}\int\limits_{-1}^{1} P(\cos\Theta)P_l(\cos\Theta)d\cos\Theta \tag{2.52}$$

for l=0,1, ….N. The first term of the before expression, l=0, $\varpi_0 = 1$, representing the normalization of the phase function. When l=1, we have

$$g = \frac{\varpi_1}{3} = \frac{1}{2}\int\limits_{-1}^{1} P(\cos\Theta)\cos\Theta d\cos\Theta \tag{2.53}$$

This term is referred to as the asymmetry parameter, which is the first moment of the phase function and an important parameter in radiative transfer. For isotropic scattering, g is zero, as it is for Rayleigh scattering. The asymmetry parameter increases as the diffraction peak of the phase function sharpens and can be negative if the phase function peaks in backward directions (90–180º). For Lorenz–Mie type particles, whose phase function has a generally sharp peak at the 0∘ scattering angle, the asymmetry parameter denotes the relative strength of forward scattering

CHAPTER 3

EXPERIMENTAL SITES AND

INSTRUMENTATION

# 3. Experimental sites and Instrumentation

Chapter 3 carries out a detailed description of the instruments used in this work. In particular, we pay special attention to the sun-photometer CE318, its measurement procedure and its calibration processes. Others instruments used in this thesis will be briefly explained.

3. Experimental sites and Instrumentation

3.1 Experimental sites

3.1.1 Monitoring station of Granada

The mostly part of the instruments used in this study are located on the rooftop of the Andalusian Center for Environmental Studies (CEAMA) at Granada (37.16ºN, 3.61ºW and 680 m a.s.l.). In this station there is available radiometric data from broadband radiometers (ultraviolet, visible and infrared), UV spectroradiometer (Bentham Dm-150c), microwave radiometer RPG-HATPRO G2 and sun-photometers (CIMEL-318-4). This last instrument is included in AERONET network. Besides, the station records continuously sky images using two All-Sky Imager. The station also includes meteorological information as atmospheric pressure, wind, temperature and humidity.

Granada is a non-industrialized medium-sized city with a population of 300,000 inhabitants that increases up to 600,000 when the metropolitan area is included. The city is located in a natural basin surrounded by mountains with altitudes over 1000 m. The near-continental conditions prevailing at this site are responsible for large seasonal temperature differences, providing cool winters and hot summers. The study area also experiences periods of low humidity regime especially in summer. This region is about 200 km from the African continent, and approximately 50 km from the western Mediterranean basin. Due to its proximity to the African continent our study area is often affected by African dust intrusions (e.g. Lyamani et al., 2005; Lyamani et al., 2006a; Olmo et al., 2006, 2008; Valenzuela et al., 2012b). Figure 3.1 shows the location of the Granada city and the radiometric station.

a)
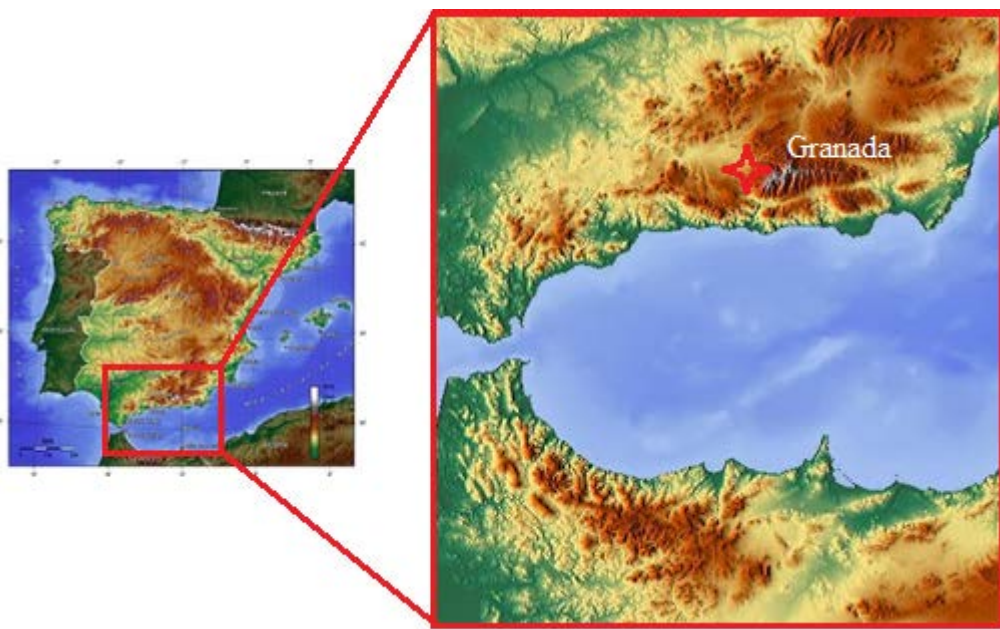
b)
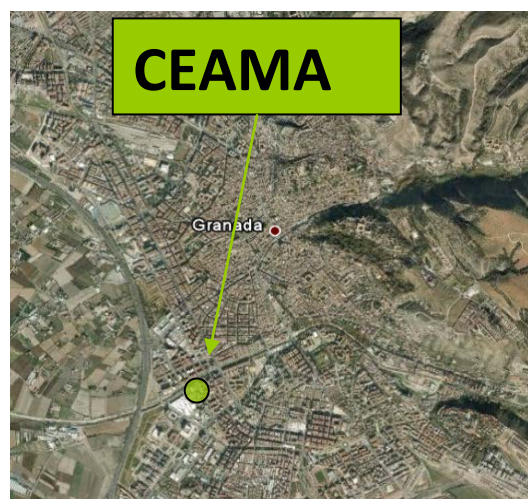
Figure 3.1: a) Location of Granada city and, b) radiometric station (CEAMA).

3. Experimental sites and Instrumentation

3.1.2 Remote Island of Alboran

The remote Alboran Island (35.95º N, 3.03º W, 15 m a.s.l) is placed 89 km away from the Southern coast of the Iberian Peninsula and 65 km from the North African coast (Figure 3.2a, b) nearby to the major sea route of ships. Summertime climates usually are dry and hot in this region due to the influence of the atmospheric subtropical high-pressure belt (Sumner et al., 2001). During winter the subtropical high is shifted to the South, allowing midlatitude storms to enter the region from the open Atlantic and bringing enhanced amounts of rainfall to the Mediterranean. Anomalous torrential rainfalls occur during this season in response to severe storms that are generated locally by extreme atmospheric convective overturn (Romero et al., 1999). It is an uninhabited island which does not have sources of anthropogenic local aerosol and the marine aerosol is expected to be the major contribution. Due to their reduced dimensions, with a length of 629 meters and an extension of 0.072 km^2, and to its strategic location, Alboran Island constitutes an ideal station to characterize aerosol optical and microphysical properties advected from different areas (Europe, Africa, North Atlantic Ocean). The measurements were conducted on the roof of a military complex located on the Alboran Island from June 2011 until January 2012. The solar direct irradiance and sky radiance measurements were registered using a sun-photometer (CIMEL-318-4). Figure 3.2 (a, b) shows the location in the map and image of the Alboran Island.

a)

b)
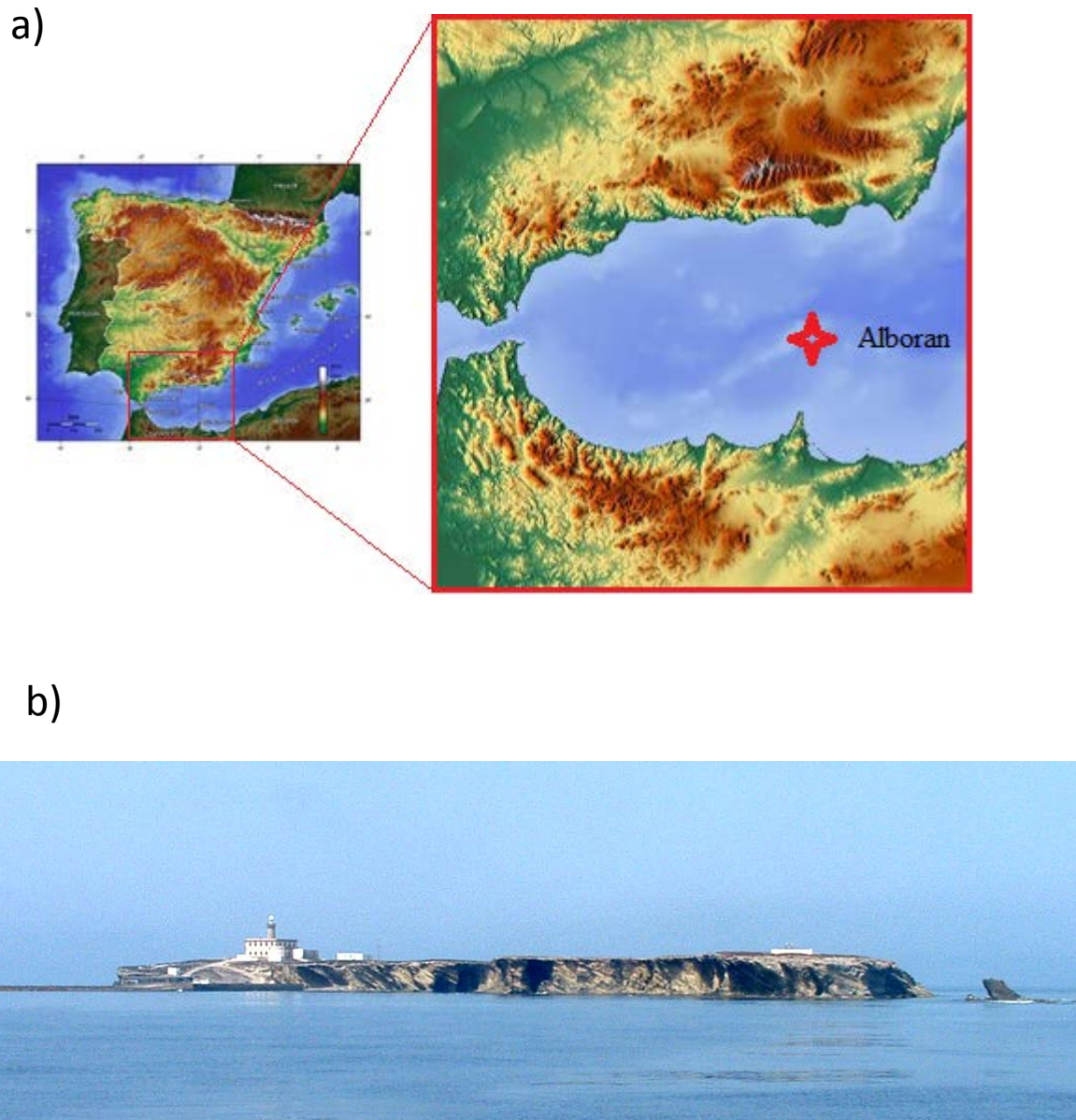
Figure 3.2: a) Location geographic in the map and, b) image of Alboran Island

3.2 Sun-photometer (CIMEL 314-8)

In this section we describe the sun-photometer (CIMEL-318-4) used, which is the standard instrument in AERONET (http://aeronet.gsfc.nasa.gov/) and RIMA

(http://www.rima.uva.es/RIMA/) networks**.** This instrument is used to the atmospheric aerosol characterization as well as of the water vapor. The sun photometer (CE-318-4) is a multi-channel, automatic sun-and-sky scanning radiometer that measures the direct solar irradiance and sky radiance in the almucantar and principal plane configurations at the Earth's surface. Measurements are taken at pre-determined discrete wavelengths in the visible and near-IR parts of the spectrum to determine atmospheric transmission and scattering properties. This instrument is weather-proof and requires little maintenance during periods of adverse weather conditions. It takes measurements only during daylight hours (sun above horizon). Table 3.1 shows the characteristic of radiometer CIMEL 318-4.

Detailed description

The sun photometer CIMEL (318-4) consists of (1) a control and measuring unit (the electronic box); (2) a two axis motorized system; and (3) a sensor head (Figure 3.3). The instrument is made by Cimel Electronique of France.

The following paragraph describes the components that make up the system. The instrument consists of the main stem containing the azimuth motor. On the top of the motor is an attached robot arm consisting of the zenith motor on one side and the sensor head on the other side (http://www.cimel.fr/). The collimators are attached to the sensor head. Inside the sensor head are two silicon detectors, one for each of the collimators. A filter wheel is placed between the collimator windows and the detectors inside the sensor head. The wheel consists of eight narrowband interference filters (at 340, 380, 440, 500, 670, 870, 936 and 1020 nm) mounted along the circumference. The 936 nm filter is used for precipitable water content calculation; the other filters are used for the

columnar characterization of the optical and microphysical properties of the atmospheric aerosol. The FWHM of the filters are 2 nm for the 340 filter, 4 nm for the 380 nm filter and 10 nm for the rest. The slit function of the filters is Gaussian. The two collimators have the same field of view (1.2 degree) but differ in the size of apertures. They are physically part of a single unit that is attached to the sensor head by a long screw tightened down to prevent light and water leakage. The larger aperture collimator (10 times as large as the sun-viewing collimator) provides the necessary dynamic range to observe the sky. The sun tracking is equipped with a four quadrant position detector (for a precise tracking on the sun). Three cables (a thick cable from the sensor head to the control box, and two battery power cables--one each to the motors) are attached to the instrument. The elements of the system are fixed on to a stable and horizontal plane and then the system is leveled with screws.

The Cimel control box consists of a control module with rectangular shaped white box that actually controls the scan and measurement sequence of sun photometer. These electronics can be programmed and the system works automatically following certain protocols established. It can also operate manually. The control box contains two microprocessors for real time operation for data acquisition and motion control. It has an internal battery that services only the software portion of the instrument. The data from the memory of the sun photometer can be transferred to a PC. The data can be retrieved for processing either by modem or internet linkage resulting in near real-time acquisition.

All the cables interconnecting the above components pass through rainproof silicone seals in their respective boxes. A wet sensor, connected to the instrument control box, effectively shuts down the scanning by the sensor head during

precipitation. The fail-safe pointing for the sensor head is the "down" position with the

collimators pointing down toward the base.
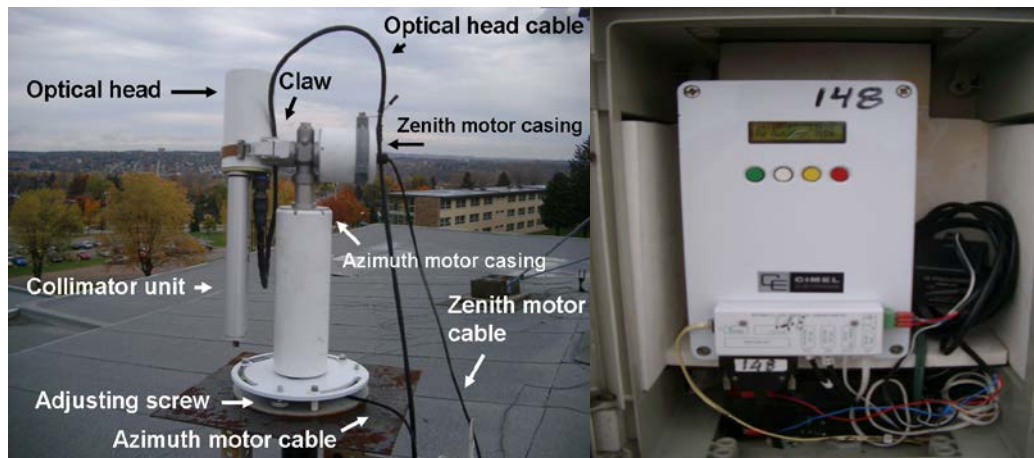
Figure 3.3: Left, CIMEL 318-4. Right, electronic box.

Radiometer CIMEL CE 318-4	
Model	Sun-photometer CE-318-4
Detector	Si Fotodiodes
Number of filters/wavelengths	8 1020-870-670-500-440-936-380-340 nm
FWHM	10-10-10-10-10-4-2 nm
Numbers of colimadores	2
FOV/Aperture	1.2°
For a precise tracking on the sun	4-quadrant position detector Accuracy of 0.05
Measurement types	Direct Almucantar Principal plane
Aplications	Atmospheric aerosol Water vapour
Motoring system	Motor step-by-step acimutal y cenital
Batteries	Internal battery in electronic box External battery to motoring system Solar panel or 220 VAC

Table 3.1: Characteristic of the sun-photometer CE-318-4

Measurement Method

Cimel operates automatically without operator assistance. It measures direct solar irradiance by first pointing the collimator toward the approximate position of the sun (provided it is aligned properly) based on an in-built program that takes into account the time of the year and the coordinates of the location that are input to the Cimel control box prior to operation. A 4-quadrant detector then positions the sun at the center of the fields of view of the collimators by using a feedback control loop. The filter wheel rotates in front of the detector to obtain a measurement sequence. Filters at 340, 380, 440, 670, 500, 870, 936 and 1020 nm are used for the direct irradiance measurements. It takes 10 seconds to measure with all the filters. This is repeated three times at 30 seconds interval to form three measurements per channel (triplet). The triplet is used for the cloud screening (Holben et al., 1998; Smirnov et al., 2000). On the other hand, the measurement sequence is defined according the relative optical air mass. If the optical air mass is less than 2, the triplet is measured every 15 minutes, if the optical air mass is between 2 and 5, the triplet is measured at 0.25 optical air mass intervals. Finally, if the optical air mass is between 5 and 7, the triplet is measured at 0.5 optical air mass intervals.

Filters at 440, 670, 870 and 1020 nm wavelengths are used for the sky radiance measurements in the almucantar and principal plane configuration (Fig.3.4). In the almucantar configuration, the sun-photometers keep the zenith angle constant (equal to the solar zenith angle θs). The measurement sequence previously executes a direct Sun measurement, and then the instrument covers the whole range of azimuth angle, starting at 6º and finishing at 180º. The movement is done first towards right (taking the sun as reference) and then, after pointing the Sun again, is repeated towards the left. The

sequence is repeated for each of the channels and the entire measurement takes about 5 minutes, depending on the instrument version. Measurements are performed every hour between 9 a.m. and 3 p.m. in solar time and also when the optical mass is 4, 3, 2 and 1.7 in both, morning and afternoon. In the principal plane configuration, the azimuth angle is the one that remains constant (and equal to the solar azimuth) and the instrument, after a direct Sun measurement again, take the sky radiance measurements from the different zenith angles. There is not possibility in this case of applying any criterion of symmetry because the different air mass. This positive sign is given to the movement of the instrument from the Sun towards the zenith. Principal plane measurements start 6º below the sun position and continue moving the optical head upwards taking approximately 40 seconds per channel. Measurements are performed every hour when the optical mass is below 2 coinciding with the lower effectiveness of the almucantar measurements.
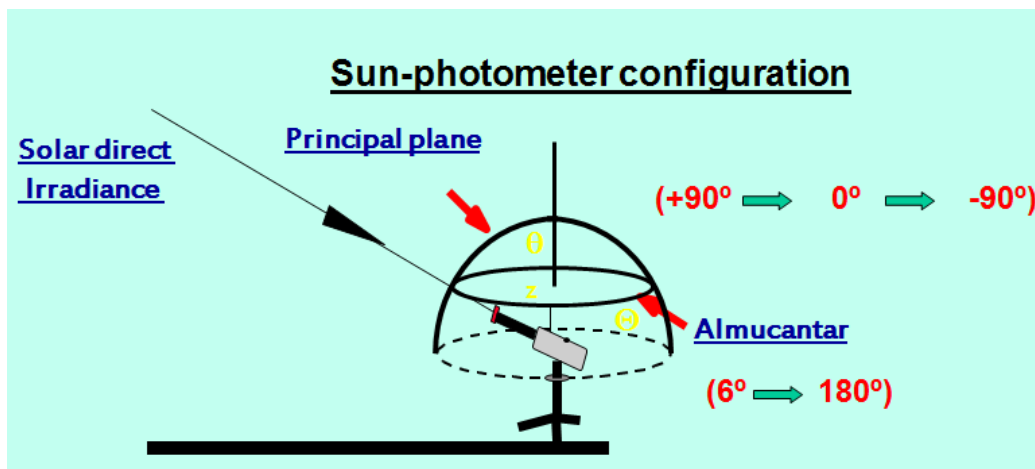

Figure 3.4: Figure describing the two geometries used for the measurements of the sky radiances (Almucantar and principal plane) and Solar direct irradiance configuration.

3. Experimental sites and Instrumentation

In this work we have used two unit of sun photometer CIMEL. The serial numbers which identified each instrument are #394 and #327.

Parameterizations considered

In Chapter 2, we have seen that the solar extinction in the atmosphere is due to the extinction for the different atmospheric constituents (Eq. 2.42). Under cloud-free conditions, the total optical depth (τ_λ) can be separated into the molecular scattering or Rayleigh scattering $\tau_{R\lambda}$, absorption by ozone $\tau_{o\lambda}$, nitrogen dioxide $\tau_{NO2\lambda}$, uniformly mixed gases $\tau_{g\lambda}$ and water vapour $\tau_{w\lambda}$, and, finally, the aerosol scattering and absorption $\tau_{a\lambda}$. The atmospheric components are not equally distributed in the atmospheric profile, so the air mass is different for each one. This is especially true at large solar zenith angles. Thus, we must considering different air masses for each element (Gueymard, 2001). The sun photometer works in the electromagnetic spectrum range 340-1020 nm. According to the filters position, the extinction is produced by ozone, nitrogen dioxide, water vapour, aerosols and Rayleigh.

In order to estimate the optical air masses and the optical depths of the atmospheric constituents, several parameterizations have been considered using the SMARTS 2.9 radiative transfer model (Gueymard, 2001) taking into account a mid-latitude atmosphere. We have used the algorithm provide by Blanco-Muriel et al.(2001) to compute the solar position. However, in order to consider the Earth-Sun distance we have employed the expression used by Michalsky et al. (1988).

The equation to compute the optical air masses is:

$$m_i = \left[\cos Z + a_{i1} Z^{a_{i2}} (a_{i3} - Z)^{a_{i4}}\right]^{-1} \qquad (3.1)$$

where m_i is the optical mass of the different atmospheric components, Z is the solar zenith angle, and the coefficients a_{ij} are given in table (3.2). This equation takes into account the atmosphere curvature smoothing the limitation of the approximation of plane-parallel atmosphere. We have considered the same optical masses for Rayleigh and Aerosols because both optical masses are coincident below 80º of solar zenith angle.

Atmospheric components	a_{i1}	a_{i2}	a_{i3}	a_{i4}
Ozone	2.6845E+2	0.5	115.420	-3.2922
Rayleigh	4.5665E-1	0.07	96.4836	-1.6970
Nitrogen dioxide	6.0230E+2	0.5	117.960	-3.4536
Water vapour	3.1141E-2	0.1	92.4710	-1.3814

Table 3.2: Coefficients for the optical masses (Gueymard, 2001)

The equation 2.33 indicates that the attenuation of the direct irradiance by the plane-parallel atmosphere follows an exponential function. This exponential function is defined like total transmittance. The total transmittance will be the sum of the transmittances of the different atmospheric components (e.g. Gueymard, 2001). The ozone transmittance is defined as:

$$T_{o\lambda} = \exp(-m_o \tau_{o\lambda}) \qquad (3.2)$$

where m_o and $\tau_{o\lambda}$ are the ozone optical mass and ozone optical depth, respectively. The ozone optical depth is calculated using the expression:

$$\tau_{o\lambda} = u_o A_{o\lambda} \tag{3.3}$$

where u_o is its reduced pathlenght (length obtained if total ozone in column vertical are to the surface temperature and pressure, and it is expressed in atm-cm), and $A_{o\lambda}$ is the spectral absorption coefficient given in cm^{-1}. Ozone content is obtained from the OMI instrument on board the AURA satellite (http://aura.gsfc.nasa.gov/instruments/omi.html). The nitrogen dioxide transmittance is calculated as:

$$T_{NO_2\lambda} = \exp(-m_{NO_2} \tau_{NO_2\lambda}) \tag{3.4}$$

where m_{NO_2} is the nitrogen dioxide optical mass and τ_{NO2} is the nitrogen dioxide optical depth obtained using the same expression that ozone optical depth:

$$\tau_{NO_2\lambda} = u_{NO_2} A_{NO_2\lambda} \tag{3.5}$$

where u_{NO_2} is its reduced pathlenght (length obtained if total nitrogen dioxide in column vertical are to the surface temperature and pressure, and it is expressed in atm-cm), and $A_{NO_2\lambda}$ its spectral absorption coefficient. The NO_2 content used is 0.00017 cm-atm given by Kneizys et al. (1988) for mid-latitudes atmosphere. From Beer-bouguer-lambert's law, the Rayleigh transmittance is defined as:

$$T_{R\lambda} = \exp(-m_R \tau_{R\lambda}) \tag{3.6}$$

where m_R is the optical mass and τ_R is the Rayleigh optical depth calculated as (Gueymard, 2001):

$$\tau_{R\lambda} = \frac{p/p_o}{117.3405 \cdot \lambda^4 - 1.3215 \cdot \lambda^2 + 3.2073 \cdot 10^{-4} - 7.6842 \cdot 10^{-5} \cdot \lambda^{-2}} \tag{3.7}$$

where p/p_o is the pressure's correction with the height, being p_o the sea level pressure. In order to compute the water vapour transmittance, Gueymard (2001) performed a slight modification of the functional form proposed by Pierluissi et al. (1989):

$$T_{w\lambda} = \exp\left\{-\left[(m_w w)^{1.05} f_w{}^n B_w A_{w\lambda}\right]^c\right\} \qquad (3.8)$$

where m_w is the water vapor optical mass, w the total precipitable water, c and n are wavelength-dependent exponents calculated as:

$$n = 0.88631 + 0.027274 \cdot \lambda - 3.5949 \cdot e^{-4.5445 \cdot \lambda} \qquad (3.9)$$

$$c = 0.53851 + 0.003262 \cdot \lambda - 1.5244 \cdot e^{-4.2892 \cdot \lambda} \qquad (3.10)$$

The $A_{w\lambda}$ are the water vapour absorption coefficients obtained from MODTRAM radiative model transfer. The MODTRAN absorption calculations are themselves based on HITRAN, a high resolution spectroscopic atlas for line-by-line calculations (e.g. Rothman et al., 1992). B_w is a correction factor because to that the absorption process varies with the distance from the band center and it is calculated as:

$$B_w = h(w,m)e^{0.1916 - 0.0785 m_w + 4.706 \cdot 10^{-4} \cdot m^2{}_w} \qquad (3.11)$$

$$h(w,m) = 0.624 \cdot m_w \cdot w^{0.457} \qquad A_{w\lambda} < 0.01 \qquad (3.12)$$

$$h(w,m) = (0.525 + 0.246 \cdot m_w \cdot w)^{0.45} \qquad A_{w\lambda} > 0.01 \qquad (3.13)$$

On the other hand, f_w is a pressure scaling factor that compensates for inhomogeneities in the water vapor pathlength by application of the Curtis–Godson approximation:

$$f_w = k_w \left[0.394 - .26946 \cdot \lambda + (0.46478 + 0.23757) \cdot (p/p_o) \right] \qquad (3.14)$$

$$k_w = (0.98449 + 0.023889 \cdot \lambda) \cdot w^q \quad \text{para } \lambda > 760 \text{ nm} \qquad (3.15)$$

$$q = -0.2454 + 0.037533 \cdot \lambda \qquad (3.16)$$

AERONET calibration protocol

The sun-photometer CIMEL CE-318-4 is included in the AERONET network. Therefore, calibrations of this instrument were performed by the AERONET-RIMA team.

Direct solar irradiance calibration (Langley calibration)

The field instruments are calibrated by comparison (inter-calibration) with reference instruments previously calibrated at high altitude stations. The accuracy of the reference calibration is about 0.5%, whereas for field instruments the calibration uncertainty is 1-2% (larger for shorter wavelengths) due to uncertainty in the calibration transfer (Holben et al., 2006). The inter-calibration procedure is based on the realization of simultaneous co-located measurements of the reference and the instruments to calibrate under certain atmospheric conditions (explained previously). These restrictions are: clear sky and aerosol optical depth (440 nm) stable and below 0.3 and the availability of enough co-located measurements to ensure the stability of the ratios between reference and field instrument over a wide range of air masses. Once these conditions are satisfied the field instrument can be calibrated just by a ratio of raw

signals of each channel ($V_{0field}(\lambda)$) with the reference raw signal ($V_{0reference}(\lambda)$) (Torres, 2012):

$$V_{0\,field}(\lambda) = V_{0reference}(\lambda)\frac{V_{field}(\lambda)}{V_{reference}(\lambda)} \tag{3.17}$$

The calibration of the reference instruments is carried out by the Langley plot method. According to the Beer–Bouger–Lambert attenuation law, the voltage, $V_{reference}(\lambda)$, obtained when the directly transmitted solar irradiance is observed over a small bandpass $\Delta\lambda$ centered at wavelength λ, is:

$$V_{reference}(\lambda) = \left(\frac{R_o}{R}\right)^2 V_{oreference}(\lambda) \cdot \exp(-m_o\tau_{ext}(\lambda)) \tag{3.18}$$

where $V_{oreference}(\lambda)$ is the instrument calibration constant, m_o is the relative optical mass, R_o is the Earth–Sun mean distance, R is the Earth–Sun distance in the measurement's time and $\tau_{ext}(\lambda)$ is the total atmospheric optical depth. From here the ratio R_o/R is named r. Taking the logarithm of Eq. (3.18) leads to:

$$\ln V_{reference}(\lambda) = \ln(r^2 \cdot V_{oreference}(\lambda)) - m_o\tau_{ext}(\lambda) \tag{3.19}$$

If a series of measurements is taken over a range of m_o during which total atmospheric optical depth, $\tau_{ext}(\lambda)$, remained constant, $V_{o\,reference}(\lambda)$ may be determined from the ordinate intercept of a least-squares fit when one plots the left-hand side of Eq. (3.19) versus m_o.

Systematic errors may arise from the finite bandwidth of the instrument, the contribution from diffuse light to the direct irradiance measurement, errors in air-mass determination, the systematic diurnal variation of optical, instability of the instrument,

no linearity between the response of the instrument and the irradiance incident and errors in the determination of $V_{o\,reference}(\lambda)$.

The Beer–Bouger-Lambert law is strictly valid for monochromatic radiation only and its application about a finite filter's bandwidth produces errors which increase with the width of the filter. These errors are below 0.1% if we used filters with bandwidth lower than 10 nm for wavelengths higher than 450 nm and filters with bandwidth lower than 5 nm for wavelengths between 370 and 450 nm (Box, 1981). The instrument used in this work have filters with bandwidth of 10 nm in visible spectrum and filters with bandwidth of 4 y 2 nm at 380 y 340 nm wavelengths, respectively.

Other error source is the diffuse radiation because the solid angle subtended by the Sun is smaller than solid angle subtended by the instrument. The particles nearby to the Sun's location produces diffuse radiation which entering the radiometer. The measurement will be the sum of direct solar irradiance and a small contribution of diffuse radiation. Grassl. (1971) computed circumsolar radiation as function of aerosol type, field of view (FOV), wavelength, and optical depth. For λ=450 nm, $FOV = 2°$, and optical depth $\tau_{ext} = 0.1$ circumsolar radiation represents 0.4% of the total incoming radiation. The error in the $V_{o\,reference}(\lambda)$ determination is considerably lower than the fractional contribution of the diffuse light to the total signal. Considering the fact that our measurements were performed with a field of view of 1.2°, we find that the influence of circumsolar irradiance on the determination of $V_{o\,reference}(\lambda)$ is negligible.

The factor which can produce the largest error in the Langley calibration is instability in the atmospheric optical depth. It is necessary that the optical depth is remaining constant during the calibration process. This instability can be due to convection processes, wind and aerosol presence. In this sense, in order to calibrate is

convenient to select sites far of aerosol sources. In addition, water vapor also presents a significant short-term variability. Therefore high altitude stations, located high above the boundary layer, are very adequate for these Langley absolute calibrations because both the aerosol and the water vapor content are low and may be often considered constant. The AERONET reference instrument is calibrated in the Mauna Loa Observatory (19.5º N-155.6º W, 3397 msl), whereas PHOTONS and RIMA calibrate their masters at Izaña Observatory (18.3 Nº-16.5º W, 2373 msl). The optimal optical masses in the spectrum visible to calibrate range between 2 and 6 (Harrison and Michalsky, 1994) and from 1.2 to 2.2 in UV spectrum (Slusser et al., 2000).

Sky radiance calibration

In order to calibrate the sky radiance is required calibration standard instrument. The radiance calibration is made with an integrating sphere (uniform radiance source). The uncertainty estimated by the manufactured for this instrument is of 2% for 380-800 nm range increasing until a 5% at 1100 nm. This sphere is in turn calibrated with a reference instrument, which is calibrated at GSFC Calibration Facility to a NIST standard. Field instruments are calibrated in radiance before and after a measurements period. The integrating sphere is calibrated with the reference instruments every 3 months. The calibration process is carried at GSFC (Lille, Valladolid). In the calibration procedure, the photometer is placed in front of the sphere port and radiances are acquired in all aureole and sky channels. Then the calibration coefficients are calculated as the ratio between the raw signal at each channel and the output radiance at the given wavelength. The main precaution in this procedure is that the sphere output must be stable, therefore it is necessary to wait some minutes for the lamps to stabilize. The

aging of the lamps must be controlled to avoid miscalibration due to degradation (Torres, 2012, Torres et al., 2013).

3.3 Additional instrumentation

In situ instruments

The aerosol scattering coefficients (σ_{sp}) were measured at three wavelengths (450, 550 and 700 nm) with an integrating nephelometer (TSI model 3563) (Figure 3.5). This instrument draws the ambient air through a temperature-monitored inlet at a flow rate of 30 l min^{-1}. The air sample is illuminated by a halogen lamp and the instrument measures the scattered light at 450, 550 and 700 nm using three photomultiplier tubes. The scattered light is integrated over an angular range of 7–170º from the forward direction. Calibration of the nephelometer was carried out every three months using CO_2 as a high span gas and filtered air as a low span gas. The averaging time was set to 5 min. The zero signals were measured hourly. Due to limitations in the nephelometer design, measurements do not cover the full (0–180) angular range, needing the scattering data a correction (e.g., Anderson and Ogren, 1998). In this study, non-idealities due to truncation errors were corrected using the method described by Anderson and Ogren (1998) that account for the particle-size dependence of the truncation error through the measured wavelength dependence of light scattering. The scattering coefficient shows a minimum dependence on relative humidity (RH) below 50%. During the study period the RH measured within the nephelometer chamber was below 50%. As a result, of same way that is considered in other studies (Lyamani et al., 2010), the light scattering measurements presented in this work can be considered as dry.

Figure 3.5: Integrating nephelometer.

The aerosol absorption coefficients (σ_{ap}) were measured with a Particle Soot Absorption Photometer (PSAP) (Figure 3.6). The PSAP instrument provides a measurement of the light absorption by aerosol particles that are collected on a filter (Bond et al. 1999). Here, a 3-wavelength version of the PSAP has been used, with measurements at 467 nm, 531nm, and 650 nm. The intensity of light passing through the filter was monitored as aerosol-laden air was pulled through the filter and the absorption coefficient was determined from the Beer-Lambert law. The PSAP data require the corrections of the aerosol light scattering and the filter loading effects on the measurement of the aerosol absorption coefficient. PSAP was operated at a flow rate of 1.5 l min^{-1}. The averaging period for PSAP data during the measurements period was one minute. The uncertainty of the PSAP absorption measurement, after application of the transmission and scattering correction, is 20–30% (Bond et al. 1999). The detection limit of this instrument is 1.8 Mm^{-1} with an averaging time of 1 min.

Figure 3.6: Particle Soot Absorption Photometer (PSAP).

CM-11 pyranometer

Solar global irradiance measurements in the 0.31-2.8 µm range were obtained by a CM-11 pyranometer (Kipp & Zonen, Delft, Netherlands) (Figure 3.7). The CM-11 complies with the specifications for the first-class WMO classification of this instrument (resolution better than ± 5 W/m^2). This instrument has been periodically calibrated at the study site using a reference CM-11 instrument which is only used for inter-comparison purposes. Four inter-comparisons were performed between March 2005 and June 2010, with variations smaller than 1% for the entire measurement period showing the great stability of the instrument used in this study.

Figure 3.7: CM-11 pyranometer.

3. Experimental sites and Instrumentation

Broadband UV radiometer

A broadband UV radiometer, model UVB-1, manufactured by Yankee Environmental Systems, Inc. (Massachusetts, US), measures spectrally integrated UV irradiance weighted with the erythemal action spectrum adopted by the Commission Internationale de l'Eclairage (CIE) (McKinlay and Diffey, 1987) (denoted as UVER). Measurements were sampled every ten seconds and recorded as one minute mean voltages on Campbell CR10X data acquisition systems. Output voltages are converted into UVER values applying the calibration factors derived from two calibration campaigns of broadband UV radiometers at the "El Arenosillo" INTA station in Huelva (Spain) in September 2007 and June 2011 (Vilaplana et al., 2009). These calibrations included spectral and angular characterization of the instruments and their absolute calibration, performed through the outdoor intercomparison with a reference Brewer spectroradiometer. Output voltages recorded by the UVB-1 radiometer were converted to UVER data applying conversion factors obtained from the "two-steps" calibration method (Seckmeyer et al., 1997, Webb et al., 2006). Antón et al. (2011) compared the UVER data provided by the UVB-1 radiometer at Granada with radiative transfer model calculations for a cloudless sky; their results have shown high quality of the UVER data used in this paper.

All-Sky Imager

An All-Sky Imager developed by the GFAT (Atmospheric Physics group of the University of Granada) was used to routinely obtain images of the whole sky dome in daytime. This instrument has been used for cloud cover and atmospheric aerosol characterizations (Cazorla et al., 2008, 2009). The All-Sky Imager is a custom

adaptation of a scientific CCD camera. The principal modifications are the lens, the environmental housing, and the solar-shadow system. The camera body is a color CCD camera by QImaging (RETIGA 1300C). It provides full color images (1280x1024 pixels) with three channels: one centered in red wavelengths, another centered in the green, and the last one centered in the blue. The lens is a Fujinon CCTV fish eye lens. This configuration guarantees a 180° field of view projected onto the CCD, and therefore the image captured shows the whole sky dome. An environmental housing built by GFAT protects the All-Sky Imager from the rain, snow, and extreme temperatures on the rooftop. The housing has a transparent acrylic dome on the top, and the walls have two layers with polyurethane foam in the middle for thermal isolation. Finally, a solar-shadow system must protect the lens, and consequently the CCD, at every moment from the direct radiation of the Sun.

Satellite data

The OMI satellite instrument is on board NASA EOS/Aura platform launched in July 2004 (e.g. Schoeberl et al., 2006). This instrument consists of a nadir viewing push-broom spectrometer that measures solar backscattered radiation in the spectral range from 270 nm to 500 nm with a resolution of 0.55 nm in the ultraviolet and 0.63 nm in the visible. The OMI instrument has a 2600 km wide viewing swath and it is capable of daily global contiguous mapping. The footprint size of satellite pixel is 13 by 24 km at nadir increasing up to ~150 km off-nadir viewing directions.

The OMI surface UV algorithm (OMUVB) is based on the UV algorithm for Total Ozone Mapping Spectrometer (TOMS) instruments developed at NASA Goddard Space Flight Center (GSFC) (e.g. Krotkov et al., 1998, 2001). This algorithm estimates

surface UV irradiance from lookup tables (LUTs) obtained by a radiative transfer model using the OMI-derived total ozone, surface albedo and cloud information as input parameters (e.g. Tanskanen et al., 2006, 2007).

In this work, the OMUVB product used is OPEDRate (Overpass Erythemal Dose Rate). In addition, OMUVB L2 (level 2) dataset contains the Lambertian Equivalent Reflectivity (LER) at 360 nm which is used for cloud characterization. Additionally, we use the Aerosol Index (AI) calculated from 331 nm and 360 nm radiances which gives information about absorbing aerosols. All these OMI products are downloaded from the Aura Validation data Center site at http://avdc.gsfc.nasa.gov for the OMI station overpass data.

CHAPTER 4

METHODOLOGY AND

DATA

4. Methodology and Data

4. Methodology and Data

Chapter 4 describes the procedures to obtain the aerosol optical depth. Afterwards, we explain the sky radiance principal plane inversion method. A sensibility analysis of the inversion method is performed. The atmospheric aerosol properties obtained with this methodology will be compared with those obtained by AERONET network. Later, quality control data procedure is explained as well as the criteria for select of desert dust days. The methodology to obtain the aerosol radiative forcing during desert dust events is developed. After, the methodology to compare column and in-situ aerosol optical properties will be explained. Finally we propose, taking into account the quality assured ground-based measurements, the application of aerosol absorption post-correction method of the OMI UVER algorithm.

4. Methodology and Data

4.1 Inversion products

From the sun-photometer solar extinction measurements, the aerosol optical depth, $\tau_a(\lambda)$, and the Angström parameter, α, have been computed following the methodology described in Alados-Arboledas et al. (2003, 2008) and Estellés et al. (2006). All measurements sequences are carried out following the AERONET protocols. The sun photometer output voltage, $V(\lambda)$ can be expressed according to the Beer–Lambert–Bouguer attenuation law:

$$V(\lambda) = V_o(\lambda)\exp(-m_o\tau_{ext}(\lambda)) \tag{4.1}$$

where $V(\lambda)$ is the signal measured by the sun photometer, $V_o(\lambda)$ is the calibration constant, m_o is the relative optical air mass associated with the different extinction processes affecting the wavelengths used: these are m_a for aerosols, m_R for Rayleigh scattering, m_{O3} for O_3 and m_{NO2} for NO_2 and $\tau_{ext}(\lambda)$ is the total atmospheric optical depth. Calibration of the sun-photometer used in this study was performed annually by the AERONET-RIMA network. Using Equation (4.1), $\tau_{ext}(\lambda)$ is derived from direct sun-photometer measurements using the appropriate calibration constants provided by AERONET (linear rate change in time is assumed for calibration constants). Therefore, the spectral aerosol optical depth, $\tau_a(\lambda)$, is obtained by subtracting the Rayleigh optical depth as well as the optical depths for O_3 and NO_2 from $\tau_{ext}(\lambda)$ following the methodology described by Alados-Arboledas et al. (2003, 2008):

$$\tau_{a\lambda} = \frac{1}{m_a(\theta)}\left\{\ln\left(\frac{V_0(\lambda)}{V(\lambda)}\right) - m_R(\theta)\cdot\tau_{R\lambda} - m_{O_3}(\theta)\cdot\tau_{O_{3\lambda}} - m_{NO_2}(\theta)\cdot\tau_{NO_{2\lambda}}\right\} \tag{4.2}$$

4. Methodology and Data

According to Russell et al. (1993) and Dutton et al. (1994) it is possible to use the same air mass for all the terms in Eq. (4.2) with negligible loss of accuracy when the measurements are performed with solar zenith angles less than 60º. We compute Rayleigh, O_3 and NO_2 optical depths, and optical air masses corresponding to the different constituents, from the equations given by Gueymard (2001). Ozone content is obtained from OMI instrument on board the AURA satellite (http://aura.gsfc.nasa.gov/instruments/omi.html). The NO_2 content used is 0.00017 cm-atm given by Kneizys et al. (1988) for mid-latitudes atmosphere.

For the retrieval of $\tau_a(\lambda)$ we first remove cloud-contaminated measurements using the cloud screening method by Smirnov et al. (2000), which used the difference of $\tau_a(\lambda)$ between two consecutive measurements as a criterion determining the clear-sky conditions (triplet measurements). Even if data pass the threshold screening test, we only take data within three standard deviations from the mean in order to further reduce uncertainties induced by cloud contamination. In fact, high differences between two consecutive values of $\tau_a(\lambda)$ data are usually associated with passing clouds or aerosol in-homogeneities.

As we have shown in Chapter 3, the most relevant error in the aerosol optical properties computations comes from the calibration uncertainties. The $\tau_a(\lambda)$ absolute errors (combined effects of uncertainty in calibration, atmospheric pressure, and total ozone amount) can be derived from Beer-Bouger-Lambert law by error propagation theory (Russell et al., 1993):

$$(\delta\tau_{a\lambda})^2 = \left(\tau_{a\lambda} \cdot \frac{\delta m_0}{m_0}\right)^2 + \left(\frac{1}{m_0}\frac{\delta V_{0\lambda}}{V_{0\lambda}}\right)^2 + \left(\frac{1}{m_0}\frac{\delta V_\lambda}{V_\lambda}\right)^2$$

$$+ (\delta\tau_{R\lambda})^2 + (\delta\tau_{O_3\lambda})^2 + (\delta\tau_{NO_2\lambda})^2 \qquad (4.3)$$

These results show that the uncertainty values for each wavelength are different, depending on the processes involved. In our case, the combined effects result in a total uncertainty in τ_a of about $\pm$ 0.01 for λ>440 nm and $\pm$0.02 for shorter wavelengths, similar to AERONET level 2.0 data (Holben et al., 1998).

The dominant aerosol particle size was estimated using the Ångström exponent (α), defined by the logarithms of aerosol optical depth and wavelength (Ångström, 1964):

$$\alpha = -d\ln(\tau_{a\lambda})/d\ln(\lambda) \qquad (4.4)$$

where α was calculated for the inclusive wavelength range from 440 to 1020 nm using a linear fit of $\tau_{a\lambda}$ versus λ on a logarithmic scale; values closer to two indicate that small particles dominate and values approaching zero indicate larger aerosol particles dominate (Holben et al., 1991; Kaufman et al., 1992; Eck et al., 1999; Holben et al., 2001).

Inversion Method

Modeling the impact of mineral dust particles on radiative net flux is of particular interest in climate research, because mineral dust particles can have a strong climate forcing effect. Thus, this is especially relevant in North-eastern Africa, Southern Europe or Asia. As example, North African dust is injected into the atmosphere through

resuspension processes at the source areas, and it is then transported at different altitudes, being the maximum dust transport in summer when large quantities of dust are carried across the Mediterranean basin to Europe and the Middle East (e.g. Escudero et al., 2005).

On the other hand, the uncertainty in the knowledge of mineral dust radiative properties enables the scientific community to obtain global aerosol data, but adequate modeling of light scattering by non-spherical particles is widely recognized as one of the major difficulties in remote sensing of atmospheric aerosol. Moreover, there are numerous experimental evidences that the non-sphericity of desert dust particles produce scattering properties significantly different from those predicted by the standard Mie theory models. In this sense, Dubovik et al (2002a, 2006) presented a non-spherical aerosol retrieval method, including different improvements, employing scattering by spheroids. This methodology and their results have been tested using the AERONET data-base in different atmospheric aerosol conditions along worldwide and also other experimental data-bases (e.g. Dubovik et al., 2002b; Dubovik et al., 2006), and actually is the methodology implemented by AERONET. However, the inversion algorithm source code is not publicly available. This implies that independent CIMEL CE-318 users cannot use this code to invert their own data neither use it for further algorithm developments. This approach allows for retrievals and proper modeling of most optically distinct mixtures of coarse mode aerosols, and they also demonstrated that the spheroid kernel look-up tables computed can be a useful tool for various remote sensing applications (e.g. Dubovik et al., 2006). The algorithm retrieves the aerosol size distribution, complex refractive index and other aerosol optical and microphysical parameters, from the almucantar spectral sky radiance distributions as measured from

the ground-based sun-photometers. This operational inversion algorithm significantly improved the performance of the aerosol optical properties retrievals for desert dust observations and other aerosol mixtures. Thus, it would be convenient to include non-sphericity features for improving the retrieval qualities for dust particles. Furthermore, aerosol scattering at large angles 100-140º is affected by the particle shape, and the difference between non-spherical and spherical scattering is near maximum at an angle of 120º. The results show that the use of spheres in modeling causes considerably larger sky-radiance errors and the effect is particularly pronounced at the top of atmosphere (TOA).

On the other hand, using the almucantar sky radiance data the authors show that the $\omega(\lambda)$ can be retrieved with reasonably high accuracy only for moderate aerosol optical depths (e.g. $\tau_a(440$ nm$) > 0.4$) and large solar zenith angles (e.g. Dubovik et al., 2002; Kim et al., 2004). Thus, the key parameters for aerosol radiative forcing computations are not provided at solar zenith angles smaller than 50º or $\tau_a(440$ nm$) < 0.4$. In fact, several inversion products that do not fulfill these restrictions are eliminated by the AERONET data base (level 2.0). This means, for instance, that AERONET sites in Spain only provide single scattering albedo values during occasional desert dust events. Besides, the columnar aerosol load can change along the day, and for instance their effective optical properties, also due to the different local sources or meteorological conditions. This last matter is of interest taking into account the need of daily aerosol radiative forcing values for climate analysis or prediction studies.

In addition, few different inversion algorithms have been proposed over the years. Nakajima et al. (1996) implemented an original algorithm called

4. Methodology and Data

SKYRAD.PACK. This software, and successive improvements, was developed to be applied on Prede POM radiometers, though was also implemented by AERONET network in a first stage for its application on the CIMEL CE 318 sun-photometers. The original SKYRAD.PACK code, and the later improvements, is based on spherical particles assumption. Detailed descriptions and uncertainty analysis –sensitivity test- of this code can be seen in literature (e.g. Nakajima et al., 1996; Boi et al., 1999; Kim et al., 2004; Estellés et al., 2012). On the other hand, using the sky radiance almucantar configuration, others authors implemented approximations to incorporate the non-sphericity properties in SKYRAD.PACK code (e.g. Olmo et al., 2006; Kobayashi et al., 2010). The improvements are based in the new kernel look-up tables added, which are based on the spheroid model. The results show that the spheroids model applied to the SKYRAD.PACK code can retrieve effective aerosol optical properties more accurately than the spheres model. Therefore, as indicated by the authors, these results need further verifications and improvements.

The SKYRAD.PACK consists in two programs. The first one (MKDATA) is for computing simulated data of direct irradiance and sky radiance from aerosol properties and, the second, (REDML) is for retrieving (inversion) aerosol properties from solar radiation data. The treatment of the radiative transfer problem concerning the optical quantities is based on the improved multiple and single scattering method which uses the delta-M approximation for the truncation of the aerosol phase function (Wiscombe, 1977), and correct the solution for the first and second order of scattering (Stamnes and Dale, 1981). The second part of the SKYRAD.PACK is the REDML program, which retrieves the aerosol features from the data of direct and normalized diffuse irradiance, so it is the part including the inversion procedure. There are four different modes of

operation selected by an index called as INDM. The possible values for INDM are -1, 0, 1 and 2. The main differences between the indexes are related to the use of the aerosol optical thickness and the way of performing the inversion. For instance, in INDM = 2, the aerosol optical thickness is not used, and only the data from sky radiance is considered. In case of INDM = 1, the aerosol optical depth is fixed in the first iteration and is varied in the next iterations while for INDM = 0;-1, it is kept fixed during all the process. Figure 4.1 shows the inversion procedure.
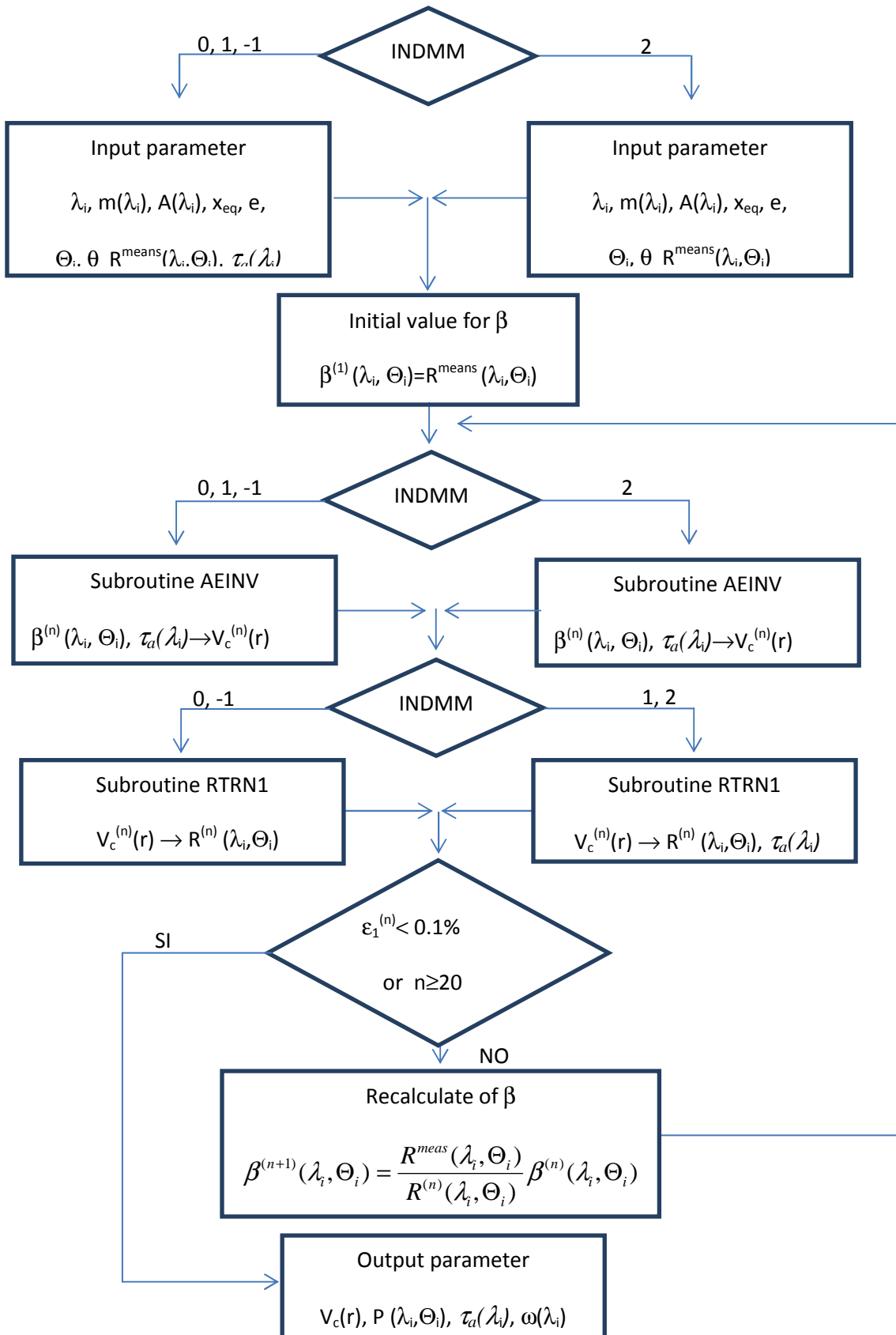
Figure 4.1: Scheme of the program REDML for SKYRAD.PACK code.

4. Methodology and Data

It start of initial values for $\beta_\lambda = R^{meas}(\Theta)$ and applying an iterative inversion method (Subroutine AEINV), it is calculate $V_c(n)$ from inversion of differential scattering coefficient ($\beta_\lambda^{(n)}(\Theta)$) and aerosol optical depth ($\tau_a(\lambda)$) (INDM=0,1, -1); from $V_c(n)$ estimation and using a radiative transfer model (Subroutine RTRN1), it is obtained a radiance value $R_\lambda^{(n)}(\Theta)$ (INDM=0,-1) and aerosol optical depth $\tau_a^{(n)}(\lambda)$ (INDM=2,1).

This process is iterates until the deviation between $R_\lambda^{(n)}(\Theta)$ and $R_\lambda^{meas}(\Theta)$, represented by $\varepsilon(R)$, reaches a threshold established. In order to obtain $\beta_\lambda^{(n+1)}(\Theta)$ it is used the final values of $R_\lambda^{(n)}(\Theta)$ and experimental data $R_\lambda^{meas}(\Theta)$, according with the expression:

$$\beta_\lambda^{(n+1)}(\Theta) = \frac{R^{meas}(\Theta)}{R^n(\Theta)} \beta^{(n)}(\Theta) \qquad (4.5)$$

The accuracy achieved in the process of obtaining aerosol properties using parameter $\varepsilon(R)$ is quantified by the relative deviation (%RMSD) between experimental normalized radiance and the calculated radiance. This calculated radiance is averaged for all scattered angles. If besides, it is averaged for all wavelengths then the parameter $\varepsilon(R)$ is denoted for $\overline{\varepsilon}(R)$. The value of $\varepsilon(R)$ is fixed to start and the iterative process is remaining until to reach the threshold established. The parameter $\overline{\varepsilon}(R)$ is stronger dependent of the real refractive index and slight of the imaginary refractive index and surface albedo (Boi et al., 1999).

On the other hand, the SKYRAD.PACK software has the option to invert the almucantar or the principal plane sky radiance measurements (e.g. Nakajima et al., 1996; Olmo et al., 2008). In this work we tested the principal plane configuration option

including the particle shape (spheroids model) in effective volume size distributions and other effective optical parameters such as $\omega(\lambda)$ and asymmetry parameter. We applied the results of this approach to characterize the columnar aerosol optical parameters along the day and the daily radiative forcing computed for the African dust events occurred at Granada from 2005 to 2010. Also, we compared the principal plane inversion results and the derived daily aerosol radiative forcing with the data-base provided by the well tested model of AERONET (level 2.0 data), that uses as input the sky radiance almucantar configuration. This assessment will be only relative due to the different measurement time protocol from almucantar and principal plane sky radiances.

Due to the lower quality on data (pointing errors, cloud screening, aerosol in-homogeneities, etc.), the current AERONET data-base does not offer any retrieval data from the principal plane measurements, and all the approaches to the study have been made using only the data obtained from "positive" scattering angle values (e.g. Torres, 2012; Torres et al., 2013). The "positive" sign in principal plane sky radiance measurement configuration is given to the movement of the instrument from the Sun towards the zenith.

Moreover, using self-consistence test, in this work it shows that using simulated measurements without error, aerosol retrievals at low solar zenith angles (θ) are misshapen due to the lack of information of scattering angles larger than $2 \cdot \theta$ in the almucantar measurements. Also, the calibration errors have more influence on the retrievals at low θ, amplifying the differences between retrievals at low and large θ (e.g. Torres, 2012; Torres et al., 2013).

Finally, if the atmospheric characteristics were know, including the vertical distribution of particles and their optical and microphysical properties, the radiation measured could be simulated with a high degree of accuracy (cloudless days) using any of the so-called direct methods (e.g. Kokhanovsky et al., 2010). The problem arises because we need to infer the aerosol size distribution and optical properties from the ground-based of sky radiance (diffuse) and solar extinction measurements (inversion methods). Unfortunately, in inversion methods, different combinations of atmospheric aerosol parameters produce the same (or nearly) radiation distribution. The solution is non-unique in the presence of minor measurement noise, and displays other features which conflict with a priori knowledge of the aerosol properties (Phillips, 1962). In this sense, we can try to solve the multiple solution problems in inversion procedure by introducing, in at appropriate way, the a priori information: input parameters and numerical constraints. As example, Dubovik and King (2000) proposed a priori assumptions on smoothness of the size distribution or spectral smoothness of the optical properties in the inversion procedure to constrain the solution while producing the measurement field within the error bars established for the measurements.

Methodology to derive the inversion parameters

The inversion method uses as input data the spectral aerosol optical depths ($\tau_{a\lambda}$) derived from sun photometer extinction measurements by using Beer-Bouger-Lambert law. In addition, for more accurate aerosol property retrievals, the inversion code uses as input the monochromatic sky radiance normalized by the monochromatic direct solar irradiance, $R(\Theta,\lambda)$, instead of the monochromatic sky radiance, that is a magnitude less

affected by interference-filter degradation of sun-photometers, and can be more accurately determined. The $R(\Theta, \lambda)$ is given by (Nakajima et al., 2006; Boi et al., 1999; Olmo et al., 2006):

$$R(\Theta, \lambda) = \frac{E(\Theta, \lambda)}{F_\lambda m_o \Delta\Omega} = \omega(\lambda)\tau_{ext}(\lambda)P(\Theta, \lambda) + q(\Theta, \lambda) = \beta(\Theta, \lambda) + q(\Theta, \lambda) \qquad (4.6)$$

where $E(\Theta, \lambda)$ is the monochromatic sky radiance ($Wm^{-2}\mu m^{-1}sr^{-1}$), F_λ is the monochromatic direct solar irradiance ($Wm^{-2}\mu m^{-1}$), $\Delta\Omega$ is the solid view angle of the sky radiometer, $\omega(\lambda)$, $P(\Theta, \lambda)$ are the total single scattering albedo and phase function at scattering angle Θ, $\beta(\Theta, \lambda)$ is the total differential scattering coefficient (single scattering term), that is the sum of the scattering coefficients for aerosol and molecules, and $q(\Theta, \lambda)$ is the multiple-scattering contribution. $E(\Theta, \lambda)$ and F_λ are obtained from sun-photometer measurements using the calibration constants provided by AERONET-RIMA.

In the solution approach of Equation (4.6), atmospheric layers are characterized by their optical depth, single scattering albedo and phase function. The scattering properties of an atmospheric aerosol layer are modeled by averaging single-particle properties. To derive the solutions, the SKYRAD.PACK code uses the spherical approximation for single-particle properties. However, in the modified version used in this study (Olmo et al., 2008), the aerosol single-scattering term, $\beta(\Theta, \lambda)$ and $\tau_{ext}(\lambda)$, are defined as functions of the volume size distribution of randomly oriented polydisperse spheroids (e.g. Dubovik et al., 2006):

$$\beta(\Theta,\lambda) = \tau_{scat}(\lambda)P(\lambda,\Theta) = \int_{\ln\varepsilon_{min}}^{\ln\varepsilon_{max}} \int_{\ln r_{min}}^{\ln r_{max}} \frac{C_{scat}(\lambda,\Theta,n,k,\varepsilon,r)}{v(r)} \frac{dn(\varepsilon)}{d\ln(\varepsilon)} \frac{dV(r)}{d\ln r} d\ln r d\ln\varepsilon \quad (4.7)$$

$$\tau_{ext}(\lambda) = \int_{\ln\varepsilon_{min}}^{\ln\varepsilon_{max}} \int_{\ln r_{min}}^{\ln r_{max}} \frac{C_{ext}(\lambda,n,k,\varepsilon,r)}{v(r)} \frac{dn(\varepsilon)}{d\ln(\varepsilon)} \frac{dV(r)}{d\ln r} d\ln r d\ln\varepsilon \quad (4.8)$$

where ε is the axis ratio of the spheroid and r the radius of a volume-equivalent sphere (same volume as the spheroid); τ_{scatt} (λ) and τ_{ext} (λ), are the scattering and extinction optical depths; C_{scat} and C_{ext} are the scattering and extinction cross sections; n and k are the real and imaginary parts of the refractive index; $V(r)$ is the volume of the particle with radius r; $dV/dlnr$ is the volume size distribution; and $dn(\varepsilon)/dln$ is the distribution of the spheroid axis ratios.

For computational convenience the integration of Equations (4.7) and (4.8) can be approximated by using the kernel matrices K_{ext} and K_{scat}:

$$\beta(\Theta,\lambda) \approx \sum_{p,s} \frac{dn(\varepsilon_p)}{d\ln\varepsilon} \frac{dV(r_s)}{d\ln r} K_{scat}(\Theta,\lambda,n,k,\varepsilon_p,r_s) \quad (4.9)$$

$$\tau_{ext}(\lambda) \approx \sum_{p,s} \frac{dn(\varepsilon_p)}{d\ln\varepsilon} \frac{dV(r_s)}{d\ln r} K_{ext}(\lambda,n,k,\varepsilon_p,r_s) \quad (4.10)$$

where $dn(\varepsilon_p)/dln\varepsilon$ and $dV(r_s)/dlnr$ are the values of the size distributions $dV(\varepsilon)/dln\varepsilon$ and $dV(r)/dlnr$ given at discrete logarithmically equidistant points.

The kernels can be pre-computed, and their dependence on n and k can be parameterized by a look-up table covering the range of expected values. The original SKYRAD.PACK code use pre-calculated kernels for spherical particles for simulating particle scattering. However, for more accurate simulations of scattering by non-spherical particles, the modified inversion code utilised in this work uses the pre-calculated kernels for randomly oriented prolate and oblate spheroids instead of spheres (Olmo et al., 2008). For the calculation of the kernels for spheroids, the EBCM, or T-

matrix theory (Waterman, 1971) has been used. Convergence procedures have been set so that phase matrix elements are calculated with an accuracy of 10^{-3}; cross sections are accurate to within one part in 10^4 (Mishchenko, 1993). The kernel matrices for randomly oriented prolate and oblate spheroids were calculated for 74 scattering angles, from 0 to 180º using equiprobable distributions, following the recommendations of Dubovik et al. (2002a, 2006). These authors showed that using the assumption of an equal presence of prolate and oblate spheroids improves the retrieval stability. Actually, the kernel matrices used in the inversion method of Olmo et al. (2008) cover the following range of aerosol parameters:

$$1.33 \le n \le 1.6$$

$$0.0005 \le k \le 0.64$$

$$0.3 \le \varepsilon \le 3.0$$

$$0.01 \le x \, (= 2\pi \cdot r / \lambda) \le 148.9$$

Stable performance of the T-matrix code depends on ε and x, and the T-matrix code becomes numerically unstable for spheroids with ε~ 2-2.4 and size parameters x larger than about 60. This is a serious limitation of the pre-calculated kernel matrices used in the retrieval procedure proposed by Olmo et al. (2008). These limitations restrict the principal plan retrievals to the particle size range of $0.05 \le r \le 7$ µm for λ from 0.44 to 1.02 µm. Future improvements of the method used in this study using other methods such as the geometric-optics-integral-equation method (e.g. Yang and Liou, 1996) are needed to generate the kernel matrices of elongated and flattened spheroids for larger x. In any case, the aerosol properties retrievals used in this study were obtained during

4. Methodology and Data

Saharan dust intrusions over Granada (far from Saharan dust sources). Therefore, dust particles with very large sizes are not expected to reach the study area due to the deposition processes during the long path way travelled by these particles. Thus, in spite of the inversion limitations, the aerosol properties used in this study are expected to be of reasonable accuracy.

For retrieving the effective columnar aerosol properties (size distribution, single scattering albedo and asymmetry parameter) by the principal plane inversion method, Equation (4.6) is iteratively inverted using as input $R(\Theta,\lambda)$, $\tau_a(\lambda)$ and varying the refractive index to determine $\beta(\Theta,\lambda)$. The $R(\Theta,\lambda)$ and $\tau_a(\lambda)$ are derived from sun-photometer experimental measurements. It is noted that $\tau_a(\lambda)$ is kept fixed in the iterative process. In each iteration the algorithm computes the effective volume size distribution, $V(r)$, by inversion of $\tau_a(\lambda)$ and $\beta(\Theta,\lambda)$, and uses this computed distribution to simulate $R'(\Theta,\lambda)$, which is compared with the experimental $R(\Theta,\lambda)$ to evaluate the relative root mean square error (RMSE). For the initial guess in the iterative process the algorithm uses $\beta^{1)}(\Theta,\lambda) = R(\Theta,\lambda)$. The process is repeated until the RMSE differences between measured and simulated normalized sky radiances and aerosol optical depths are less than 10% and 5%, respectively. In this method the refractive index is assumed invariant with wavelength. The real part of the refractive index used in the iterative process is varied within the range 1.33–1.6 in 0.02 steps, while the imaginary part is varied over the range 0–0.01 in 0.0005 steps, covering the expected range of refractive indices for diverse aerosol mixtures (e.g. D'Almeida et al., 1991). The output of the retrieval algorithm includes the effective aerosol columnar size distribution, the refractive index, the single scattering albedo and asymmetry parameter for which the

RMSE differences between measured and calculated radiances and aerosol optical depths are minimal.

On the other hand, in order to verify the contribution of the fine mode, as well as to know the spectral information given by the Angstrom exponent, the Gobbi's method was employed (Gobbi et al., 2007). These last authors presented a simple graphic method to visually convert α and $\delta\alpha$, defined as the difference between $\alpha(440,670)$ and $\alpha(670,870)$, which allows for quantifying the contribution of fine aerosols to the τ_a and the size of the fine particles. This method is based on Mie computation (using air refractive index $m = 1.4 - 0.001i$) correlating the α versus $\delta\alpha$ with fine mode fraction at 670 nm (η) and the effective radius of fine mode aerosols (R_f). In order to avoid errors larger than 30% only $\tau_a > 0.15$ values were employed.

Accuracy assessment of individual retrievals

To analyze the accuracy of individual retrievals of the principal plane inversion method used in this work, an extensive sensitivity test was performed using assumed and retrieved aerosol properties for cases characterized by different loads of mineral dust particles. The purpose of the sensitivity tests is to verify the algorithm efficiency and check the results regarding the setting of the inversion algorithm.

We have generated a set of synthetic data using the direct code (MKDTA software) included in the SKYRAD.PACK code, replacing the spherical kernels by the non-spherical kernels computed in Olmo et al. (2008). These synthetic data (assumed data) are computed varying the particle mean radius, the volume concentrations, the standard deviations and the refractive index (different dust-like aerosol models). In

these tests the properties of the fine mode are assumed as constant. The analysis was performed for 440, 670, 870 and 1020 nm wavelengths, and the maximum scattering angle used was 140º.

Then, we applied the principal plane inversion algorithm to derive the aerosol optical parameters, using as input parameters the spectral aerosol optical depth and the normalized sky radiances retrieved by the direct method. The differences between retrieved and assumed values of aerosol properties give the apparent errors of the retrievals inherent to the inversion algorithm.

The following equation describes the bimodal log-normal model assumed in the simulations:

$$\frac{dV(r)}{d\ln r} = \sum_{i=1}^{2} \frac{V_i}{\sqrt{2\pi}\sigma_i r} \exp\left[-\frac{(\ln r - \ln r_i)^2}{2\sigma_i^2}\right] \qquad (4.11)$$

where *dV(r)/dlnr* is the particle volume size distribution, *r* is the particle radius, *i* denotes fine or coarse modes, V_i is the volume concentrations, and σ_i the standard deviations.

Table 4.1 shows an example of the assumed parameters used in the sensitivity tests.

Volume mean radius	$r_f = 0.16$ $r_c = 1.33$
Ratio of particle volume concentration	$V_f / V_c = 0.05$
Standard deviations	$\sigma_f = 0.25$ $\sigma_c = 0.52$
Refractive Index	$n = 1.51$ $k = -0.002$

Table 4.1: Example of the assumed aerosol parameters used in the sensitivity tests. (f: fine mode, c: coarse mode)

Considering the importance of aerosol absorption in radiative forcing, it is also of interest to evaluate the agreement between the assumed (direct method) and retrieved (inversion algorithm) values of single scattering albedo. Figure 4.2 shows the assumed and retrieved effective single scattering albedo, volume size distribution, phase function and normalized sky radiances for the example presented in Table 4.1. As seen in Figure 4.2, the retrieved aerosol properties by the inversion procedure were close to the assumed values. The RMSE% (root mean square error) computed for the data sets (assumed vs. retrieved) –Figure 4.2-, including all wavelengths and/or scattering angles for each data set, is close to 1% for single scattering albedo, close to 2% for phase functions and close to 3% for normalized sky radiances. For the volume size distribution the RMSE% are close to 3% in coarse mode, but could increase up to 30% for radius close to 0.1 and 7 µm. Outside this range of radius, the RMSE% increases drastically.
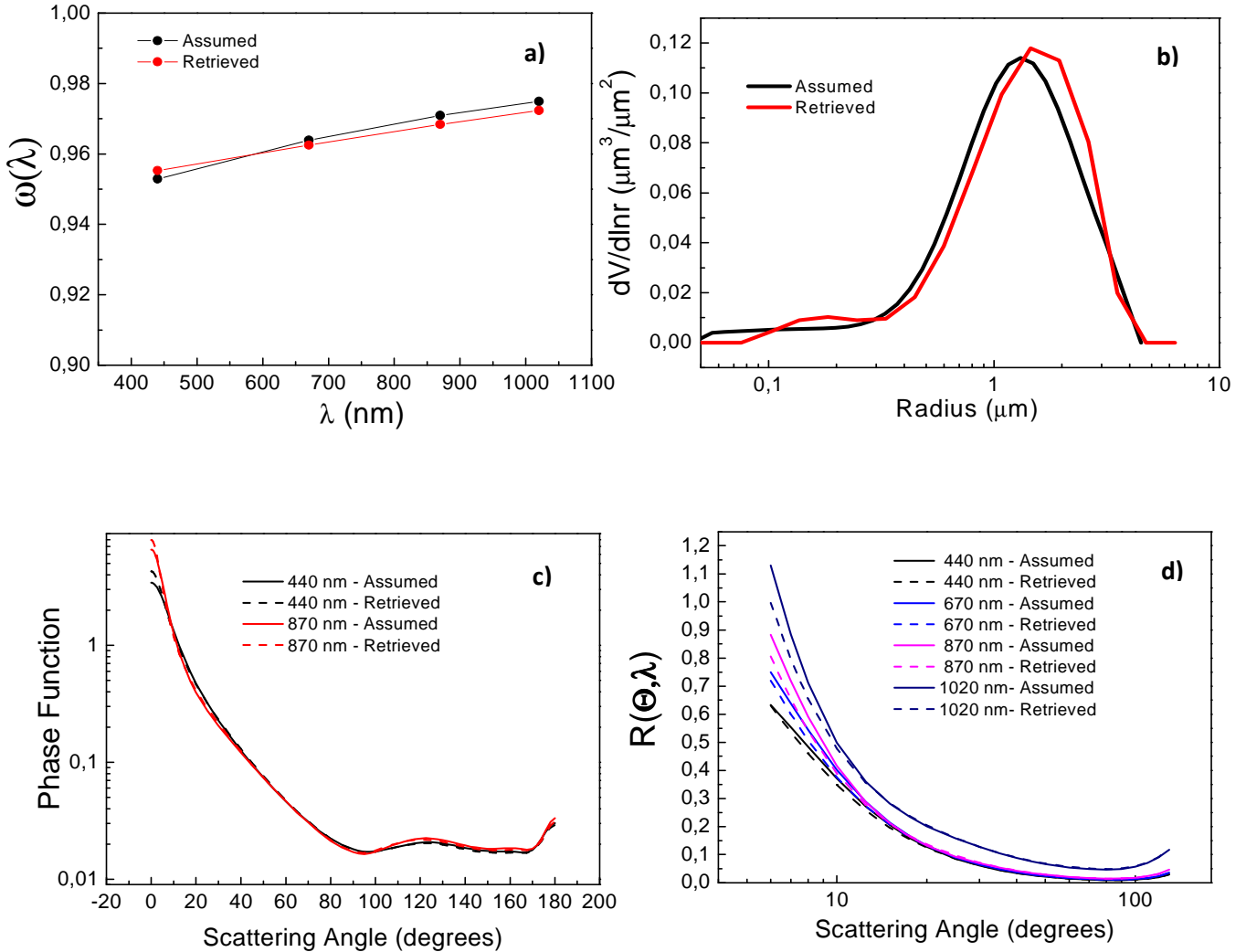
Figure 4.2: Assumed and retrieved data for the analysed case presented in Table 4.1: a) spectral single scattering albedo, b) Volume size distribution, c) spectral phase function, and d) spectral normalized sky radiance in the principal plane.

Figure 4.3 shows the relative deviations between the assumed and retrieved $R(\Theta,\lambda)$ for the analyzed case (Table 4.1), that is computed as follows:

$$\frac{(R_{\mathrm{Retrieved}}(\Theta,\lambda) - R_{Assumed}(\Theta,\lambda))}{R_{Assumed}(\Theta,\lambda)} \qquad (4.12)$$

As seen in Figure 4.3, the relative deviations have a clear angular dependence that increases for lower scattering angles and reaches a maximum of 12% at scattering angles close to 6°.
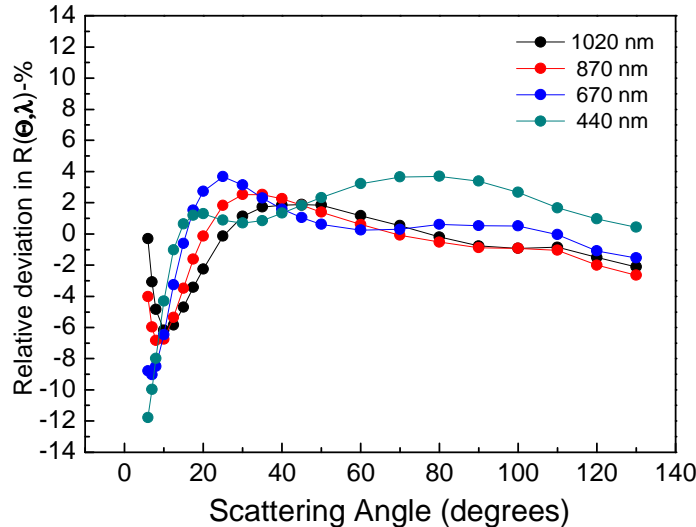

Figure 4.3: Relative deviations between assumed and retrieved $R(\Theta,\lambda)$ for the analyzed case presented in Table 4.1.

Similar results are obtained for the different dust-like aerosol models tested using the spheroid model. In all cases, the optical parameters retrievals were performed with RMSE% close to 5% or less, and close to 10% or less for normalized sky radiances and volume size distributions. These results are in agreement with the criteria used in inversion algorithm for the cloud-screening method and also with the minimization of the normalized sky radiance residuals in the iterative procedure.

On the other hand, to analyze the behavior of the inversion code taking into account the possible errors on input parameters (e.g. calibration or systematic errors), we have performed different test on data with errors of 3% and 5% in $\tau_a(\lambda)$, $R(\Theta,\lambda)$ (also 7%), surface albedo and refractive index. These error variations also include the possible errors in radiance calibrations (e.g. Torres, 2012; Torres et al., 2013). As

example, Figure 4.4 shows different retrievals obtained from experimental data corresponding to the Saharan dust event that affected Granada in June, 23 2008.
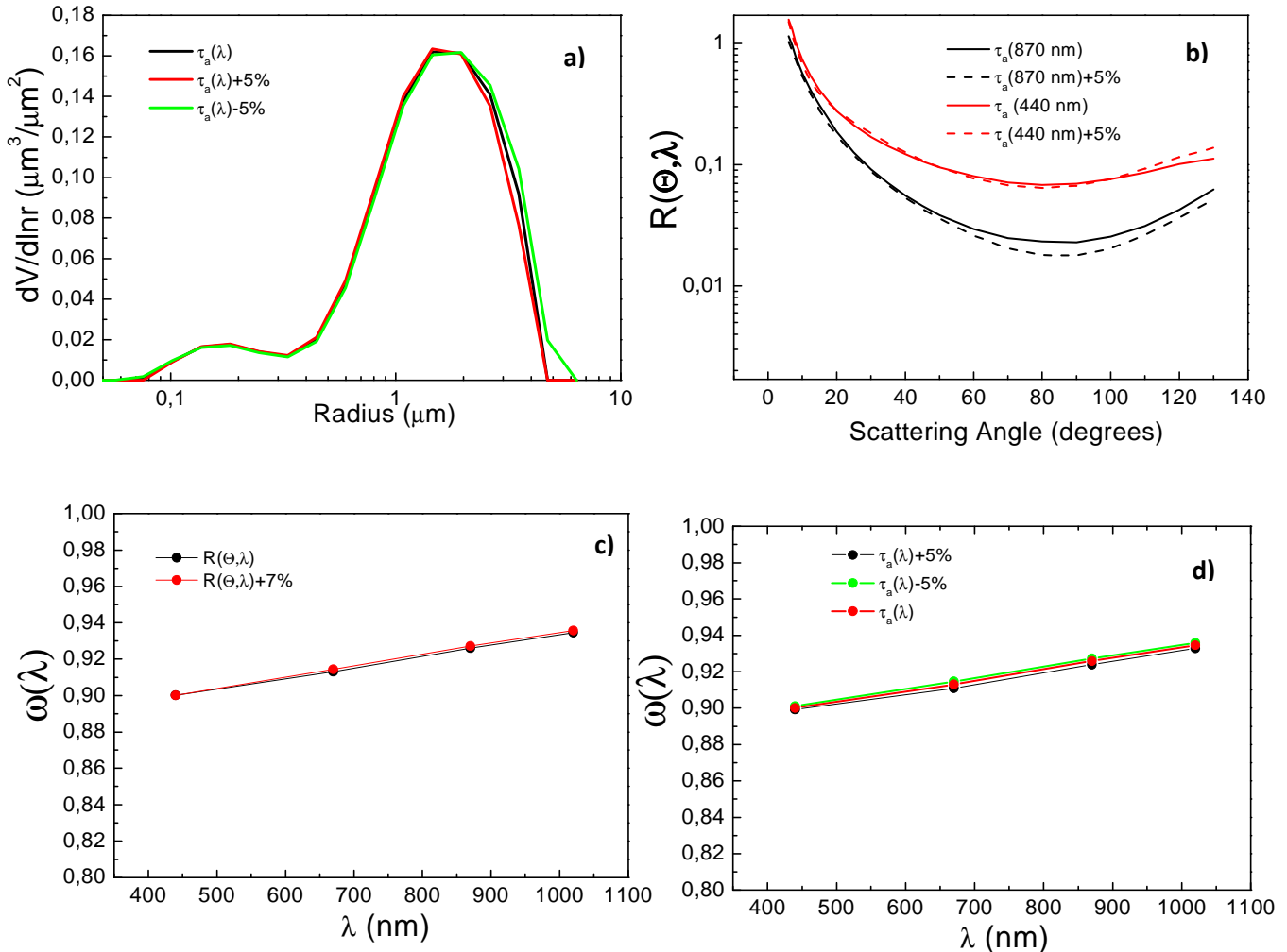
Figure 4.4: Retrieval results with and without errors in input data for the Saharan dust case detected over Granada on 23 June, 2008. a) Volume size distribution retrievals derived using as input parameters $\tau_a(\lambda), \tau_a(\lambda)$-5% and $\tau_a(\lambda)$+5%; b) $R(\Theta,\lambda)$ retrievals derived using as input parameters $\tau_a(\lambda), \tau_a(\lambda)$-5% and $\tau_a(\lambda)$+5%; c) $\omega(\lambda)$ retrievals derived using as input parameters $R(\Theta,\lambda)$ and $R(\Theta,\lambda)$+7%, and d) $\omega(\lambda)$ retrievals derived using as input parameter $\tau_a(\lambda), \tau_a(\lambda)$-5% and $\tau_a(\lambda)$+5%.

In this case, we assumed errors of 5% and 7% in $\tau_a(\lambda)$ and $R(\Theta,\lambda)$. The RMSE% for the data sets presented in Figure 4.4 is less than 5% in all cases. Also, the different

tests performed show that the differences between assumed (without errors) and retrieved (with errors) optical parameters, in absence of strong systematic biases, is about 5% or less in all cases. Therefore, this residual value can be adopted as an indicator of the quality of the retrievals.

In addition, Figure 4.5 shows the effective $\omega(\lambda)$ derived for this dust event using a spectrally constant value for the surface albedo (0.15) and using the spectrally dependent surface albedo provided by AERONET network. The results show, in agreement with other authors (e.g. Dubovik and King, 2000; Dubovik et al., 2002b), that the $\omega(\lambda)$ is minimally affected by surface albedo.
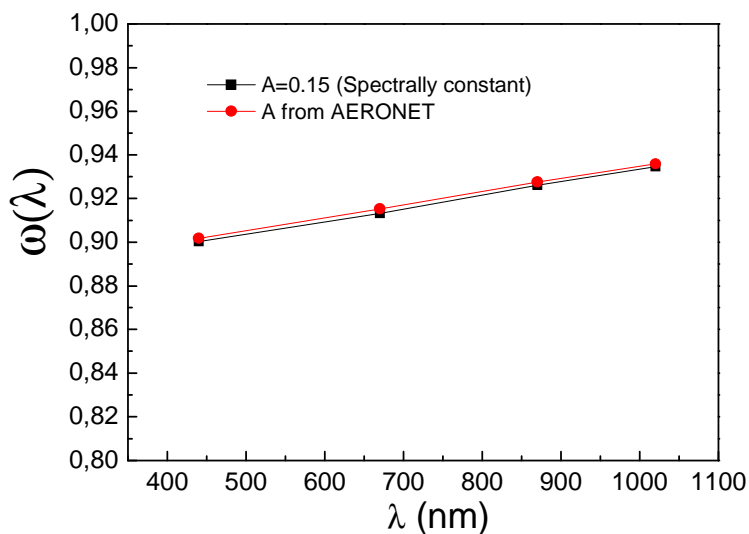

Figure 4.5: $\omega(\lambda)$ retrievals derived for desert dust case (23 June, 2008) using a spectrally constant value of 0.15 for the surface albedo (*A*), and using the spectrally dependent values of *A* provided by AERONET network.

4. Methodology and Data

Finally, using this methodology and in view of the previous results, the accuracies of single scattering albedo and asymmetry parameter retrievals, using scattering angles up to 100º or greater, are about 5% for different mineral aerosol loading. For volume size distributions, the error depends on the particle size. For the radius interval 0.1-7 µm, the retrieval errors do not exceed 10%. Even taking into account the limitations of this methodology, these results are comparable to those derived by other authors using the almucantar configuration (e.g. Dubovik and King, 2000; Dubovik et al., 2002b).

Data quality control criteria

Following the procedure proposed by Olmo et al. (2008), to eliminate cloud contaminated aerosol optical depths, and the corresponding principal plane sky radiance measurements, first we applied the triplet stability criteria (Smirnov et al., 2000) to the spectral extinction data measured at the beginning of the principal plane scan. Even if data pass the threshold screening test, we take only data within three standard deviations of the mean in order to further reduce uncertainties induced by cloud contamination. In fact, high differences between two consecutive values of $\tau_a(\lambda)$ data are usually associated with passing clouds or aerosol in-homogeneities. In addition, the possible influence of thin clouds and spatially inhomogeneous clouds, which are difficult to completely eliminate and could contribute to the sky radiance errors, have been considered. Thus, we have obtained a smoothed principal plane sky radiance data set by applying a moving-average smoothing algorithm with a sliding window of five-point width. If the maximum difference between the smoothed and the initial sky radiances set (point to point) was higher than threshold 5% the data were rejected. Also, if the

number of scattering angles in the measured sky radiance distributions is less than 20, the measurement record is eliminated. In addition, in order to accept a principal plane inversion as valid, the relative differences (residuals) between the measured and computed normalized sky radiances must be less than 10%. Finally, to eliminate those clouds contaminated sky radiances that passed the previous filters we used a supervised inspection of sky images acquired with an All-Sky Imager (e.g. Cazorla et al., 2008). In this sense, the methodology is not completely automatic.

According to our experience, the cloud screening procedure presented above is very effective for removing cloud contaminated data. For example, Figure 4.6 (a, b) shows the all-sky images registered for two consecutive days at the same hour (6 October 2010 at 10:15 h GMT, representing cloudless situation, and 7 October 2010 at 10:15 h, representing cloudy condition). Also, Figure 4.6c shows the evolution of the normalized principal plane sky radiances measured during these two situations. As can be seen, there is an abrupt change in the spectral normalized sky radiance at scattering angles around 100º on 7 October, which was associated with clouds (Figure 4.6b). The normalized sky radiance data measured in this case were successfully identified as cloud-affected data by the cloud screening algorithm used in this work. As expected, sky radiance data measured on 6 October (cloudless case) passed this cloud screening procedure.

a)

b)

c)
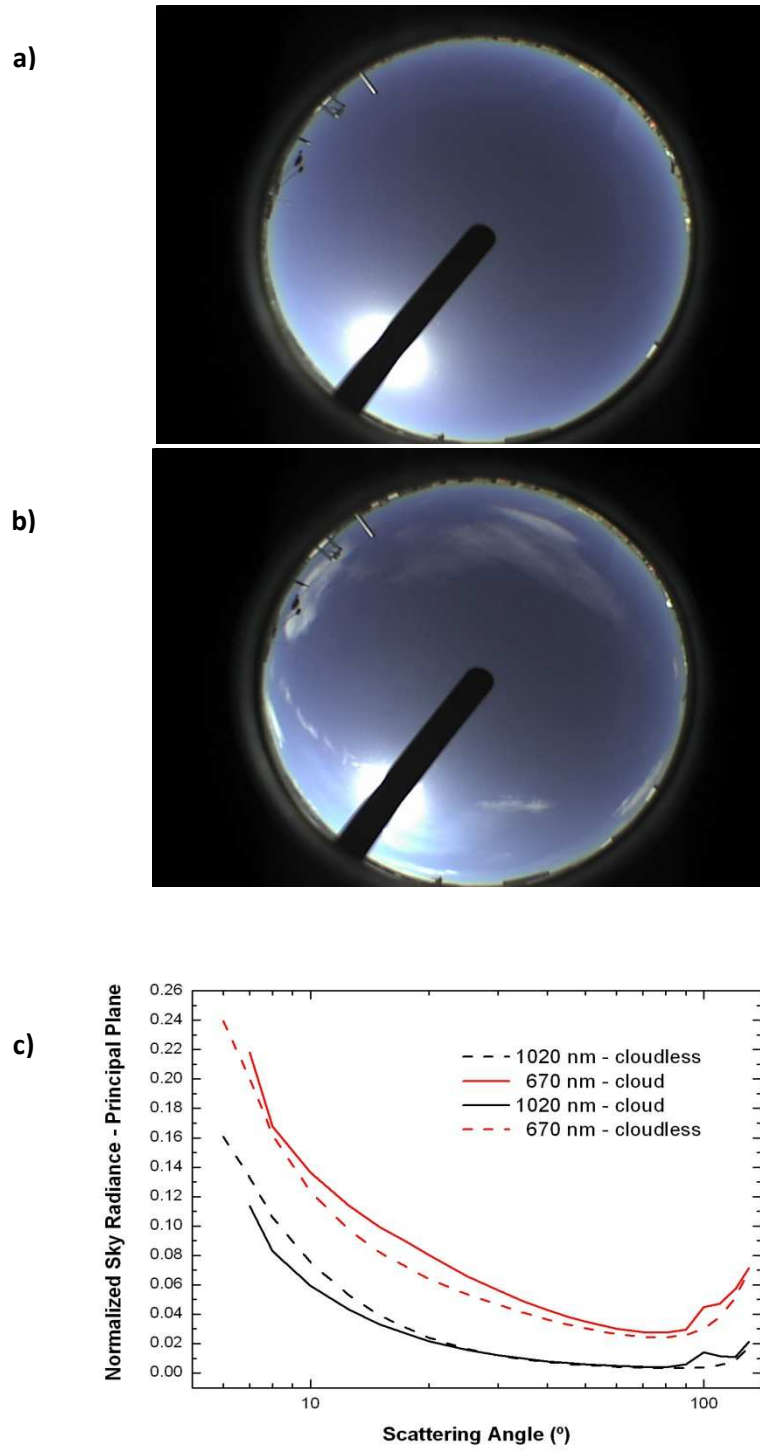
Figure 4.6: All-sky image registered on: a) 6 October 2010 at 10:15 h GMT –cloudless-; b) 7 October 2010 at 10:15 h GMT –clouds-; and c) normalized principal plane sky radiances at 670 and 1020 nm derived for the two situations.

4.2 Detection of desert dust days

In this work we focus on African dust events from January 2005 to December 2010 that have been confirmed by CALIMA network (www.calima.ws) on South-eastern of the Spain. The CALIMA network produces periodically reports on the 24 h forecasts of dust outbreaks (e-mail alerts sent to air quality networks 24 h in advance). Later, the CALIMA network produces a report of validations taking into account the different Spanish areas. To perform these reports the network uses the information on the PM10 levels recorded at regional background stations in Spain, the HYSPLIT4 model (Draxler et al., 2003; http://www.arl.noaa.gov/ready/hysplit4.html), synoptic meteorological charts (http://www.ecmwf.int/), the maps of aerosol index of Ozone Monitoring Instrument (OMI) (ftp://toms.gsfc.nasa.gov/pub/omi/images/aerosol/), the SeaWiFS maps information (http://oceancolor.gsfc.nasa.gov/SeaWiFS/HTML/dust.htlm), the daily results of the aerosol models outputs such as SKIRON (http://forecast.uoa.gr), BSC-DREAM (http://www.bsc.es/projects/ earthscience/DREAM/) and NAAPs (http://www.nrlmry.navy.mil/aerosol/), and, finally, the levels of PM10 recorded at regional background stations from air quality monitoring. Therefore, the reports of validated days correspond to African desert dust events tested by models, back-trajectories analysis, synoptic meteorological charts, satellite and surface data.

4.3 Validation of the retrieved aerosol optical properties

The aerosol optical properties retrieved from principal plane measurements using the algorithm proposed by Olmo et al. (2008) have been compared against the AERONET retrievals based on nearly coincident almucantar measurements.

Firstly, we compared the spectral aerosol optical depths computed in this work and those provided by AERONET (level 2.0). In this comparison, only $\tau_a(\lambda)$ data obtained during the desert dust events detected over Granada from 2005 to 2010 are used. Figure 4.7a shows the scatter plot of $\tau_a(670nm)$ data provided by AERONET versus that computed in this work. As can be seen the $\tau_a(\lambda)$ data obtained by both methods are well correlated with coefficient of determination (R^2) of 0.99. The slope of the linear fit is equal to 1 and the intercept value is very small (0.006). The mean absolute difference between the $\tau_a(670nm)$ computed in this work and that provided by AERONET is equal to 0.009 (Table 4.2). For $\tau_a(\lambda)$ at 440, 870 and 1020 nm the mean absolute differences are 0.009, 0.005 and 0.009, respectively (Table 4.2). Taking into account the uncertainty in $\tau_a(\lambda)$ computations (0.01), these results show good agreement between the $\tau_a(\lambda)$ computed by both methods.

Table 4.2 also shows the comparison between $\omega(\lambda)$ and $g(\lambda)$ retrieved by the principal plane inversion method of Olmo et al., (2008) and the AERONET almucantar inversion method during the desert dust intrusions observed at Granada from 2005 to 2010. In this comparison only nearly coincident measurements are used. On the other hand, only small number of $\omega(\lambda)$ achieved the AERONET level 2.0 due to the limitations imposed by the AERONET inversion algorithm ($\tau_a(440nm) > 0.4$ and solar zenith angle > 50º). Thus, for comparing both data sets we used $\omega(\lambda)$ corresponding to AERONET level 1.5 (cloud screened data with pre- and post-calibrations applied) that fulfil the following conditions: $\tau_a(440nm) > 0.2$ and solar zenith angle > 50º.
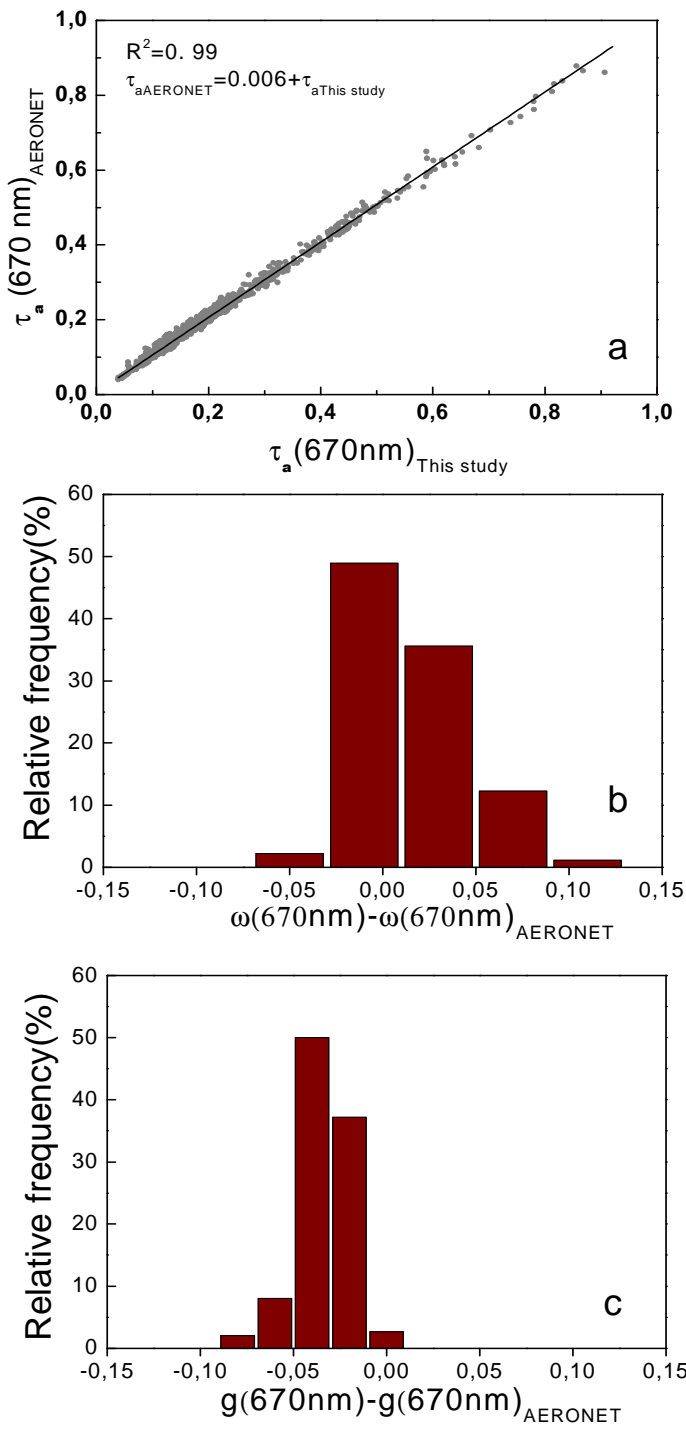
Figure 4.7: a) τ_a*(670 nm)* provided by AERONET vs the computed by our methodology. b) and c) Frequency distributions of the absolute differences between ω(670 nm) and g(670 nm) provided by AERONET and computed by the Principal plane inversion algorithm.

	440 nm	670 nm	870nm	1020nm
$\tau_{aa}(\lambda)$	0.27±0.15	0.22±0.15	0.21±0.14	0.20±0.13
$\tau_{an}(\lambda)$	0.28±0.15	0.23±0.14	0.21±0.14	0.20±0.13
$\omega_a(\lambda)$	0.89±0.03	0.93±0.02	0.94±0.02	0.95±0.02
$\omega_n(\lambda)$	0.90±0.03	0.91±0.03	0.92±0.03	0.93±0.03
$g_a(\lambda)$	0.72±0.02	0.70±0.02	0.70±0.02	0.71±0.02
$g_n(\lambda)$	0.70±0.02	0.67±0.02	0.66±0.02	0.67±0.02
RMSE ($\tau_a(\lambda)$)	0.007	0.012	0.007	0.012
RMSE ($\omega(\lambda)$)	0.048	0.034	0.028	0.026
RMSE ($g(\lambda)$)	0.031	0.036	0.042	0.043
$\Delta\tau_a(\lambda)$	0.009±0.008	0.009±0.009	0.005±0.006	0.009±0.008
$\Delta\omega(\lambda)$	0.037±0.031	0.027±0.021	0.022±0.018	0.021±0.016
$\Delta g(\lambda)$	0.026±0.017	0.033±0.014	0.039±0.015	0.039±0.016

Table 4.2: Mean values (±standard deviation) of spectral aerosol optical depth ($\tau_a(\lambda)$), single scattering albedo ($\omega(\lambda)$) and asymmetry parameter ($g(\lambda)$); RMSE is the root mean square error and refers to the absolute differences between retrievals obtained by our method and the AERONET code at 440, 670, 870 and 1020 nm for all nearly coincident measurements during desert dust events from 2005 to 2010. Subscript "a" and "n" refers to AERONET and our method, respectively.

The uncertainty in the AERONET retrieval of $\omega(\lambda)$ is about ± 0.03 for high aerosol loads (τ_a(440 nm) ≥ 0.4) and solar zenith angles > 50°. For measurements with lower aerosol loading the retrieval accuracy of $\omega(\lambda)$ significantly decreases because of the decrease of the information content, and the accuracy drops down to 0.05-0.07 for $\tau_a(440nm) \leq 0.2$ (Dubovik et al., 2000, 2002a).

4. Methodology and Data

These differences are within the estimated error (0.03-0.07) for $\omega(\lambda)$ (Dubovik et al., 2002b). The root mean square error for $\omega(\lambda)$ ranges between 0.03 and 0.05 at 1020 and 440 nm, respectively. Figures 4.7b and 4.7c show the absolute differences of ω(670nm) and g(670nm) computed by our methodology versus AERONET. As can be seen, up to 70% and 80% of the absolute differences are within the estimated errors by AERONET g(670nm) and ω(670nm), respectively. The root mean square error for g(670nm) varies between 0.03 and 0.04 at 440 and 1020 nm, respectively. In all channels the mean spectral asymmetry parameter computed using our method is smaller than that from AERONET (Table 4.2).

Figure 4.8 shows an example of the temporal evolutions of ω(440nm) and g (440nm) computed by the two methodologies for June 23 (2008). The AERONET data are level 2.0 data. Taking into account the uncertainty in both optical parameters, Figure 4.7 shows that ω(440nm) and g (440nm) obtained by the two methods is comparable. The mean daily values (± standard deviations) of ω(440nm) and g (440nm) are 0.90±0.01 and 0.74±0.01 for the AERONET inversion code (almucantar configuration), and 0.89±0.02 and 0.71±0.01 for the principal plane code, respectively. The slight differences obtained are due to the different input parameters (almucantar and principal plane radiances), time measurements, different kernel matrices, and also to the internal restrictions and convergence levels of both codes.
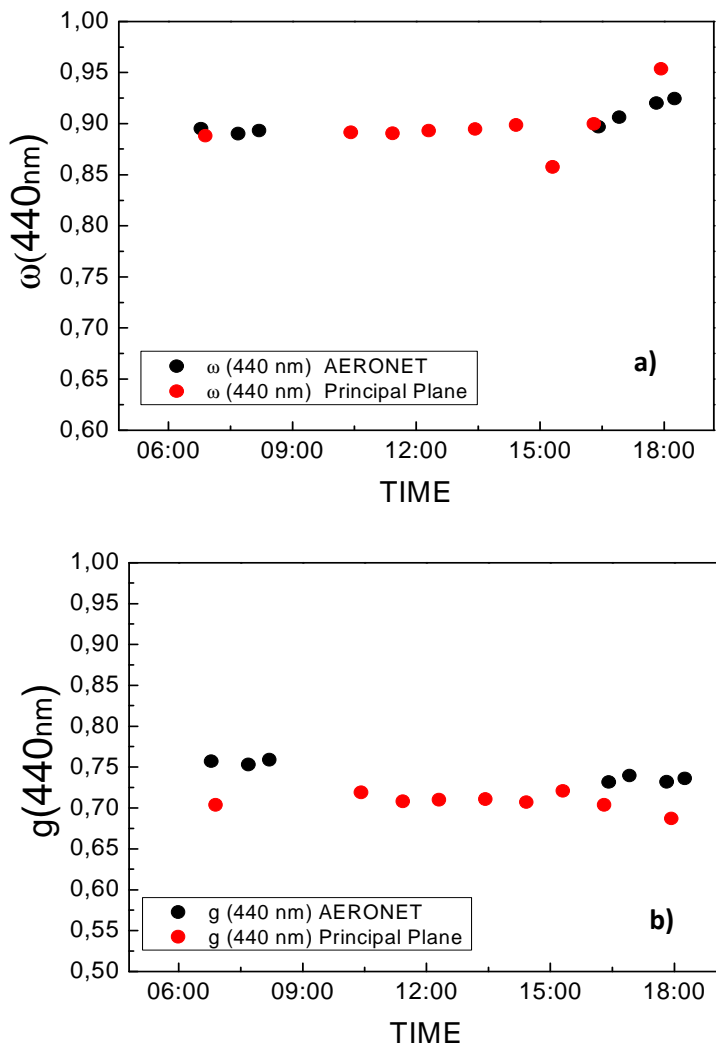
Figure 4.8: a) ω(440 nm) and b) g(440 nm) evolutions derived by AERONET code (Level 2.0 data) and by the Principal plane inversion code at Granada (23 June, 2008).

On the other hand, the sun-photometer pointing errors (misalignments) can affect the principal plane measurements as well the derived aerosol properties by the inversion methods (Torres, 2012; Torres et al., 2013). This author showed that these anomalies are significant for largest errors and shortest scattering angles, showing lower $\omega(\lambda)$ values at noon (about 10% or more) while $\tau_a(\lambda)$ remain unchanged. In our results (Figure 4.8) we observe no artefacts in the retrievals - due to the experimental pointing

errors - like those shown by Torres (2012). Similar results are obtained for other days affected by high loads of Saharan dust particles at Granada (AERONET level 2.0 data).

4.4 Aerosol radiative forcing

Aerosol radiative forcing (ARF) at the surface (TOA) is defined as the instantaneous increase or decrease of the net radiation flux at the surface (TOA) that is due to an instantaneous change of aerosol atmospheric content. The atmospheric ARF is defined as the radiative forcing at TOA minus the radiative forcing at the surface.

In this work, we have chosen the atmosphere without aerosols as the reference case. Thus, the instantaneous values of ARF can be derived from the following expression (Meloni et al., 2005):

$$ARF = \left(F^{\downarrow} - F^{\uparrow}\right) - \left(F_0^{\downarrow} - F_0^{\uparrow}\right) \tag{4.13}$$

where F and F_0 denote the global irradiances with aerosol and without aerosol, respectively. The arrows indicate the direction of the global irradiances (down and up). To carry out instantaneous global solar irradiance computations, we have used the radiative transfer computer code SBDART (Ricchiazzi et al., 1998), which is a discrete ordinates radiative transfer model (Stamnes et al., 1988). This algorithm includes multiple scattering in a vertically inhomogeneous, non-isothermal plane-parallel media, and has been shown to be computationally efficient in reliably resolving the radiative transfer equation. This radiative transfer computer code characterizes atmospheric aerosol radiative effects using as input the solar zenith angle, the spectral aerosol optical depth, the spectral single scattering albedo, and the spectral asymmetry parameter. Logarithmic interpolation (or extrapolation for $\lambda < 414$ nm or $\lambda > 860$ nm) was used to

supply SBDART with aerosol optical depths, $\tau_a(\lambda)$ covering the entire wavelength range of the calculation (310–2800 nm). Linear extrapolation is used for $\omega(\lambda)$ and $g(\lambda)$. In this thesis, we used the spectral aerosol optical depth, the spectral single scattering albedo, and the spectral asymmetry parameter obtained from the CIMEL sun-photometer. With respect to the vertical distribution of aerosol, we used the SBDART profile which takes into account the aerosol-loaded atmosphere fitting an exponential-decay to the aerosol optical depth derived by sun-photometer. Input data include the total ozone column derived from the satellite Ozone Monitoring Instrument (OMI) and the surface spectral albedo provided by the AERONET algorithm, based on a dynamic spectral and spatial model estimation at four wavelengths: 440, 675, 870 and 1020 nm. For land surface covers, the Lie-Ross model was adopted (Lucht and Roujean, 2000), considering the bidirectional reflectance distributions from MODIS (Moody et al., 2005). Mean values of surface spectral albedo of 0.05±0.04 at 440 nm, 0.16±0.03 at 675 nm, 0.31±0.04 at 870 nm and 0.32±0.04 at 1020 nm for the analyzed days were used in this work.

The parameters output by the code are the downward and the upward global irradiance at surface and at TOA. Calculations were performed and integrated over the 0.31-2.8 µm solar spectral range for solar zenith angles varying from 20º to 80º.

Daily mean values of the aerosol radiative forcing at the surface (TOA) are derived from integration of the instantaneous aerosol radiative forcing at the surface (TOA) averaged 24 hours (Bush and Valero, 2003):

$$DARF = \int \frac{ARFdt}{24} \qquad (4.14)$$

The atmospheric heating rate was computed for each layer, based on finite difference estimates of the irradiance divergence at each pair of levels (Liou, 2002);

$$\frac{\partial T}{\partial t} = \frac{g}{C_p} \frac{\Delta F_{Atmosferic}}{\Delta p} \tag{4.15}$$

where T is the temperature (K), t is the time (s), g is the gravitational acceleration (9.8 ms^{-2}), C_p is the specific heat of dry air (~1004 J/kgK), F is the net all-wave flux (W/m^2), and p is the pressure (Pa). In this work, we calculated the aerosol heating rate for the whole atmospheric column which is the difference in heating rates between an aerosol laden and an aerosol free atmosphere.

4.5 Comparison between columnar and in-situ ground-based aerosol optical properties

Remote sensing techniques can quantify the aerosol particle size using spectral aerosol optical properties, but inferring aerosol type requires knowledge of the source regions usually obtained through use of ancillary data sets (e.g. back-trajectories models, satellite products and electron microscopy) to determine emission sources, transport mechanisms, composition, and morphology. The discrimination of aerosol types increases accuracy of the assessment of the aerosol radiative impact and therefore is important to climate modeling (Giles et al., 2012). Variations in spectral aerosol absorption magnitudes can enable partitioning among aerosols from various source regions, fuel types, or combustion phases. Aerosol absorption together with size can potentially determine dominant aerosol types from remote sensing and in situ measurements.

4. Methodology and Data

In this sense, in this work are assessments the aerosol optical properties during desert dust events and dust-free conditions at atmospheric column and at surface over Granada from 2008 to 2010. For this purpose, measurements of a passive remote sensing (sun-photometer CIMEL) and ground-based "in situ" instruments (integrating nephelometer and Particle Soot Absorption Photometer, PSAP) are used.

Aerosol characterization inferred by scattering and absorption properties in atmospheric column

Various methods have been proposed using aerosol optical and microphysical properties to distinguish aerosol types. The magnitude of the aerosol optical depth ($\tau_{a\lambda}$) and the spectral dependence of $\tau_{a\lambda}$ with respect to wavelength (i.e., Ångström exponent, α) is commonly used in aerosol remote sensing to infer dominant aerosol types given knowledge of the source region or typical aerosol transport mechanisms (Boselli et al., 2012). Although size varies among particle types, the spectral absorption also varies. Some studies (Russell et al., 2010) have suggested relationships utilizing the aerosol absorption and size properties to determine the dominant aerosol type from Aerosol Robotic Network (AERONET) retrievals (Holben et al., 1998; Dubovik et al., 2006). Information content from these relationships varies from identification of major aerosol particle types (e.g., dust, mixed, urban/industrial pollution, and biomass burning smoke) to specific degrees of absorbing aerosols. Recently, Russell et al. (2010) have proposed using the absorption Ångström exponent (*AAE*), the spectral absorption aerosol optical depth dependence on wavelength, to further define aerosol type from AERONET retrievals.

4. Methodology and Data

For this work we use solar extinction (direct irradiance) and sky radiances at the almucantar configuration, both measured with a CIMEL CE-318-4 sun-photometer included in the AERONET network (Holben et al., 1998). In this work to assessment the aerosol optical properties at atmospheric column the AERONET retrieval was used because AERONET algorithm provide aerosol fine mode fraction (FMF). Due to the strong limitations imposed by the AERONET inversion algorithm (τ_a(440nm) > 0.4 and solar zenith angle > 50º) and the reduced sampling of sky radiances (almucantar sky radiance measurements) as well as the presence of clouds during measurements, there was few $\omega(\lambda)$ level 2 retrieval at Granada. Thus, the AERONET level 1.5 cloud screened was used. Although in this level the condition for aerosol load (τ_a(440nm) > 0.4) is not satisfied, we have required that the solar zenith angle was above 50º. In addition, pre- and post-field calibration, automatically cloud cleared and manually inspected were applied (similar procedure to AERONET level 2.0 τ_a data). In this sense, the quality of data is guaranteed. The total uncertainty in aerosol optical depth (τ_a) and sky-radiance measurements is about $\pm$ 0.01 and $\pm$5%, respectively.

However, to ensure sufficient sensitivity to aerosol absorption, only almucantar scans where τ_a(440nm) > 0.2 and solar zenith angle >50º (e.g. Dubovik et al., 2000) were selected. The accuracies of at 440 nm drops down to 0.02-0.07, for τ_a(440nm) <0.2 (Dubovik et al., 2000).

The spectral absorption optical depths $\tau_{aabs}(\lambda)$ is derived from the extinction aerosol optical depths ($\tau_a(\lambda)$) and the single scattering albedo, ($\omega^{col}(\lambda)$), in atmospheric column (Rusell et al., 2010):

$$\tau_{aabs}(\lambda) = (1 - \omega^{col}(\lambda)) \cdot \tau_a(\lambda) \tag{4.16}$$

The scattering optical depths ($\tau_{asct}(\lambda)$) is obtained by subtracting the spectral absorption optical depths to the extinction optical depths. The scattering Angström exponent ($SAE^{col}(\lambda)$) is computed from linear regression of $\ln \tau_{asct}(\lambda)$ versus $\ln \lambda$ for all $\tau_{asct}(\lambda)$ data available between the wavelengths of 440 nm and 1020 nm. Finally, the absorption Angström exponent ($AAE^{col}(\lambda)$) is computed using absorption aerosol optical depth following the same method that to obtain the traditional Angström exponent in those same wavelengths. The superscript "col" mean that these parameter have been retrieved in atmospheric columnar.

In situ measurements

Absorption coefficients ($\sigma_{ap}(\lambda)$) obtained at three wavelengths 467, 531 and 650 nm are used to derive the absorption Angstrom exponent ($AAE^{is}(\lambda)$) employing the Angstrom relation (Anderson et al., 2005);

$$AAE^{is}(\lambda) = -\frac{\ln(\sigma_{ap}(\lambda_1)/\sigma_{ap}(\lambda_2))}{(\lambda_1/\lambda_2)} \tag{4.17}$$

where $\sigma_{ap}(\lambda)$ is the absorption coefficient at a specific wavelength, λ is the wavelength and $AAE^{is}(\lambda)$ is the absorption Angstrom exponent. The scattering Angström exponent ($SAE^{is}(\lambda)$) is derived from equation 2 but employed scattering coefficients ($\sigma_{scat}(\lambda)$) instead of absorption coefficients ($\sigma_{ap}(\lambda)$). This $\sigma_{scat}(\lambda)$ variable is used in the Angstrom relation ($\sigma_{scat}(\lambda_i) = \beta_{ap} \cdot \lambda^{-\alpha}$) to obtain the absorption coefficient at the same wavelengths (450, 550 and 700 nm) that the scattering

coefficient measured with the integrating nephelometer. The scattering and absorption coefficients were derived at surface every 5 min to estimate the single scattering albedo at surface ($\omega^{is}(\lambda)$) at 467, 531 and 650 nm. The $\omega^{is}(\lambda)$ was estimated using the standard relation;

$$\omega^{is}(\lambda) = \frac{\sigma_{scat}(\lambda)}{\sigma_{scat}(\lambda) + \sigma_{ap}(\lambda)} \tag{4.18}$$

where $\sigma_{scat}(\lambda)$ and $\sigma_{ap}(\lambda)$ are the scattering and absorption coefficients. The superscript "is" mean that this parameter has been retrieved from in situ measurements.

4.6 Aerosol relative transmittance in Erythemal spectral band (T_{UVER})

Mineral dust aerosol has been characterized in numerous studies. Some of these studies focused in determinate the main sources of mineral dust (Prospero et al., 2002). Several studies analyzed Saharan dust contribution to ambient levels of suspended particulate matter, studying the synoptic meteorological conditions responsible for the transport of the dust air masses (Escudero et al.,2005; Querol et al., 2009). Other studies focused on the retrievals of micro-physical and optical properties of Saharan dust using passive remote sensing measurements with sun-sky photometers (Alados-Arboledas et al., 2003, 2008; Lyamani et al., 2006a; 2006b; Toledano et al., 2007; Valenzuela et al., 2012a,2012b). However, there are relatively few studies analyzing effects of dust intrusions on shortwave solar radiation reaching the Earth's surface (Díaz et al., 2001; Lyamani et al., 2006; Cachorro et al., 2008; Antón et al., 2012a). To our knowledge, only Díaz et al. (2007) and Antón et al. (2012b) have analyzed the atmospheric aerosol

effects on spectral UV irradiance during two Saharan dust events in South Spain. In general, there are only a few works about this subject in literature (e.g., di Sarra et al., 2002; Meloni et al., 2003; Kalashnikova et al., 2007; García et al., 2009) due to the scarcity of routinely operational ground-based stations with high-quality instrumentation to measure simultaneously UV irradiance and aerosol data during desert dust intrusions. The advantage of the Granada radiometric station is that there are available in-situ ground based and remote sensing instrumentation which enable to study those dust aerosol effects in UV irradiance.

In this work, the dust effect on the UVER is described in terms of the relative aerosol transmittance (T_{UVER}), relative to no-aerosol clear sky $UVER^0$ (Krotkov et al. 1998):

$$T_{UVER} = \frac{UVER}{UVER^0} \tag{4.19}$$

In this expression UVER represents the erythemal measurements recorded during desert dust intrusions, and $UVER^0$ corresponds to the erythemal data for the same solar zenith angle (θ) estimated from the empirical expression (Madronich, 2007):

$$UVER^0 = a \left(\mu_0\right)^b \left(\frac{TOC}{300}\right)^c \tag{4.20}$$

where μ_0 is the cosine of the θ and TOC is the total ozone column in Dobson Units (DU) provided by the OMI satellite instrument (OMTO3 product using NASA TOMS V8 retrieval algorithm (Bhartia and Wellemeyer, 2002). This parameterized radiative model can be adjusted using available experimental data, at the local site (Koepke et al., 1998). Antón et al. (2011) calculated the coefficients (a, b and c) in equation (4.20) for

4. Methodology and Data

Granada site using UVER measurements during cleanest air conditions at the site. They validated this empirical model using measurements collected during a period not previously used for calculating fitting coefficients. The results show a reliability of the empirical model (4.20), which estimates $UVER^0$ with a mean absolute bias less than 2.5%.

Finally, the atmospheric aerosol transmittance is calculated from equation (4.19) by using measured UVER values averaged within ±2 min of each Cimel $\tau_a(\lambda)$ retrieval during desert dust events (2006-2010).

In order to analyze the effects of desert dust events on OMI-derived surface UV irradiances a single OMI ground pixel most closely collocated with Granada station is selected as the best match for each day. We used OMI pixels with centers from 1 km to 78 km from the study site, with the mean and median values being 17 and 11 km, respectively. Five surface UVER measurements within ±2 min from the OMI overpass at ~13:30 are averaged for comparison with the OMI data. Additionally, aerosol information derived from Cimel sun-photometer is averaged between 12:30 and 14:30 solar time on each day.

CHAPTER 5

AIR MASSES

CLASSIFICATION METHODS

5. Air masses classification methods

5. Air masses classification methods

In this Chapter we explain the two methodologies used in this work to classify air mass back-trajectories coming from North Africa to the monitoring stations (Granada and Alborán Island). In next chapters, the aerosol optical and radiative properties obtained using sun-photometric measurements have been related according to these classification methodologies.

5. Air masses classification methods

5.1 Air masses

An air mass is a body of air extending over a large area (usually from hundreds to thousands kilometers). It is generally an area of high pressure that stagnates for several days where surface terrain varies little. During this time, the air mass takes on characteristics of the underlying surface. Properties of temperature, moisture (humidity), and lapse rate remain fairly homogeneous throughout the air mass (Barry and Chorley, 1987). The characteristics of an air mass are acquired in the source region, which is the surface area over which the air mass originates. The ideal source region has a uniform surface (all land or all water), a uniform temperature, and is an area in which air stagnates to form high-pressure systems. The properties (temperature and moisture content) of an air mass acquired in its source region are dependent of a number of factors such as the time of year (winter or summer), the nature of the underlying surface (whether land, water, or ice covered), and the length of time it remains over its source region. Our study region is a place of special interest for the study of the atmospheric aerosol due to its geographic location surrounded by continents with different surface characteristics and where local winds, complex coastlines and orography have strong influence on the atmospheric flow. In this sense, due to the proximity of North Africa desert regions the contribution of mineral particles to the total aerosol load over our location is significantly relevant. Other potential aerosols sources affecting our station are Western Europe, Mediterranean region and Atlantic Ocean.

5.2 Back-trajectories. Hysplit model

The paths followed by the air masses are given by their back trajectories at different height levels. This fact gives us a first approximation of the regions with which the air masses interacts with their boundary layer. One of the most used models for calculating back trajectories is the Hybrid Single-Particle Lagrangian Integrated Trajectory Model (HYSPLIT) developed by NOAA (Draxler and Rolph, 2003). This model combines a Langrangian approximation for resolving air mass transport with an Eulerian approximation for the diffusion of pollutants. The accuracy of backward trajectories shows position errors with the travel's distance (Stohl, 1998). These errors which cause deviation in the back-trajectories are related to five factors (Harris et al., 2005): differences in computational methodology, 3–4%; time interpolation, 9–25%; vertical transport method, 18–34%; meteorological input data, 30–40%; and combined two-way differences in vertical transport method and meteorological input data, 39–47%. This sensibility test was performed for 96 hours of flight time. In this work, the back-trajectories were computed for 120 hours of flight time. Therefore, a greater flight time will imply greater differences. Nevertheless, numerous studies use five day back trajectories as a compromise between accuracy and the need to reconstruct as completely as possible the average life cycle of aerosol particles in the atmosphere (Estelles et al., 2007).

Five-day back-trajectories of air masses arriving at monitoring station at 500, 1500 and 3000 m a.g.l. were computed using HYSPLIT_4 model including vertical wind (Draxler and Rolph, 2003). At Granada these back-trajectories were computed coincident with African desert dust days established by CALIMA network. The NCEP/NCAR reanalysis database was used as model input (NOAA Operational Model

Archive Distribution System server at NCEP). The 500 m above ground level back-trajectory was computed because in the boundary layer is produced greater part of the interactions between atmospheric aerosol and air masses. However, due to these same interactions, the largest uncertainty in the compute of back-trajectories corresponds to this level. The 1500 m high level back-trajectories represent the top of the boundary layer. Finally 3000 m above ground level back-trajectory represent air within the free troposphere. The pattern for dust transport suggested evaluating cases with like air masses at 1500 and 3000 m level (Toledano et al., 2009; Escudero et al., 2011). For every day, a trajectory at each height level was computed with endpoint in monitoring station at 12:00 UTC. For this reason, we computed trajectories at 500, 1500, and 3000 m a.g.l., corresponding to pressure levels at approximately 950, 850 and 700 hPa, respectively. Numerous authors have computed trajectories between 500 and 3000 m a.g.l. for African air masses arriving at Iberian Peninsula (Escudero et al., 2011; Toledano et al., 2009; Guerrero-Rascado et al., 2009; Wagner et al., 2009).

5.3 Air masses classification methods employed

The atmospheric columnar aerosol optical and microphysical properties have been classified using two different methodologies: A) taking into account the potential aerosol source regions, and B) the pathway of the back-trajectories.

5. Air masses classification methods

A) Identification of potential aerosol origin sources.

We used the criteria of Pace et al. (2006) to identify potential aerosol source regions. This method assumes that the particles are confined in the mixed layer at the source region, and that the air mass is loaded by aerosol when the air mass altitude, $z_{back-traj}$, is lower or close to the altitude of the mixed layer, z_{mxl}, (entrainment condition). The geographical sector where the entrainment condition is met along the trajectory is identified as the source of the observed aerosol. If the entrainment condition is met at more than one point, the geographical position where the difference ($z_{back-traj}$. $-z_{mxl}$) is the lowest (sign included) is selected as the potential source of aerosol particles. In this study, both the air mass back-trajectories and mixed layer altitudes were supplied by the HYSPLIT model.

This methodology has been applied to classified back-trajectories from North Africa arriving at Granada at 500, 1500 and 3000 m a.g.l coincident with African desert dust days established by CALIMA network. After that, we have performed a visual inspection of the air masses trajectories at all levels. We have checked that the 500 m a.g.l. air masses arriving at Granada never over pass for the North Africa. Therefore, we have only classified African air masses at 1500 and 3000 m a.g.l. arriving at Granada. Finally, to verify the input of dust, we have exploited MODIS satellite imagery products and we have compared them with air masses trajectories transported from North Africa. In this sense, three regions as potential sources of aerosol particles have identified, displayed in Figure 5.1. The defined sectors are: 1) Sector A (North Morocco, North-western Algeria), 2) Sector B (Western Sahara, North-western Mauritania and South-western Algeria) and 3) Sector C (Eastern Algeria, Tunisia).
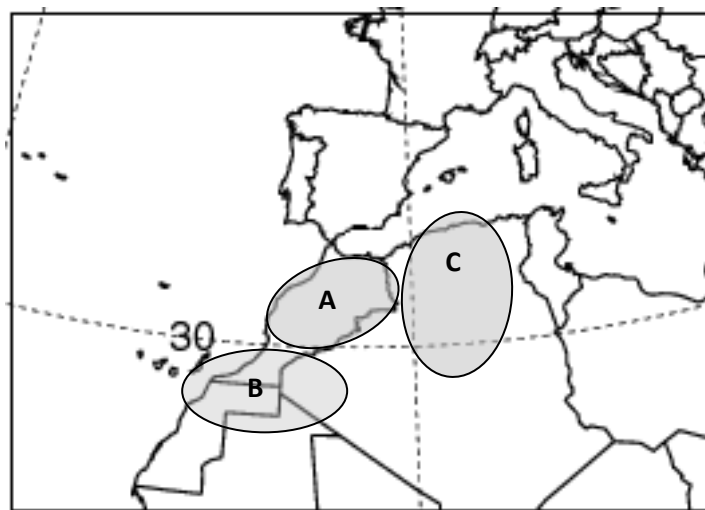
Figure 5.1: Potential desert dust origin sources.

The methodology to classified back-trajectories according to the potential aerosol origin sources has also been applied over Alborán Island. According to this method, three regions as potential sources of aerosol particles have been identified, displayed in Figure 5.2: 1) Sector A (Central Europe, Mediterranean Sea), 2) Sector B (North Africa) and 3) Sector C (Atlantic Ocean and Iberian Peninsula).
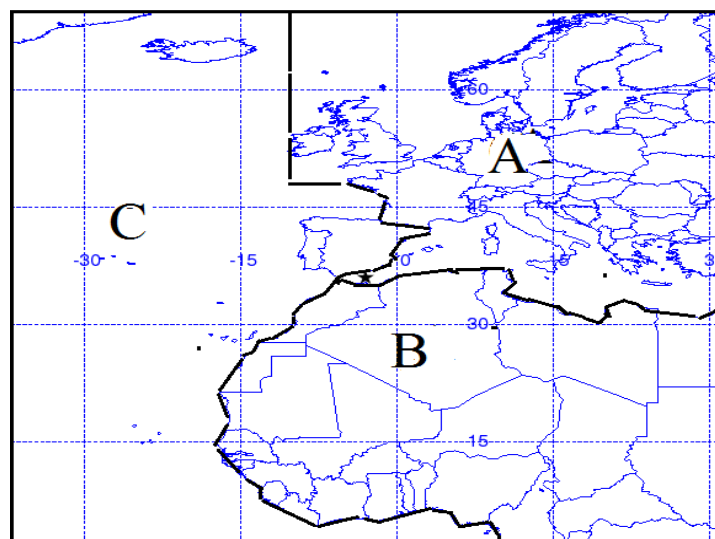
Figure 5.2: Different source regions are split into three sectors (A, B and C).

5. Air masses classification methods

B) Cluster analysis.

In order to obtain information about air flow patterns, we have applied statistical techniques to a database of individual trajectories from North Africa air masses over Granada radiometric station. This method is based on the geometric distance between individual trajectories and it takes into account speed and direction of the trajectory. The final results are centroids (clusters-mean trajectories) which grouping individual trajectories with similar behavior of their direction and speed of passage over certain areas. The African air masses affecting Granada from 2005 to 2010 were classified according to their transport pathways using HYSPLIT clustering algorithm (http://www.arl.noaa.gov/). The trajectory types are interpretable in terms of the synoptic conditions that form them. Large scale circulation features are associated with certain trajectory clusters. The cluster analysis does not assume the existence of desert dust sources and their geographic locations for clustering the air mass types. However, according to this method the researcher chooses the number of cluster that physically represents airflow patterns for the specific site. The centroid represents the average of the trajectories included in that cluster. The HYSPLIT model has a clustering tool based on the variations in both the total variance between clusters (TSV, Spatial Variance Total) and the variance between each component trajectory (SPVAR, Spatial Variance) (Draxler et al., 2009). First, we have generated a set of 183 back-trajectories arriving over Granada. The grouping process started with an initial number of individual trajectories and ended with the creation of a single cluster that group some of them. In each stage were unified two trajectories that caused the minimum increase of TSV and SPAVR. The appropriate number of clusters was computed from the percent change in total spatial variance (TSV) as the sum of the SPVAR. This parameter is derived from

the sum of the squared distances between the endpoints of the cluster's component trajectories and the mean of the trajectories in that cluster. Large changes were interpreted as the merging of significantly different trajectories into the same cluster. Accordingly, the approximate number of clusters would be found just prior to the large percent change in TSV. Although the determination of the number of cluster group may be subjective, two groups for each level were chosen in order to a better explanation of the transport regimes during the study period after additional analysis for different cluster numbers. Within each cluster, individual trajectories were averaged to produce a cluster-mean trajectory.

CHAPTER 6

RESULTS AND DISCUSSION

6. Results and Discussion

6. Results and Discussion

Chapter 6 presents the main results of this thesis. Firstly, we analyze the atmospheric aerosol optical and microphysical properties during desert dust events over Granada from 2005 to 2010. This work is focused on those desert dust events which reached the surface (CALIMA.ws). Therefore, in the next section, we will assess the aerosol optical properties during desert dust events and dust-free conditions at atmospheric column and at surface. For this purpose, measurements of a passive remote sensing (sun-photometer CIMEL) and ground-based "in situ" instruments (integrating nephelometer and Particle Soot Absorption Photometer, PSAP) will be used. On the other hand, there are relatively few studies analyzing analyzed the atmospheric aerosol

6. Results and Discussion

effects on spectral UV irradiance during Saharan dust events in South Spain. In this sense, the UVER transmittance results will be determined and the results of applying the aerosol absorption post-correction method of the OMI UVER algorithm will be showed. In this work, the analysis of the aerosol properties was performed away from the desert dust source region, giving sufficient time for efficient mixing of the mineral particles with other aerosol types. On the other hand, the mineral optical properties could change depending on the desert dust source region. In this sense, the aerosol optical and microphysical properties will be classified according to the potential origin sources and also applying cluster analysis. The desert dust, among the different aerosol types present over the South-eastern Spain, produces larger radiative perturbation at the surface and at the top of the atmosphere (TOA). Later, aerosol radiative forcing will be compute according to the origin sources classification. Therefore, in this study photometric measurements are combined with a radiative transfer model (SBDART) to quantify the aerosol radiative forcing in (310-2800 nm) spectral range both at the surface and at TOA during desert dust events. Finally, it is interesting to study the atmospheric aerosol transported from North Africa to Europe before its mixing with antropogenic aerosol originated in Europe. In this sense, Alborán Island, located in between the North African coast and the South-eastern Iberian Peninsula offers an appropriate place to perform this type of studies. The small Alborán Island, is located in the Western Mediterranean Basin around 90 km North of Africa coast and 60 km South-eastern of the Iberian Peninsula. The analysis of the aerosol properties over Alborán Island will be performed in detail. We pay special attention in aerosol optical and microphysical properties during desert dust events over this Island.

6.1 Aerosol optical and microphysical properties.

6.1.1 Annual evolution

CALIMA project reported 626 days affected by African desert dust air masses over the South-eastern Iberian Peninsula from January 2005 to December 2010 (www.calima.ws): 78, 93, 139, 107, 115 and 94 days in 2005, 2006, 2007, 2008, 2009 and 2010, respectively. During the entire period 29% of days were characterized by the presence of African desert dust air masses, including events associated with cloudy conditions. The African dust intrusions were more frequent in summer (Jun, July and August) with a 45% of occurrence and less frequent in winter (11%). The numbers of days affected by these African desert dust air masses with sun-photometer cloud-free measurements were 12, 31, 25, 37, 33 and 45 for 2005, 2006, 2007, 2008, 2009 and 2010, respectively. This means a percentage of 9% for period 2005-2010. Toledano et al. (2007a) at El Arenosillo (South-western Spain) from 2000-2004 reported that between 14% and 21% of days were affected by desert dust intrusions. The large difference with our percentage of African desert dust events at Granada is due to the difference in detection method, considering only desert dust air masses detected at surface in our work.

The statistics of the $\tau_a(\lambda)$ and α(440-1020nm) during the African desert dust events recorded at Granada from 2005 to 2010 are summarized in Table 6.1. The mean value ($\pm$ one standard deviation) of τ_a(440 nm) (as reference wavelength for turbidity) was 0.27$\pm$0.15. The large $\tau_a(\lambda)$ standard deviation indicates a large variability in the

atmospheric aerosol load during desert dust events. In this direction, the coefficient of variation (CV), defined as the ratio of the inter-quartile range (difference between the 75th and 25th percentile) to the median, also presents an elevated value (between 67% at 440 nm and 82% at 1020 nm). This large variation could be related to several factors such as different meteorological conditions, source region and the chemical and physical processes occurring during dust transport. Additional information on aerosol properties over the study area can be obtained from the analysis of the Angström parameter, α(440-1020nm).

		τ_{a1020}	$\tau_{a\,870}$	$\tau_{a\,670}$	$\tau_{a\,440}$	$\alpha_{440\text{-}1020}$
Nº Days Desert dust	183					
Nº Observations	8680					
Mean		0.20	0.21	0.22	0.27	0.42
STD		0.13	0.14	0.14	0.15	0.21
Median		0.17	0.18	0.19	0.24	0.40
P25		0.11	0.25	0.28	0.17	0.26
P75		0.25	0.11	0.13	0.33	0.56

Table 6.1: Statistical parameters of $\tau_a(\lambda)$, α(440-1020nm) during African desert dust events for the period 2005-2010, including: the mean, the standard deviation, the median, the first and the second quartile (P25 and P75).

The CV of this parameter presents a high value (75%) which indicates the presence of particles with different size during African dust episodes at Granada. Nevertheless, its mean value was small (0.4±0.2), suggesting a significant contribution

6. Results and Discussion

of coarse particles during these dust events. The values of the $\tau_a(\lambda)$ and α(440-1020nm) during African dust events obtained in Granada are in good agreement with those reported by Lyamani et al. (2005) during Sahara dust outbreak in the same study site. These authors, using sun-photometer data, have reported values of τ_a(500 nm) ranging from 0.20 to 0.6 and values of α(368-778nm) in the range 0.36-0.37. In addition, there is a good agreement with the data recorded on other AERONET sites influenced by desert dust. For example, Prats et al. (2008) reported at El Arenosillo during desert events mean values of τ_a(440 nm) and α(440-870nm) of 0.40±0.23 and 0.45±0.26, respectively. At this same location, Toledano et al. (2007a) have obtained during desert dust events a mean τ_a(440nm) value of 0.33 and mean α value of 0.52.

Fig. 6.1 (a, b) shows the frequency histograms of the τ_a(440nm) and α(440-1020 nm). Up to 35% of the τ_a(440nm) values were below 0.2. The principal frequency mode was centered at 0.24. Up to 7% of the τ_a(440nm) values were above 0.5. Two well-defined modes are observed in the histogram of α(440-1020nm) parameter. The principal frequency mode was centered at 0.4 and second mode was centered at 0.2. In addition, we also find mean values of α around 0.9. This situation could be related to the background conditions in this urban location, and also with the advection of air masses coming from Atlantic, Europe or the Mediterranean area, that leads to the simultaneous presence of desert dust with polluted aerosol in the atmospheric column. Toledano et al. (2007a) have found at El Arenosillo two main frequency modes of α. First the mode around 0.5 was related to the desert dust events, when the τ_a(440 nm) increased and α(440-1020nm) decreased down to 0.2-0.4. On the other hand, the main frequency mode around 1.2 was related to the background conditions, that is, the mixture of

6. Results and Discussion

marine aerosol with continental or urban-polluted aerosol. Prats et al. (2008) have shown a low alpha-mode centered ~ 0.4 at El Arenosillo in summer 2004 which was associated with desert dust aerosol and marine background.
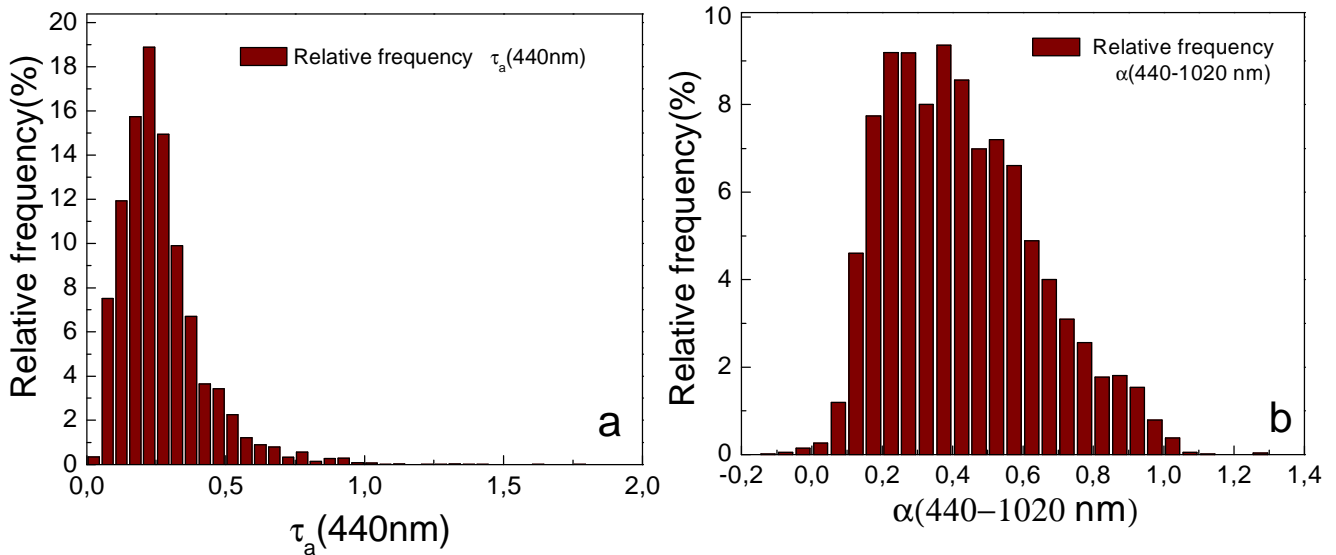

Figure 6.1: Frequency histograms of: a) τ_a(440 nm) and b) α(440-1020 nm) during African dust events for 2005-2010 period.

Fig. 6.2 (a, b) shows a box diagram of the seasonal variability of τ_a(440 nm) and α(440-1020nm) during the African dust events analyzed. In these box diagrams, the mean is represented by a blank dot and the median by a middle line. The top/bottom box limits represent the monthly mean plus/minus the standard deviation. In addition, the error bars of the box are the percentiles 5% and 95%. The number of data recorded during the months of January, November and December is quite limited due to the major presence of cloudy days. Fig. 6.2 (a) shows maximum monthly mean values of τ_a(440 nm) in April (0.44±0.24), and minimum values in October (0.19±0.10). The

spring and early summer months showed τ_a(440 nm) values above 0.3 with a large variability for April. It is interesting to note that for almost all months the τ_a(440 nm) mean values were higher than the median values, thus indicating the importance of scenarios with high aerosol load. Fig. 6.2 (b) shows that α(440-1020 nm) varied in the range 0-1. The minimum mean values of α(440-1020nm) were registered in May (0.27±0.16), while the highest monthly mean value of this parameter was reached in September, with a mean value of 0.63±0.21.

The clear anti-correlation between τ_a(440 nm) and α(440-1020 nm), together with the reduced value of this last variable, is an evident signature of the large contribution of coarse particles to the atmospheric aerosol during African desert dust episodes, in agreement with the observations reported by different authors (e.g. Smirnov et al., 1998; Cachorro et al., 2008; Toledano et al., 2007a; El-Askary et al., 2009; Eck et al., 2010). Nevertheless, the large error bars in both plots indicate significant variability in the aerosol load and particle size distribution at Granada during African dust events.
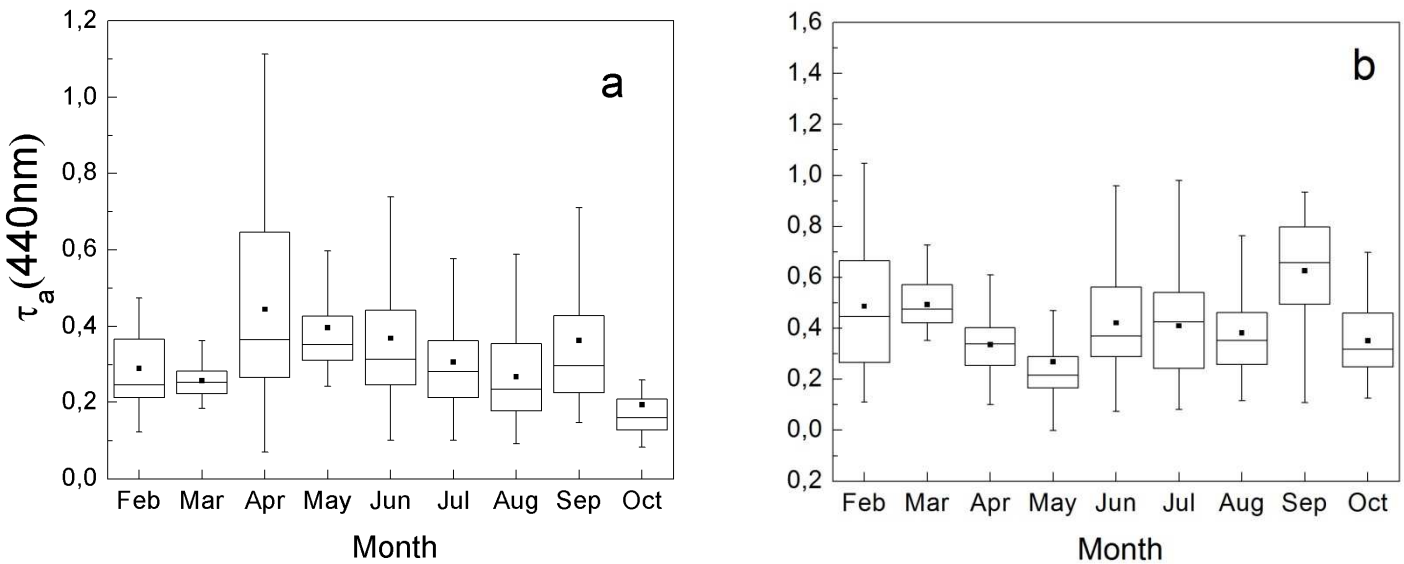
Figure 6.2: Monthly statistics of τ_a(440 nm) (left plot) and α(440-1020 nm) (right plot) during African dust events from 2005 to 2010 represented as box diagrams. In these box diagrams, the mean is represented by a blank dot and the median by a middle line. The top/bottom box limits represent the monthly mean plus/minus the standard deviation. In addition, the error bars of the box are the percentiles 5% and 95%.

Table 6.2 summarizes the annual means of parameters related to columnar aerosol volume size distribution. The parameters r_c and r_f are the modal radius for coarse and fine particles modes, respectively, and V_c and V_f are their volume concentrations. The cutoff radius used in size distributions for fine and coarse modes is 0.5 μm. The fine mode volume concentration, V_f, showed little changes during desert dust events with a mean value of 0.015±0.007 μm^3/ μm^2. The fine modal radius presents a mean value for the entire period close to 0.20±0.04 μm.

	Coarse Mode		Fine Mode		V_c/V_f
	V_c ($\mu m^3/\mu m^2$)	r_c (μm)	V_f ($\mu m^3/\mu m^2$)	r_f (μm)	
February	0.14±0.10	1.98±1.18	0.016±0.006	0.22±0.03	8±3
March	0.09±0.03	1.46±0.33	0.015±0.003	0.20±0.03	6±2
April	0.42±0.36	2.24±1.27	0.031±0.019	0.21±0.05	14±7
May	0.15±0.12	2.29±1.25	0.016±0.005	0.20±0.03	9±6
June	0.16±0.09	2.35±1.39	0.015±0.007	0.21±0.04	10±6
July	0.18±0.09	2.47±1.33	0.015±0.005	0.20±0.04	12±5
August	0.14±0.07	2.62±1.43	0.012±0.005	0.20±0.03	12±6
September	0.16±0.09	3.01±1.62	0.017±0.008	0.19±0.03	11±7
October	0.12±0.09	2.34±1.46	0.012±0.004	0.20±0.04	10±5
Annual	0.17±0.12	2.41±1.38	0.015±0.007	0.20±0.04	11±6

Table 6.2: Monthly and annual mean values of parameters related to aerosol volume size distribution at Granada during African dust events for 2005-2010 period.

The fine mode aerosol showed no significant variation over the annual cycle in Granada which may be related mainly to the influence of the city: heavy traffic in the rather narrow streets together with the re-suspension of material available on the ground (e.g. Lyamani et al., 2006b, 2010). The coarse mode volume concentration, V_c, showed a mean value of 0.17±0.12 $\mu m^3/\mu m^2$ for the entire period, experiencing a notable seasonal change with the highest mean value in April (0.4±0.4 $\mu m^3/\mu m^2$). In addition, the coarse modal radius showed a decreasing trend in February and March. The lowest mean value corresponded to March, 1.5±0.3 μm, while the highest mean value corresponded to September (3.0±1.6 μm). The coarse mode observed at Granada may

be the result of a combination of different processes and sources regions such as surface generated or transported dust particles from African desert regions.

The annual mean ratio V_c/V_f (11±6) indicated the prevalence of large particles with respect to small particles, which is characteristic of desert dust events. This ratio showed maximum mean values in April and minimum mean values in February and March, in concordance with the annual evolution of the α(440-1020 nm).

For volume concentrations, Toledano et al. (2007b) found at El Arenosillo a mean V_c value of 0.11 $\mu m^3/\mu m^2$, lower than the value reported in this work for Granada (0.17±0.12 $\mu m^3/\mu m^2$). In contrast, the mean V_f value given by Toledano et al. (2007b) (0.023 $\mu m^3/\mu m^2$) for El Arenosillo was significantly higher than the value showed here (0.015±0.007 $\mu m^3/\mu m^2$). Prats et al. (2008), during desert dust event at El Arenosillo, showed an increase by a factor from up to 20 in the volume concentration of the coarse mode with respect to the fine mode. The differences respect to our results may be due to three reasons: a) differences related to the different measurement period (there is an inter-annual variability in the desert dust intrusions), b) differences related to the detection method, and c) different pathways of the desert dust air masses during the transport until the two stations. These authors found mean values of 1.74±0.15 μm for r_c and 0.13±0.02 μm for r_f. These values are smaller than those obtained in the present work. On the other hand, Tafuro et al. (2006) found an averaged value of 2.2 μm for r_c, and an averaged value close to 15 for the ratio V_c/V_f at Lampedusa Island. This last radiometric station is located 200 km away for Northwest coast of Africa, approximately. Differences in dust amounts, anthropogenic or biomass burning contributions and air mass trajectories arriving at Lampedusa must be responsible for

6. Results and Discussion

the differences with respect to our study. On the other hand, the volume concentration and the modal radius of coarse particles obtained in our study have higher standard deviations, which is indicative of the wide dust particles variability with different optical and microphysical properties. The standard deviations for modal radius of fine particles present small values, close to ±0.03 μm, showing the lower variability of particles size with anthropogenic or biomass burning origin. Finally, Table 6.2 shows that the fine mode parameters present no significant change whereas the coarse mode parameters were a good indicator of the dust desert arrival. These values were consistent with those obtained by other authors for desert dust events (e.g., Olmo et al., 2006, 2008; Dubovik et al., 2002; Toledano et al., 2007a; Lyamani et al., 2006a).

Both single scattering albedo ($\omega(\lambda)$) and asymmetry parameter ($g(\lambda)$) are key parameters for estimating the direct radiative impact of aerosol particles. The $\omega(\lambda)$ is defined as the ratio of the scattering coefficient and the extinction coefficient, and it is related to the absorptive capacity of the aerosol, taking a value of 1 for pure scattering particles and below 1 for absorbing ones. Absorption of solar radiation by atmospheric particles results mainly from elemental carbon originated from anthropogenic activities, biomass burning and mineral dust. According to the literature, the $\omega(\lambda)$ varies between 0.78 and 0.94 for cases of biomass burning particles and between 0.92 and 0.99 when the dominant particles are of desert type (Dubovik et al., 2002b). The asymmetry parameter, $g(\lambda)$, provides information of the angular distribution of the scattered radiation. For hemispherically symmetric scattering, Rayleigh scattering, the asymmetry parameter is considered to be 0 and for pure forward scattering $g(\lambda)$ would be 1.

6. Results and Discussion

In the analyzed period, mean values of $\omega(\lambda)$ ranged from 0.89±0.02 at 440 nm to 0.92±0.03 at 1020 nm. These results are in a good agreement with the results obtained during the dust outbreaks by Lyamani et al. (2006a) and Olmo et al. (2006) in the same study area. Perrone et al. (2005) also showed similar results at Lecce (Italy) with values of ω(440 nm) ranging from 0.85 to 0.9 when their study area was affected by Saharan dust together with anthropogenic aerosols from the central Mediterranean. However, the values of $\omega(\lambda)$ reported in this work were lower than those reported by other authors for cases of pure desert dust. Dubovik et al. (2002b) at Cape Verde obtained an averaged ω value at 440 nm of 0.93. Kim et al. (2011) found in Tamanraset (in 2006-2009 period) that ω ranging from 0.90 to 0.94 at 440 nm during desert dust events. The columnar values retrieved at Granada include the urban contribution that could be responsible of lower $\omega(\lambda)$ values (Lyamani et al., 2006b, 2010). On the other hand, the aging process during the transport of mineral dust from source region could be another reason for the lower $\omega(\lambda)$ values (e.g. Lyamani et al., 2006b; Lyamani et al., 2010; Gomez-Amo et al., 2011). Close to the source region mostly pure dust is found, but after a long range transport the aging of the dust and mixing with other aerosol types modify the optical properties of the desert dust (e.g. Bauer et al., 2011). The mixing of desert dust with anthropogenic particles may prompt changes in the physical properties and chemical composition of the desert dust and this may have important consequences in processes affecting climate (e.g. Rodriguez et al., 2011). The low values of $\omega(\lambda)$ obtained in our study area reveal the importance of aerosol absorption during desert dust events at Granada.

6. Results and Discussion

Fig. 6.3 shows the annual evolution of monthly mean $\omega(\lambda)$ for 440, 670, 870 and 1020 nm. The most important feature of $\omega(\lambda)$ was its spectral variation (slight increase with wavelength) as shown in other studies for desert dust events (e.g., Collaud Coen et al., 2004; Lyamany et al., 2006; Alados-Arboledas et al., 2008; Cachorro et al., 2008; Xingna Yu et al., 2011; Su and Toon, 2011; Toledano et al., 2011). In addition, it can be seen that the highest monthly mean value was found in February with $\omega(\lambda)$ ranging from 0.94±0.02 (at 440 nm) to 0.96±0.03 (at 1020 nm), respectively. For spring and summer months the monthly mean values increased with wavelength. Mean values of ω for July ranged from 0.88±0.02 to 0.91±0.03 at 440 and 1020 nm, respectively. This last fact is characteristic of mineral dust (e.g., Eck et al., 2010). Additionally, Fig. 6.3 also shows a decreasing of $\omega(\lambda)$ at all wavelengths in spring and summer seasons, indicating higher contribution of absorbing particles at Granada, probably due to the anthropogenic or biomass burning contributions associated with the synoptic situations of these months (e.g., Lyamani et al., 2005; 2006b; 2010).The difference between ω (440 nm) and ω (1020 nm) shows higher values in spring (March, April and May) and summer (Jun, July and August) than in February and October. The $\omega(\lambda)$ values show strongly wavelength dependence during spring and summer and relatively lesser dependence in February and October. This fact could be related to a larger influence of absorbing aerosol during warm-seasons. Kim et al. (2011) shows in Tamanraset (in the center of the Saharan desert) that in the months between March and September there are more dusty days. However, they found in the annual evolution of the single scattering albedo lower values in the months from May to August (ω=0.90±0.02 at 440 nm).This result is similar to the annual evolution of the single scattering albedo during desert dust events in our site from 2005-2010 period.

6. Results and Discussion
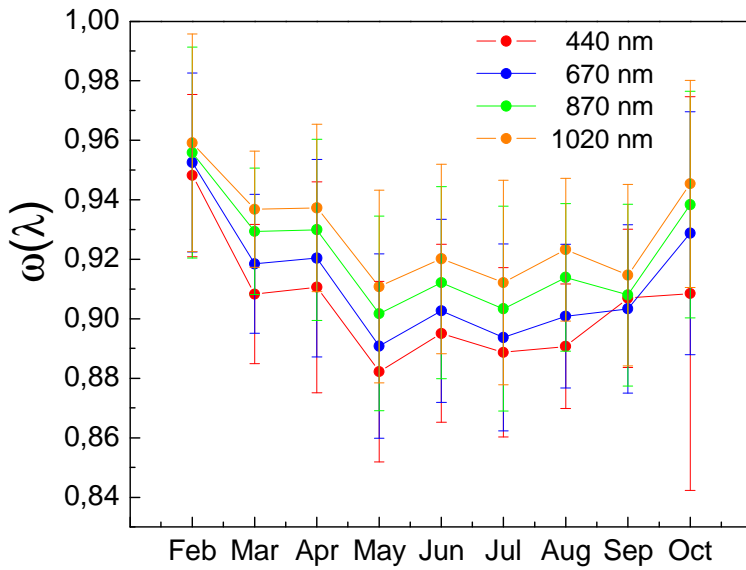
Figure 6.3: Monthly mean values and standard deviations of $\omega(\lambda)$ for 440, 670, 870 and 1020 nm during African dust events from 2005 to 2010.

The asymmetry parameter, $g(\lambda)$, showed distinct wavelength dependence with mean values ranging from 0.70 ± 0.02 at 440 nm to 0.67 ± 0.02 at 1020 nm. Ours results confirm the values derived by Olmo et al. (2006) with 0.69 ± 0.02 at 440 nm to 0.66 ± 0.02 at 1020 nm during Saharan dust episodes in the same study area. Dubovik et al. (2002), for desert dust episodes, have obtained values of g(440nm) around 0.69 ± 0.04 at Solar Ville, Saudi Arabia, and around 0.73 ± 0.04 at Cape Verde in these same wavelengths.

6. Results and Discussion

Fig. 6.4 shows the monthly mean values of $g(\lambda)$ at 440, 670, 870 and 1020 nm. The $g(\lambda)$ values showed no significant seasonal and spectral variation for the four wavelengths. This behaviour is characteristics of mineral dust (e.g. Alaldos-Arboledas et al., 2008). Nevertheless, a slightly higher value for g(440 nm) values is observed. These differences agree with the results reported by Lyamani et al. (2006b) for the extreme desert dust event registered during the 2003 heat wave at Granada. Kim et al. (2011) show the annual evolution for $g(\lambda)$ in several locations in North Africa (Tamanraset, Cape verde, Solar Village and Banizoumbou). They compare the evolution of $g(\lambda)$ for the entire data set and only in case of desert dust. The difference of $g(\lambda)$ between the two data set is close to zero. In addition, similar to our study, $g(\lambda)$ not shows significantly differences between all months.
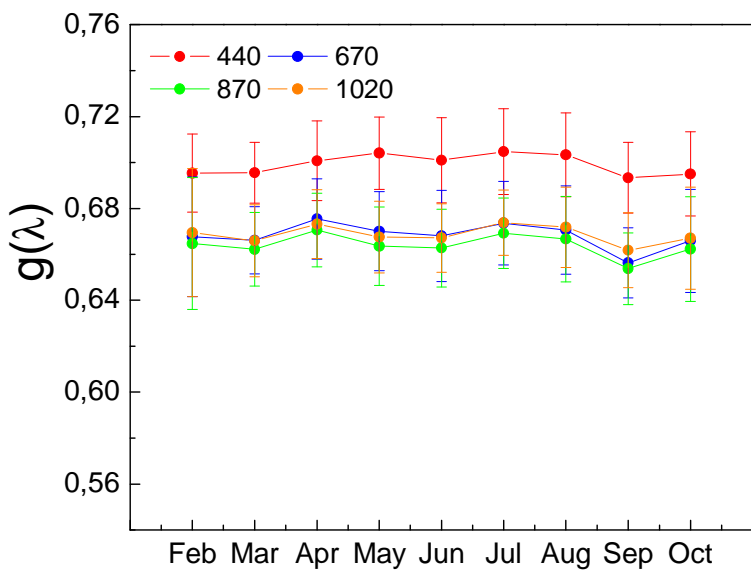

Figure 6.4: Monthly mean values and standard deviations of $g(\lambda)$ for 440, 670, 870 and 1020 nm during African dust events from 2005 to 2010.

6. Results and Discussion

The CALIMA network takes only into account desert dust events which reach the surface. Therefore, it is interesting to assessment if the aerosol optical properties retrievals in column atmospheric are reproduced at surface. In addition, the aerosol optical properties retrievals during desert dust events will be compared with those retrievals during free-dust days.

6.1.2 Column and in-situ ground-based aerosol optical properties

The synergetic used of in-situ ground-based measurements together with AERONET data retrievals is performed to evaluate potential changes occurred in the aerosol optical properties during desert dust and free-dust days. Optical properties at ground level are analyzed with the aim to evaluate the impact of dust over Granada sites. Comparison with the AERONET columnar-integrated data is also analyzed.

Spectral single scattering albedo, scattering and absorption Angström exponents

The fraction of light extinction (sum of scattering and absorption) due to scattering is defined as the single scattering albedo ($\omega(\lambda)$). This parameter is an intensive property determined by the particle composition while independent of the total aerosol concentration and represents a relevant variable in climate modeling (e.g. Bodhaine, 1995). Figure 6.5 shows the mean values of single scattering albedo retrieved for the atmospheric column ($\omega^{col}(\lambda)$) and computed at the surface ($\omega^{is}(\lambda)$) during desert dust and dust-free conditions. These values have been averaged from instantaneous values in the atmospheric column as well as at surface. During desert dust events, the mean $\omega^{col}(\lambda)$ values exhibited a weak increase with wavelength. The mean $\omega^{col}(\lambda)$ ranged from 0.89±0.03 at 440 nm to 0.96±0.03 at 1020 nm. This behavior was reported in other studies for desert dust events (e.g., Collaud Coen et al., 2004; Lyamani et al., 2006;

6. Results and Discussion

Alados-Arboledas et al., 2008; Cachorro et al., 2008; Su and Toon, 2011; Toledano et al., 2011). The increase of $\varpi^{ol}(\lambda)$ with wavelength is a typical pattern for dust particles (Eck et al., 2010) due to the spectral absorption properties of iron oxides in ultraviolet-visible spectral region (Sokolik and Toon, 1999). However, in our study, $\varpi^{ol}(\lambda)$ in the entire spectral range was lower than those values obtained in other studies during desert dust intrusions (Dubovik et al., 2002b). For example, Kim et al. (2011) obtained the mean $\varpi^{ol}(\lambda)$ values between 0.90 and 0.94 at 440 nm in Tamanrasset (center of the Saharan desert). On the other hand, the single scattering albedo recorded in our study was comparable to those obtained by other authors in the Mediterranean sites. Lyamani et al. (2006b) retrieved $\varpi^{ol}(\lambda)$ values of 0.89 and 0.88 for 440 and 1020 nm respectively, during desert dust events coincident with the heat wave in South-eastern Spain in 2003.
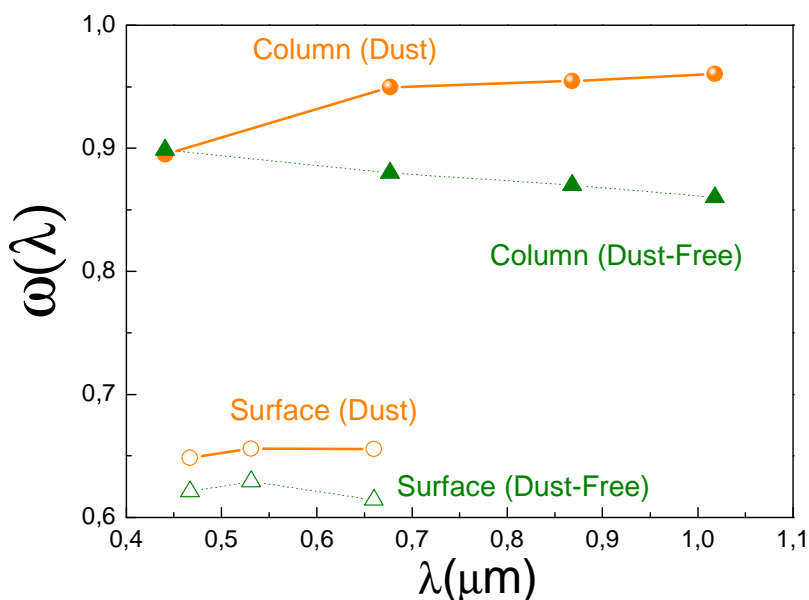

Figure 6.5: Single scattering albedo during desert dust events (atmospheric column: full circle symbol; surface: unfilled circle symbol) and during dust-free conditions (in atmospheric columnar with full triangle symbol, in surface with unfilled triangle symbol).

6. Results and Discussion

On the other hand, Perrone and Bergamo (2011) reported $\omega^{col}(\lambda)$ values at 550 nm in the range 0.87-0.95 at Lecce (40.33ºN, 18.10º E) in the Central Mediterranean during desert dust events. These authors showed that the contribution of anthropogenic particles can be relevant during desert dust events. The results indicated the fine mode aerosol contribution during desert dust intrusions over Granada. Fine mode aerosol can be of local or regional origin. Other authors established that those large amounts of light-absorbing anthropogenic pollutants were added to the dust plume during transport. Namely, the reduction in $\omega^{col}(\lambda)$ as the air mass moves from the dust source region to reception sites is due to the addition of fine pollution particles to the mineral dust (Höller et al., 2003; Clark et al., 2004). Cachorro et al. (2008) during a desert dust episode found values of about 0.90 at 440 nm to 0.98 at 870 nm for $\omega^{col}(\lambda)$ at El Arenosillo (South-western of the Iberian Peninsula).

The spectral dependence of $\omega^{col}(\lambda)$ under dust-free conditions is opposite to desert dust cases. In fact, the mean $\omega^{col}(\lambda)$ values decrease as the wavelength increases, changing from 0.88±0.03 at 440 nm to 0.85±0.03 at 1020 nm. This is a typical spectral characteristic of an urban-industrial ambient (e.g. Dubovik et al., 2002b; Eck et al., 2001a, b). Similarly, mean $\omega^{col}(\lambda)$ values of 0.91±0.02 and 0.85±0.02 at 440 and 1020 nm, respectively were found by Lyamani et al. (2006b) over Granada during anthropogenic events originated from Europe.

The mean $\omega^{js}(\lambda)$ values estimated with surface measurements of absorption and scattering coefficients show almost neutral variation with wavelength during desert dust events (Figure 6.5). Thus, the values of this parameter ranged from 0.65±0.13 at 467 nm to 0.66±0.14 at 650 nm. This neutral spectral dependency can be related to the increased contribution of absorbing particles from local anthropogenic activities (domestic heating

6. Results and Discussion

based on fuel oil combustion and vehicular emission) concentrated near the surface. This situation caused that the absorption effect of the mineral particles were weakened against the large absorbing aerosol concentration near the surface. Similar value was found by Lyamani et al. (2010) who obtained a mean $\omega^{js}(\lambda)$ value of the 0.68±0.07 at 670 nm from 2005 to 2007 over Granada reflecting the large absorbing fraction in the aerosol population over Granada. This result was lower than those obtained in Gosan, Korea (0.91±0.03 at 550 nm), and Beijing, China (0.90±0.04 at 550 nm) by Kim et al. (2005) and Yang et al. (2009), respectively during desert dust episodes in surface. Under dust-free conditions the mean $\omega^{js}(\lambda)$ values showed a slight decrease with wavelength at the surface. This parameter ranged from 0.62±0.13 at 467 nm to 0.61±0.13 at 650 nm. In general, the mean $\omega^{js}(\lambda)$ value indicate a large absorbing aerosol fraction over this region $\omega^{js}(\lambda)$ values at surface measured in our study site were smaller than those obtained in Delhi, India, (0.70±0.07 at 550 nm), Toulon, France, (0.73±0.08 to 0.78±0.07 at 525 nm), and Guangzhou, China (0.83±0.05 at 540 nm) by Soni et al. (2010), Saha et al. (2008) and Andreae et al. (2008), respectively. The significantly low values of $\omega^{js}(\lambda)$ recorded at Granada indicate a large absorbing aerosol fraction over this region, which consequently will have implications on the regional radiative forcing.

The values obtained for $\omega^{col}(\lambda)$ during desert dust conditions were higher to those obtained during dust-free conditions. The $\tau_{asct}(\lambda)$ values at the four-channel of the sun-photometer and $\sigma_{sp}(\lambda)$ values measured by the nephelometer are shown in figure 6.6 (dust and dust-free conditions). The mean $SAE^{col}(\lambda)$ value in the atmospheric column during desert dust events computed in 440-1020 nm spectral range was of 0.5±0.2. The low wavelength-dependence in scattering on average is characteristic of coarse particles that scatter in the geometric regime. The mean $SAE^{is}(\lambda)$ value obtained at surface in

450-700 nm spectral range was of 1.1±0.4 representative mixture of coarse and fine particles. It is noticed the large difference between SAE^{col}(440-1020nm) obtained in the atmospheric column and SAE^{is}(450-700nm) obtained at surface during desert dust events which may be due to the relatively high concentration of fine particles near of the surface and the large desert dust concentration in high levels
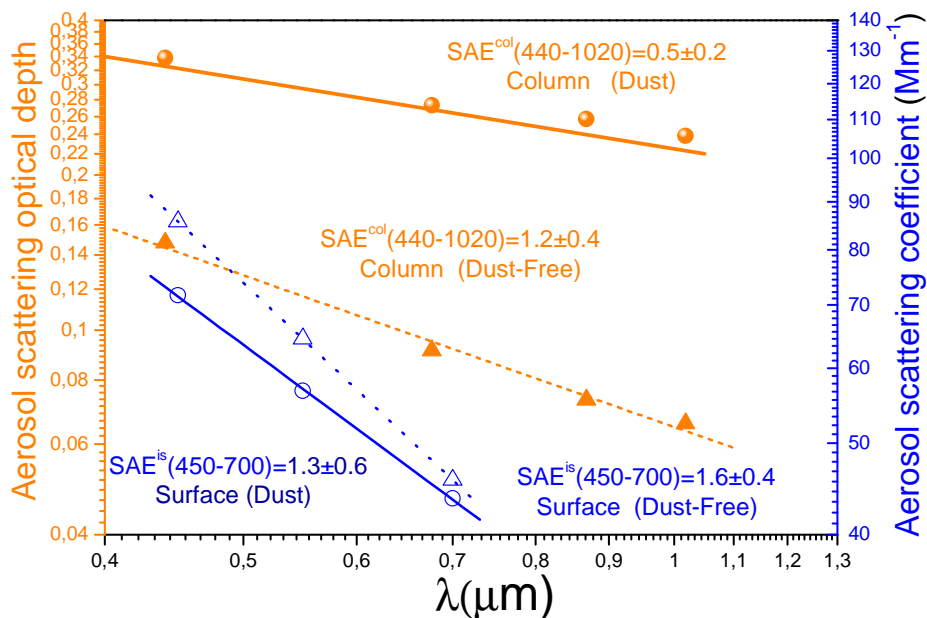

Figure 6.6: Aerosol scattering optical depth in atmospheric columnar (during desert dust events with full circle symbol and dust-free conditions with full triangle symbol) and aerosol scattering coefficient in surface (during desert dust events with unfilled circle symbol and dust-free conditions with unfilled triangle symbol).

6. Results and Discussion

The mean SAE^{col}(440-1020nm) value obtained in atmospheric column is slightly higher than that obtained by Kim et al. (2005) at Gosan (Korea) with a value of 0.38 measured in 412-862 nm spectral range in presence of mineral dust. The difference can be related to the major presence of the fine mode aerosol during desert dust events or differences in dust intensity. On the other hand, the mean SAE^{is}(450-700nm) value (1.1±0.4) obtained during desert dust events over Granada at surface was larger than those given by other authors for desert dust intrusions. For instance, Yang et al. (2009) reported a mean SAE^{is}(450-700nm) value of 0.59±0.41 during desert dust events in Beijing, China. In this same location under coal pollution influence, the SAE^{is}(450-700nm) showed a mean value of 1.39±0.20. Kim et al. (2005) obtained a mean SAE^{is}(450-700nm) value of 0.66±0.41 in Gosan, Korea, during dust particles presence increasing to 1.40±0.16 under anthropogenic influence in accordance with our results employing similar instrumentation. The larger mean SAE^{is}(450-700nm) value in our station could be justified because that substantial amount of fine particles (black carbon) was mixed with mineral particles during desert dust events. In that sense, we have found that under dust-free conditions, the mean SAE^{is}(450-700nm) value was of 1.6±0.2, slightly higher than the mean value of 1.1±0.4 under desert dust conditions at the surface. In the atmospheric column, the mean SAE^{is}(450-700nm) value was close to 1.2±0.4 during dust-free conditions. The significant contribution during dust-free conditions of fine particles from the urban area in the whole atmospheric column was evident according to the mean SAE^{col}(440-1020nm) value. These values of SAE^{col}(440-1020nm) under pollution urban influence were similar to those obtained in Gosan, Korea (~1.4 in the surface and ~1.3 in the atmospheric column) by Kim et al. (2005). The mean SAE^{col}(440-1020nm) value in our study during free-dust conditions was

6. Results and Discussion

consistent with the range of 1.2-1.7 observed for pollution episodes also in Gosan, Korea by Flowers et al. (2010).

As it was mentioned above the single scattering albedo depends on the aerosol composition. Several authors, (e.g. Rusell et al. ,2010; Cazorla et al., 2013) showed that there are connections between aerosol composition and the spectral dependence of absorption. In the absence of information on the aerosol chemical composition, the values of AAE^{col}(440-1020nm) and AAE^{is}(467-650nm) have been used as an indicator of the dominant absorbing particle type in the aerosol (Fig.6.7). When black carbon particles are the absorbing dominant aerosol, the value of AAE^{col}(440-1020nm) (AAE^{is}(467-650nm)) would be close to the unity (e.g. Bergstrom et al., 2007). The mean AAE^{col}(440-1020nm) value was of 0.9±0.4 during dust-free conditions over Granada, suggesting that black carbon was the principal absorber. This result is consistent with those mean AAE^{col}(440-870nm) values obtained by Giles et al. (2012) for urban-industrial aerosol in Shirahama (1.1±0.5), Moldova (1.2±0.3) and Mexico City (1.3±0.3). Rusell et al. (2010) obtained in Maldives a mean AAE^{col} (440-1020nm) value of 0.87 showing that black carbon with either absorbing or non-absorbing coatings can produce $AAE<1$. The mean AAE^{is}(467-650nm) value at surface was of 1.2±0.3 in this same situation implying that these aerosols were the most similar to black carbon. However, this AAE^{is}(467-650nm) value is still 20% higher than what is expected for black carbon only (unity); this indicates the ubiquitous presence of other light absorbing aerosols near surface. This value was slight lower that the value of 1.5±0.2 for pollution plumes, reported in Beijing, China (Yang et al., 2009).
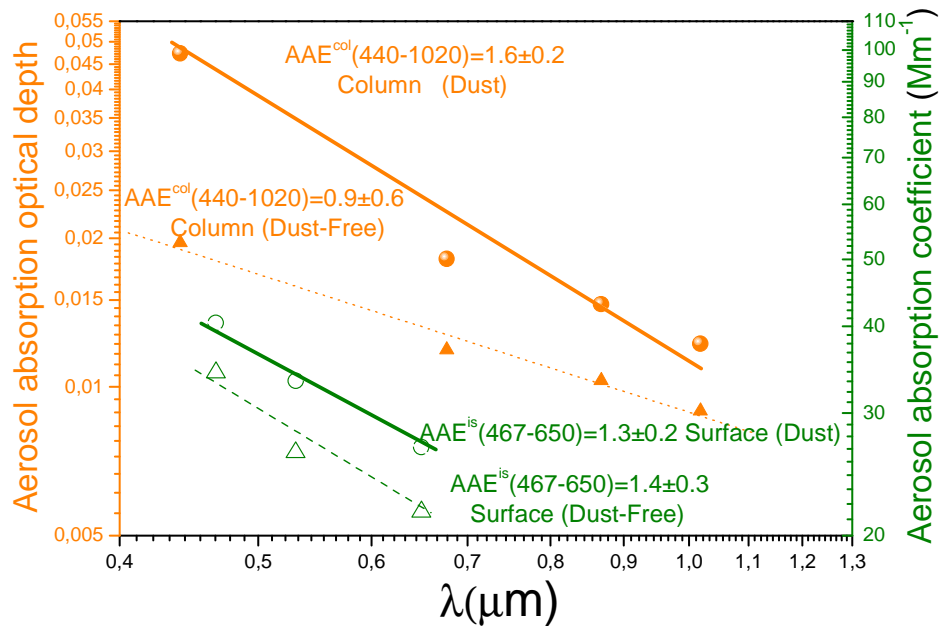
Figure 6.7: Aerosol absorption optical depth in atmospheric columnar (during desert dust events with full circle symbol and dust-free conditions with full triangle symbol) and aerosol absorption coefficient in surface (during desert dust events with unfilled circle symbol and dust-free conditions with unfilled triangle symbol).

The mean $AAE^{col}(\lambda)$ values derived from the sun-photometer were 1.5±0.2 and 2.2±0.2 on the spectral ranges 440-1020 nm and 440-670 nm, respectively which are higher than those obtained during dust-free days. Similarly mean $AAE^{col}(\lambda)$ values were reported in Solar Village (~1.6 and ~2.1 on wavelength range 440-1020 nm and 440-670 nm, respectively) by Rusell et al. (2010). The increasing or decreasing trends of

6. Results and Discussion

$AAE^{col}(\lambda)$ depend on the wavelength interval (Lack and Cappa 2010). Lack and Cappa (2010) established that AAE values ranging between 1 and 1.6 can be attributed to the presence of black carbon. Other authors as Yang et al. (2009) suggest that for AAE ~1.5 the total light absorption cannot be explained by black carbon alone, which is also evident in the relatively strong wavelength-dependence. Rather, other light absorbing materials were presented also and absorbed a lot more at shorter wavelengths than at longer wavelengths. Brown carbon and dust are two potentially significant light absorbers that are known to have high AAE in the visible spectrum. Giles et al. (2011) established that SAE^{col}(440-1020nm) ~0.5 with AAE^{col}(440-1020nm) ~1.5, likely represents an optical mixture of fine mode Black carbon and coarse mode dust as the dominant absorbers. Bergstrom et al. (2004) showed that the mixed urban pollution and desert dust provide a mean $AAE^{col}(\lambda)$ value of 2.2 in the ACE (Asian Aerosol Characterization Experiment). Therefore, during desert dust outbreaks AAE^{col}(440-1020nm) should not be used alone to determine aerosol types without the use of other information as SAE^{col}(440-1020nm) over our location. The desert dust episodes mainly happened over our location during warm season (Valenzuela et al., 2012b). In this season, stable meteorological conditions favor the stagnation of the air masses and accumulation of pollutants which led to a superposition of dust particles and anthropogenic aerosols (Lyamani et al., 2012). During Transport and Chemical Evolution over the Pacific (TRACE-P) and Asian Aerosol Characterization Experiment (ACE-Asia), Clarke et al. (2004) showed that during desert dust events if black carbon is generated and emitted into dusty air with elevated surface area, then significant fractions of condensates like combustion-derived organic carbon (OC) may accumulate on the dust instead of becoming associated with black carbon in the accumulation mode.

6. Results and Discussion

On the other hand, in the surface, the mean AAE^{is}(467-650nm) value was of 1.2±0.5, similar to dust-free conditions. Therefore, in view of the small difference of AAE^{is}(467-650nm) during desert dust days and dust-free days, and the mean AAE^{col}(440-1020nm) value during desert dust outbreaks this parameter should not be used alone to determine aerosol types without the use of other information (e.g., aerosol size) at ground level in urban locations as Granada with significant anthropogenic aerosol presence.

The large variation of SAE^{col}(440-1020nm)(SAE^{is}(450-700nm)) and AAE^{col}(440-1020nm) (AAE^{is}(467-650nm)) values obtained at Granada is indicative of a wide range of particle size in addition to various absorbent components. Thus, frequency distributions of these two parameters in both column and surface are shown in Figure 6.8. The SAE^{col}(440-1020nm) values were below unity up to 90% of AERONET data with a maximum around 0.5 (Figure 6.8a). On the other hand, the AAE^{col}(440-1020nm) ranged from a few values below unity to around 2.5 value with several maximum centered in 1.9, 1.4 and 1 (Figure 6.8b). These results were not reproduced at surface with ground-based in-situ instrumentation, as we can observe (Figures 6.8e and 6.8f). The SAE^{is}(450-700nm)values ranged from 0 about 2, with a maximum close to 1.4 during desert dust events indicating that a significant fine mode fraction were present at surface. On the other hand, the mean AAE^{is}(467-650nm) values ranged from 1 to 1.6 with a maximum centered on 1.1 and a second maximum centered on 1.5.
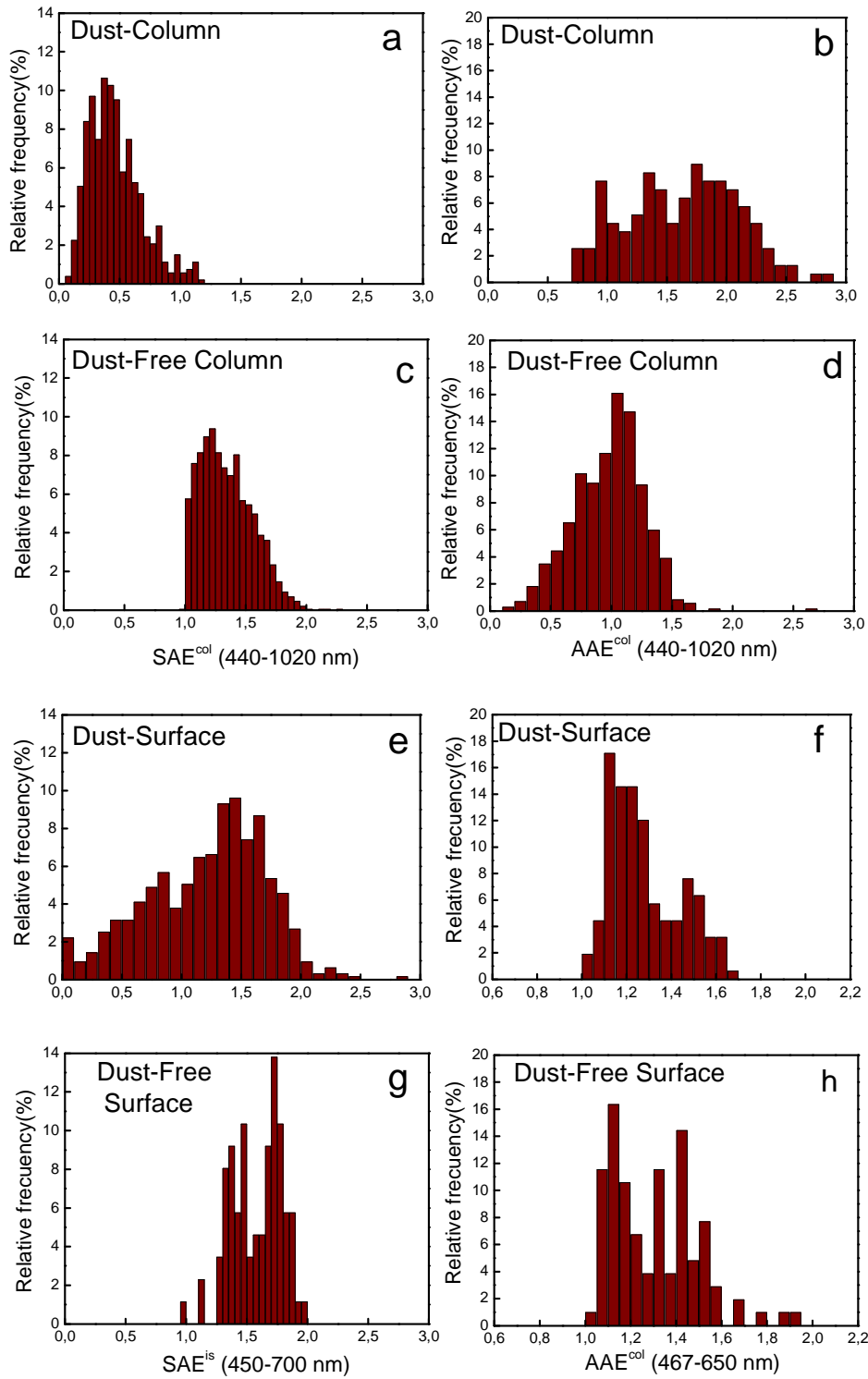
**Figure 6.8:** Relative frequency of scattering and absorption Angstrom exponent during desert dust events in atmospheric column (a, b), in surface (e, f), and during dust-free conditions in atmospheric column (c, d) and surface (g, h).

6. Results and Discussion

According to the previous comments for AAE^{col}(440-1020nm) obtained in the atmospheric column the absorption cannot only attributed to the dust and another other light absorbing materials also were responsible of absorption as black carbon and brown carbon. This fact could be due to the higher concentrations of fine absorbing particles near the surface. Thus, the effect of these fine absorbing particles probably increased during dust events which coincided with a stable meteorological situation that favored the air masses stagnation and the pollutants accumulation.

During dust-free conditions we found a maximum for SAE^{col}(440-1020nm) centered around 1.3 while that AAE^{col}(440-1020nm) showed a maximum value centered on 1.0 (Figures 6.8c and 6.8d). At the surface, SAE^{is}(450-700nm) showed a maximum value centered on 1.7 and a second maximum around 1.5, suggesting the important contribution of fine particles while that AAE^{is}(467-650nm) showed similar pattern that during desert dust events with several maximum. Therefore, the use of the mean SAE^{is}(450-700nm) and AAE^{is}(467-650nm) values from ground-base in-situ instruments are not a useful tool for detecting desert dust events in our urban station with a PSAP.

We performed a non-parametric test (Kolmogorov-Smirnov) in order of compare the optical parameters during desert dust and dust-free conditions. There was significant difference of SAE^{col}(440-1020nm) and AAE^{col}(440-1020nm) during desert dust events respect dust-free conditions in the atmospheric columnar. The same happened for SAE^{is}(450-700nm) at surface. However, this test revealed that not significant differences were found for AAE^{is}(467-650nm) between desert dust and free-dust conditions.

6. Results and Discussion

Relationships between single scattering albedo and Fine mode Fraction of τ_a during desert dust events

According to the values of SAE^{col}(440-1020nm) and SAE^{is}(450-700nm) shown in the previous sections there are evidences of the significant contribution absorbing fine particles in atmospheric column and at surface during both desert dust and dust-free conditions. In order to quantify the fine mode particles contribution during desert dust events and its relationship with SAE^{col}(440-1020nm) and AAE^{col}(440-1020nm) we have assessed the fine mode fraction (FMF) of the τ_a(675nm) in atmospheric column. In this section, the relationship between single scattering albedo and fine mode fraction (FMF) versus wavelength is evaluated.

The fine mode fraction of τ_a(675nm) was computed based on the retrieved size distributions using the Dubovik et al. (2006) algorithm. The single scattering albedo as a function of FMF is shown in Figure 6.9. The single scattering albedo was averaged for the 675 nm fine mode fraction of τ_a bins with ranges of 0–0.2, 0.2–0.3, 0.3–0.4 and >0.4 (four bins).

6. Results and Discussion
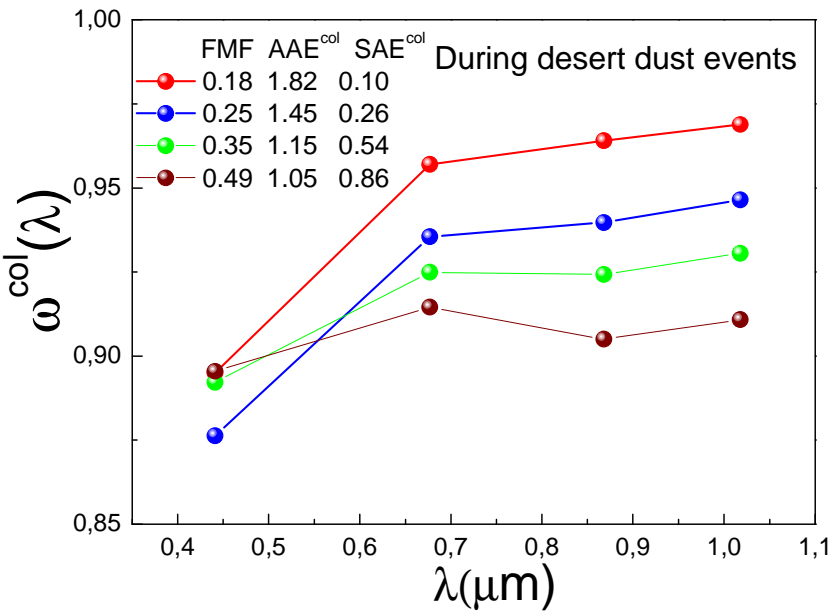
Figure 6.9: Spectral single scattering albedo averaged for the complete range of the fine mode fraction of τ_a(675nm) as well as scattering and absorption Angstrom exponent averaged corresponding to each range of the fine mode fraction over Granada during desert dust events.

The FMF was below 50% during desert dust events in atmospheric column. In 51% of case FMF was 0.25. From Figure 6.9, it is clear that the spectral dependence shown by $\omega^{col}(\lambda)$ is more pronounced with decreasing FMF. This is the typical pattern dominated by desert dust with strong absorption in the ultraviolet and less absorption in the infrared. As increase FMF, the spectral dependence becomes smooth to be practically neutral for FMF=0.49. This fact indicated that large part of FMF was associated with the anthropogenic aerosol (as black carbon) which is absorbent in the entire spectral range.

We have also computed the SAE^{col}(440-1020nm) and AAE^{col}(440-1020nm) as a function FMF during desert dust events. The SAE^{col}(440-1020nm) presented a good agreement with FMF (R^2=0.9) (Figure 6.10). It is evident that an increase of FMF

was related to an increase of SAE^{col}(440-1020nm). Regarding the AAE^{col}(440-1020nm), an increase of FMF implied a decrease of AAE^{col}(440-1020nm), values until around one (typical of the black carbon).
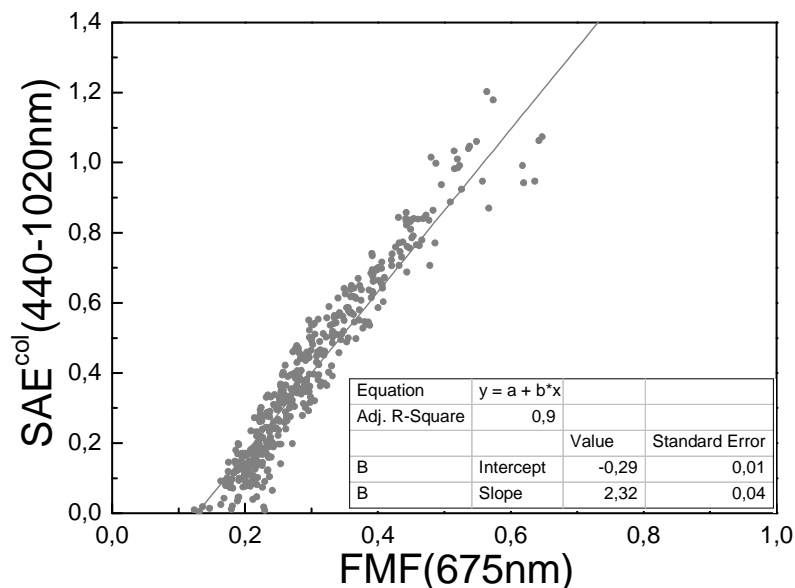
Figure 6.10: Correlation of SAE^{col}(440-1020nm) versus FMF(675nm) for desert dust cases

6.1.3 Influence of desert dust events on ground-based and satellite UV measurements

This section focuses on the analysis of the influence of desert dust aerosol on the UV erythemally weighted surface irradiance (UVER) measured at Granada, a non-industrialized medium-sized city in South-eastern of Spain. In addition, the study analyzes desert dust intrusions detected during a period from January 2006 to December 2010 to evaluate the differences between the UVER measurements and the satellite retrievals from Ozone Monitoring Instrument (OMI) on NASA EOS Aura satellite.

6. Results and Discussion

Dust effects on ground-based UVER measurements

The atmospheric aerosol transmittance (equation 4.19) was calculated from modeled and experimental UVER measurements averaged within ±2 min of each retrieved $\tau_a(\lambda)$ data recorded during the desert dust events (2006-2010). The mean value (± 1 standard deviation) of this transmittance was 0.89±0.06 which indicate that UVER values at surface decreases on average about 11% taking the inventory of desert dust intrusions over Granada. From this inventory, the percentages of cases with a UVER decrease higher than 20% (T_{UVER} below 0.8) was 12.5%. This threshold of 0.8 was used by Krotkov et al. (1998) to identify significant reductions in UV irradiance at surface due to aerosol absorption.

Experimental studies about the evaluation of atmospheric transmittance in the UV range associated with desert dust episodes are very scarce in literature. For instance, Diaz et al. (2007) reported atmospheric transmittance values between 0.92–0.95 for global UV irradiance (280-363 nm) measurements during one week at South-eastern Spain. Kalashnikova et al. (2007) evaluated the atmospheric transmittance at 340–380 nm during dust aerosols conditions for 2 days in Australia, showing values larger than 0.90. These two studies are focused on specific short-term dust events and not for a long inventory like in our study, hence the interest of the results shown in this work.

Figure 6.11 shows the UVER transmittance as function of τ_a at 380 nm in the slant path (aerosol optical thickness) for θ less than 60º. This variable takes into account the aerosol extinction in the slant column and it is derived from the normalization of the $\tau_a(\lambda)$ with the air mass factor (cosine of θ) for each measurement (Garcia et al., 2006; Kazadzis et al., 2009).
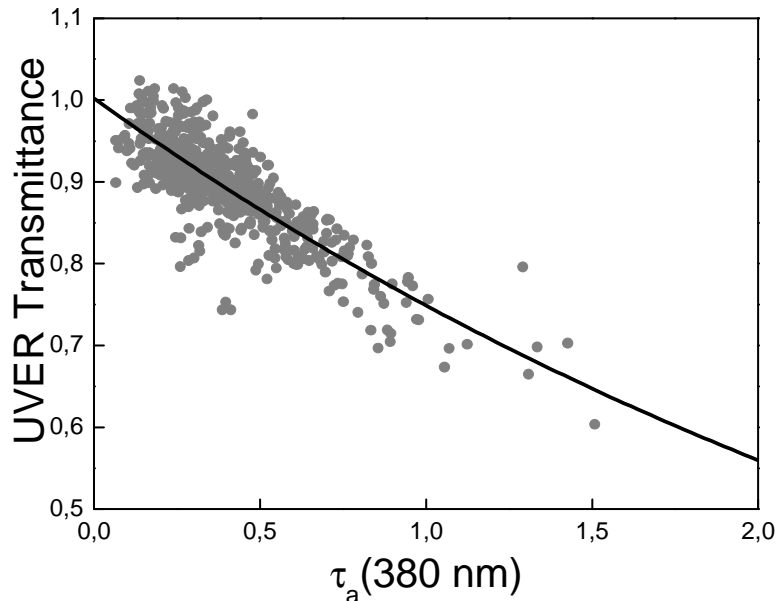
Figure 6.11: Atmospheric transmittance in the UV erythemal spectral range as a function of aerosol optical depth at 380 nm in the slant path (aerosol optical thickness) for solar zenith angles smaller than 60º. The solid exponential curve represents the values given by the equation 6.1.

From this figure, it can be clearly seen that T_{UVER} decreased as τ_a increases, founding minimum T_{UVER} values around 0.6 for τ_a of 1.5 (attenuation of ~40%) which highlights the great influence of desert dust aerosols on UVER measurements. The UVER transmittance obtained in our study can be related to the τ_a by means of the following expression (Krotkov et al. 1998):

$$T_{UVER} = \exp(-k \cdot \tau_a)$$

(6.1)

where k informs about the influence of aerosol load on the transmission of UV radiation through the atmosphere. This parameter has been derived from the lineal regression analysis between the logarithm of T_{UVER} and τ_a, showing a value of $k=0.291\pm0.008$ (R^2~0.7). The curve given by the equation 6.1 has been added to Figure 6.11.

6. Results and Discussion

Krotkov et al. (1998) used a radiative transfer code to obtain the parameter k for different aerosol models. For non-absorbing aerosol (e.g., anthropogenic sulfate), these authors shows k values less than 0.15 which is explained by the compensation between the reduction of the direct component by aerosol extinction and the increase of the diffuse component by aerosol scattering. For two dust models, those authors showed that the k values are substantially higher (between 0.3 and 0.9) which may be associated with the strong absorption of the direct solar component in the ultraviolet range by the mineral compounds of the desert dust such as the hematite and goethite (Horvath, 1993; Alfaro et al., 2004). The *k* reported in our work corresponded to the lowest value in the interval given by Krotkov's simulations for dust models. This result could be explained by the localization of the study station which is not close to the desert dust source origins, but separated hundreds of kilometers. Thus, pure desert dust is only found in the vicinity of the source regions and after a long range transport the aging of the dust and mixing with other aerosol types modify its optical properties (Bauer et al., 2011). Recently, Rodríguez et al. (2011) have showed that anthropogenic emissions from crude oil refineries and power plants, located in North African industrial areas, contribute to desert dust mixing with other type of particles.

Correction of satellite data from well-tested ground-based measurements

The current OMI surface UV algorithm assumes that clouds and aerosols are non-absorbing and, therefore, the satellite-derived surface UV irradiances are expected to show overestimation for regions that are affected by absorbing aerosols such as smoke or desert dust (Taskanen et al., 2007).

The variability of cloudiness within the OMI pixel (13 by 24 km for nadir viewing and ~50 km off-nadir viewing directions) can lead to a significant difference

6. Results and Discussion

between ground-based (a single point) and satellite UVER data (Weihs et al., 2008; Antón et al., 2010). Thus, to study the influence of desert dust aerosols on OMI UVER data, only cloud-free pixels must be taken into account in the analysis. For that, we have selected those satellite UVER data with Lambertian Equivalent Reflectivity (LER) smaller than 10% (Kallikosta et al., 2000). Figure 6.12 shows the relationships between OMI and experimental UVER data for the desert dust events detected at Granada under cloud-free satellite pixels.
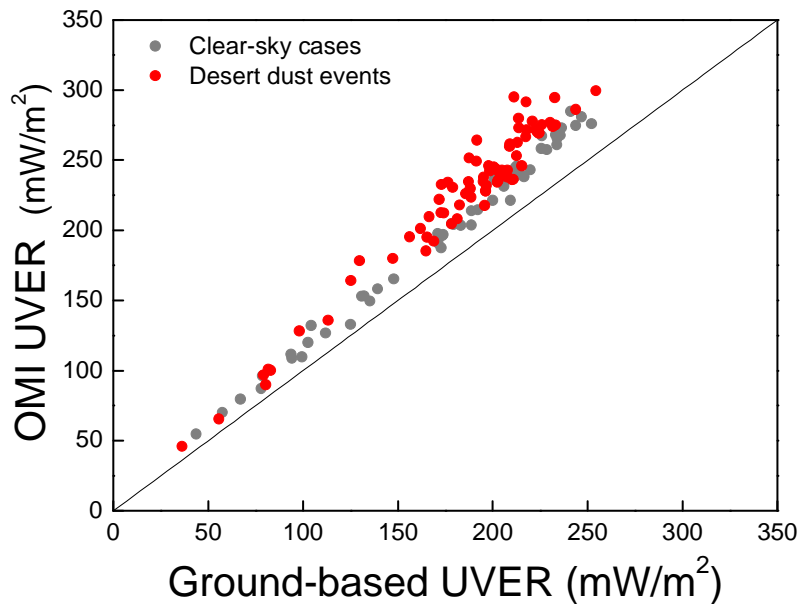
Figure 6.12: Correlation between OMI and ground-based UVER data for desert dust cases under cloud-free satellite pixels (in red). Subset of data for pristine (clear-sky) cases under cloud- and aerosol-free conditions are shown in grey. The study period is between January 2006 and December 2010. The solid black line is the zero bias line, unit slope.

The number of dusty cloud-free days analyzed is 75 (69% of all dusty days). It can be seen that the correlation between satellite-ground-based UVER data was good ($R^2 \sim 0.95$), but a strong bias is clearly appreciated. Thus, the mean bias error (MBE) calculated as the average of the relative differences between OMI and experimental

6. Results and Discussion

UVER data (UVER^{OMI}-UVER^{EXP}/UVER^{EXP}) presented a high value of (+22.2±6.5)% where the uncertainty is characterized by the standard deviation.

In order to evaluate what part of this elevate OMI bias can be associated with the presence of desert dust particles during the satellite overpass, the relationship between OMI and ground-based data was also analyzed for clear-sky conditions during the study period. Three different criteria were simultaneously applied for selecting these cases. Thus, LER values smaller than 10% allow working with cloud-free satellite pixels. Additionally, the clearness index (k_t) was used to characterize the atmospheric turbidity during satellite overpass. This variable is obtained from the ratio of the global solar irradiance to the extraterrestrial global solar irradiance on a horizontal surface (e.g. Alados-Arboledas et al., 2000). In order to select clear-sky cases, a threshold of k_t equal to 0.75 was chosen instead the value of 0.65 used by other authors (e.g., Kudish et al., 1983; Udo, 2000). This higher threshold guarantees the clear-sky conditions of the selected cases. The third criteria was to select those cases with τ_a at 440 nm smaller than 0.1. Thus, we have implicitly assumed that the atmospheric aerosol detected on clear-sky cases is the natural background. The pairs of satellite and ground-based UVER data recorded during clear-sky conditions are added to Figure 6.12. From this plot, it is highlighted that the OMI bias was substantially reduced when clear-sky conditions were presented during satellite overpass. Thus, the MBE decreased to (+14.2±4.1) % for these clear cases. Therefore, the desert dust intrusions over Granada caused a positive increase of the OMI bias by 8 percentage points which is mainly related to the fact that current OMUVB algorithm assumes no absorbing aerosols (Tanskanen et al., 2007). The main effect of this assumption on OMUVB algorithm was the obvious surface UVER overestimation due to the neglected aerosol absorption. Nevertheless, we would

6. Results and Discussion

like to point out that the analysis for clear-sky conditions showed a significant positive OMI bias around 14% which is not due to aerosol absorption, but can be related to several sources of uncertainty both in satellite and ground-based data.

Several works (e.g., Krotkov et al., 2005; Arola et al., 2005; 2009; Ialongo et al., 2008; Kazadzis et al., 2009; Cachorro et al., 2010) have used the aerosol absorption optical depth (τ_{aabs}) to quantify the error in the OMI UVER product due to the no inclusion of absorbing aerosols in the current OMI UV algorithm. This variable was calculated from the following expression:

$$\tau_{aabs}(\lambda) = \tau_a(\lambda) \cdot (1 - \omega(\lambda))$$ (6.2)

where $\omega(\lambda)$ is the single scattering albedo which is retrieved from the radiances measured by the Cimel sun-photometer at 440, 675, 870 and 1020 nm (Olmo et al., 2006; 2008).

For the OMI bias correction it is necessary to obtain the τ_{aabs} at UV wavelengths where no retrieval methodology is currently available with Cimel data. In order to solve this issue, we have estimated the τ_{aabs} at 310 nm using the following power-law wavelength dependence (Bergstrom et al., 2007):

$$\tau_{aabs}(\lambda) = c \cdot \lambda^{-AAE}$$ (6.3)

where *AAE* is the Absorption Angstrom Exponent which has been derived from the τ_{aabs} at 440 and 870 nm.

The ratios of OMI to ground-based UVER data are plotted against τ_{aabs} at 310 nm in Figure 6.13. All dusty cloud-free data recorded for the period January 2006-

December 2008 are included in this plot. It can be noticed that the ratio increases with increasing τ_{aabs}, confirming that dust aerosol absorption can partially explain the positive OMI UVER bias found in the satellite-ground-based comparison.
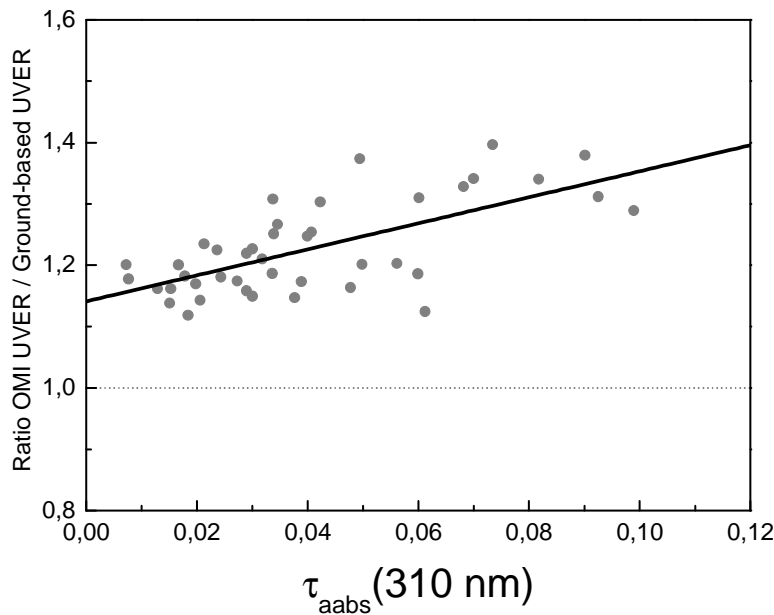
Figure 6.13: Ratio of OMI to ground-based UVER data as a function of the aerosol absorption optical depth (τ_{aabs}) extrapolated to 310 nm from Cimel values at 440nm and 870nm using Absorbing Angstrom Exponent for desert dust cases detected between January 2006 and December 2008. The solid line represents the regression line, with the slope of the fit b=2.69 (b parameter in equation 6.4).

The regression analysis provided a slope of the fit of 2.1±0.4, indicating the way in which the OMI bias increases with an increasing amount of aerosol absorption. Additionally, the linear least squares fit showed an intercept value of 1.14±0.02 which reports about the remaining bias under absorbing aerosol-free conditions. This value suggests that OMI data overestimate around 14% the ground-based measurements under these cases in agreement with the mean relative difference obtained for clear-sky conditions.

Based on the above results, OMI UVER data can be post-corrected using the expression proposed by Krotkov et al. (2005):

$$UVER_{corr}^{OMI} = \frac{UVER_{operational}^{OMI}}{\left(1 + b \cdot \tau_{aabs}\right)} \tag{6.4}$$

where the denominator informs about the correction associated with the presence of absorbing aerosols during OMI overpass time, being *b* the slope of the regression analysis performed in the previous paragraph.

Figure 6.14 shows the relationship between the reference ground-based UVER measurements and corrected OMI data for an independent dataset corresponding to the period January 2009-December 2010 (not previously used for calculating the b parameter).
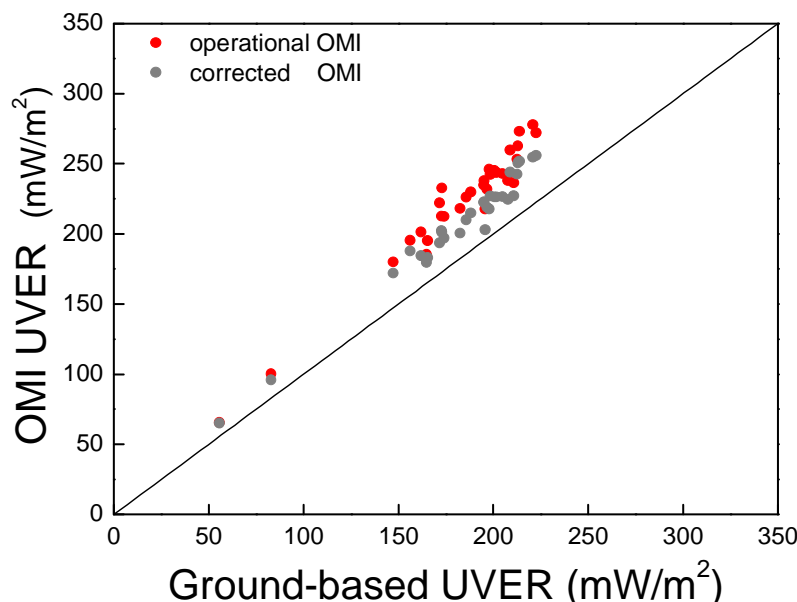

Figure 6.14: Correlation between OMI and ground-based UVER data for evaluation dataset: desert dust cases detected between January 2009 and December 2010. Operational satellite data are in red and corrected satellite data in grey. The solid black line is the zero bias line, unit slope.

Additionally, the operational OMI data have also been included in the plot. It can be seen that correction method produced a clear reduction of the OMI bias. Thus, the MBE decreased from (+21.3±4.9)% for operational satellite data to (+13.4±3.5)% for corrected data, slightly smaller than the bias obtained for clear sky conditions (14.2%) which marked the level of improvement that may be reached with the off-line correction methodology.

For the aerosol correction of the OMI UV data, Arola et al. (2009) used the equation 6.4 with *b* parameter equal to 3 and monthly τ_{aabs} values from the global aerosol climatology of Kinne (2009). The improvement in the OMI UV that can be achieved with this correction has been evaluated by comparing with experimental UVER data recorded at Granada for the period January 2009-December 2010. The MBE presented a value of (+12.6±5.1)% close to the bias obtained with the correction method used in our work, but with a larger standard deviation. Therefore, the Arola's correction method could be successfully applied to operational OMI UV products over geographical regions where experimental aerosol measurements are not available. This correction is expected to be implemented in the next re-processing of the OMI data set.

6.1.4 Aerosol properties according to desert dust origin sources

African dust intrusions over our study area during the period 2005-2010 have been confirmed by the CALIMA network (www.calima.ws). For detecting the African desert dust intrusions over the Iberian Peninsula, CALIMA uses the models SKIRON, BSC-DREAM and NAAPs as well as HYSPLIT4 back-trajectory analyses (Draxler et al., 2003), synoptic meteorological charts, satellite images, and surface data (particulate

6. Results and Discussion

matter recorded at air quality monitoring background stations). The air mass backward trajectories calculated by HYSPLIT were used to detect the source regions of desert dust observed over our study area. This method assumes that the dust particles are confined to the mixed layer at the potential source region, and that the air mass is loaded by desert dust when the air mass altitude is lower or close to the altitude of the mixed layer at potential source. According to this criterion three source regions were identified: 1) sector A (Northern Morocco, North-western Algeria) where the more frequent meteorological scenario favouring dust transport from this source was the low pressure over Atlantic and high pressure systems over Mediterranean Sea or North-Eastern Africa, 2) sector B (western Sahara, North-western Mauritania and South-western Algeria) where the desert dust transport was favoured by a high pressure over the Northern African continent, and 3) sector C (Eastern Algeria, Tunisia) where the synoptic scenario favouring dust transport from this source was the low pressure over Morocco and high pressure over North-Eastern Africa.

Figure 6.15 shows the monthly frequencies of African air masses classified by sector origins for the period 2005-2010. To derive the frequency distributions we have considered only days with desert dust intrusions in which aerosol optical and microphysical properties were available. In annual basis, the most frequent African air masses affecting our study area were associated with sector A and B, with an average of occurrence of 47% and 31% for all episodes, respectively.
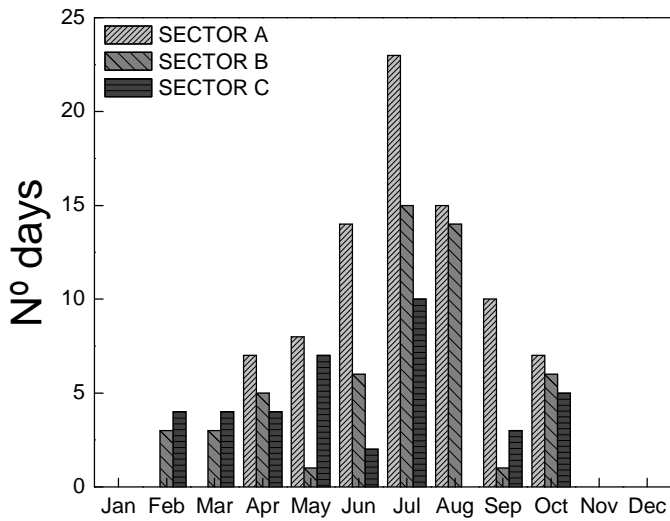
Figure 6.15: Monthly frequency of African air masses according to the classification by origin sectors.

The most frequent synoptic situation in spring and early summer associated with the dust transport to the South-eastern of the Iberian Peninsula (from sector A) is a low pressure (observed from sea level to 700 hPa centred South-western of the Portugal coast with an associated high over the central Mediterranean sea). On the other hand, the dust transport from sector B is favoured in most cases by an anticyclone (observed from sea level to 700 hPa) centred over North Africa, South-eastern Iberian Peninsula and western Mediterranean sea (Figure 6.16).

6. Results and Discussion
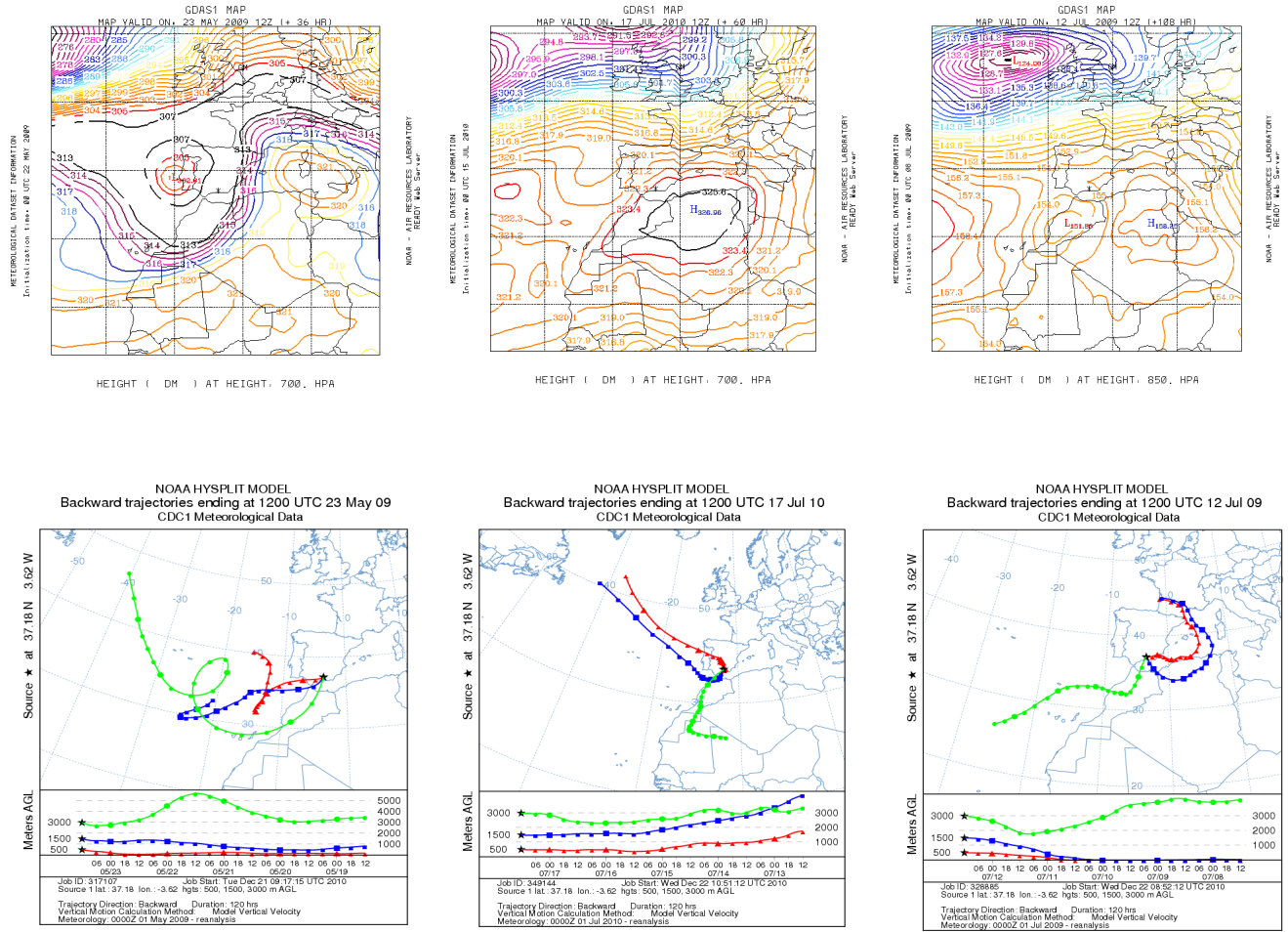
Figure 6.16: The main synoptic sceneries and back-trajectories at the 500, 1500 and 3000 m levels according to the classification by origin sectors.

The most frequent meteorological scenario (22% of all) related to the air masses transport from sector C is a low pressure centred over Morocco and a high (observed from sea level to 850 hPa) centred over eastern of the Algeria and Tunisia (Figure 6.16). In this last sector the frequency of desert dust events was the lowest throughout the annual cycle. The largest frequency of dust episodes was obtained in July for all sectors, followed by August. Statistical summary of τ_a(440 nm) and α(440-1020 nm), classified by sector origins, are reported in Table 6.3. In addition, the histograms of relative

frequency of these two variables are shown in figure 6.17. For all sectors we have found relatively high mean values of τ_a(440nm) and low mean values of α(440-1020nm) during African dust intrusions. Although the differences obtained in the values τ_a(440 nm) and α(440-1020nm) between the different sectors were within standard deviation, a slightly higher mean τ_a(440nm) value of (0.29±0.13) and a slightly lower mean α(440-1020nm) value of (0.36±0.19) were obtained when air masses were transported from sector B. The Saharan desert (sector B) is the largest source of mineral desert dust (e.g. Goudie et al., 2001). It is well known that the dust production and transport in sector B (Saharan desert) experience a marked seasonal evolution. The sources of soil desert dust included into this sector (northern subtropical Saharan latitudes) are activated in summer (e.g. Engelstaedter et al., 2006; Sunnu et al., 2008). The intense heating of the Sahara desert and the consequent development of the North-African thermal low and the vertical growth of the boundary layer (Escudero et al., 2005) together high pressure over eastern Algeria and Tunisia favoured the air masses transport from sector B toward Iberian Peninsula. This fact may explain the high mean value of τ_a(440nm) and the low mean value of α(440-1020nm) for sector B.

| | Sector A | | Sector B | | Sector C | | 1500 m | | | | 3000 m | | | |
| | | | | | | | Cluster 1 | | Cluster 2 | | Cluster 1 | | Cluster 2 | |
	τ_a	α	τ_a	α	τ_a	α	τ_a	α	τ_a	α	τ_a	α	τ_a	α
Number of days	86	86	56	56	41	41	56	56	67	67	25	25	35	35
Number of observations	4129	4129	2836	2836	1715	1715	2658	2658	3056	3056	1360	1360	1606	1606
Mean	0.26	0.45	0.29	0.36	0.26	0.46	0.29	0.39	0.24	0.44	0.29	0.38	0.26	0.45
Standard deviation	0.17	0.20	0.13	0.19	0.11	0.23	0.14	0.20	0.16	0.21	0.13	0.20	0.16	0.19
Minimum[a]	0.04	-0.05	0.04	-0.05	0.11	0.03	0.07	-0.08	0.04	-0.05	0.08	0.10	0.05	-0.04
Maximum[b]	1.60	1.04	1.41	1.01	0.98	1.05	2.01	1.05	1.60	1.03	0.79	1.04	1.41	1.03
Median	0.22	0.42	0.28	0.33	0.23	0.43	0.26	0.36	0.20	0.42	0.27	0.33	0.23	0.42

[a]Minimum of the observations.

[b]Maximum of the observations.

Table 6.3: Statistical summary of $\tau_a(440\text{nm})$ and $\alpha(440\text{-}1020\text{nm})$, classified by origin sectors and cluster analysis from 2005 to 2010.
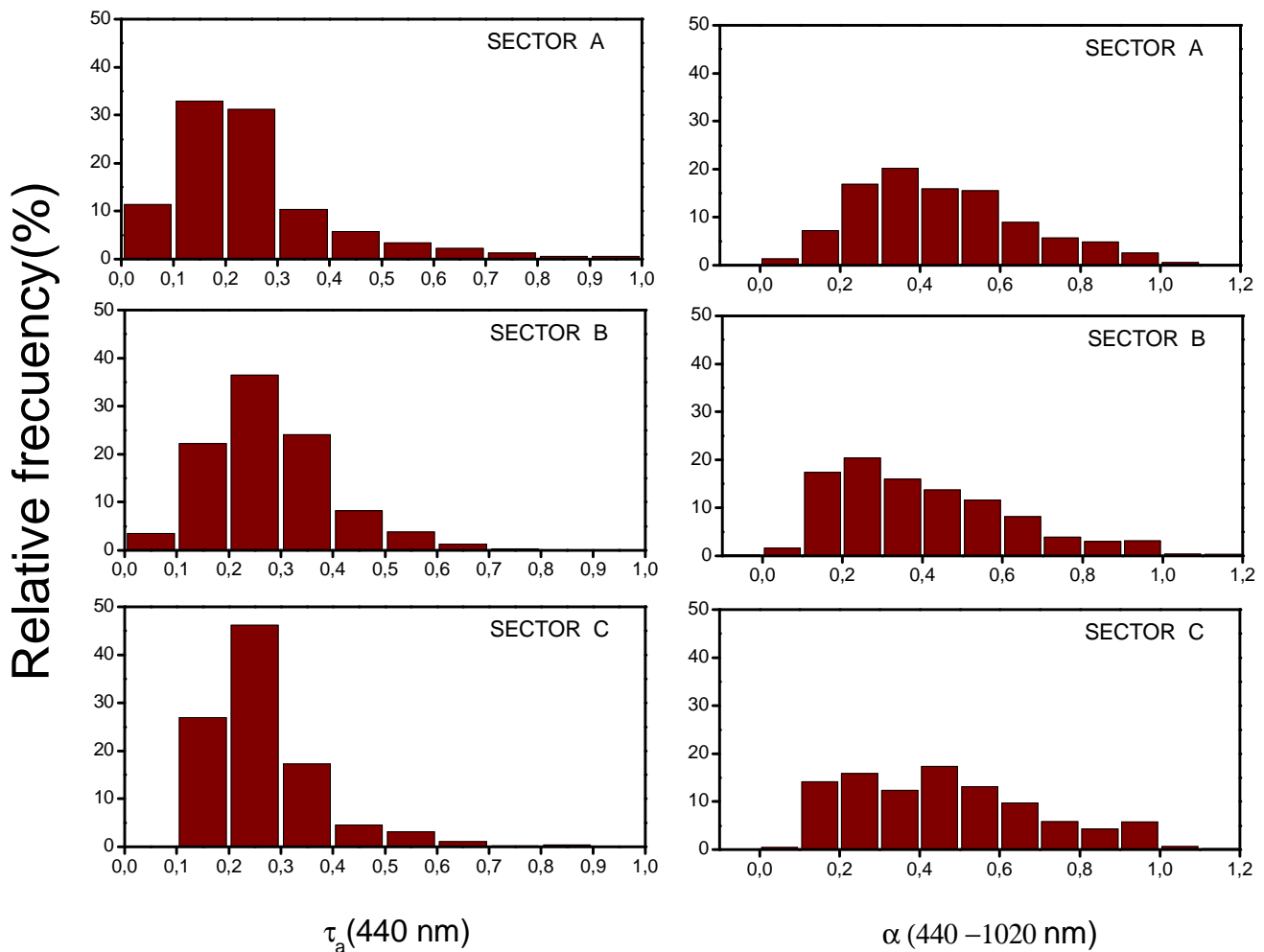
Figure 6.17: Frequency distribution of τ_a(440nm) and α(440-1020nm) according to the classification by origin sectors.

The large standard deviations of the mean τ_a(440nm) values within of each sector origin (Table 6.3) indicate a large variability in the atmospheric aerosol load during desert dust events. This large variation could be related to several factors such as different meteorological conditions and the interactions of the desert dust with other pollutants which can modify their physical and chemical properties, such as chemical composition, morphology or hygroscopicity occurring during dust transport. The τ_a(440nm) and α(440-1020nm) values obtained in this study for each sector are coherent with the values reported by other authors analysing desert dust events, and by the data recorded at AERONET sites influenced by desert dust. As example, Lyamani et

6. Results and Discussion

al. (2005), using sun-photometer data, analysed a Saharan dust outbreak during summer 1998 at Granada (Spain). These authors have reported values of τ_a(500 nm) ranging from 0.20 to 0.6 and values of α in the range 0.36-0.37. Prats et al. (2008) reported mean values of τ_a(440nm) and α(440-870nm) of 0.40±0.23 and 0.45±0.26, respectively, at El Arenosillo (Spain) during the dust intrusion events in summer 2004. At this same location, Toledano et al. (2007a) have obtained during other desert dust events a mean τ_a(440 nm) value of 0.33 and mean α value of 0.52 for the 2000-2005 period. El-Askary et al. (2009) obtained an average value of 0.82 for τ_a(675nm) and 0.08 for α(440-675nm) in the Alexandria (31.14ºN, 29.59ºE), Egypt, for a desert dust intrusion event. Nevertheless, these authors have reported τ_a and α values similar to the obtained here for a mixture episode of desert dust and anthropogenic aerosol; τ_a(675nm) and α(440-675nm) mean values of 0.37 and 0.44, respectively. The differences in these values compared to those obtained in our study could be due to differences related to the different measurement period (there is an inter-annual variability in the desert dust intrusions) and different pathways of the desert dust air masses during the transportation until the different stations.

According to our results, the small difference in aerosol optical properties encountered between the different sectors classes appear to be not sufficient to help to discriminate the mineral dust optical properties from different source areas, except for sector B.

To take more insight on the contribution of coarse dust particles to τ_a, we have applied the method proposed by Gobbi et al. (2007) to our classification by sectors. This method gives us a first approximation of the fine mode fraction (η) as well as fine

6. Results and Discussion

modal radius (R_f) and allows us to quantify the contribution of desert dust to τ_a with no need of inversion. We have used the τ_a(670nm) to classify the aerosol properties as a function of α(440-870nm) and its spectral curvature, represented by $\delta\alpha = \alpha(440,670) - \alpha(670,870)$.

The results of Gobbi classification for the three sectors are shown in Figure 6.18. According to the recommendation of Gobbi et al. (2007), we have used in our study daily mean values of τ_a(670nm) > 0.15, in order to avoid errors in α larger than 30%. τ_a values below 0.15 caused great uncertainty in the determination of the Angstrom exponent. Nevertheless, our study is focused on situations dominated by desert dust. Therefore, the bias introduced by the τ_a > 0.15 filter is not expected to be so relevant (~5%). As shown in Figure 6.18, in up to 90% of data the coarse mode contribution to the τ_a was always > 50% for the three sectors. Angström parameter remained usually below 1. Kaufman et al. (1993) established that strong negative values of $\delta\alpha$ ranging from -0.5 to -0.3 indicate the dominance of aerosol fine mode. Basart et al. (2009) found that under the dominance of coarse aerosol particles, such as desert dust, δα tends to be negative or slightly positive with values in the range (-0.3, 0.1). Values of δα larger than 0.1 indicate the presence of two separate particle modes, suggesting dust mixed with fine anthropogenic particles. Sector A showed τ_a(670nm) values above 0.25 in the 55% of cases, with δα varying from -0.15 to 0.45 (Figure 6.18a).
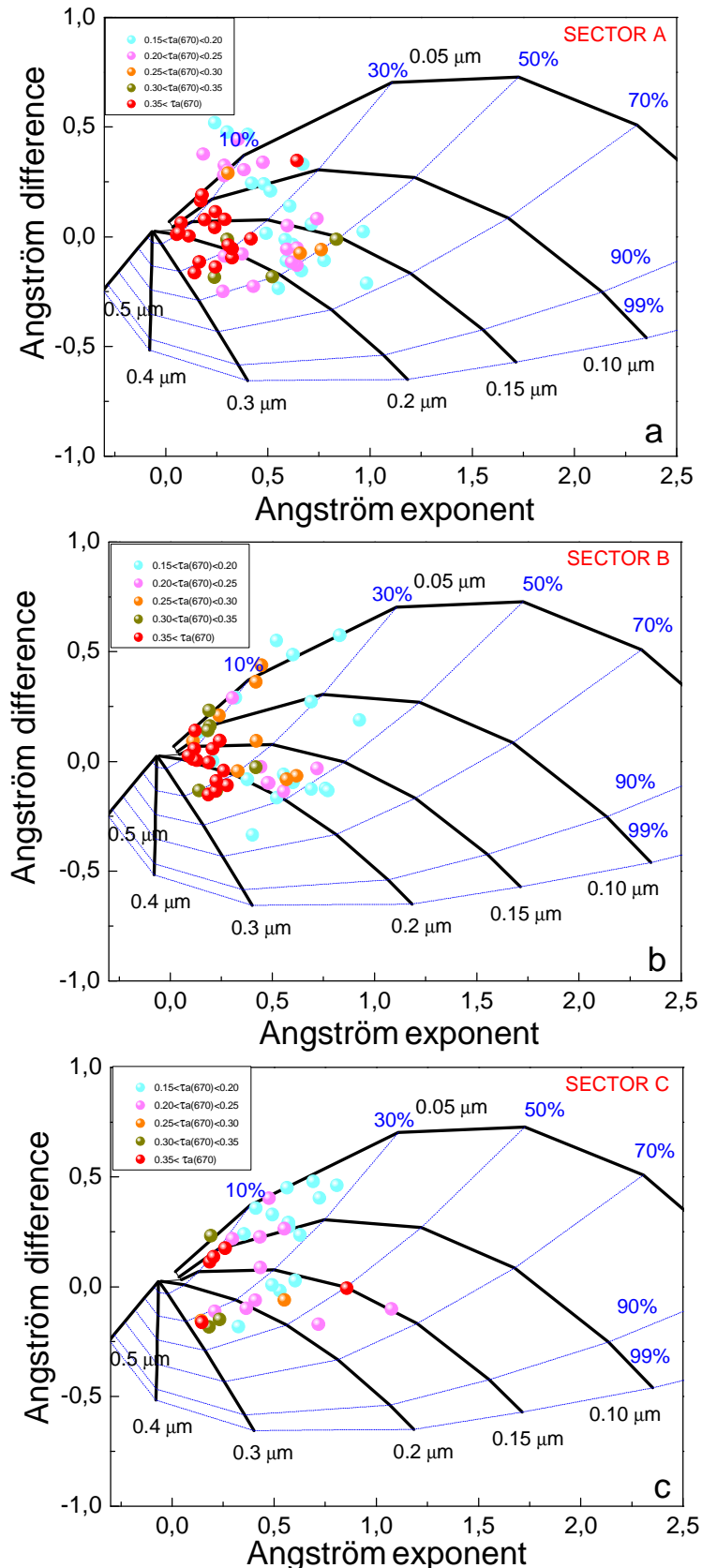
Figure 6.18: Angström exponent difference, $\delta\alpha = \alpha(440,670) - \alpha(670,870)$, as a function of $\alpha(440\text{-}670)$ and $\tau_a(670\text{ nm})$ for (a) Sector A, (b) Sector B and (c) Sector C.

6. Results and Discussion

This result suggests the possible existence of two situations: first, one dominated by coarse particles, and other one associated with the mix of both coarse and fine particles. High extinction values (τ_a at 670 nm > 0.3) were found up to 45 % of days for sector B which are often related to the presence of the coarse mode particles with $\alpha < 0.5$ and $\eta < 40\%$. In this sector, we found two predominant situations: 1°) 30 %$\leq \eta \leq$ 50 % and 0.15 $< R_f <$0.3 µm, and 2°) $\eta <$30% and 0.05$\leq R_f \leq$ 0.2 µm. In the first situation, the values of δα slightly negative or close to zero indicate the most contribution of coarse mode fraction to the τ_a. In the second situation, the cases with δα $\geq$0.1 indicate the presence of two separate particles modes related to dust particles mixed with fine anthropogenic particles (Figure 6.18b). Sector C presented two well-defined sets of daily mean values. The first one with30 %$\leq \eta \leq$ 50 %, 0.15$\leq R_f$ and δα $\leq$ 0, which is indicative that the main contribution to the calculation of τ_a is the coarse mode fraction. The second one $\eta \leq$ 30 % and 0.05 $< R_f \leq$ 0.3 µm with δα $\geq$ 0.1 and indicates a fine mode and coarse mode contribute to the calculation of τ_a (Figure 6.18c). Basart et al. (2009), based on AERONET data for the period 1994-2007 and applying the graphical method of Gobbi et al. (2007), performed an aerosol characterization for different Mediterranean areas (including the Iberian Peninsula). The result obtained in our study reveals a good agreement with the work of Basart et al. (2009) for the South-eastern Iberian Peninsula. Both studies showed that the coarse mode normally appears mixed with other types of small particles as indicated by positive δα values.

6. Results and Discussion

Aerosol volume size distribution

In all sectors the aerosol volume size distributions exhibited two well defined modes (Table 6.4). The volume concentration and modal radius of the fine mode showed similar mean values for the three origin sectors (volume concentration around 0.015 ± 0.009 $\mu m^3/\mu m^2$ and fine mode radius around 0.20 ± 0.03 μm). These results indicate that the fine mode was independent of the sector origin. Thus, this mode could be related to the anthropogenic aerosol produced locally or transported from polluted areas in European continent and of the most industrialized areas of the North Africa coast.

		V_c ($\mu m^3/\mu m^2$)	r_c (μm)	V_f ($\mu m^3/\mu m^2$)	r_f (μm)	η (0.5 μm)
Sector A		0.17±0.14	2.74±1.49	0.015±0.009	0.20±0.03	0.34±0.11
Sector B		0.16±0.09	2.04±1.37	0.015±0.006	0.21±0.03	0.29±0.11
Sector C		0.13±0.09	2.05±1.11	0.014±0.004	0.20±0.03	0.36±0.12
Cluster 1	1500 m	0.16±0.11	2.21±1.24	0.015±0.005	0.21±0.03	0.32±0.11
Cluster 2	1500 m	0.15±0.14	2.58±1.44	0.014±0.010	0.20±0.03	0.33±0.10
Cluster 1	3000 m	0.17±0.09	2.29±1.23	0.015±0.006	0.21±0.04	0.30±0.11
Cluster 2	3000 m	0.15±0.10	2.55±1.44	0.016±0.008	0.20±0.03	0.34±0.10

[a]V_c and V_f are the columnar volume of coarse and fine mode, respectively; r_c and r_f are modal radius at coarse and fine mode, respectively; and η is the fine mode fraction in 0.5 μm.

Table 6.4: Mean volume size distribution parameters for the different origin sectors and cluster analysis.

6. Results and Discussion

Olmo et al. (2006) have obtained the same value of fine mode volume concentration (V_f) when our station was affected by Saharan air masses and during polluted episodes (0.020 ± 0.007 $\mu m^3/\mu m^2$). Thus, the results suggest that the dust transport to our study area could be accompanied by the transport of anthropogenic particles from industrialized areas in North Africa. In this sense, Rodriguez et al. (2011) established that the main industrial emissions in this region occur along the Atlantic coast of Morocco, Northern Algeria, Eastern Algeria and Tunisia. Additionally, during the SAMUM 2006 campaign, Kaaden et al. (2009) found that the smallest aerosol particles were probably anthropogenic background aerosol. Prats et al. (2008) showed that the fine mode volume concentration during desert dust days increased with respect to dust-free days at El Arenosillo, indicating that the intrusions of desert dust aerosol contributed to the fine mode in this station. Fu et al. (2010) studied the impact of dust events on the air quality and demonstrated the mixing characteristics of dust aerosol with anthropogenic pollution along the transport pathway from the deserts to the northern cities in China.

On the other hand, we have also computed the ratio between the coarse and fine volume concentrations (V_c/V_f). For all sectors, the mean value of the ratio V_c/V_f shows the dominance of coarse mode particles during desert dust events, being more pronounced for sectors A and B with mean value of 11 ± 6. In sector C a mean value of 9 ± 5 was obtained for V_c/V_f. The V_c/V_f ratios up to about 15 were retrieved at Lampedusa by Tafuro et al. (2006). The difference between the V_c/V_f ratios of Lampedusa and the ratios obtained in our study site may be due to differences in dust load and sedimentation effects that reduce the contribution of large particles as well as to the difference in the local aerosol anthropogenic contribution.

Single scattering albedo and asymmetry parameter

The most important feature of $\omega(\lambda)$ for all sectors (Figure 6.19) was its spectral variation (slight increase with wavelength) as shown in other studies for desert dust events (e.g., Collaud Coen et al., 2004; Lyamani et al., 2006; Alados-Arboledas et al., 2008; Cachorro et al., 2008; Su and Toon, 2011; Toledano et al., 2011). The increase of $\omega(\lambda)$ with wavelength is a typical pattern for dust (Eck et al., 2010) due to the spectral absorption properties of iron oxides in dust (Sokolik and Toon, 1999). Although the differences in $\omega(\lambda)$ values obtained for the three sectors are in the range of the standard deviations, it can be seen that the high mean values were found for sector B and C, ranging from 0.90±0.03 at 440 nm to 0.93±0.03 at 1020 nm. The slightly lower mean $\omega(\lambda)$ values were found for sector A at all wavelengths, ranging from 0.89±0.03 at 440 nm to 0.91±0.03 at 1020 nm.
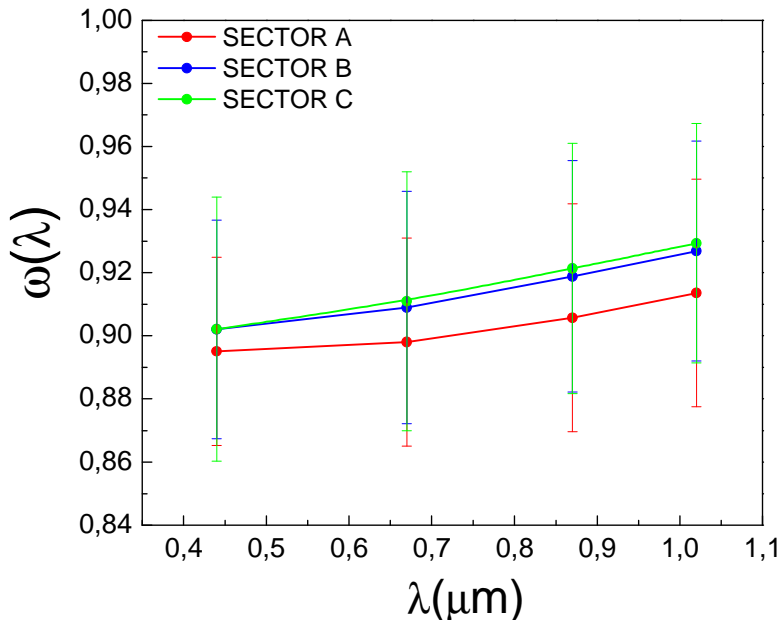

Figure 6.19: Single scattering albedo according to the classification by origin sectors.

6. Results and Discussion

To corroborate the $\omega(\lambda)$ values between different sectors, we have applied the Kolmogorov-Smirnov non-parametric test. On the one hand, this test revealed, at the 95% confidence level, that mean $\omega(\lambda)$ values at all wavelengths at the sector A are significantly different with respect the $\omega(\lambda)$ values at all wavelengths at the sectors B and C. On the other hand, the same test revealed that the $\omega(\lambda)$ values at all wavelengths from sector B and C are not significantly different.

Kim et al. (2011) obtained mean $\omega(\lambda)$ values between 0.90 and 0.94 at 440 nm in Tamanrasset (center of the Saharan desert). The lower $\omega(\lambda)$ mean values obtained in our study compared to those retrieved by other authors may be due to local urban contribution and aerosol mixtures during the dust transport. Several works (e.g, Lyamani et al., 2006; Lyamani et al., 2010; Perrone and Bergamo, 2011; Rodríguez et al.., 2011) have reported that the contribution of anthropogenic particles could be significant during desert dust events over sites several hundred km off North Africa. Mladenov et al. (2011) showed that Saharan dust is an important source of anthropogenic matter during desert events detecting at the remote observatory at the Sierra Nevada monitoring station (OSN). During those same desert dust events, columnar aerosol data were retrieved in the Granada city (Spain). Mean daily $\omega(\lambda)$ ranged from 0.89±0.03 at 440 nm to 0.92±0.03 at 1020 nm. These values are in accordance with the mean values obtained in our study. Additionally, Tafuro et al. (2006) have also obtained a low mean value of 0.89±0.03 at 440 nm at Lampedusa (a small Italian island located about 130 km east of the coasts of Tunisia), during desert dust events. These results highlight the great influence of the anthropogenic aerosol in the Mediterranean area. Numerous studies based on the chemical composition of the

6. Results and Discussion

ground-collected particulate matter (PM) have revealed the significant role of anthropogenic particles to the PM collected during dust intrusion events over Mediterranean areas as South-eastern Italy (e.g. Bellantone et al., 2008). Pereira et al. (2011) established that during the influence of North African air masses, the scattering was dominated by fine particles indicating that either dust at the surface was not so frequent or that it was mixed with anthropogenic pollution.

Kaaden et al. (2009) found that the Saharan aerosol at Tinfou (Morocco) consists of a combination of anthropogenic compounds (predominantly non-natural sulphate and carbonaceous particles) and mineral dust. In situ measurements in the same station showed that during low dust concentration, $\omega(\lambda)$ ranged from 0.91±0.02 at 537 nm to 0.93±0.01 whereas the absorption could be explained by soot-type particles (Schladitz et al., 2009). Müller et al. (2009) showed that soot absorption is correlated with particles smaller than 550 nm in diameter and the dust absorption is correlated with particles larger than 550 nm during the SAMUM 2006 campaign.

The mean values of asymmetry parameter, $g(\lambda)$ showed a little variation with wavelengths for the three sectors (0.67±0.02) (Figure 6.20). This result was similar to that obtained by Olmo et al. (2008) in Granada during desert dust events. The differences in $g(\lambda)$ values obtained in the three sectors were within the standard deviations. The Kolmogorov-Smirnov non-parametric test has been also applied to the mean $g(\lambda)$ values between the different sectors. This test revealed, at the 95% confidence level, that the differences in the mean $g(\lambda)$ values are no significant by three sectors.
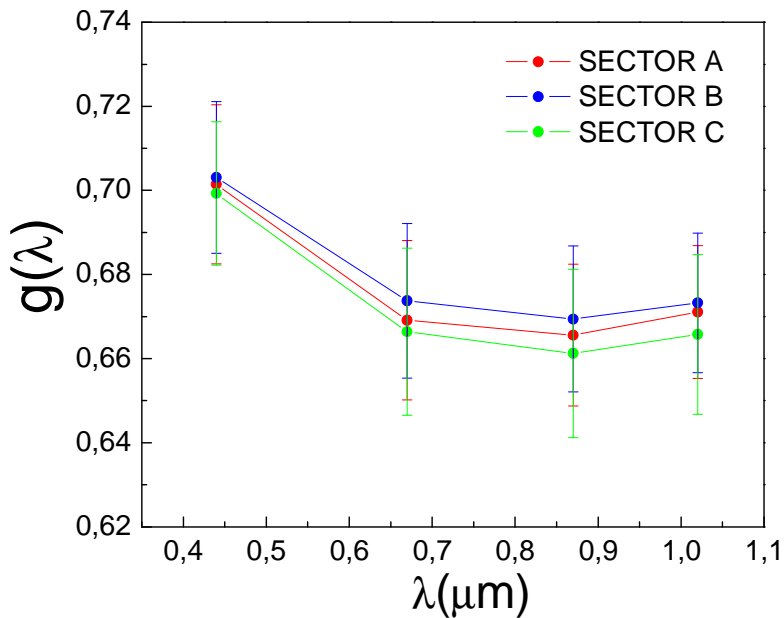
Figure 6.20: Asymmetry parameter according to the classification by origin sectors.

6.1.5 Aerosol properties according to cluster analysis

In this section, we investigate the dependence of aerosol radiative properties on air mass pathways. During the analysed desert dust events, the air masses arriving at Granada at 500 m a.g.l. never passed over the North Africa continent. This suggests that the transport of desert dust occur mainly at higher level and vertical mixing as well as gravitational settling processes were responsible for the presence of desert dust particles near surface. Tesche et al. (2009) showed that the height that can reach the dust particles when they are injected to the atmosphere were up to 7 km during SAMUM campaign. Papayannis et al. (2008) performed more than 130 observation days of the horizontal

6. Results and Discussion

and vertical extent of Saharan dust intrusions over Europe by means of a coordinated lidar network in the frame of the European Aerosol Research Lidar Network (EARLINET). They found that Saharan dust source regions play a key role in the dust transport to Europe in the height region between 3 and 5 km. In addition, they analysed the main pathways of Saharan dust transport over Europe, founding that Western Europe is mainly affected by the Western Saharan region. In our analysis, we assumed that the trajectories ending at 1500 and 3000 m provide information on the transport of desert dust. The 1500 m level represents the interaction of the air masses trajectories with boundary layer over reception site while the 3000 m level represents of the air masses transport at the free troposphere. The cluster analysis resulted in two groups or clusters of back-trajectories for African air masses arriving at Granada at 1500 and 3000 m levels. Flow patterns were different at each level. Each level had a distinctive set of mean flow patterns that represents clusters of back-trajectories. The air masses trajectories along with their cluster-mean for 1500 and 3000 m levels are shown in Figure 6.21.

The difference between this type of analysis and the classification by sector origin is that the cluster method groups together the back-trajectories with similar lengths and same curvature. The trajectories grouped in cluster 1 at 1500 m level came from Northern Algeria and correspond to 44% of the trajectories in this level arriving from North African. Its mean length was 1370 km.
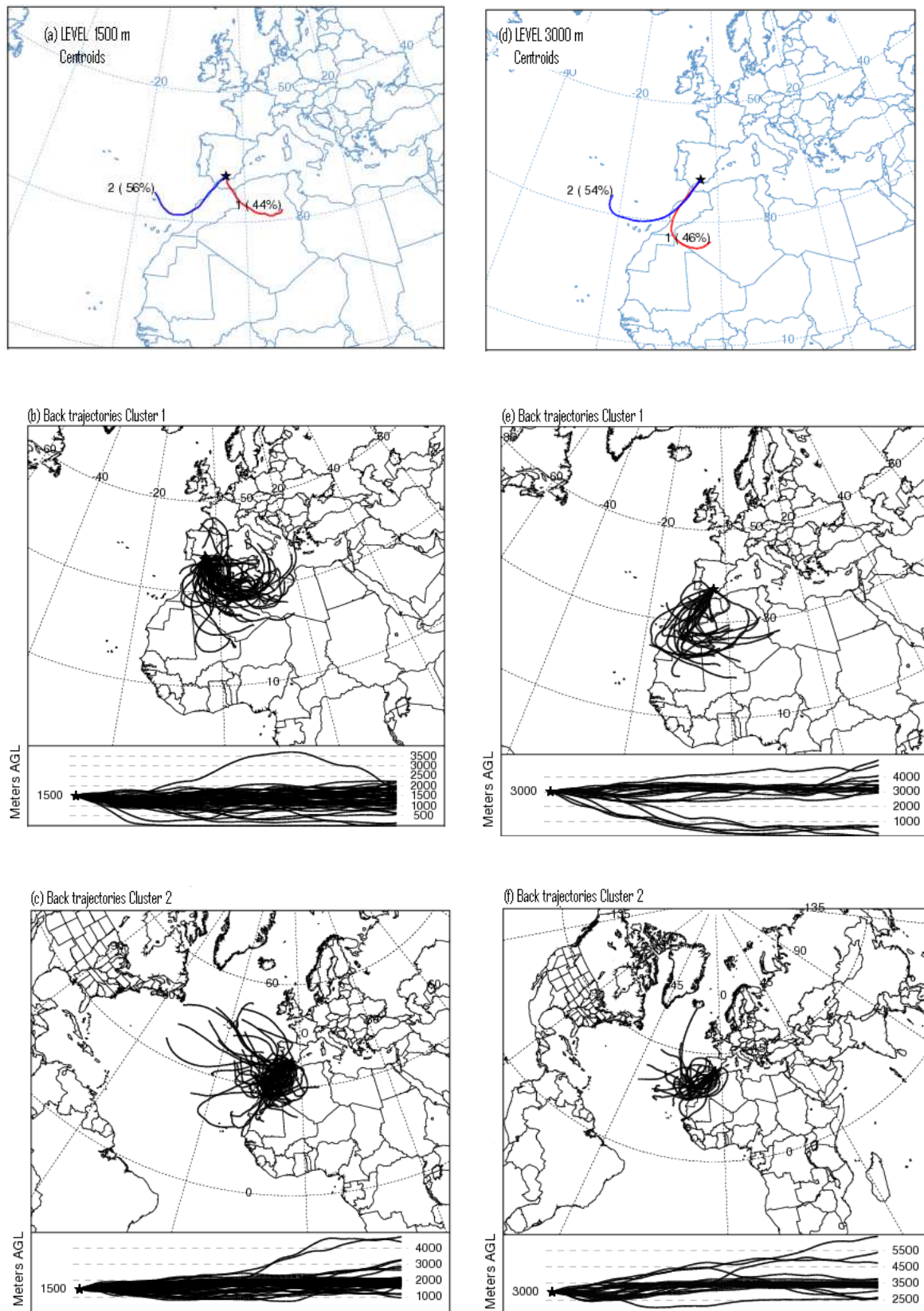
Figure 6.21: Centroids of cluster classification at (a) 1500 m level, and (b) 3000 m level.

6. Results and Discussion

The air masses transport according to the pathway of cluster 1 was favoured in the most cases with high pressure system (at level 850 hPa) centred over Mediterranean sea associated with a low pressure over Morocco. This meteorological scenario favoured the desert dust transport toward the South-eastern of the Iberian Peninsula across the North Algeria. According to this scenario, the dust sources should be Northern of Algeria, Tunisia and North-eastern Morocco. At 1500 m level the trajectories grouped in cluster 2 (56% of cases) were associated in the most cases with low pressures (observed from sea level to 850 hPa) centred South-western Portugal coast (Figure 6.22). This situation is coincident with one of the main synoptic sceneries that permit the air masses transport from North Africa toward Iberian Peninsula established by Escudero et al. (2005). Source areas of mineral dust should vary widely but according to the transport scenario, western regions of Morocco should be the main emission sources areas. At 3000 m level, the trajectories tended to be longer, indicating greater wind speeds. The two clusters at 3000 m level showed more curvature than the 1500 m level clusters. The meteorological scenario associated with cluster 1 was caused in the most cases by the intense ground heating in the Sahara region during the summer months enhances atmospheric convection, favouring dust injection at high altitudes up to 5000 m a.s.l. (Prospero and Carlson, 1972). The dust layer is transported at these altitudes by a compensatory high-pressure centre (Figure 6.22). The surface low pressures were located over North-western Africa while the high pressures (at level 700 hPa) were located over North Africa and the South of the Iberian Peninsula. According to this scenario, the dust sources should be South-western Algeria, Northern Mauritania and Western Sahara. This cluster grouped 46% of the trajectories in this level. Its mean length was of 2049 km.
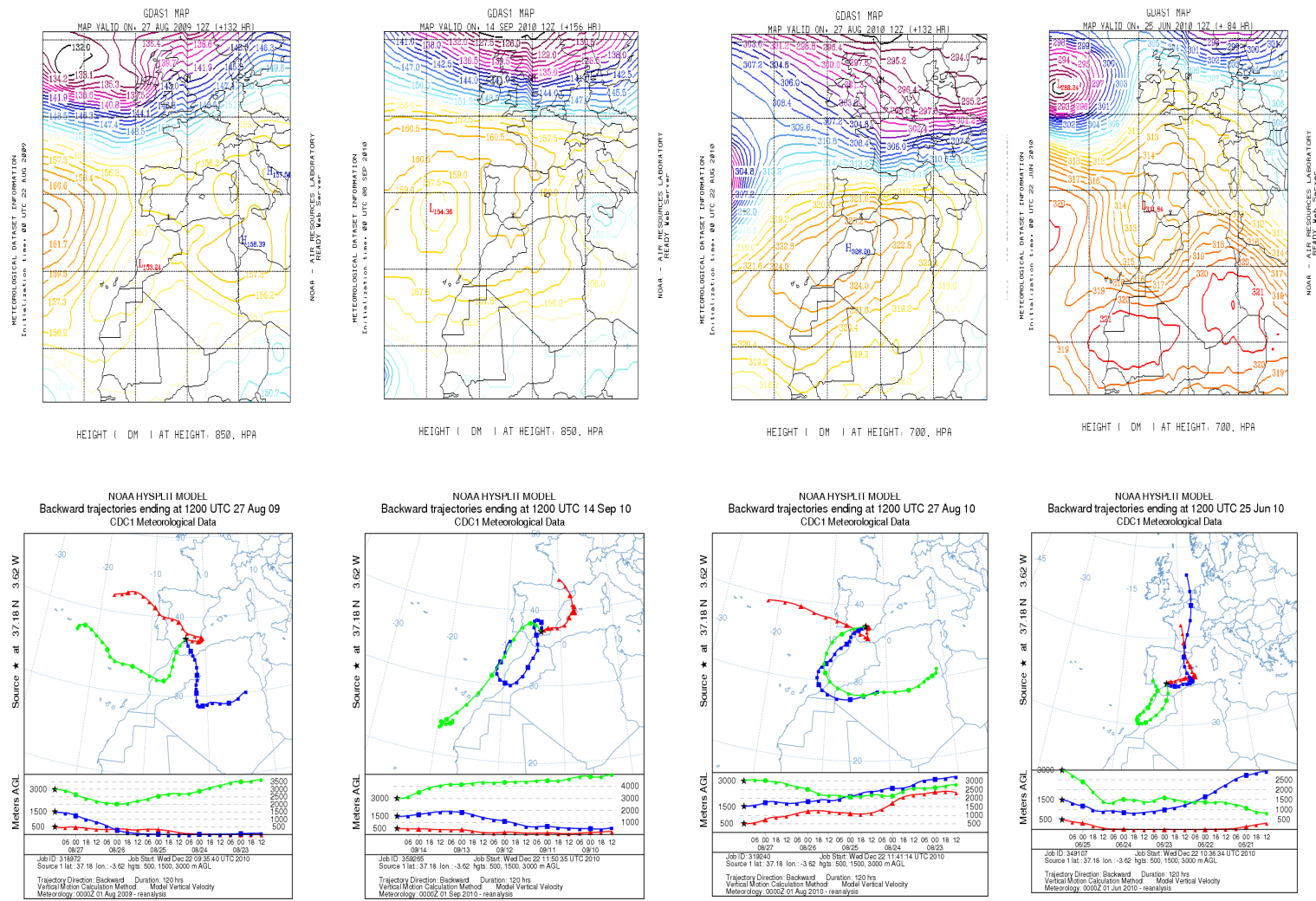
Figure 6.22: The main synoptic sceneries and back-trajectories at the 500, 1500 and 3000 m levels according to the cluster analysis.

The most frequent synoptic situation related to the trajectories associated with cluster 2 was caused by low pressure located in front of the South Portugal coast (at level 700 hPa) associated with a high pressure located in the interior of North Africa at the same level (Figure 6.22). At the surface level, a low pressure (Figure not shown) may permit the injection of dust at high levels. This meteorological scenario could favour the air masses transport from North Africa toward the Iberian Peninsula. This

cluster grouped 54% of the trajectories. Its length was the longest with a mean value of 2393 km. Table 6.5 shows the main synoptic scenarios that favoured the North Africa air masses transport toward the South-eastern of the Iberian Peninsula. The synoptic scenario that has a higher frequency was the low Atlantic pressure and high Mediterranean Sea pressure or northeast Africa. The second synoptic scenario in frequency distribution was a high pressure over northern African continent that favoured the air masses transport from Western Saharan desert. Finally, another relevant synoptic scenario was low pressure over Morocco and high pressure over northeast Africa.

	Sector sources origin	Clúster analysis
Low pressure Atlantic and high pressure Mediterranean sea or northeast Africa	Sector A (47%)	Cluster 2 (56%) at the 1500 m level Cluster 2 (54%) at the 3000 m level
Low pressure over Morocco and high pressure over northeast Africa	Sector C (22%)	Cluster 1 (44%) at the 1500 m level
High pressure over northern continent African	Sector B (31%)	Cluster 1 (46%) at the 3000 m level

Table 6.5.The most main synoptic scenarios that favoured the air masses transport from North Africa toward the Iberian Peninsula from 2005-2010 period.

Annual frequencies of air masses assigned to each cluster at each level are show in Figure 6.23. At 1500 m level grouped 67% of air masses from North Africa, cluster 1 (Northern Algeria) showed maximum frequency in May-August and cluster 2 in July-August. The classification at 3000 m level grouped 33% of air masses from North

6. Results and Discussion

Africa. In this level, cluster 1 showed two maxima during annual evolution, in May and July. Cluster 2 grouped air masses which arrived between June and October.
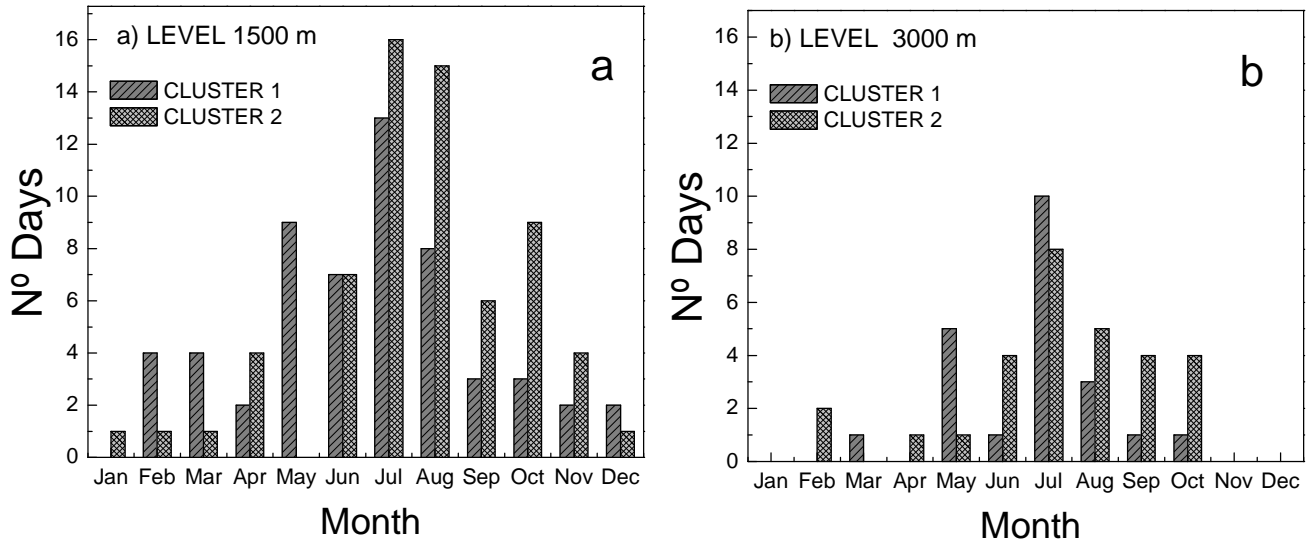
Figure 6.23: Monthly frequency of African air masses according to the cluster analysis at a) 1500 m, and b) 3000 m.

Table 6.3 shows the statistical summary of τ_a(440nm) and α(440-1020nm) according to the cluster classification. At the 1500 m level, the air masses transported from Northern Algeria Tunisia and North-eastern Morocco which have been grouped in cluster 1, had a higher mean value of τ_a(440nm) (0.29±0.14) than cluster 2 (0.24±0.16). In addition, the histograms of relative frequency of both variables are shown in figure 6.24.The slightly higher value of τ_a(440nm) for cluster 1 than for cluster 2 could be due to the large time travel and the slow movement of the air masses in cluster 1 over mineral dust sources in comparison with cluster 2.
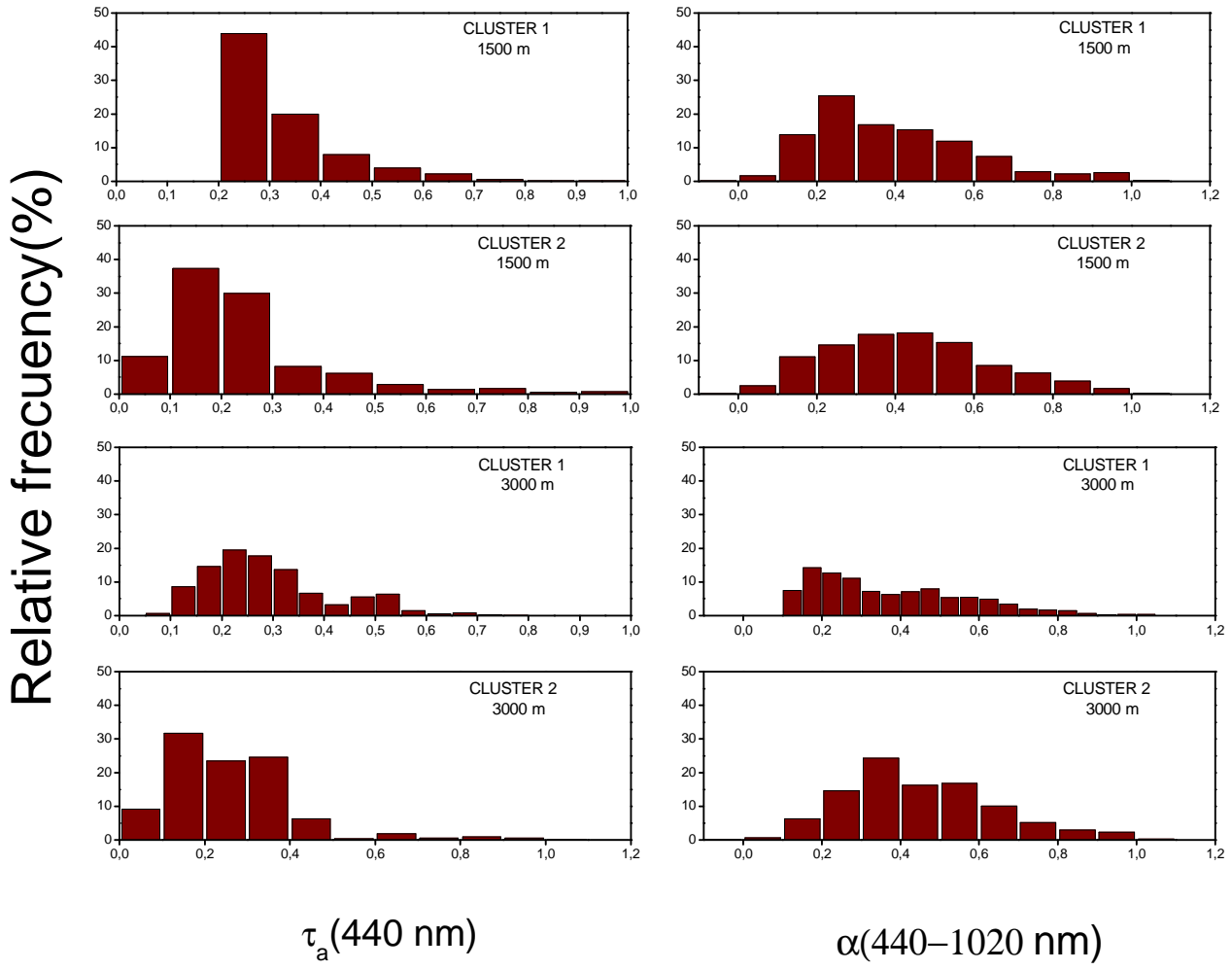
Figure 6.24: Frequency distribution of τ_a(440 nm) and α(440-1020 nm) according to the cluster analysis.

Moreover, α(440-1020nm) presented a lower mean value for cluster 1 than for cluster 2 with mean values of 0.39±0.20 and 0.44±0.21, respectively. Therefore, cluster 1 showed a higher proportion of coarse particles than cluster 2. At 3000 m level, the τ_a(440nm) for cluster 1 showed a higher mean value than cluster 2 with 0.29±0.13 and 0.26±0.16, respectively, and α(440-1020nm) presented a lower value for cluster 1 (0.38±0.20) than for cluster 2 (0.45±0.19). These results can be justified by the longer travel time over mineral dust sources of air masses assigned to cluster 1.

6. Results and Discussion

The results using the Gobbi et al. (2007) method for all clusters shows that in up to 90% of observations the fine mode fraction was < 50%. However, this mode was always present during desert dust intrusions which could be related with anthropogenic aerosol contribution. High extinction values (τ_a(670 nm)>0.4) were found for cluster 1 at 1500 m and 3000 m levels which are often related with the presence of dust particles with $\alpha < 0.5$ and $\delta\alpha{\sim}0$. We could found for all clusters high τ_a(670 nm) values combined with low α in two situations: 1°) η <40% and R_f ~0.2 µm, and 2°) η <30% and R_f ~0.12 µm. In the first case, the cases with $\delta\alpha{\sim}0$ indicate the predominance of one mode associated to coarse dust particles. En the second case, the cases with $\delta\alpha \geq 0.1$ indicate the presence of two separate particles modes, related with dust mixed with fine anthropogenic particles.

Aerosol volume size distribution

The volume size distribution was found to be bimodal. The size distribution parameters are shown in Table 6.4. The volume concentration (V_f) and modal radius (r_f) of the fine mode showed small variations for all the clusters with mean values of V_f between 0.014±0.010 µm^3/µm^2 and 0.016±0.008 µm^3/µm^2 and mean value of r_f close to 0.20±0.03 µm. The fine mode was independent of the height and speed of the air masses transport from North Africa and it could be related to local emissions or anthropogenic aerosol transport from the Mediterranean areas (Lyamani et al., 2006b). On the other hand, the volume concentration (V_c) and modal radius (r_c) of the coarse mode showed a large standard deviation within the different clusters. At 1500 m level, cluster1 had a mean V_c of 0.16±0.11 µm^3/µm^2 with the centre of the peak in 2.21±1.24 µm while cluster 2 had a mean V_c of 0.15±0.14 µm^3/µm^2 with the centre of the peak in 2.58±1.44

µm. This large variation could be related to the interactions of the desert dust with other aerosol types occurring during dust transport.

At 3000 m level, cluster1 showed a higher V_c with a mean value 0.17±0.09 µm^3/µm^2 and the centre of the peak in 2.29±1.23 µm compared with the values found at 1500 m level, while for cluster 2 a mean value of V_c of 0.15±0.10 µm^3/µm^2 with the centre of the peak in 2.55±1.44 µm was found. At 1500 m level the mean value of the ratio V_c/V_f was 11±6 for both clusters, indicating the dominance of coarse mode particles during desert dust events. At 3000 m level V_c/V_f was 11±6 for cluster 1 and 10±5 for cluster 2. The results given by Tafuro et al. (2006) at the Lampedusa Island (V_c/V_f ratio of 15) are not in accordance with the results shown in our work. This difference may be due to three reasons: a) differences related to the different measurement period (there is an inter-annual variability in the desert dust intrusions), b) differences related to the different of the desert dust intrusions detection method, and c) different pathways of the desert dust air masses during the transport until the two stations

Single scattering albedo and asymmetry parameter

During desert dust events $\omega(\lambda)$ showed slight spectral dependence increasing with wavelength for all the clusters (Fig. 6.25a, b). In cluster 1 $\omega(\lambda)$ ranged from 0.90±0.03 at 440 nm to 0.93±0.03 at 1020 nm, while in cluster 2 this parameter ranged from 0.89±0.03 at 440 nm to 0.92±0.03 at 1020 nm. At 1500 m level, cluster 1 showed slightly higher values of $\omega(\lambda)$ than cluster 2, indicating that probably the air masses in the last cluster transported more absorbing particles. Air masses grouped into cluster 2 passed mainly over the indusial areas in Atlantic coast of Morocco where desert dust

could be mixed with anthropogenic particles emitted in these areas. At 3000 m level,

cluster 1 and 2 showed similar mean values of $\omega(\lambda)$.
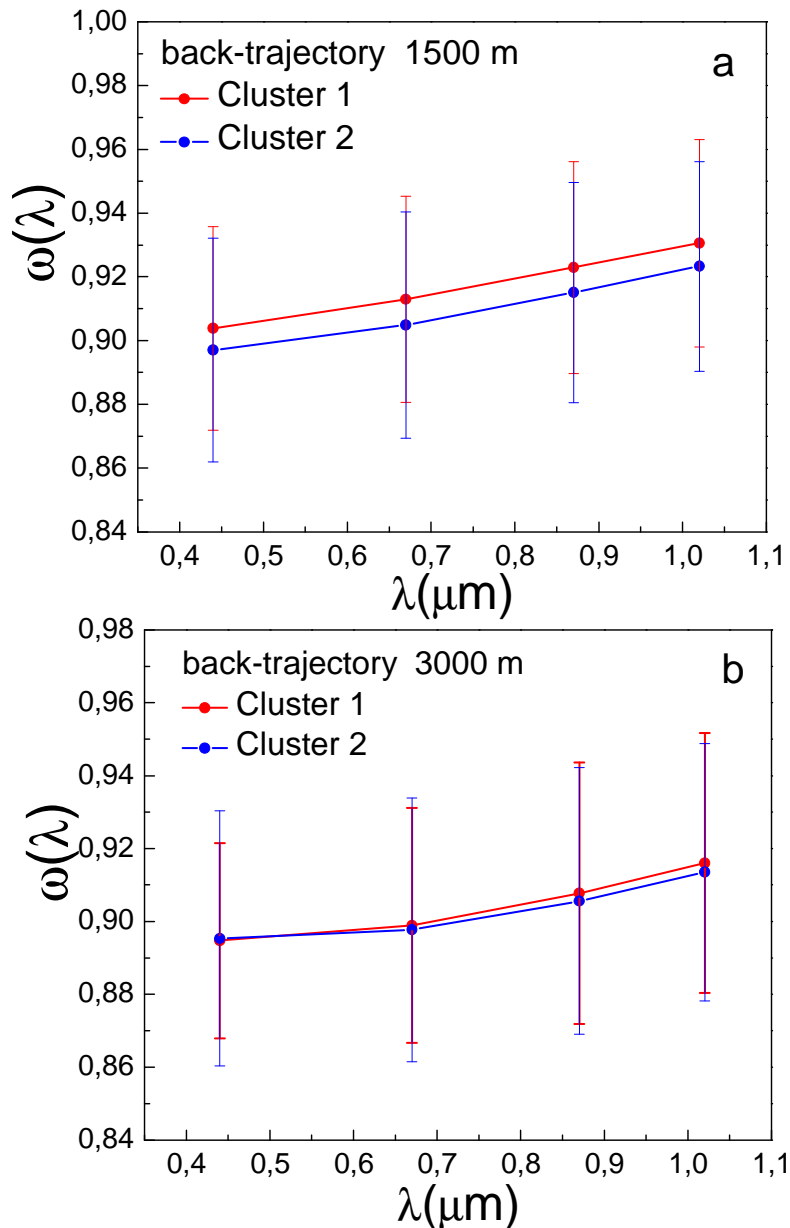
**Figure 6.25:** Single scattering albedo a) 1500 m level and b) 3000 m level according to the cluster analysis.

On the other hand, as in the classification by origin sectors the mean values of $g(\lambda)$ showed similar values (0.67±0.02) with wavelengths for all the clusters (6.26a,b).
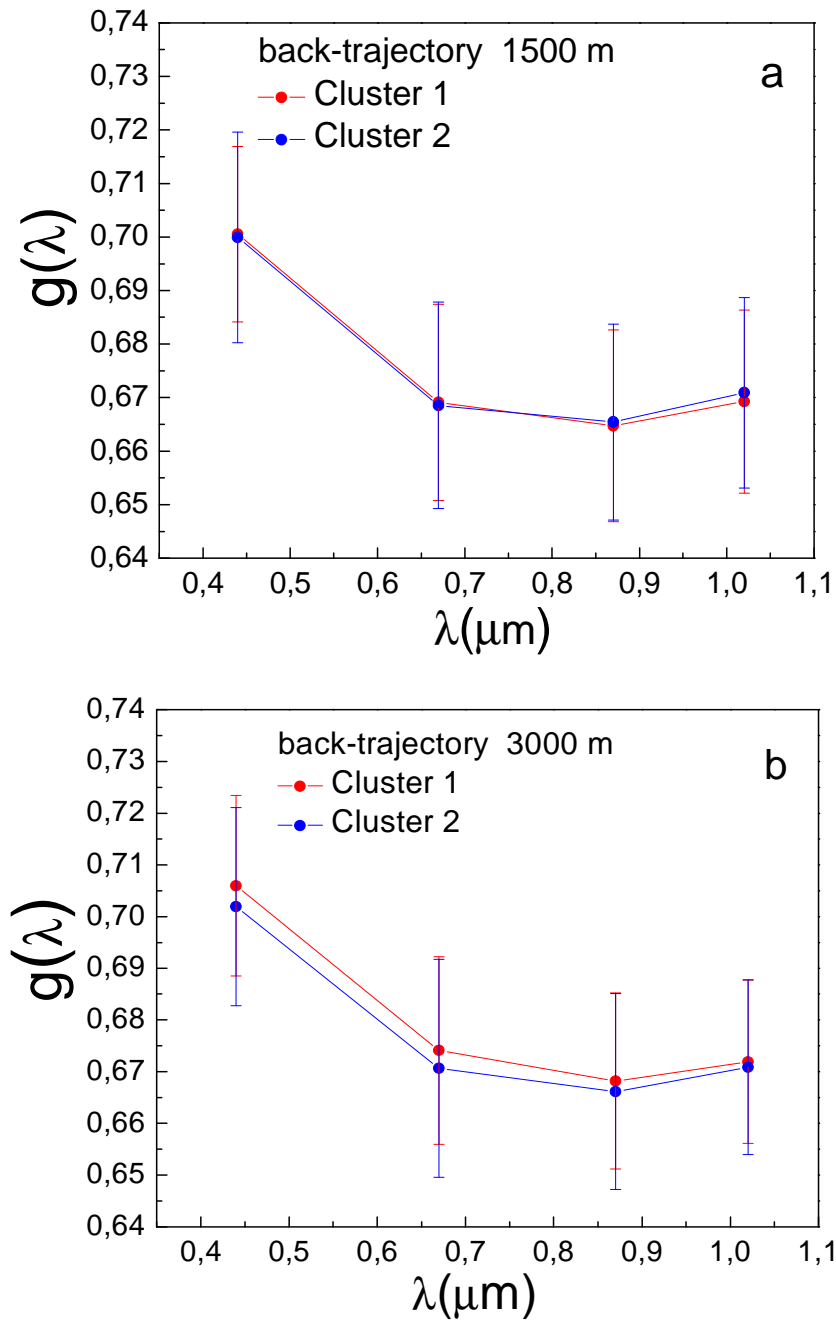

Figure 6.26: Asymmetry parameter a) 1500 m level and b) 3000 m level according to the cluster analysis.

6.2 Aerosol radiative forcing during desert dust events

Model output fluxes comparison against ground-based measurements and AERONET data

Simulated net irradiances at the surface and TOA during desert dust intrusions at Granada (2005-2010) have been obtained from the SBDART radiative transfer model, using the experimental aerosol information (aerosol optical depth, single scattering albedo and asymmetry parameter) derived from the principal plane retrievals as input. Additionally, net (down minus up) shortwave irradiances at the surface and TOA under a clean atmosphere (cloud-free conditions and absence of aerosol) have been derived from the SBDART code. Thus, a simulated ARF was calculated from Equation (4.13) for the 911 instantaneous measurements obtained during desert dust events. As previously noted, the spectral aerosol optical properties used as input for the SBDART model calculations in this work were analyzed and classified in three groups according to the desert dust origin sources.

Firstly, the reliability of the SBDART model was analyzed. For that purpose, we compared the experimental downward irradiances and corresponding SBDART simulations for all desert dust cases analyzed in this study. Figure 6.27 shows three plots with the correlation between the measured and simulated values for the three desert dust origin sectors; sector A (Northern Morocco, Northwestern Algeria), sector B (Western Sahara, Northwestern Mauritania and South-western Algeria) and sector C (Eastern Algeria, Tunisia).
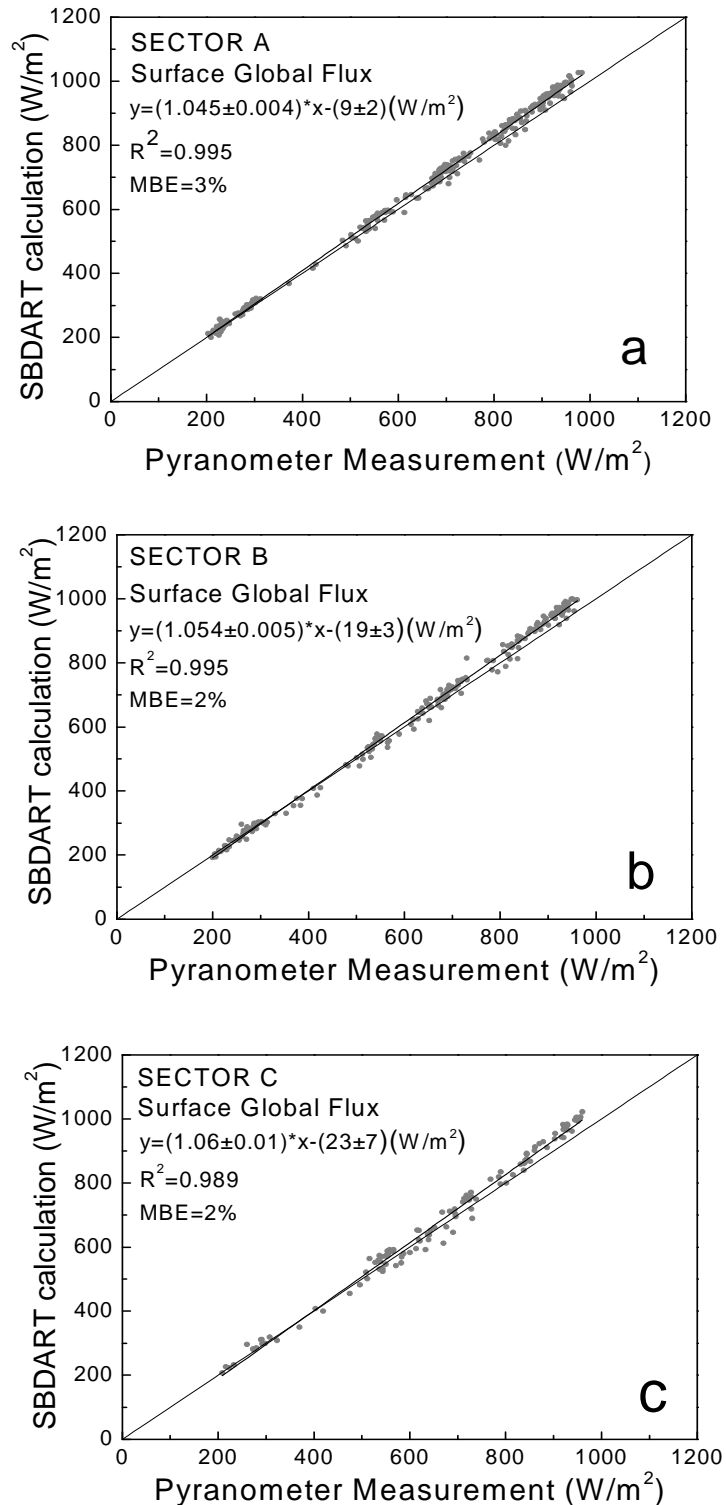
Figure 6.27: Comparisons of surface global irradiance measurements obtained during desert dust events occurred at Granada during 2005-2010 with SBDART modeled results for a) Sector A, b) Sector B and c) Sector C. The regression equations, determination coefficients and biases are included in these figures.

6. Results and Discussion

The solid line represents the zero bias line (slope equal to one) which fits the data well, confirming the high degree of agreement. A linear regression analysis between the measured and modeled downward irradiances has been performed. The correlation coefficient values were higher than 0.98, indicating that the measured and modeled values were well correlated in the three dust origin classes. The statistical analysis gives slopes very close to unity, supporting the validity of the radiative transfer model computations of ARF presented in this work.

Figure 6.28 shows the relative differences between the experimental and modeled downward global irradiances (F_{mod}-F_{exp}/F_{exp}) as a function of the experimental values (F_{exp}). It can be seen that SBDART code slightly overestimates the experimental global irradiance with most of the differences around 3%, indicating the reliability of the radiative transfer model used in this work for the ARF calculations. The mean values of these relative differences are +3%, +2% and +2% for sectors A, B and C, respectively. These small discrepancies between modeled and experimental values could be associated with errors in the model input parameters as well as errors in the experimental measurements of the global irradiance. Additionally, these differences could be partially related to the overestimation of the diffuse component by the SBDART model (e.g. Pinker et al., 2010; Won et al., 2004; Kim et al., 2005).
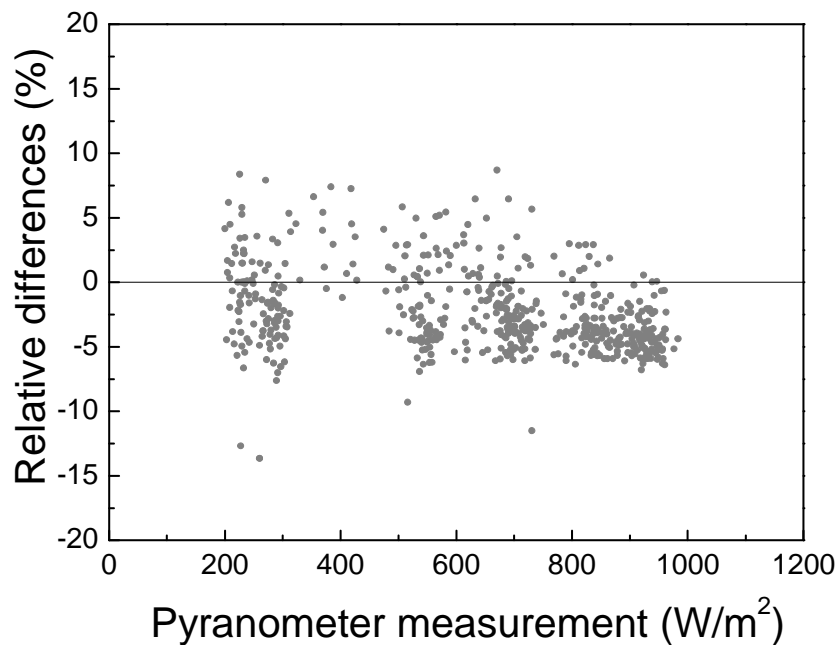
Figure 6.28: Relative differences between modeled (SBDART) and experimental (CM-11) downward irradiances against experimental values.

The SBDART model simulated instantaneous direct, diffuse and global (direct plus diffuse) irradiances at the surface for desert dust intrusions over Granada during 2005-2010 for the three desert dust origin classes that have been obtained. In addition, the corresponding simulated surface irradiances for aerosol-free conditions for these three classes were calculated. In aerosol-free conditions the calculated mean net global irradiances at surface were of ~700±250 W/m^2 for sector A and ~690±250 W/m^2 for sectors B and C. During African dust intrusions the mean values were of 650±250 W/m^2, 640±250 W/m^2 and 650±230 W/m^2 for sectors A, B and C, respectively. This means that desert dust events over the study location caused an average decrease in the net global solar radiation at surface of 7.1% (sector A), 7.7% (B), and 6.6% (C), which means less energy reaching the ground and, therefore, more surface cooling. This

decrease in the net global radiation was due to the balance between the strong increases in the diffuse irradiance around 250% and the substantial reduction of the direct irradiance around 26%. The diffuse irradiance ranged from ~50 W/m^2 in aerosol-free conditions to 175-194 W/m^2 in desert dust conditions for the three sectors. The direct irradiance ranged from ~645-653 W/m^2 in aerosol-free conditions to 447-478 W/m^2 in desert dust conditions for the three sectors. These large changes in direct and diffuse irradiances highlight the importance of desert dust intrusions over South-eastern Spain, indicating that these types of particles significantly affect the propagation of solar radiation through the atmosphere. We have also computed mean values of the upward radiation at TOA for desert dust intrusions and for the corresponding aerosol-free conditions. The desert dust particles produced an increase in the upward radiation of 8.2%, 10.3% and 9.4% for sectors A, B and C respectively. These results reveal that desert dust particles cause significant planetary cooling.

Aerosol radiative forcing (ARF) cannot be directly validated against AERONET measurements considering the methodological differences (Garcia et al., 2011). This comparison can be only indirectly and partly achieved, through validation of ARF components (at surface and at TOA) (Fig.6.29). Considering that AERONET determines instantaneous global irradiances in the spectral range from 0.2 to 4.0 μm, we have run the SBDART model again considering this spectral range. The comparison of the downward instantaneous global irradiances at the surface corresponding to both data sets were in good agreement, as can be seen from the regression fit and the coefficient of determination. Nevertheless, there was a small relative difference of 1% and 2.4% between upward global irradiances at TOA and downward global irradiances at the

surface, respectively. These small differences between the SBDART output and AERONET irradiance data could be due to the small differences in the input data.
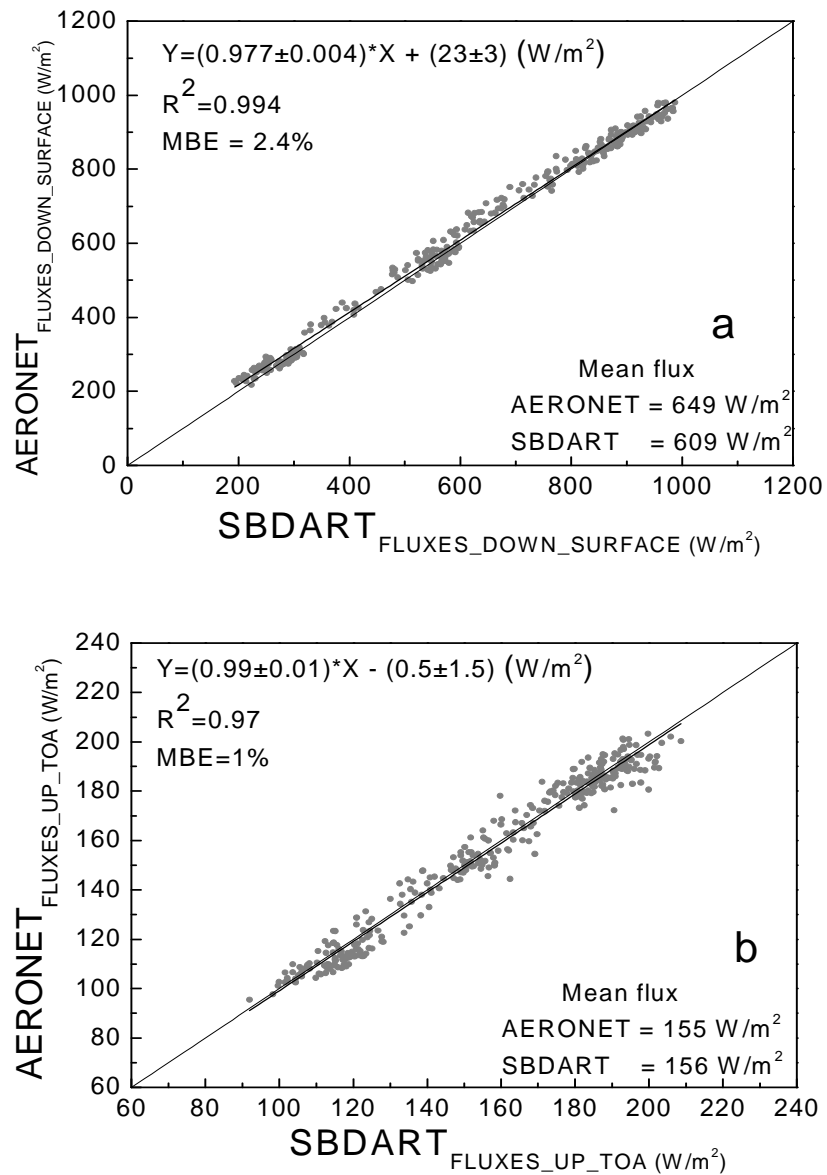
Figure 6.29: Scatter plots of the instantaneous global irradiances using SBDART model against corresponding AERONET fluxes for a) downward fluxes at surface and b) upward fluxes at TOA. The black lines are the linear fits. The regression equations, determination coefficients and biases are included in these figures.

6. Results and Discussion

In any case the good agreement between AERONET and SBDART irradiances suggests that the aerosol optical properties used as input in this work appropriately represent aerosol properties during desert dust outbreaks over our study area.

Annual evolution of aerosol radiative forcing

The overall mean daily ARF at TOA during all desert dust events was (-6±5) W/m^2, while the overall mean daily ARF at surface was (-20±11) W/m^2, producing an atmospheric mean daily ARF value of (+14±8) W/m^2. Considering only the aerosol effect this situation produced a mean aerosol heating rate of 0.13±0.07 K per day, for the entire atmospheric column, during desert dust events. The negative daily ARF value at TOA indicates that desert dust aerosol increased light scattered back to space, inducing thus a significant Earth-atmosphere cooling. In addition, the negative value at the surface reveals that the desert dust aerosol reduces significantly the solar radiation reaching the ground level producing thus a large surface cooling. This result suggests a relevant absorption of solar radiation in the atmosphere, leading to significant atmospheric warming.

The monthly mean values of daily ARF at the surface, TOA and atmosphere during all desert dust events occurred at Granada from 2005 to 2010 are shown in Figure 6.30a. Additionally, the τ_a(440nm) and $\omega(\lambda)$ at 440 nm and 1020 nm are shown in Figure 6.30b. The month of April had the largest mean τ_a(440nm) value (0.56±0.25) followed by May (0.31±0.14), July (0.32±0.16), June (0.29±0.14) and September (0.29±0.20). The lowest mean τ_a(440nm) value corresponded to October (0.23±0.17).
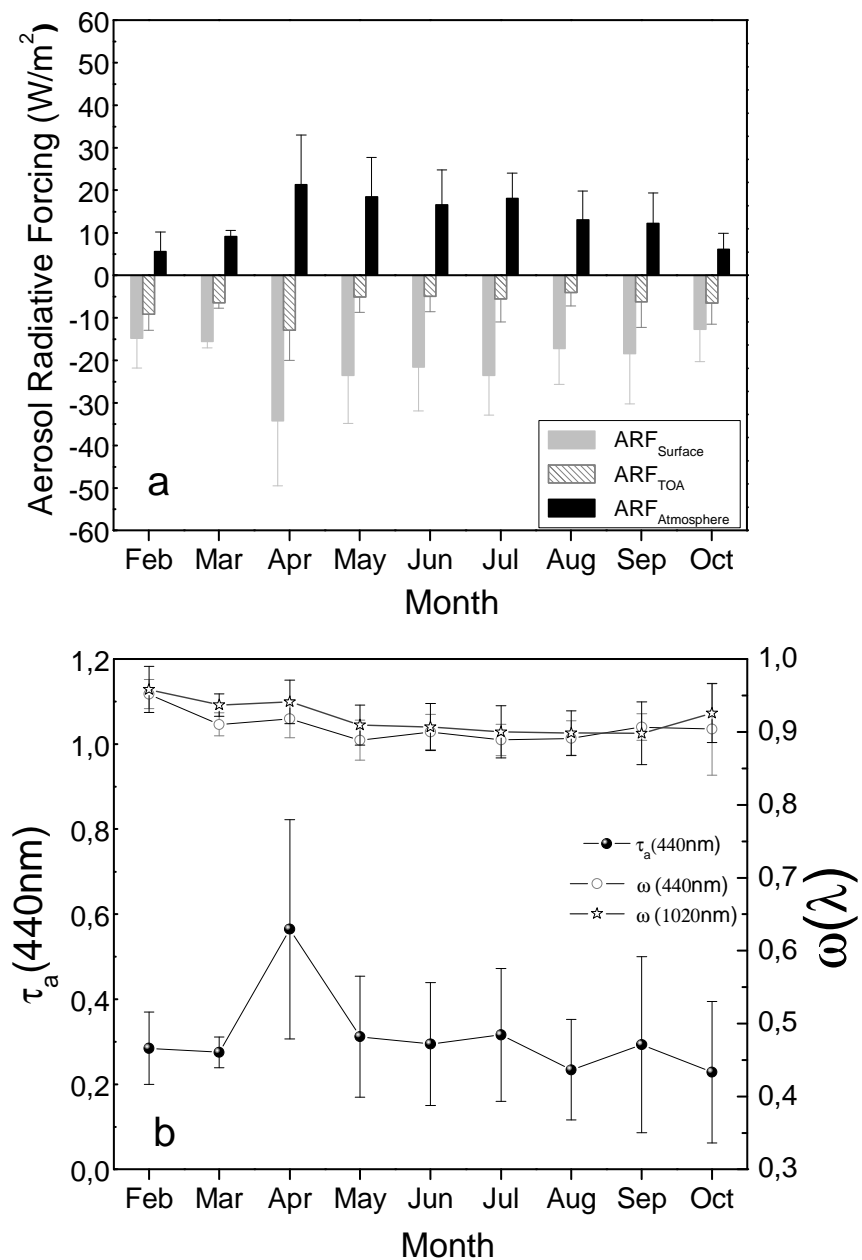
Figure 6.30: a) Monthly mean values of aerosol radiative forcing at TOA, surface and in the atmosphere during desert dust events at Granada during 2005-2010. b) Monthly mean aerosol optical depth at 440 nm and single scattering albedo at 440 nm and 1020 nm. The error bars correspond to standard deviation

6. Results and Discussion

Daily ARF values ranged from -13±8 W/m2 to -34±15 W/m^2 at surface, from -4±3 W/m^2 to -13±7 W/m^2 at TOA being this change from +6±4 W/m^2 to +21±12 W/m^2 in the atmosphere, and the corresponding aerosol atmospheric heating rates, for the entire atmospheric column, from 0.05±0.04 K/day to 0.19±0.10 K/day. The monthly mean ARF value at surface was larger in warm seasons with a maximum in April. It is important to note that the monthly evolution of the ARF at surface follows the monthly evolution of the aerosol optical depth. However, the relationship between the monthly evolution of the ARF at TOA and the monthly evolution of $\tau_a(\lambda)$ is not clear. This behavior could be attributed to effects induced by other aerosol properties such as single scattering albedo. The typical $\omega(\lambda)$ increase with wavelength for desert dust particles occurred in all months except September and October. However, during warm seasons the monthly mean $\omega(\lambda)$ value decreased in all wavelengths with respect to other seasons. In fact, the lowest values of daily ARF at TOA corresponded to the lowest monthly values of the single scattering albedo for those months (Valenzuela et al., 2012a). This result is in agreement with the works of Di Biagio et al. (2009) and Antón et al. (2011) who showed that the single scattering albedo has a large influence on the daily ARF. The small values of the forcing at TOA during those months and the corresponding high values at the surface mean that less solar energy reached the ground and more energy was absorbed by atmosphere. For this reason, the atmospheric daily ARF was higher from April to September than the rest of months.

6. Results and Discussion

Aerosol radiative forcing by desert dust origin sectors

As noted in the methodology section, the aerosol optical and microphysical properties have been analyzed and classified during dust events over Granada according to the desert dust sources. These instantaneous optical properties have been used as inputs to the SBDART model to derive the aerosol radiative forcing for each desert dust origin sector.

Firstly, we have studied the dependence of aerosol radiative forcing on solar zenith angle (θ) for each sector. Figure 6.31 shows the ARF at surface and TOA for each class as a function of θ. For all θ, there are small differences in ARF at TOA between the three sectors. From this figure, the dependence of the ARF at TOA on θ is obvious. As the solar zenith angle increases the ARF at TOA tends to increase (in absolute value) up to a θ of 70º, since part of the scattered light goes back to space, even with predominant forward scattering. In contrast, the ARF at surface only presents a slight θ dependence. The ARF at surface for the three sector increases slightly (absolute value) up to a θ of 70º. This is due to the increase in photon path length and the associated increase in the attenuation, scattering and absorption, of direct solar radiation (Meloni et al. 2005). For θ larger than 70º the ARF at surface and TOA decrease (in absolute value) because the slant path is no longer optically thin (Boucher at al., 1998). Additionally, it can be seen that the ARF at surface presents larger values (in absolute term) when air masses are transported from sector B. This is consistent with higher value of $\tau_a(\lambda)$ obtained for this sector.
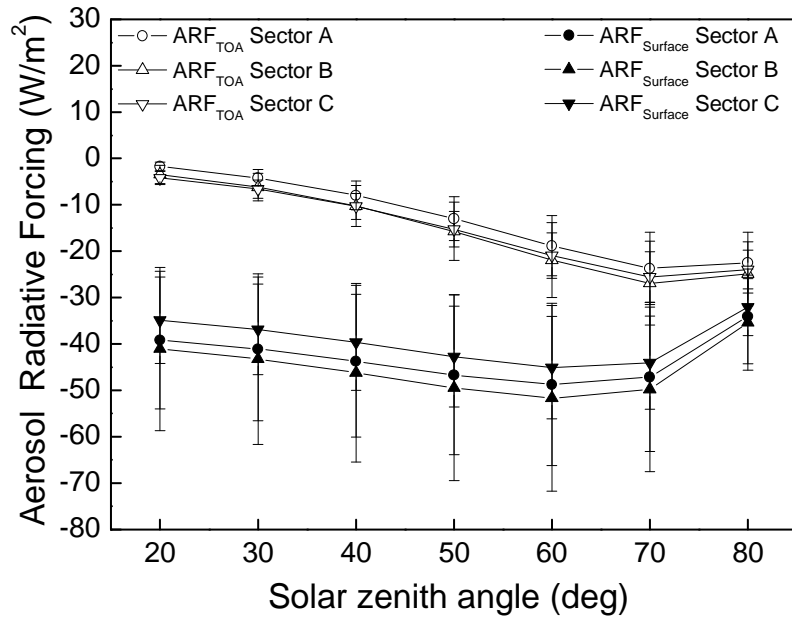
Figure 6.31: Computed aerosol radiative forcing at TOA (open symbols) and at surface (full symbols) as a function of solar zenith angle for the sectors A, B and C during desert dust events occurred at Granada from 2005 to 2010. The error bars correspond to standard deviation.

Considering interest from a climatic point of view, we have computed the daily average of the ARF (Equation 4.14). Thus, daily mean ARF values at surface (TOA) were -20±12 (-5±5) W/m^2, -21±9 (-7±5) W/m^2 and -18±9 (-6±5) W/m^2 for sectors A, B and C, respectively. The mean daily ARF values at the surface and TOA for the different desert dust origin sectors were within the standard deviations, so there are no significant differences among them. The atmospheric daily ARF ranged between 15±9 W/m^2, 14±7 W/m^2 to 12±8 W/m^2 for sectors A, B and C, respectively. The mean aerosol heating rate (K/day) for the entire atmospheric column was 0.14±0.08 K/day, 0.13±0.06 K/day and 0.11±0.07 K/day for sector A, sector B and sector C, respectively. The slightly larger mean aerosol heating rate for sector A was attributed to high

atmospheric absorption when air masses were transported from this sector. To corroborate possible differences between daily mean ARF values from these sectors, a set of non-parametric statistical-significance test (Kolmogorov-Smirnov) was applied on the data. This test revealed, at the 95% confidence level, which sectors were statistically different (Table 6.6).

	Sector A	Sector B	Sector C
	Daily *ARF* at TOA		
Sector A	---------	**0.008**	**0.009**
Sector B	0.493	--------	0.601
Sector C	0.555	0.084	---------
	Daily *ARF* at surface		

Table 6.6: The *p* values of the Kolmogorov-Smirnov statistical test applied to ARF at surface and TOA data for each pair of origin sectors. The *p* values above the diagonal, for each pair of data, correspond to the daily *ARF* at TOA, while the values below the diagonal correspond to the daily *ARF* at surface. Values of $p < 0.05$ indicate statistical significant differences between the means at the 95% confidence level.

The values above the diagonal, for each pair of desert dust sources, indicate the p value of the test with respect to the daily ARF at TOA, while the values below the diagonal correspond to the daily ARF at surface. If $p<0.05$, the difference in daily ARF means was significant. The test revealed that differences in daily ARF at TOA for sector A were significant with respect to sectors B and C. However, these two last sectors did not show significant differences. Additionally, the test revealed the absence of significant differences in daily ARF at surface between the three different origin sectors.

6. Results and Discussion

A possible explanation for this result could be the different single scattering albedo between sector A and the other sectors and its great influence on the daily ARF at TOA.

Uncertainties in our daily ARF computation may be related to uncertainties in the retrieval of optical variables, $\tau_a(\lambda)$, $\omega(\lambda)$ and $g(\lambda)$. The sensitivity analysis performed by Pandithurai et al. (2008) using the SBDART model showed that an error of 0.02 in $\tau_a(\lambda)$ and in $\omega(\lambda)$ could result in an uncertainty of 1.5 and 3.0 W/m^2, respectively, in daily ARF at the surface. The corresponding errors in daily ARF at TOA would be 0.5 and 1.6 W/m^2, respectively. Another error source could be the uncertainties related to the spectral surface albedo considered and uncertainties in meteorological parameter considered by radiative transfer model. The overall uncertainty in the estimated daily ARF due to deviations in simulation was found in the range ~10–15% (e.g. Prasad et al., 2007; Alam et al., 2012).

The daily aerosol radiative forcing efficiency (ARFE), calculated as daily aerosol radiative forcing per unit of τ_a(440nm), was also investigated in this study. Thus, we have computed daily aerosol radiative forcing efficiency (ARFE) as the ratio of daily aerosol radiative forcing by the corresponding daily mean τ_a(440nm). Using these daily ARFE we also computed the ARFE for each desert dust sector. The daily ARFE values at the surface showed a maximum (absolute value) for sector A (-74±12 W/m^2), a minimum (absolute value) for sector C (-65±16 W/m^2) and an intermediate value for sector B (-70±14 W/m^2). These daily ARFE values at the surface indicated that the surface was deprived of a substantial amount of solar energy in the presence of African desert dust over the South-eastern of Spain. Figure 6.32a shows the monthly mean values of the ARFE at the surface according to the classification of the desert dust

origin sources. ARFE at the surface was larger in warm seasons for three sectors with maxima of -80±13 W/m^2 for both sector C in May and sector A in July. The minimum values were of -54±5 W/m^2 and -47±14 W/m^2 for sectors B and C in March and February, respectively.
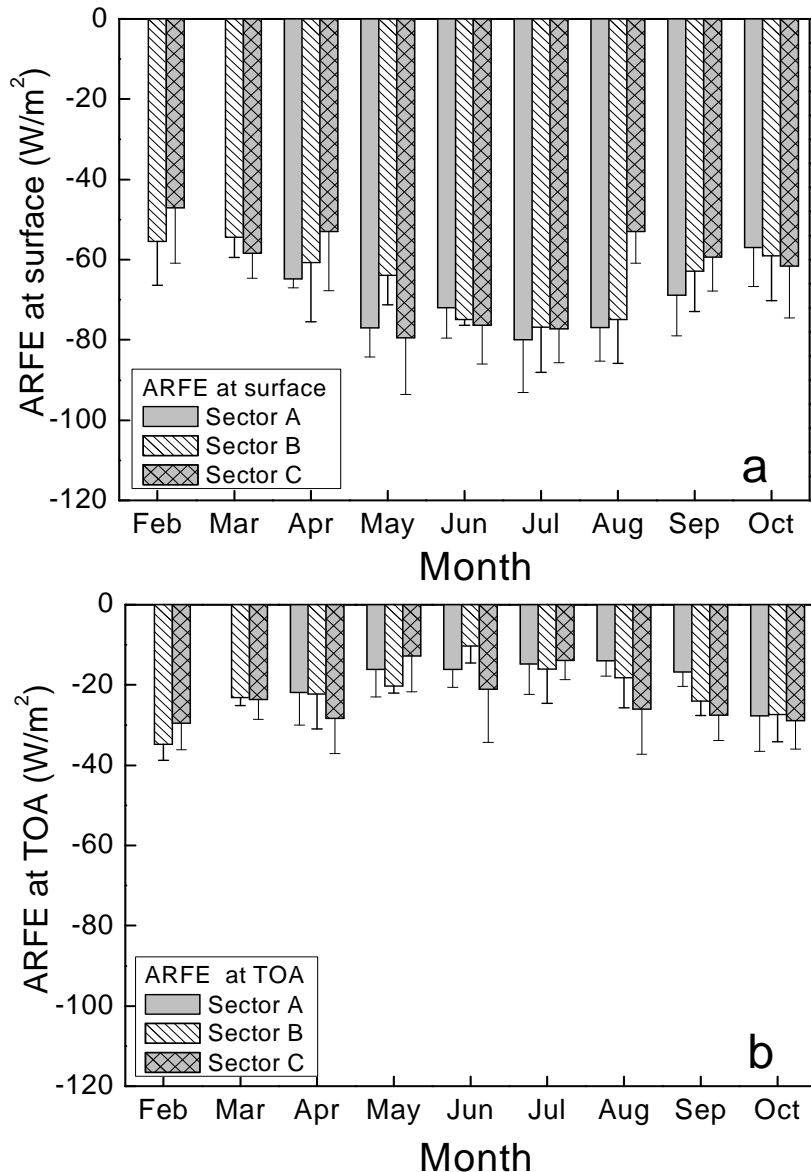

Figure 6.32: Monthly mean values of aerosol radiative forcing efficiency (*ARFE*) according to the classification by origin sources during desert dust events occurred at Granada during 2005-2010, a) at surface and b) at TOA. The error bars correspond to standard deviation.

6. Results and Discussion

The high load of mineral particles and higher likelihood of desert dust intrusions during warm months could explain higher ARFE at our site when air masses were transported from any of the three desert dust origin sources. Additionally, the daily ARFE values at TOA ranged from a mean -17 ± 7 W/m^2 (sector A) to -22 ± 10 W/m^2 (sector C), again with an intermediate value of -20 ± 9 W/m^2 for sector B. The daily ARFE values obtained in sector A (slightly lower absolute value at the TOA and higher absolute value at the surface) could be explained by the lowest single scattering albedo in this sector. Monthly evolution of the ARFE at TOA (Figure 6.32b) did not show important differences between the three origin sources. In fact, we have found that during warm seasons, ARFE was lower than for other months in all three sectors. In warm months we found lower single scattering albedo values for three sectors.

Comparison with other data sets

It is interesting to compare our results with those obtained during desert dust events in other regions. In Table 6.7, we present the daily ARF and daily ARFE values given by several authors for situations dominated by desert dust, and for cases where dust is mixed with other aerosol types. Daily ARF values ranged from -2.1 W/m^2 (Negev, Israel) to -26 W/m^2 (Kanpur, India) at TOA, from -6.4 W/m^2 (Negev, Israel) to -87.5 W/m^2 (Kanpur, India) at the surface, and from ~ 4 W/m^2 (Lampedusa) to ~78.8 W/m^2 (Taklimakan Desert, China) in the atmosphere. The results of the comparisons of the ARF and ARFE showed that the values obtained in our study were within the range reported by other authors during desert events. The differences may likely be related to the differences in the methods used, measurement periods, desert dust load, chemical composition of dust, aerosol mixing state and surface albedo.

Reference	λ(μm)	A	ARF TOA	ARF Surface	ARF Atmosphere	ARFE TOA	ARFE Surface	Location
Meloni et al. (2005)	0.4 - 0.7	0.02-0.37	-5.1 to -8.7	-11.0 to -14.2	3.7 to 9	-15.0 to -16.4	-28.4 to -30.1	Lampedusa, Italy
Derimian et al. (2006)	0.175 – 2.270	0.23-035	-2.1	-6.4	--------	-22	-65	Negev, Israel
Derimian et al. (2008)	0.2 – 4.0	spectral depen.	-8.1	-29.1	21.0	-15.7	-56.4	M'Bour, Senegal
Prasad et al.(2007)	0.3 – 3.0	0.25	-2.9 to -26	-29.5 to -87.5	--------	-17±3	-46±3	Kanpur, India
Lyamani et al. (2006)	0.4 – 0.7	0.15	-4.0	-20.4	16.4	-14.5	-73.4	Granada, Spain
Di Sarra et al. (2011)	0.3 – 3.0	0.07	--------	-69.9±3.4	--------	--------	-59.9±2.6	Lampedusa, Italy
Huang et al. (2009)	0.175 – 4.0	spectral depen.	14.11	-64.72	78.8	--------	--------	Taklimakan Desert China
Saha et al.(2008)	0.28 – 2.8	spectral depen.	-7.7 to -9.8	-61.8 to -64.4	54.1 to 54.6	-9.7 to -12.4	-78.2 to -81.5	Toulon, France
Present study	0.31 – 2.8	spectral depen.	-5±5	-20±12	15±9	-17±7	-74±12	Granada, Spain
Present study	0.31 – 2.8	spectral depen.	-7±5	-21±9	14±7	-20±9	-70±14	Granada, Spain
Present study	0.31 – 2.8	spectral depen.	-6±5	-18±9	12±8	-22±10	-65±16	Granada, Spain

Table 6.7: Daily aerosol radiative forcing (W/m²) and daily aerosol radiative forcing efficiency (W/m²) at surface, TOA and in the atmosphere observed over different locations during desert dust events. The second column (λ) indicates the spectral range considered and third column shows the surface albedo (A) used in each study.

Additionally, the right characterization of the surface albedo is a crucial issue to evaluate the aerosol radiative forcing (Myhre et al., 2003). However, few studies have taken into account the spectral dependence of surface albedo, many using a fixed value of this variable which makes inter-comparison difficult.

Daily ARFE differences presented in Table 6.7, mainly at TOA, could be due to stronger dependence on surface albedo and $\omega(\lambda)$. The high daily ARFE values at the surface obtained during desert dust events over at Granada could be explained in terms of significant contributions of anthropogenic pollutants (especially absorbing particles). In fact, Valenzuela et al. (2012a) reported values of $\omega(\lambda)$ (0.89 at 440 nm) during these desert dust events lower than those reported in the literature for desert dust aerosols (e.g. Dubovik et al., 2002b). However, single scattering albedos obtained in our study were comparable to those obtained at the Mediterranean sites by other authors. For instance, Perrone and Bergamo (2011) showed that the contribution of anthropogenic particles can be relevant during desert dust events. These authors reported $\omega(\lambda)$ values at 550 nm in the range 0.87-0.95 at Lecce (40.33ºN, 18.10º E) in the Central Mediterranean during desert dust events.

6.3 Aerosol optical properties over Alborán Island

In the previous analysis has been proposed the possibility of that anthropogenic aerosol is mixed with desert dust in North Africa and after it is transported to the South-eastern Iberian Peninsula. This possibility is also pointed by other authors (e.g. Rodriguez et al., 2011). In order to analyze this fact the Alborán Island constituted a

6. Results and Discussion

strategic location to perform this analysis using sun-photometric measurements. A measurements campaign was carried out at Alborán Island from June 2011 to January 2012. During this time, air masses arriving over Alborán Island have been classified according with the potential aerosol origin sources. In this sense, three regions have been identified (Figure 5.2): 1) Sector A (Central Europe, Mediterranean Sea), 2) Sector B (North Africa), and 3) Sector C (Atlantic Ocean and Iberian Peninsula).

A total of 5996 cloud-free measurements (158 days) were performed from June 2011 to January 2012. Figure 6.33 (a,b) shows the temporal evolution of τ_a(440 nm) and Angström exponent, α(440-1020 nm), taking into account the source sectors. High τ_a and low α values (30 June, 1-3 and 9 August) were found when air masses were transported from sector B (North Africa), indicating high load of coarse particles. The τ_a values decreased and α increased from summer to winter for this sector, and showed predominance of coarse particles (desert dust contributions) for several days in September and October. During the whole period, the mean τ_a(440 nm) for sector B was 0.38±0.13, which is comparable to that found in the Lampedusa island, τ_a(495.7 nm) of 0.36±0.16, during desert dust events in the period July 2001–September 2003 (Pace et al., 2006). The $\tau_a(\lambda)$ values also agrees with that reported by Toledano et al. (2009) in "El Arenosillo", South-western Spain", with a value of 0.35±0.19 for τ_a(440 nm) during African dust episodes from 2000 to 2004. The mean α value for sector B at Alborán Island was 0.59±0.24, comparable to that found by Toledano et al. (2009) with a value for α(440-870 nm) of 0.6±0.4. However, this value was slightly higher than the mean value reported in Lampedusa island; α(415.6-868.7nm) was 0.4±0.4 (Pace et al., 2006).

6. Results and Discussion

Therefore, the difference in the results in both studies could be due to the different measurement periods and/or that desert dust likely came mixed with anthropogenic fine particles to our station. Air masses transported from sector C showed low τ_a(440nm) (0.15±0.08) and high α(1.1±0.4) values. Considering that the computation of α for rather low τ_a(440nm) values present high uncertainty (e.g.Holben et al., 1998) then low α(440-1020nm) values for this sector must be considered with caution. The air masses transported from sector A affected mainly in autumn, with high mean τ_a(440nm) of 0.27±0.12 linked to relatively high mean α(440-1020nm) of 1.2±0.3, indicating that this region contributes mainly with fine-mode aerosol accumulated in Mediterranean basin or transported from Central Europe (e.g. Lyamani et al., 2006b). Pace et al. (2006) reported similar τ_a(495.7nm) (0.23±0.11) and slightly higher α(1.5±0.4) values when air masses were transported from Central-Eastern Europe. Figure 6.33 (a, b) also shows the large day-to-day variability of τ_a(440nm) (mainly for sector A and B) and α(440-1020nm) values (for the three sectors). Thus α(440-1020nm) values in this station can change from typical values of desert dust to values of fine mode aerosols coincident with the beginning or the end of the episodes.

The scatter plot of α(440-1020nm) versus τ_a(440nm) is a useful tool to identify the different aerosol types. Whereas the τ_a(440nm) mainly depends on the aerosol load, α(440-1020nm) is related to the aerosol particles size (e.g. Kaufman et al., 1998; Eck et al., 1999; Smirnov et al., 2000; Dubovik et al., 2002; Pace et al., 2006; Toledano et al., 2007; Prats et al., 2008). Figure 6.33c shows three main clusters of particles corresponding to the three source regions considered.
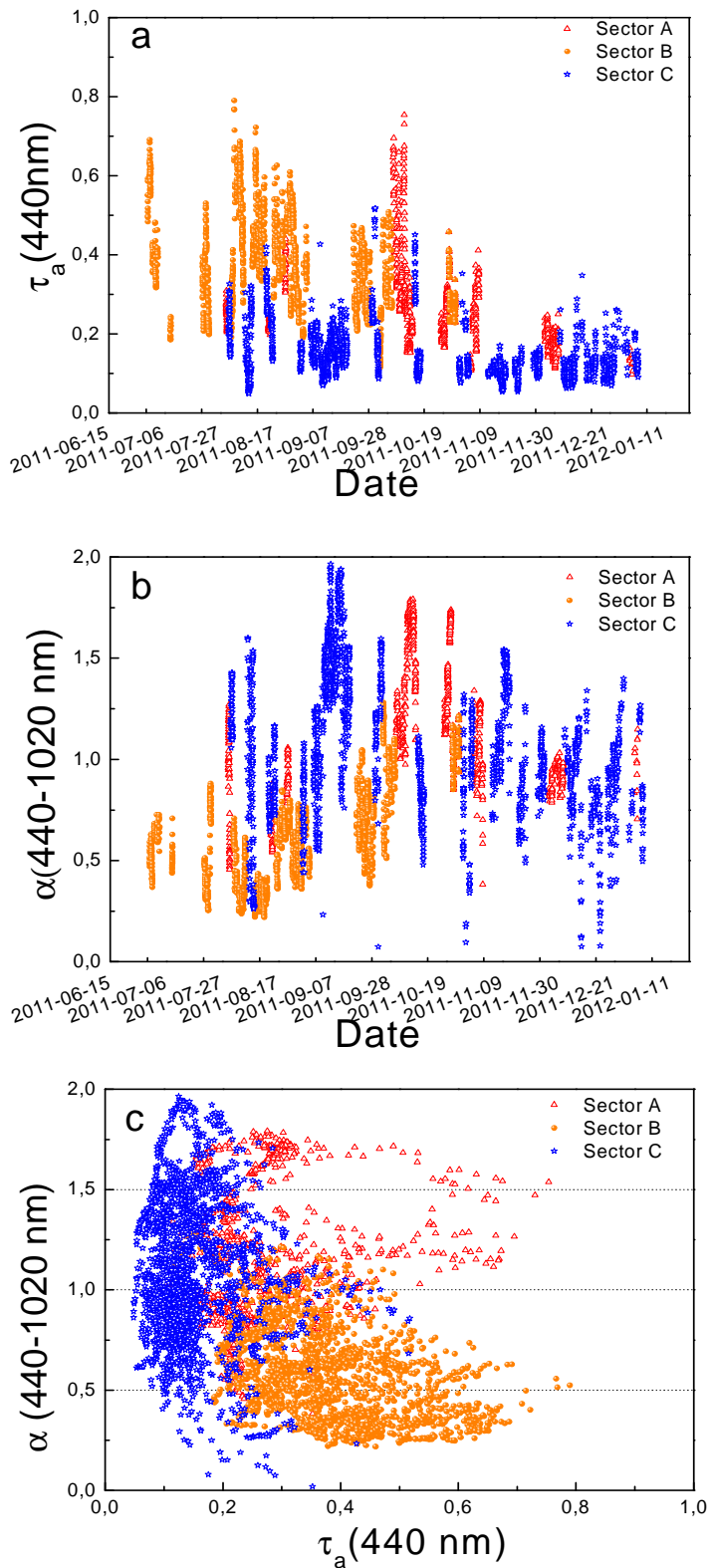
**Figure 6.33:** Temporal variation of: a) τ_a(440nm), b) α(440-1020nm) values over Alboran Island according with the sector origin classification. c) Correlation between τ_a(440nm) and α(440-1020nm) for each origin sector.

6. Results and Discussion

The observations for sector B show high τ_a(440nm) linked to low α(440-1020nm) indicating large aerosol load due to coarse particles. It is worth to mention that for this sector some values showed α(440-1020nm) values higher than 1, indicating the fine particles contribution. Although the Atlantic Ocean is the main aerosol source for sector C, this sector also includes the Iberian Peninsula and a non-homogeneous origin of the particles is expected. An important number of observations present τ_a(440nm) values bellow 2 with α(440-1020nm) mainly concentrated in the range from 0.5 to 1.0. According to Smirnov et al. (2002), this cluster could be related with marine aerosol, although can also be assigned to continental aerosol considering that according to the trajectories these air masses could drag some particles in their pathway over Iberian Peninsula. Sector A data presents τ_a(440nm) values in the range 0.2-0.8 while α(440-1020nm) present values mainly above 1, typical of fine mode aerosol from urban/industrial activities or biomass burning.

To get a better understanding on the contribution of fine mode particles to τ_a according our sector origin classification, the method proposed by Gobbi et al. (2007) was applied. The result of Gobbi's method for sector origin classification is shown in Figure 6.34. For sector A, Figure 6.34a shows the dominance of the fine mode fraction being up to 80% of the observations with η>50 % and with α>1. An increase in τ_a showed a shift to larger α values linked to more negative $\delta\alpha$, indicating an increase of the fine-mode under high τ_as.
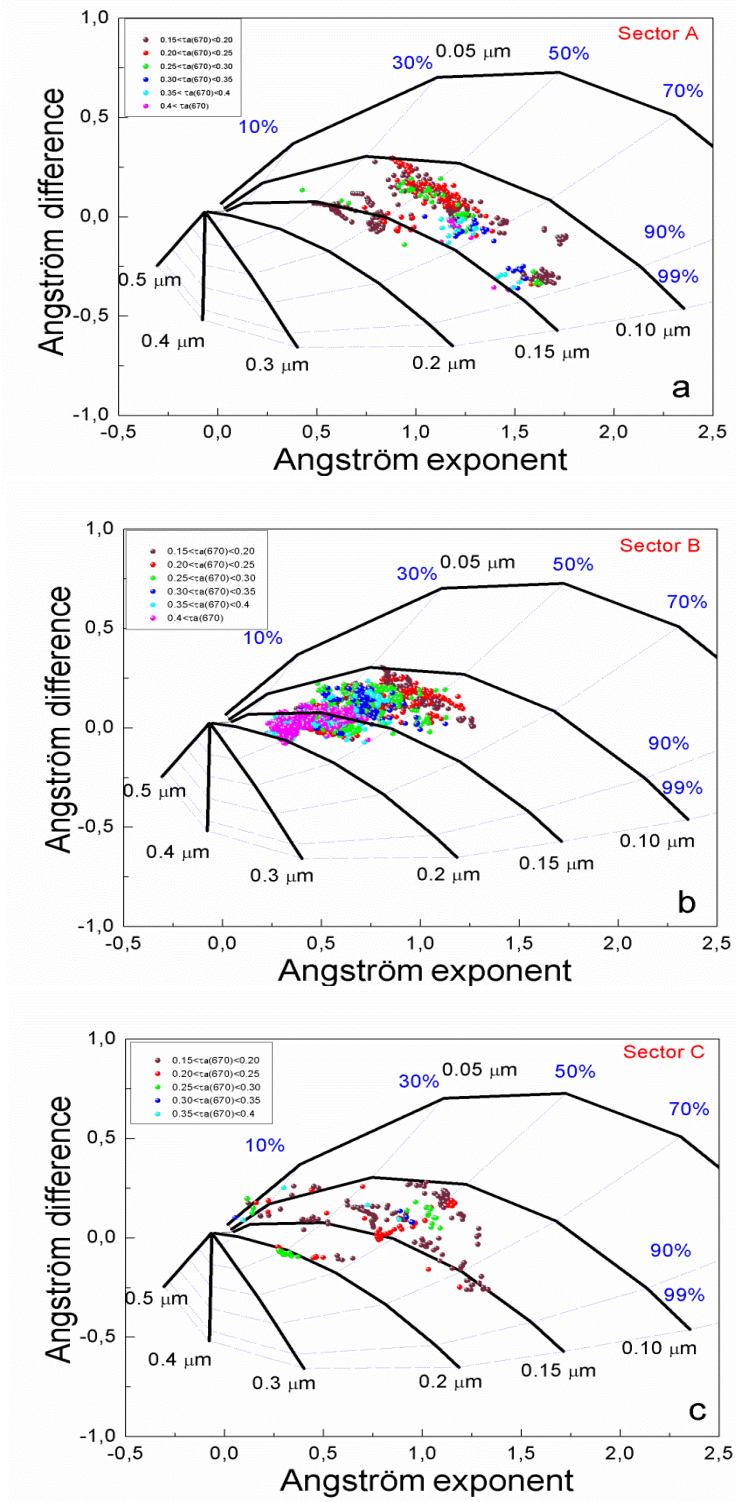
Figure 6.34: Angström exponent difference, $\delta\alpha = \alpha$ (440,670) - α (670,870), as a function of α (440-670) and τ_a(670 nm) for (a) Sector A, (b) Sector B and (c) Sector C.

6. Results and Discussion

In addition, there were small group of data ($1.3 \leq \alpha \leq 1.7$ and $-0.1 \leq \delta\alpha \leq 0.3$) related to high extinction ($\tau_a > 0.3$) which corresponds to $0.80\% \leq \eta \leq 90\%$ and $R_f \sim (0.10\text{-}0.13 \ \mu m)$. These observations could be related to strong pollution aerosol episodes. For sector B (Fig.6.34b), up to 95% of the observations showed $\eta < 50\%$ with $\alpha < 1$ and $\delta\alpha$ ranged from -0.16 to 0.25. Values of $\delta\alpha \geq 1$ indicated that fine mode fraction also contributed to the calculation of τ_a during desert dust events. An increase in τ_a showed a shift to lower α values with $\delta\alpha$ close to zero, indicating a stronger contribution of the coarse mode fraction to the total τ_a. It is noteworthy that for observations with τ_a in the range (0.35-0.4) the fine mode radius ranged from 0.12 to 0.2 μm. On the other hand, the small group of observations with $\eta > 50\%$ could be due to the transition situation at the beginning and at the end of the desert dust episodes. Basart et al. (2009), using a similar methodology in Lampedusa, reported values of $\alpha < 0.5$ and $\delta\alpha \sim 0$ associated to frequent Saharan dust outbreaks that corresponded to $\eta \leq 50\%$. Figure 6.34c shows that no homogeneous aerosol type is related to sector C because $\delta\alpha$ ranged between -0.25 and 0.3, indicating that both fine and coarse particles were present when air masses were transported from Atlantic Ocean. The group of observations with α values ranging from 0.25 to 0.75, which corresponds to $\eta \leq 40\%$ and $0.15 \leq R_f \leq 0.20 \ \mu m$, could be related to marine aerosols and mineral particles of the arid zones in the Iberian peninsula.

In view of the results obtained in this first analysis, the aerosol optical properties were influenced by changes in aerosol characteristics in the whole atmospheric column. Alborán, being a remote island with negligible landmass, does not have relevant local aerosol sources. Thus, any change in the prevailing wind pattern over the region would

lead to large changes in the aerosol properties depending on the air masses pathways and on the aerosol sources.

Aerosol optical properties according to source regions

Figure 6.35 illustrates the mean single scattering albedo values, $\omega(\lambda)$, retrieved for the three origin source sectors over the entire measurement period at four wavelengths. The $\omega(\lambda)$ at the shortest wavelength was similar for sectors A and B (0.88±0.03 at 440 nm) and slight lower for sector C (0.86±0.03 at 440 nm). Relatively small difference of ω at 440 nm (~0.02) were observed for three origin sources suggesting that the magnitude of absorption for fine mode aerosols (due to black carbon) and coarse mode dust (due to iron oxides) is similar at three origin sources in the short wavelength visible region. This fact contrasts with relatively large variation of ω at 1020 nm (~0.07) for the three origin sources. The small variation in ω at 440 nm for these air masses types suggests an advantage in satellite retrievals of τ_a at 440 nm or other shorter wavelengths of the visible range, since ω must either be assumed a priori in many satellite retrieval algorithms (Eck et al., 2010). As expected, $\omega(\lambda)$ increased with wavelength for sector B (mineral dust absorbs radiation more efficiently at the ultraviolet spectral range). However, the values obtained in infrared wavelengths were lower (0.91±0.03 at 1020 nm) than those reported for other authors during desert dust events (e.g. Dubovik et al., 2002). Air masses from sector A could transport different aerosol types (polluted and continental aerosols) mixed with particles from biomass burning mainly in summer, which could justify the wide range of $\omega(\lambda)$ values (e.g. Meloni et al, 2006). This fact is also evidenced by the large standard deviations of this parameter at longer wavelengths. The $\omega(\lambda)$ decreased with wavelength (0.88±0.03 at

440 nm to 0.84±0.05 at 1020 nm), which is an indicator of the predominance of absorbing aerosol. Higher $\omega(\lambda)$ retrieval uncertainty was obtained for sector C due to the low aerosol optical depth associated to this sector.
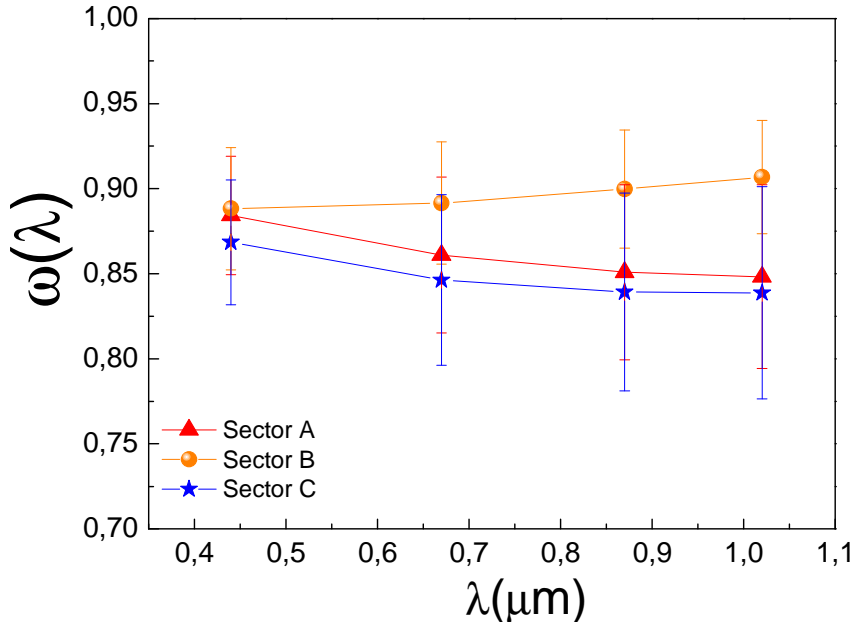
Figure 6.35: Single scattering albedo for sector A, sector B and sector C.

Derimian et al. (2008) used the difference between $\omega(\lambda)$ at 440 nm and 1020 nm ($d\omega$) to analyze the aerosol absorption properties, which provides two advantages: firstly, it is expected that the difference will provide better accuracy than absolute values, since the retrieval of spectral dependence is more reliable than that of an absolute value; and secondly, the spectral behavior of an $\omega(\lambda)$ curve can be characterized by only one parameter, $d\omega$. Negative values of the difference $\omega(440nm)$–$\omega(1020nm)$ will be related to stronger absorption by iron oxide at 440 nm, while positive values are related to stronger absorption at 1020 nm by black carbon particles. In addition, we have also used $\alpha(440\text{-}1020nm)$, which is a qualitative indicator of

aerosol particles size. Figure 6.36 shows all quality-assured observations of α(440nm)–α(1020nm) versus α(440-1020nm) for the three sector origin. This figure reveals that, as the α(440-1020nm) increases from about 0.2 to about 1.8, the difference α(440nm)–α(1020nm) becomes positive and larger (indicating a decreasing contribution of coarse dust particles and increasing fraction of fine pollution particles) for the three sectors. Derimian et al. (2008) established that α values in the range 0.5-1.0 and strong absorption at 440 nm are related to mixtures of dust and pollution. In our study, some values mainly from sector B satisfied this condition. On the other hand, sector B also showed some values with $d\omega$>0 linked α(440-1020nm) higher than 0.8. Therefore, during desert dust episodes the contribution of fine particles transported from North Africa was significant. This situation was pointed by Rodriguez et al. (2011). In this sense, Perrone and Bergamo. (2011) also established that the contribution of anthropogenic particles can be significant during desert dust events over Mediterranean sites.
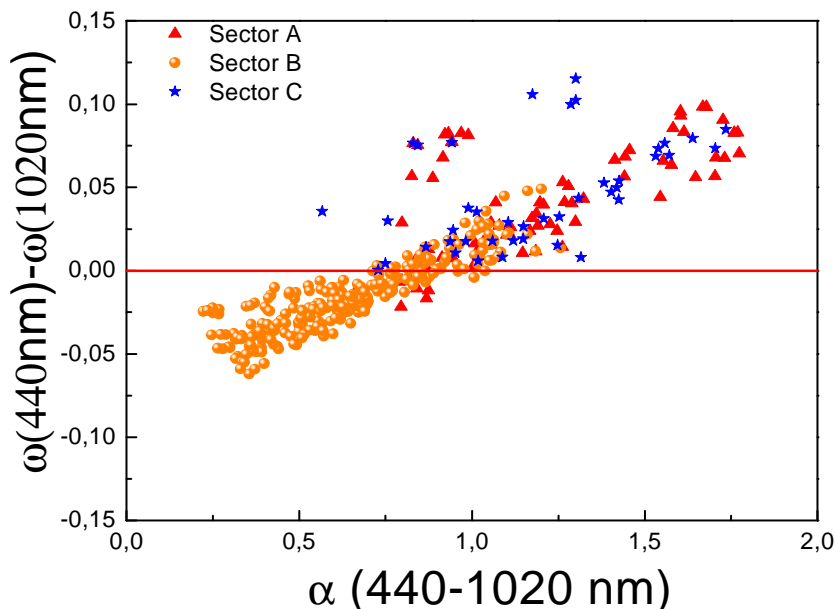

Figure 6.36: Difference of ω(440nm)–ω(1020nm) versus α(440-1020nm).

6. Results and Discussion

Aerosol properties for air masses transported from North Africa

Focusing on air masses transported from North Africa, the aerosol origin sources method has been used to determine the desert dust origin sources in North Africa affecting the Alboran island. In this sense, two mainly desert dust origin sources have been considered: North-western Africa (Morocco, Eastern Argelia, North-western Mauritania) and Eastern Africa (Centre and Eastern Argelia). Air masses from North-western Africa represented the 78% while those air masses from North-eastern Africa were less frequent in this measurements period, and represented only the 22 % of the total air masses from North Africa coincident with sun-photometer measurements over Alborán Island.

Frequency histograms plots for the τ_a(440nm) and α (440-1020nm) for the two desert dust origin sources are shown in Fig.6.37. For North-western Africa air masses, the frequency histogram for τ_a(440nm) -Fig. 6.37a- shows a main peak at 0.39, with the 84% of the observations ranging from 0.23 to 0.53. The frequency histogram of α(440-1020nm) -Fig. 6.37c- presents one frequency mode. The main frequency peak is centered at α(440-1020nm)~0.5, being representative of predominance of coarse particles (e.g. Holben et al., 2001). On the other hand, values around of 1.1 represented aerosol mixture of different sizes, showing intermediate values when the desert events are starting or finishing. The frequency for air masses of the North-eastern Africa (Fig.6.37b) shows a single mode centered at 0.38, with the 97% of the observations above 0.23. The frequency histogram of α(440-1020nm) -Fig.6.37d- showed a main peak centred at 0.65, with the 70% of the observations in the narrow range between 0.65 and 0.85, indicative of a stable situation in the size of particles affecting the monitoring station.
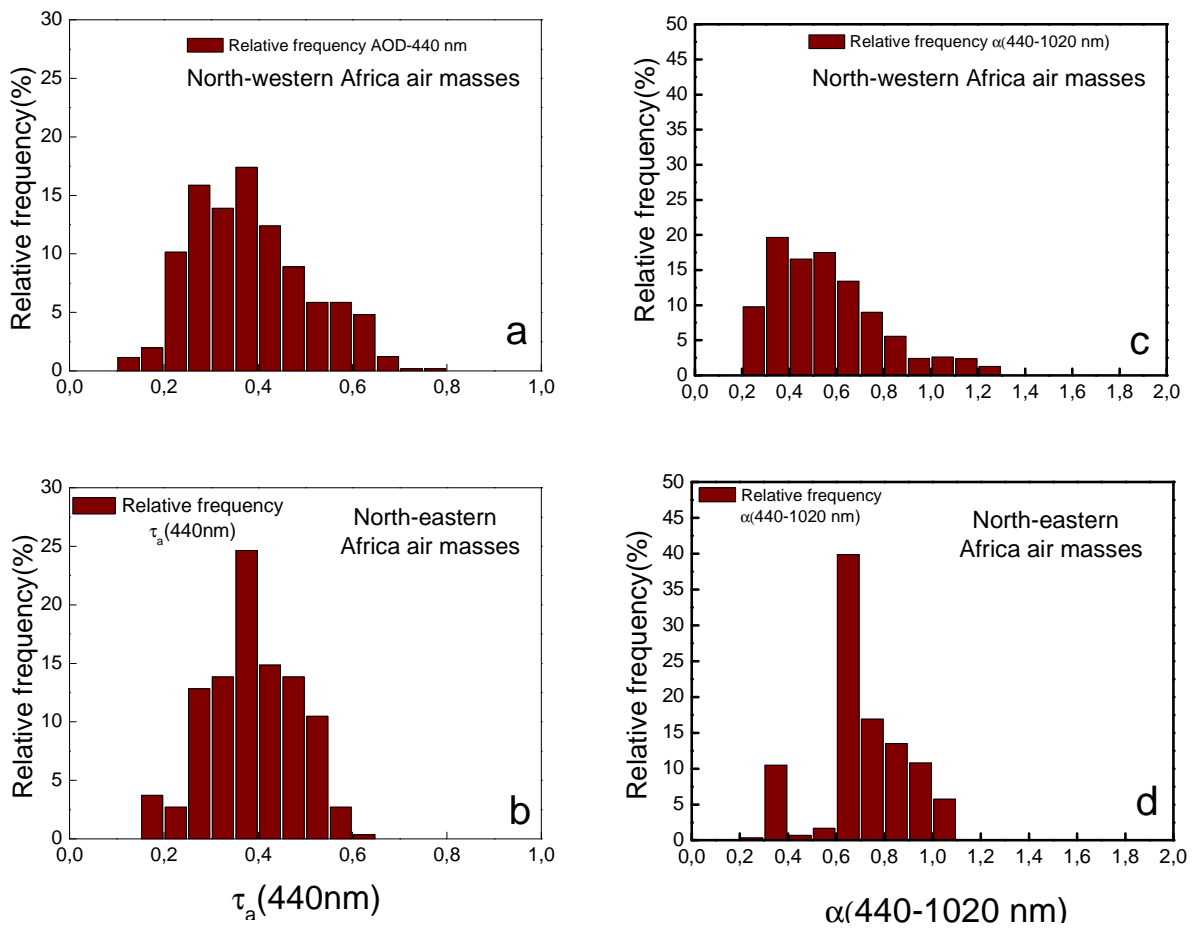
Figure 6.37: Frequency histograms of τ_a(440 nm) (left) and α (440-1020nm) (right) for North-western (a, c) and North-eastern (b, d) air masses transported from North Africa.

Fig.6.38 shows the relative frequency of the retrieved ω at 440 nm (Fig. 6.38a) and at 1020 nm (Fig. 6.38b) for the two desert dust origin sources. It is noticed that not significant differences wavelength dependence on the $\omega(\lambda)$ for two desert dust origin sources were found. Moreover, the $\omega(\lambda)$ increased slightly with wavelength for both sectors. However, in general the $\omega(\lambda)$ values in the longest wavelengths were lower than those typical for desert dust conditions using sun-photometer measurements (e.g. Dubovik et al., 2002b). Therefore, this fact indicated that important absorbing aerosol has conditioned the mean $\omega(\lambda)$ values in the atmospheric column during desert dust

events arriving from both North African sectors. On the other hand, other authors using different instrumentation have obtained $\omega(\lambda)$ values no coincident with those retrieved in our work during desert dust episodes nearby the Lampedusa Island. For instance, Meloni et al. (2006) showed values for $\omega(\lambda)$ of 0.81±0.05 at 415.6 nm and of 0.94±0.05 at 968.7 nm during desert dust intrusions.
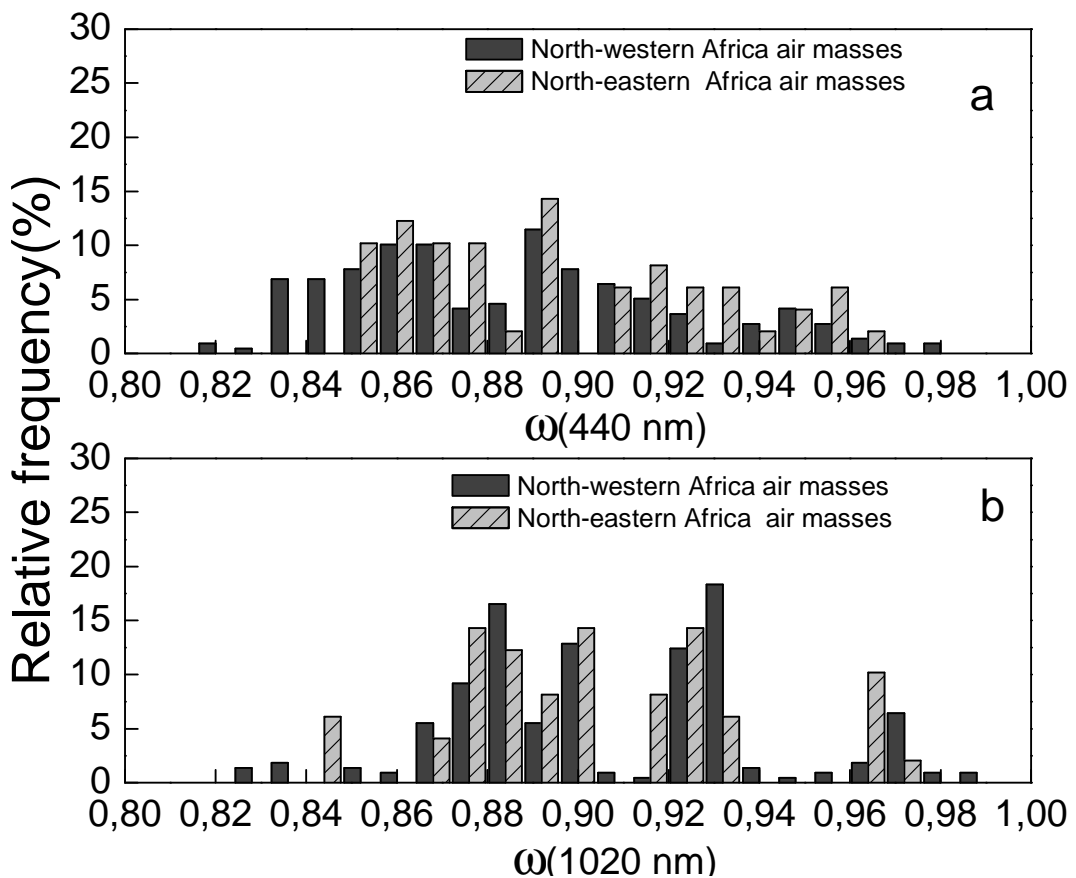
Figure 6.38: Relatives frequencies of a) $\omega(440$ nm), b) $\omega(1020$ nm) during the transport of North Africa air masses for two sectors.

Figures 6.39 (a, b) show the $\omega(\lambda)$ versus wavelength with predominantly coarse aerosol ($\alpha(440$-1020nm)<0.7) and increased contribution of fine aerosol ($\alpha(440$-1020nm)>0.7) for both North African sectors. The $\omega(\lambda)$ for $\alpha(440$-1020nm)<0.7

6. Results and Discussion

decreases towards short wavelengths indicating the presence of iron oxide for both sectors. The $\omega(\lambda)$ for α(440-1020nm)>0.7 decreases towards long wavelengths indicating the presence of anthropogenic pollution aerosols that contain black carbon (Dubovik et al., 2002b). Figures 6.39 (c, d) show ω(440 nm)–ω(1020 nm) versus α(440-1020nm) for two sectors. The data presented in this figure are classified into two different ranges of ω(1020 nm) in order to indicate observations with different levels of absorption at 1020 nm. Strong absorption at 440 nm (low ω(440 nm)) was linked to smaller values of α(440-1020nm) for both sectors. As the contribution from fine particles increases with α(440-1020nm) ranging between 0.5-0.9, the absorption is still strongest at 440 nm. However, the absorption at 1020 nm becomes significant in this range. According to Derimian et al. (2008), this situation is related to mixture of desert dust and pollution. In addition, some observations also showed values of $d\omega > 0$ with α(440-1020nm) higher than 0.9. Therefore, the significant fine mode particles presence conditioned stronger absorption at 1020 nm (low ω(1020nm)) for both desert dust origin sources. It is noteworthy that ω(440 nm)–ω(1020 nm) is weaker for observations with ω(1020 nm) > 0.91 than observations with ω(1020 nm) < 0.91. That is, for similar α(440-1020nm) values there was a wide range of ω(440 nm)–ω(1020 nm) values. In this sense other aerosol properties as the fine mode radius play a fundamental role. In figure 6.34b we have seen that for τ_a values ranging between 0.35 and 0.4 the fine mode radius ranged between 0.12 and 0.2 µm. As the fine mode radius increases then the scattering also increases. Therefore, this variation of the fine mode radius modifies the ω(440 nm) values.
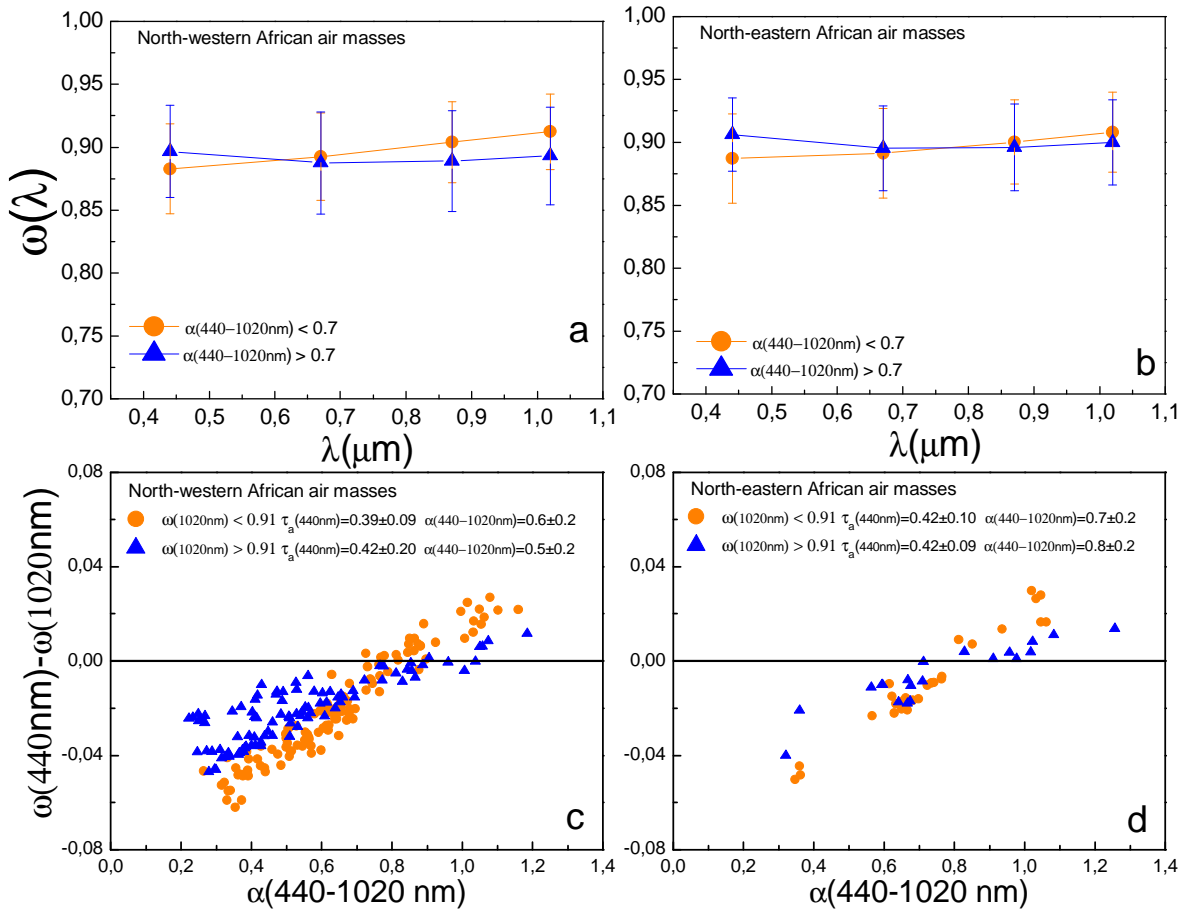
Figure 6.39: Single scattering albedo versus wavelength for a) North-western Africa air masses, b) North-eastern Africa air masses. The $\omega(440nm)$–$\omega(1020nm)$ versus $\alpha(440\text{-}1020nm)$ for c) North-western Africa air masses and d) North-eastern Africa air masses.

Results for the selected study cases are presented in the following subsections. In particular, the dust outbreaks occurred in August 24 and 21, 2011 are analysed in this study. These days were representative over Alborán Island of typical dust events grouped in these two desert dust origin sources.

6. Results and Discussion

Study case of August 24, 2011

Five-day back-trajectories of air masses arriving over Alborán Island at 500, 1500 and 3000 m a.g.l., on August 24 at 12:00 UTC, were calculated using HYSPLIT_4 model including vertical wind (Draxler and Rolph, 2003) (Fig. 6.40a). The back-trajectories for the three levels passed over North-western Africa before reaching Alborán Island. DREAM model (http://www.bsc.es/projects/earthscience/DREAM) forecast is presented in Fig. 6.40b. Their results were in agreement with those provided by NAAPs model (Figure not shown). DREAM model forecast showed the outflow of an aerosol layer from North Africa on 24 August with $\tau_a(550$ nm) values in the range of those obtained using sun-photometer measurements. $\tau_a(\lambda)$ and $\alpha(440\text{-}1020$ nm) values throughout the day are shown in Fig. 6.40c. Many studies have shown that desert dust in the Mediterranean basin is characterized by large $\tau_a(\lambda)$ and small α values (e.g. Pace et al., 2006; Tafuro et al., 2006). Therefore, dust events could be clearly identified from aerosol optical properties values. This analyzed day was representative of air masses transported from the North-western Africa sector. $\tau_a(\lambda)$ and $\alpha(440\text{-}1020$ nm) values indicated the presence of desert dust. The $\tau_a(\lambda)$ analyses shows higher values early in the morning and in the afternoon. A slight maximum was observed around midday for $\alpha(440\text{-}1020$ nm) parameter.
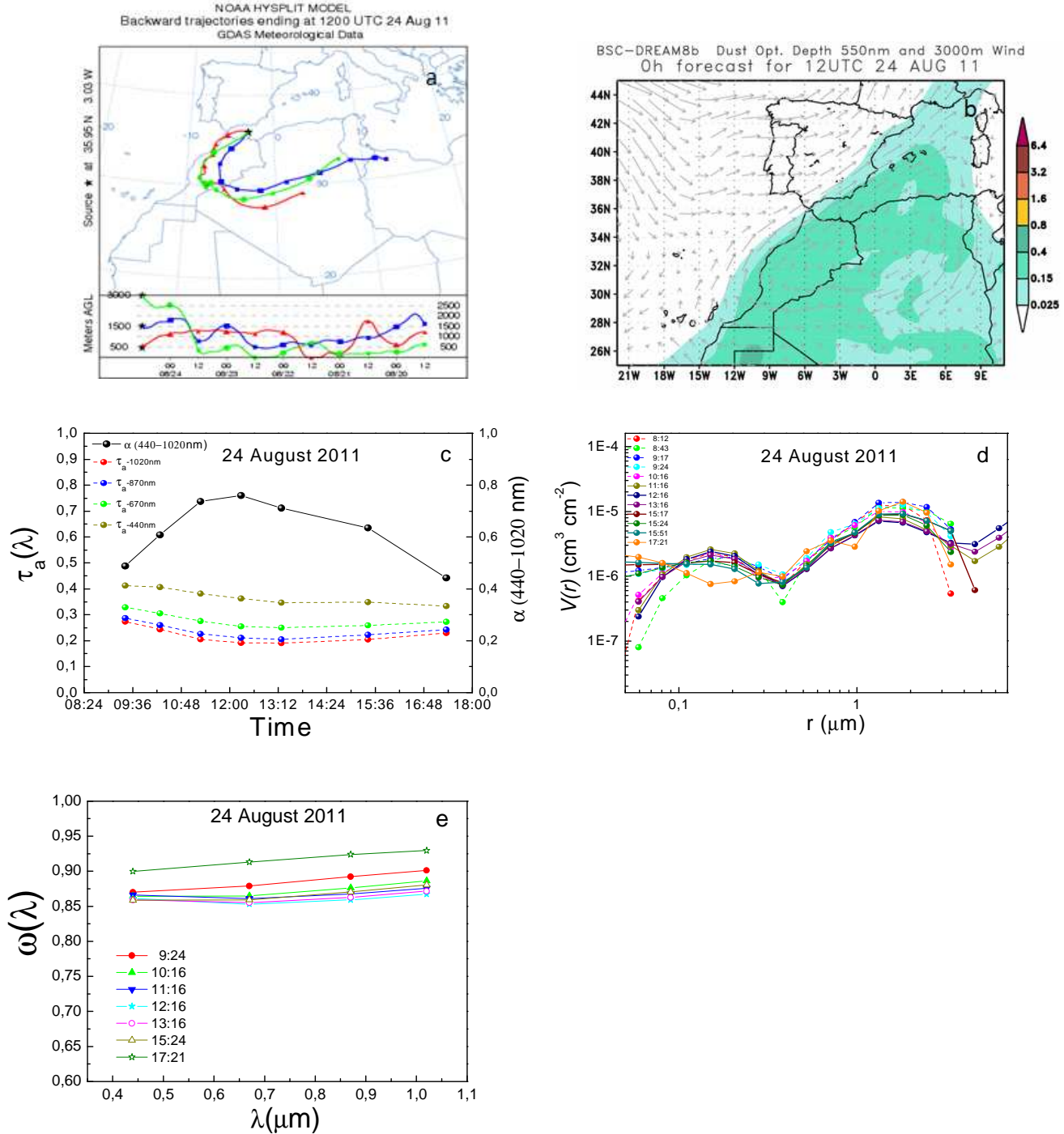
**Figure 6.40:** a) Pathways of the 5-day back-trajectories at 500, 1500 and 3000 m reaching Alboran Island at 12:00 UTC, b) dust optical depth at 550 nm and wind vectors 3000 m computed by DREAM model, c) $\tau_a(\lambda)$ and α(440-1020 nm) as function of time, d) columnar volume size distributions derived from sun-photometer measurements and e) single scattering albedo at 440, 670, 870 and 1020 nm in August 24, 2011.

6. Results and Discussion

Fig.6.40d shows the columnar volume size distributions, *V(r),* retrieved at different day hours. It can be observed that along with coarse mode particles, fine mode particles also contributed to the total aerosol load. The $\omega(\lambda)$ slightly increased with the wavelength as it is characteristic of mineral particles (Fig. 6.40e). However, $\omega(\lambda)$ values decreased in the entire solar spectrum range around midday, in coincidence with maximum values of α(440-1020 nm). The values of this parameter revealed a slight increase of small particles just around midday which is supported for the large values by fine mode size distribution. In addition, higher absorption was found at this time according with lower $\omega(\lambda)$ values when air masses were transported from North-western Africa.

During the night of 24 August, the lidar CALIOP onboard CALIPSO satellite (Cloud-Aerosol Lidar and Infrared Pathfinder Satellite Observation, http://www-calipso.larc.nasa.gov) crossed the Mediterranean Western basin and overpassed the area surrounding the Alborán Island (< 50 km). Following the Scene Classification Algorithm (SCA) based on integrated attenuated backscatter at 532 and 1064 nm and integrated volume depolarization ratio at 532 nm (e.g. Liu et al., 2005), CALIPSO identified a plume of mineral dust particles extending from 0.5 up to 4 km a.s.l. over the Alborán Island around 02:20 UTC (Fig. 6.41). Additionally, the elevated layers located at South-western latitudes from Alborán (over North-western Africa) were classified as a mixture of pure mineral dust and polluted dust at that time. These aerosol plumes characterized by larger extinction-to-backscatter ratio, i.e. containing more absorbing particles, were transported from Africa during the night until reaching Álboran Island. The analysis of back-trajectories and CALIPSO ground-track confirm the North Africa air masses arriving over radiometric station (Fig. 6.41). Therefore, this mixtures between mineral dust and absorbing particles induces a decrease of $\omega(\lambda)$ values over the

Alborán Island. The mixing between desert dust and North African industrial pollutants has already been observed in previous studies (e.g. Rodriguez et al., 2011).
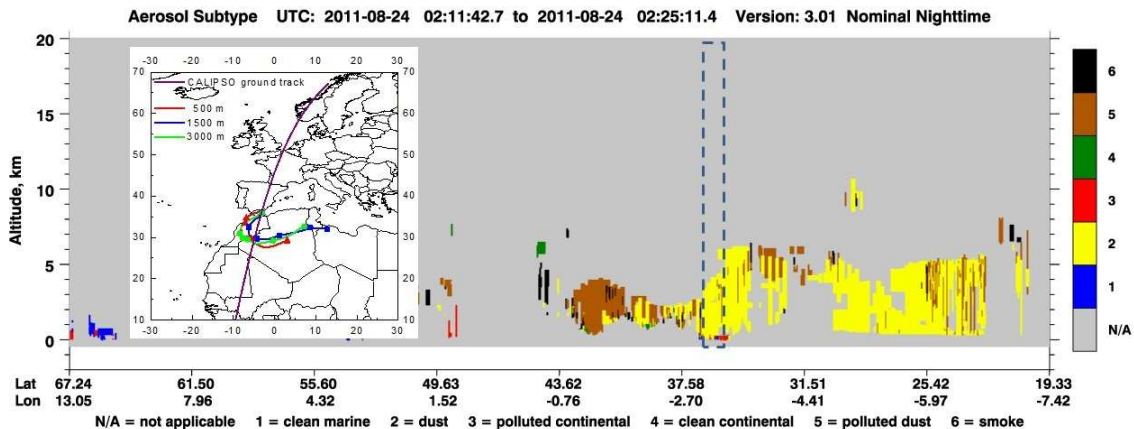
Figure 6.41: Vertical cross section of aerosol types classified by CALIPSO satellite during the nighttime overpass on 24 August 2011 over North-eastern Africa and Europe. The CALIPSO ground track is also included.

Study case of August 21, 2011

Five-day back-trajectories reaching Alborán Island at 500, 1500 and 3000 m a.g.l., on 21 August, at 10:00 UTC are shown in Fig.6.42a. The back-trajectories at 1500 and 3000 m a.g.l originated over the Mediterranean Sea crossed Tunisia and North Algeria. Conversely, the 500 m back-trajectory spent long time over Mediterranean basin before arriving to Alboran Island. This kind of trajectories was assigned previously to the North-eastern Africa sector. DREAM model forecast is shown in Fig. 6.42b. This clearly showed an outflow of desert dust crossing over the monitoring station towards the Iberian Peninsula, with τ_a(550 nm) values up to 0.4. This value was coincident with those obtained by the sun-photometer measurements. τ_a(440nm)

showed values around 0.5, increasing up to 0.7 at 11:00 UTC. α(440-1020nm) presented low values ranging between 0.65-0.75 (Fig. 6.42c). The bimodal feature of *V(r)* indicates that along with the coarse mode, the fine mode size distribution also contributed to the total aerosol load during desert dust events. The evolution of α(440-1020nm) showed a slightly increase during the analysed hours (Fig. 6.42d). $\omega(\lambda)$ slightly increased with the wavelength and this trend remained during the day. However, $\omega(\lambda)$ values decreased in the entire solar spectrum range around 11:00 UTC (Fig. 6.42e). This indicates that more absorbing particles were present at this time.

Finally, these results indicated the coexistence of coarse and fine particles during desert dust events over Alboran Island. More absorption is observed around midday, related to an increase in the fine mode supported by the size distribution and α(440-1020 nm) values. Therefore, absorbing fine particles far away of being reduced during desert dust events are increasing. This could be due to the mixing of mineral particles with absorbing particles in the most industrialized areas of the North African coast.
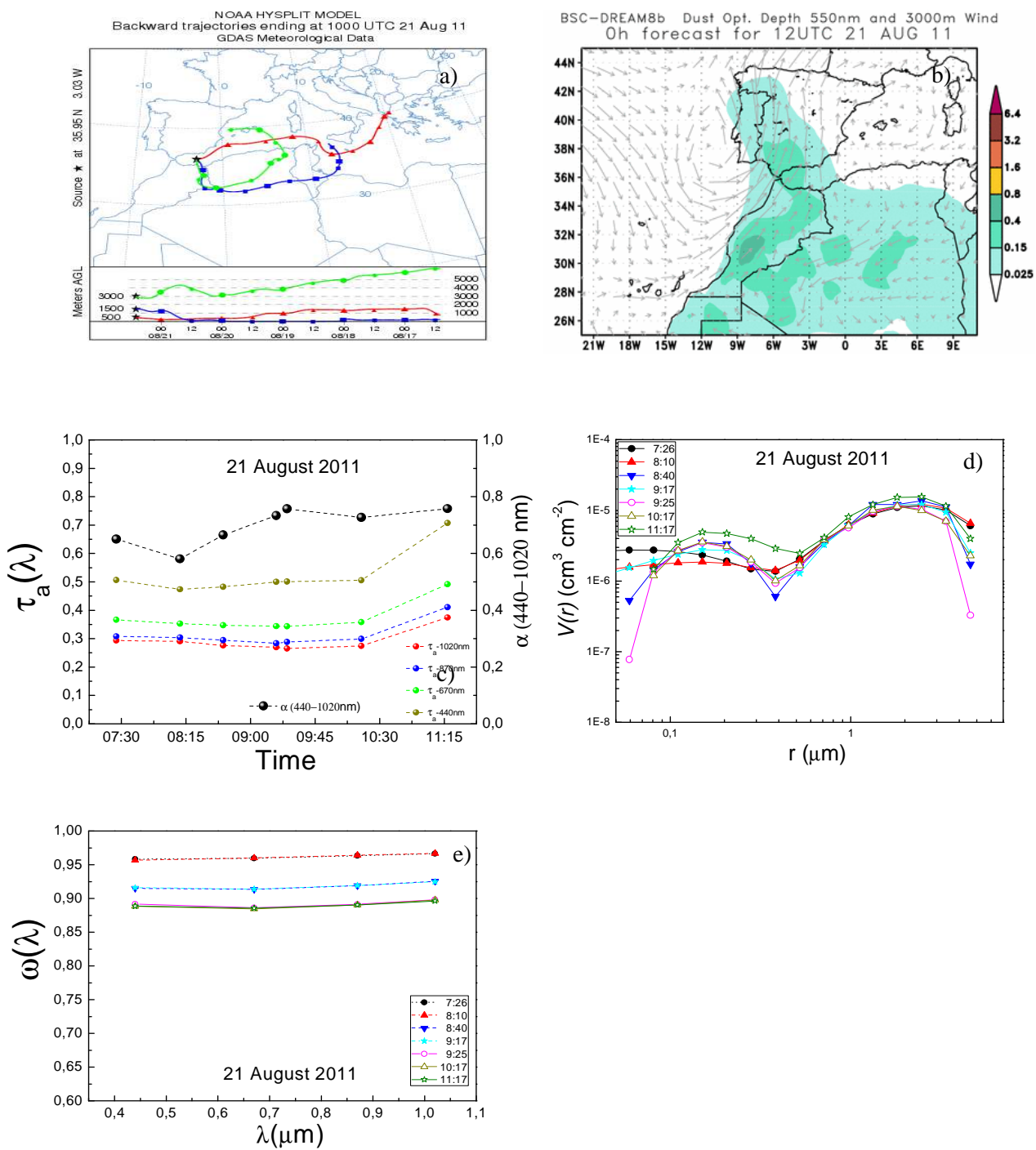
Figure 6.42: a) Pathways of the 5-day back-trajectories at 500, 1500 and 3000 m reaching Alboran Island at 10:00 UTC, b) dust optical depth at 550 nm and wind vectors 3000 m calculated by DREAM model, c) $\tau_a(\lambda)$ and α (440-1020nm) as function of time, d) columnar volume size distributions derived from sun-photometer measurements and e) ω at 440, 670, 870 and 1020 nm in August 21, 2011.

6. Results and Discussion

CHAPTER 7

CONCLUSIONS AND OUTLOOK

7. Conclusions and outlook

The main goal of this PhD thesis has been to analyze the columnar aerosol radiative properties over Granada (Spain) during the African dust events registered from 2005 to 2010, as well as their influence on radiative forcing both at the surface and at the top of the atmosphere (TOA). In order to accomplish this goal, the sun-photometric measurements (extinction and sky radiances) for cloudless days, and considering only desert dust events confirmed by the CALIMA project, have been analyzed.

Major advances presented in this work are related to the implementation and application of a new methodology for deriving atmospheric columnar optical and microphysical properties using sky radiance in principal plane configuration, and considering that the particles are not spherical. The spectral aerosol optical properties are computed using the methodology described by Alados-Arboledas et al. (2003) and Olmo et al. (2008). The principal plane inversion method used is based on the methodology developed by Nakajima et al. (1996) –SKYRAD.PACK-, updated to account for particle non-sphericity in modeling of aerosol properties (Olmo et al., 2008). As input parameters, the inversion code uses the spectral normalized sky radiance and the spectral aerosol optical depth. To eliminate cloud contaminated cases, we applied the triplet stability criteria to the aerosol optical depth measurements, and smoothed sky radiance measurements with a five-point, moving-average. Additionally, the residuals between the measured and computed spectral normalized sky radiances were required to be less than 10%. Also, the sensitivity of the inversion algorithm was checked against simulated data from aerosol models, and the derived aerosol properties were satisfactory compared against well-know AERONET products.

In terms of results, during African desert dust events from 2005 to 2010, the mean values of τ_a(440nm) and α(440-1020nm) at Granada were 0.27±0.15 and 0.42±0.21, respectively. For the entire period a seasonal pattern was found with two

annual peaks in late spring and early summer and September, and a clear decrease in October and February. The high τ_a values and low α values indicated the prevalence of coarse particles during desert dust events. The magnitude of the Angstrom exponent (α) presented low values throughout the year with the lowest ones in spring and summer. The columnar effective aerosol volume size distributions showed bimodal distributions, with the fine and coarse mode radius close to 0.20±0.04 μm and 2.41±1.38 μm, respectively. The most relevant result has been the high mean value of coarse mode volume concentration, which is indicative of its outstanding contribution of dust particles. This mode was evidently dominant during the entire period due to the prevalence of dust particles with relatively large size, leading to a volume concentration ratio (coarse to fine modes) of 11±6. The averaged values of $\omega(\lambda)$ and $g(\lambda)$ were 0.91±0.03 and 0.68±0.02, respectively. These values were consistent with those obtained by other authors in the same study area for desert dust events. However, $\omega(\lambda)$ showed smaller values than those reported in the literature for pure desert dust. The mixing of desert dust with absorbing particles from anthropogenic origin (during all year) and biomass burning contribution (mainly in summer) could explain these low $\omega(\lambda)$ values at the study area.

The analysis of the columnar optical and microphysical aerosol properties during African dust events is carried out far away from the source regions. In this sense, it may produce efficient mixing of mineral particles with other particles from sources in the air masses path. Also, the aerosol properties may change depending on the African dust source regions. Therefore, the aerosol optical and microphysical properties have been classified according to potential sector origin sources and also applying a cluster analysis. Both classification methods agree in that the air masses transport from North Africa toward the South-eastern of the Iberian Peninsula follow three main pathways;

either from Northern Algeria and Tunisia, the Northern of Morocco and over the Sahara region. The two methods also show that the aerosol optical and microphysical properties during North Africa desert dust events over Granada have a weak dependence on the sources origin and pathways. Nevertheless, significant differences are found when air masses are transported from the Sahara area (Sector B and cluster 1 at the 3000 m level). The larger mean value of τ_a(440 nm) and lower mean value of α(440-1020nm) are successfully identified by both methods. Additionally, the sectors methodology and the clusters analysis are in accordance with the slightly lower $\omega(\lambda)$ values obtained when air masses are transported from the Northern of Morocco area (sector A and cluster 2 in the 1500 m level). This result may be probably due to the mixing of desert dust with absorbing pollutants from North African industrial areas. Nevertheless, for the three sectors, $\omega(\lambda)$ values were lower than the values obtained at others locations during desert dust events. This result points out the strong contribution of local anthropogenic aerosol and polluted air masses transported from Mediterranean areas at Granada. The sectors classification and clusters analysis showed that Granada was affected during desert dust intrusions by two particle size modes, where the coarse mode was the dominating mode according to the V_c/V_f ratio values.

Taking into account the previous result, it is interesting to analyze the atmospheric aerosol properties at some distance of its sources before mixing with particles originated in other regions. Alborán Island, located in between the North African coast and the Southern Iberian Peninsula (Western Mediterranean Sea), offers an appropriate place to perform such studies. In this sense, seven months of observations (June 2011 to January 2012) of the aerosol optical and microphysical properties were carried out at this remote Island. To our knowledge, this is the first study over this region using sun-photometer measurements and inversion products in

the almucantar and principal plane configurations. The air masses affecting this area were classified according to three potential origin sources. In this sense, optical properties were grouped according to those potential origin sources. τ_a(440 nm) showed high mean values (0.27±0.12) linked to high mean values of α(440-1020 nm) (1.17±0.33), indicating a large contribution of fine particles when air masses were transported from central Europe and Mediterranean basin sector. Maximum aerosol loads (mean τ_a(440 nm) of 0.38±0.13) in conjunction with the lowest mean value of α(440-1020 nm) with 0.59±0.24, were found for North Africa sector. The cleanest conditions during the whole measurement period were found for North Atlantic Ocean sector, with the lowest mean τ_a(440 nm) value (0.15±0.08) and α(440-1020 nm) value close to 1.11±0.35. An increase in $\tau_a(\lambda)$ showed a shift to larger α values linked to more negative $\delta\alpha$, indicating an increase of the fine fraction parallel to the line of constant fine radius under high $\tau_a(\lambda)$ values for central Europe and Mediterranean basin sector. This classification scheme indicated an extremely large contribution of coarse particles for North Africa sector, being up to 95% of the observations with η<50%, $\alpha < 1$. However, $\delta\alpha$>0.1 indicated a mixed situation between coarse and fine mode of particles for this sector. The small variation in ω(440 nm) for these air masses types suggests an advantage in satellite retrievals of τ_a(440 nm) or other shorter wavelengths of the visible range, since $\omega(\lambda)$ must either be assumed a priori in many satellite retrieval algorithms. The sectors classification method was again applied only when air masses were transported from North Africa. This analysis revealed two mainly airflow patterns toward the Alborán Island: from North-western Africa (78% of cases from North Africa) and North-eastern Africa (22% of cases). High $\tau_a(\lambda)$ values linked to low α values were reproduced for both sectors. However, it should be noted that α values above 1 for the two sectors in North Africa were found, indicating that fine particles

were also transported. The $\omega(\lambda)$ values were similar for both sectors, but with lower mean values than those identified in other studies for desert dust at the longest wavelengths. The $\omega(440\ nm)$-$\omega(1020\ nm)$ difference showed values positives with α (440-1020nm) above 1 for both sectors, which was indicative of stronger absorption by fine particles at 1020 nm. In this sense, aerosol optical properties during two special desert dust events have been analyzed in detail. These properties confirm that mineral particles were mixed with North African industrial pollutants, which imply that aerosol properties are different of those typical of pure desert dust.

In this PhD thesis, we evaluated the aerosol radiative forcing (ARF) at the surface and TOA during African desert dust events over Granada (Southeastern Spain) at temporal scales from daily to seasonal. In addition, the aerosol radiative forcing efficiency (aerosol radiative forcing per unit of aerosol optical depth) was also analyzed according to desert dust sources. For this task, the daily values of the ARF at the surface and TOA were computed by means of the SBDART radiative transfer code. The columnar aerosol properties retrieved from the extinction and the principal plane sky radiance measurements by an AERONET sun-photometer were used as input parameters in the simulations. The global irradiances simulated by the SBDART radiative transfer code have been evaluated by comparison with experimental global irradiance values measured with a CM-11 pyranometer. The agreement was good with a mean bias around 3%. Moreover, the simulated instantaneous solar global irradiances were validated against of those provided by AERONET. In general, the agreement was acceptable between AERONET and SBDART for both downward fluxes at surface and upward fluxes at TOA. The results show that the aerosol optical properties used to estimate ARF in this work appropriately represent the aerosol properties observed during desert dust outbreaks over our study area. The evolution of ARF mean monthly

values (computed from daily ARF values) obtained in this study ranged from -13±8 W/m^2 to -34±15 W/m^2 at the surface, and from -4±3 W/m^2 to -13±7 W/m^2 at TOA. The largest monthly mean values (in absolute term) of ARF both at the surface and TOA were obtained in April, according to the highest mean monthly value of the aerosol optical depth at 440 nm. The mean monthly values of atmospheric ARF (ARF at TOA minus ARF at surface) ranged from +6±4 to +21±12 W/m^2, and the corresponding aerosol atmospheric heating rates, for the entire atmospheric column, range from 0.05±0.04 K/day to 0.19±0.10 K/day. The daily ARF at the surface (TOA) has been classified according to the desert dust sources, being -20±12 (-5±5) W/m^2, -21±9 (-7±5) W/m2 and -18±9 (-6±5) W/m^2 for sectors A (Northern Morocco; Northwestern Algeria), B (Western Sahara, Northwestern Mauritania and Southwestern Algeria), and C (Eastern Algeria, Tunisia), respectively. The Kolmogorov-Smirnov statistical test revealed that there are no significant differences between the daily ARF values at the surface obtained for the different desert dust sources. However, this test showed that daily ARF values at TOA for sector A were significantly different from the other two sectors, likely as a result of the lower values of single scattering albedo (high aerosol absorption) obtained for sector A in comparison to the other sectors. The daily values of aerosol radiative forcing efficiency (ARFE-aerosol radiative forcing per unit of aerosol optical depth at 440 nm) at the surface and TOA were also evaluated according to the desert dust source. The daily mean ARFE values at the surface (TOA) were -74±12 W/m^2 (-17±7 W/m^2) -sector A-, -70±14 W/m^2 (-20±9 W/m^2) -sector B-, and -65±16 W/m^2 (-22±10 W/m^2) -sector C-, being comparable between the three sectors in all seasons.

In our atmospheric station operates routinely in-situ instrumentation for estimating atmospheric aerosol properties on the surface. In this sense, we have

compared the aerosol properties derived in the atmospheric column and at surface for African dust events and dust free days. The scattering and absorption Angström exponent parameters as well as the single scattering albedo during these conditions were evaluated. It is clear from values of scattering Angström exponent in the atmospheric column (SAE^{col}) the significant contribution of large particles during desert dust events. However, in these same conditions, although the single scattering albedo increased with wavelength, this parameter showed lower values than those for pure desert dust cases. In addition, it is noticed that the absorption Angström exponent in the atmospheric column (AAE^{col}) presented a value of 1.5±0.2 for wavelength of 440-1020 nm. In other studies established that AAE values in the range of 1 to 1.6 can be due to the presence of black carbon particles. On the other hand, the FMF (Fine Mode Fraction) was below 50% during desert dust events in atmospheric column. In 51% of cases FMF was 0.25. Finally, the application of a non-parametric test revealed that no significant differences were found for absorption Angström exponent at surface (AAE^{is}) in two situations: with desert dust and dust-free conditions. This result may be due to the relevant contribution of urban absorbing aerosol in this location. Therefore, in view of the small difference of AAE^{is} during desert dust days and dust-free days, and the mean AAE^{col} value of 1.5±0.2 during desert dust outbreaks, this parameter should not be used alone to determine aerosol types without the use of other information (e.g., aerosol size) at ground level in urban locations as Granada with significant anthropogenic aerosol presence

Finally, due to the scarcity of routinely operational ground-based stations with high-quality instrumentation to measure simultaneously UV irradiance and aerosol data during desert dust intrusions, there are few studies that analyze the effects of atmospheric aerosol on UV spectral range during African dust events. Therefore, the influence of desert dust particles on broadband surface UV irradiance weighted by

erythemal action spectrum (UVER) as retrieved by satellite (OMI) and measured by ground-based instruments have been also evaluated. The presence of desert dust particles over the study area causes average reductions of the UVER by about 11% with respect to clear-sky conditions. Reductions larger than 20% are found in 12.5% of all desert dust events analyzed. These results reveal that the desert dust particles markedly affect the propagation of the UV radiation through the atmosphere. The UVER data derived from the OMI satellite instrument are biased high compared the ground-based UVER measurements during the desert dust cases with a mean relative difference of 22%. The analysis of clear-sky cases shows that 8% of the bias can be attributed to the fact that current OMI UV algorithm assumes no absorbing aerosols. Therefore, the effect of desert dust events on the UV irradiance derived from the OMI instrument cannot be neglected for regions like Southern Spain, where the intrusions of the desert dust are frequent. The aerosol absorption bias can be corrected off-line. The post-correction has been tested using an independent dataset and resulted in reduction of the bias from ~21% for operational satellite UVER data to ~13% for corrected data. The remaining positive bias (OMI being higher), indicate additional sources for discrepancy. Thus, OMI -derived UVER data have been shown to be overestimated in locations affected by desert dust. Therefore, reliable estimates of UV in these locations are dependent on the availability of quality assured ground-based measurements.

Future work could improve these results:

- We have found that anthropogenic fine particles play a significant role in the aerosol optical and microphysical properties. It will be interesting to evaluate the radiative effects considering only anthropogenic fine aerosol presence over Granada.

- The aerosol radiative forcing has been computed in shortwave (SW) spectral range. In a future work, this assessment will be extending to longwave spectral range during desert dust events over Granada.

- A comparative study will be performed of the results derived from inversion models using spheroid and sphere particle approximation.

- An automatic method will be implemented in order to check and verify the quality of data in the principal plane sky radiance configuration.

- The aerosol radiative forcing will be computed and analyzed using as input the aerosol optical properties retrieved in the Alborán Island.

- The black carbon and organic carbon in the atmospheric column will be evaluated using sun-photometric measurements during 2005-2012 period.

References

REFERENCES

Alfaro, S.C., Lafon, S., Rajot, J.L., Formenti, P., Gaudichet, A. and Maille, M., (2004), Iron oxides and light absorption by pure desert dust: An experimental study, J. Geophys. Res., 109, D08208, doi:10.1029/2003JD004374.

Andreae, M.O., Schmid, O., Yang, H., Chand, D., Zhen Yu, J., Zeng, L.-M., Zhang, Y.-H., (2008), Optical properties and chemical composition of the atmospheric aerosol in urban Guangzhou, China, Atmos. Environ., 42, 6335-6350.

Alados-Arboledas, L., Olmo, F. J., Alados, I. and Pérez, M., (2000), Parametric models to estimate photosynthetically active radiation in Spain, Agric. For. Meteorol., 101, 187–201, doi:10.1016/S0168-1923(99)00163-X.

Alados-Arboledas, L., Lyamani, H., Olmo, F.J., (2003), Aerosol size properties at Armilla, Granada (Spain), Q. J. R. Meteorol.Soc., 129, 1395-1413.

Alados-Arboledas, L., Olmo, F.J., Ohvril, H., Teral, H., and Arak, M., (1997), Evolution of solar radiative effects of Mount Pinatubo at ground level, Tellus, 49B, 190-198, 1997.

Alados-Arboledas, L., A. Alcántara, F.J. Olmo, J.A. Martínez-Lozano, V. Estellés, V. Cachorro, A.M. Silva, H. Horvath, M. Gangl, A. Díaz, M. Pujadas, J. Lorente, A. Labajo, M. Sorribas, and G. Pavese., (2008), Aerosol columnar properties retrieved from CIMEL radiometers during VELETA 2002, Atmos. Environ., 42, 2654–2667.

Alam, K., Trautmann, T., Blaschke, T., Majid, H., (2012), Aerosol optical and radiative properties during summer and winter seasons over Lahore and Karachi, Atmos. Environ., 50, 234-245.

d'Almeida, G. A., Koepke, P. and Shettle, E. P., (1991), Atmospheric Aerosols: Global Climatology and Radiative Characteristics, A. Deepak Publishing, Hampton, VA.

Anderson, T. L. and Ogren, J. A., (1998), Determining aerosol radiative properties using the TSI 3563 integrating nephelometer, Aerosol. Sci. Tech., 29, 57–69.

Ångtröm, A., (1964), The parameters of atmospheric turbidity, Tellus, 16, 64-75.

References

Antón, M., Cachorro, V. E., Vilaplana, J. M., Toledano, C., Krotkov, N. A., Arola, A., Serrano, A. and, de la Morena, B., (2010), Comparison of UV irradiances from Aura/Ozone Monitoring Instrument (OMI) with Brewer measurements at El Arenosillo (Spain) – Part 1: Analysis of parameter influence, Atmos. Chem. Phys., 10, 5979–5989, doi:10.5194/acp-10-5979-2010.

Antón, M., J. E. Gil, J. Fernández-Gálvez, H. Lyamani, A. Valenzuela, I. Foyo-Moreno, F. J. Olmo, and L. Alados-Arboledas.,(2011); Evaluation of the aerosol forcing efficiency in the UV erythemal range at Granada, Spain, J. Geophys. Res., 116, D20214, doi:10.1029/2011JD016112.

Antón, M., Valenzuela, A., Cazorla, A., Gil, J.E., Fernández-Gálvez, J., Lyamani, H., Foyo-Moreno, I., Olmo, F.J. and Alados-Arboledas, L.,(2012a), Global and diffuse shortwave irradiance during a strong desert dust episode at Granada (Spain), Atmos. Res., 118, 232–239, doi:10.1016/j.atmosres.2012.07.007.

Antón, M., Sorribas, M. , Bennouna, Y., Vilaplana, J.M., Cachorro, V.E., Gröbner, J. and Alados-Arboledas, L., (2012b), Effects of an extreme desert dust event on the spectral ultraviolet irradiance at El Arenosillo (Spain), J. Geophys. Res., 117, D03205, doi:10.1029/2011JD016645.

Arola, A., Kazadzis, S., Krotkov, N., Bais, A., Gröbner, J. and Herman, J.R., (2005), Assessment of TOMS UV bias due to absorbing aerosols, J. Geophys. Res., 110, D23211, doi:10.1029/2005JD005913.

Arola, A., Kazadzis, S., Lindfors, A., Krotkov, N.A., Kujanpä, J. and Tamminen, J., (2009), A new approach to correct for absorbing aerosols in OMI UV, Geophys. Res. Lett., 36, L22805, doi:10.1029/2009GL0411137.

Basart, S., Perez, C., Cuevas, E., Baldasano, J.M., Gobbi, G.P., (2009), Aerosol characterization in Northern Africa, Northeastern Atlantic, Mediterranean Basin and Middle East from direct-sun AERONET observations, Atmos.Chem.Phys., 9, 8265-8282.

Barry, R. G., and Chorley, R. J., (1998), Atmosphere, Weather and Climate, 7th ed., Routledge, Boca Raton, Fla.

References

Bergstrom, R.W., Pilewskie, P., Pommier, J., Rabbette, M., Russell, P.B., Schmid, B., Redemann, J., Higurashi, A., Nakajima, T., Quinn, P.K., (2004), Spectral absorption of solar radiation by aerosols during ACE-Asia, J. Geophys. Res., 109, D19S15, doi:10.1029/2003JD004467.

Bergstrom, R.W., Pilewskie, P., Russell, P.B., Redemann, J., Bond, T.C., Quinn, P.K., Sierau, B., (2007), Spectral absorption properties of atmospheric aerosols, Atmos. Chem. Phys., 7, 5937-5943.

Bhartia, P. K. and Wellemeyer, C., (2002), TOMS-V8 total O3 algorithm, in OMI Algorithm Theoretical Basis Document, vol. II, OMI Ozone Products, edited by P. K. Bhartia, pp. 15– 31, NASA Goddard Space Flight Cent., Greenbelt, Md. (Available at http://eospso.gsfc.nasa.gov/eos_homepage/for_scientists/atbd/index.php)

Bauer, S., Bierwirth, E., Esselborn, M., Petzold, A., Macke, A., Trautmann, T., and Wendisch, M., (2011), Airborne spectral radiation measurements to derive solar radiative forcing of Saharan dust mixed with biomass burning smoke particles, Tellus 63B, 742–750.

Bellantone, V., Carofalo, I., De Tomasi, F., Perrone, M.R., Santese, M., Tafuro, A.M., Turnone, A., (2008), In situ samplings and remote sensing measurements to characterize aerosol properties over South-East Italy, J. Atmos. Oceanic Technol., 25 (8), 1341–1356.

Blanco-Muriel, M., Alarcón-Padilla, D.C., López Moratalla, T., and Lara-Coira, M., (2001), Computing the solar vector, Solar Energy, 70(5), 431-441.

Bodhaine, B.A., (1995), Aerosol absorption measurements at Barrow, Mauna Loa and the south pole, J. Geophys. Res., 100, 8967-8975.

Boi P, Tonna G, Dalu G, Nakajima T, Olivieri B, Pompei A, et al., (1999), Calibration and data elaboration procedure for sky irradiance measurements, Appl. Opt., 38(6), 896–907.

Bond, T. C., Anderson, T. L. and Campbell, D., (1999), Calibration and intercomparison of filter-based measurements of visible light absorption by aerosols, Aerosol Sci. Technol., 30, 582– 600.

References

Boselli, A., Caggiano, R., Cornacchia, C., Madonna, F., Mona, L., Macchiato, M., Pappalardo, G. and Trippetta, S., (2012), Multi-year Sun photometer measurements for aerosol characterization in a Central Mediterranean site, Atmos. Res., 104–105, 98–110, doi:10.1016/ j.atmosres.2011.08.002.

Bösenberg, J., et al., (2003), A European aerosol research lidar network to establish an aerosol climatology, MPI Rep., 348, Max-Planck-Inst. Für Meteorol., Hamburg, Germany.

Boucher, O., Schwartz, S.E., Ackerman, T.P., Anderson, T.L., Bergstrom, B., Bonnel, B., Chylek, P., Dahlback, A., Fouquart, Y., Fu, Q., Halthore, R.N., Haywood, J.M., Iversen, T., Kato, S., Kinne, S., Kirkevag, A., Knapp, K.R., Lacis, A., Laszlo, I., Mishchenko, M.I., Nemesure, S., Ramaswamy, V., Roberts, D.L., Russell, P., Schlesinger, M.E., Stephens, G.L., Wagener, R., Wang, M., Wong, J., Yang, F., (1998), Intercomparison of models representing direct shortwave radiative forcing by sulfate aerosols, J. Geophys. Res., 103, 16979-16998.

Box, M.A. and Deepak, A., (1981), An aproximation to multiple scattering in the Earth's atmosphere: Almucantar radiation formulation, Journal of Atmospheric Science 38, 1037-1048.

Bush, B.C., and Valero, F.P.J., (2003), Surface aerosol radiative forcing at Gosan during the ACE-Asia campaign, J. Geophys. Res., 108, D23, 8660, doi: 10.1029/2002JD003233.

Carofalo, I., Fermo, P., Perrone, M.R., Piazzalunga, A., (2008), Advection patterns and composition of TSP and PM2.5 samples over south-east Italy, Proc. Chem. Eng. Trans., 18, 185–192.

Cachorro, V.E., C. Toledano, N. Prats, M. Sorribas, S. Mogo, A. Berjón, B. Torres, R. Rodrigo, J. de la Rosa, and A. M. De Frutos., (2008), The strongest desert dust intrusion mixed with smoke over the Iberian Peninsula registered with Sun photometry, J. Geophys. Res., 113, D14S04, doi:10.1029/2007JD009582.

Cazorla, A., Olmo, F.J. and Alados-Arboledas, L., (2008), Development of a sky imager for cloud covers assessment, J. Opt. Soc. Am.-A, 25(1), 29-38.

References

Cazorla, A., Shields, J.E., Karr, M.E. , Olmo, F.J., Burden, A. and Alados-Arboledas, L., (2009), Technical Note: Determination of aerosol optical properties by a calibrated sky imager, Atmos. Chem. Phys., 9, 6417–6427, doi:10.5194/acp-9-6417-2009.

Cazorla, A., Bahadur, R., Suski, K. J., Cahill, J. F., Chand, D., Schmid, B., Ramanathan, V., and Prather, K., (2013), Relating aerosol absorption due to soot, organic carbon, and dust to emission sources determined from in-situ chemical measurements, Atmos. Chem. Phys. Discuss., 13, 3451-3483, doi:10.5194/acpd-13-3451-2013.

Clarke, A.D., Shinozuka, Y., Kapustin, V.N., Howell, S., Huebert, B., Doherty, S., Anderson, T., Covert, D., Anderson, J., Hua, X., Moore, K.G., McNaughton, C., Carmichael, G., Weber, R., (2004), Size distributions and mixtures of dust and black carbon aerosol in Asian outflow: Physiochemistry and optical properties, J. Geophys. Res., 109, D15S09, doi:10.1029/2003JD004378.

Collaud Coen, M., Weingartner, E., Schaub, D., Hueglin, C., Corrigan, C., Henning, S., Schwikowski, M., Baltensperger, U., (2004), Saharan dust events at the Jungfraujoch: detection by wavelength dependence of the single scattering albedo and first climatology análisis, Atmos.Chem.Phys., 4, 1–16.

Córdoba-Jabonero, C., Sorribas, M., Guerrero-Rascado, J.L., Adame, JA., Hernandez, Y., Lyamani, H., Cachorro, V., Gil, M., Alados-Arboledas, L., Cuevas, E., de la Morena, B., (2011), Synergetic monitoring of Saharan dust plumes and potential impact on surface: a case study of dust transport from Canary Islands to Iberian Peninsula, Atmos. Chem. Phys., 11(7), 3067-3091.

Derimian, Y., Karnieli, A., Kaufman, Y.J., Andreae, M.O., Andreae, T.W., Dubovik, O., Maenhaut, W., Koren, I., Holben, B.N., (2006), Dust and pollution aerosols over the Negev desert, Israel: Properties, transport, and radiative effect, J. Geophys. Res., 111, D05205, doi:10.1029/2005JD006549.

Derimian, Y., Leon, J.F., Dubovik, O., Chiapello, I., Tanre, D., Sinyuk, A., Auriol, F., Podvin, T., Brogniez, G., Holben, B.N., (2008), Radiative properties of aerosol mixture observed during the dry season 2006 over M'Bour, Senegal (African Monsoon Multidisciplinary Analysis campaign), J. Geophys. Res., 113, D00C09, doi:10.1029/2008JD009904.

References

Díaz, J. P., Expósito, F. J., Torres, C. J., Herrera, F, Prospero, J. M. and Romero, M. C., (2001), Radiative properties of aerosols in Saharan dust outbreaks using ground–based and satellite data: Applications to radiative forcing, J. Geophys. Res., 106, 18403– 18416.

Díaz, A.M., O. E. García, J. P. Díaz, et al., (2007), Aerosol radiative forcing efficiency in the UV region over southeastern Mediterranean: VELETA2002 campaign, J. Geophys. Res., 112, D06213, doi:10.1029/2006JD007348.

Di Biagio, C., di Sarra, A., Meloni, D., Monteleone, F., Piacentino, S. and Sferlazzo, D., (2009), Measurements of Mediterranean aerosol radiative forcing and influence of the single scattering albedo, J. Geophys. Res., 114, D06211, doi:10.1029/2008JD011037.

Di Sarra, A., di Biagio, C., Meloni, D., Monteleone, F., Pace, G., Pugnaghi, S., Sferlazzo, D., (2011), Shortwave and longwave radiative effects of the intense Saharan dust event of 25-26 March 2010 at Lampedusa (Mediterranean Sea), J. Geophys. Res., 116, D23209, doi:10.1029/2011JD016238.

di Sarra, A., Cacciani, M., Chamard, P., Cornwall, C., DeLuisi, J. J., Di Iorio, T., Disterhoft, P., Fiocco, G., Fua, D. and Monteleone, F., (2002), Effects of desert dust and ozone on the ultraviolet irradiance at the Mediterranean island of Lampedusa during PAUR II, J. Geophys. Res., 107(D18), 8135, doi:10.1029/2000JD000139.

Dorling, S. R., Davies, T. D. and Pierce, C. E., (1992), Cluster analysis: A technique for estimating the synoptic meteorological controls on air and precipitation chemistry—Results from Eskdalemuir, south Scotland, Atmos. Environ., 26, 2583–2602.

Draxler, R. R., and Rolph, G., (2003), HYSPLIT (Hybrid Single-Particle Lagrangian Integrated Trajectory) Model, NOAA Air Resour. Lab., Silver Spring, Md. [Available at http://www.arl.noaa.gov/ready/hysplit4. html.]

Dubovik, O., Smirnov, A., Holben, B.N., King, M.D., Kaufman, Y.J., Eck, T.F., I. Slutsker, I., (2000), Accuracy assessment of aerosol optical properties retrieved from Aerosol Robotic Network (AERONET) Sun and sky radiance measurements, J. Geophys. Res, 105, D8, 9791-9806.

References

Dubovik, O., and King M. D., (2000), A flexible inversion algorithm for retrieval of aerosol optical properties from sun and sky radiance measurements, J. Geophys. Res., 105, 20673–20696.

Dubovik O, Holben BN, Lapyonok T, Sinyuk A, Mishchenko M.I., Yang P, and Slutsker, I., (2002a), Non-spherical aerosol retrieval method employing light scattering by spheroids, Geophys. Res. Lett., 29(N10), 1415, doi:10.1029/2001GL014506.

Dubovik, O., Holben, B., Eck, T.F., Smirnov, A., Kaufman, Y.J., King, M.D., Tanre, D., Slutsker, I., (2002b), Variability of absorption and optical properties of key aerosol types observed in worldwide locations, J. Atmos. Sci., 59, 590-608.

Dubovik, O., Sinyuk, A., Lapyonok, T., Holben, B.N., Mishchenko, M., Yang, P., Eck, T.F., Volten, H., Muñoz, O., Veihelmann, B., van der Zande, W.J., Leon, J.F., Sorokin, M., Slutsker, I., (2006), Application of spheroid models to account for aerosol particle nonsphericity in remote sensing of desert dust, J. Geophys. Res., 111, D11208, doi:10.1029/2005JD006619.

Draxler, R. R., and G. Rolph., (2003), HYSPLIT (Hybrid Single-Particle Lagrangian Integrated Trajectory) Model, NOAA Air Resour. Lab., Silver Spring, Md. [Available at http://www.arl.noaa.gov/ready/hysplit4. html.].

Dutton, E. G., Reddy, P., Ryan, S. and DeLuisi, J., (1994), Features and effects of aerosol optical depth observed at Mauna Loa, Hawaii 1982–92, J. Geophys. Res., 99, 8295–8306.

Eck, T.F., Holben, B.N., Sinyuk, A., Pinker, R.T., Goloub, P., Chen, H., Chatenet, B., Li, Z., Singh, R.P., Tripathi, S.N., Reid, J.S., Giles, D.M., Dubovik, O., O'Neill, N.T., Smirnov, A., Wang, P., Xia, X., (2010), Climatological aspects of the optical properties of fine/coarse mode aerosol mixtures, J. Geophys. Res., 115, D19205, doi: 10.1029/2010JD014002.

Eck, T. F., Holben, B. N., Ward, D. E., Dubovik, O., Reid, J. S., Smirnov, A., Mukelabai, M. M., Hsu, N. C., O'Neill, N. T., Slutsker, I., (2001a), Characterization of the optical properties of biomass burning aerosols in Zambia during the 1997 ZIBBEE field campaign, J. Geophys. Res., 106, 3425–3448.

References

Eck, T. F., Holben, B. N., Dubovik, O., Smirnov, A., Slutsker, I., Lobert, J. M., Ramanathan, V., (2001b), Column integrated aerosol optical properties over Maldives during NE monsoon for 1998–2000, J. Geophys. Res., 106, 28 555–28 566.

El-Askary, H., Farouk, R., Ichoku, C., Kafatos, M., (2009), Transport of dust and anthropogenic aerosols across Alexandria, Egypt. Ann. Geophys., 27, 2869-2879.

Escudero, M., Castillo, S., Querol, X., Avila, A., Alarcón, M., Viana, M.M., Alastuey, A., Cuevas, E., Rodríguez, S., (2005), Wet and dry African dust episodes over eastern Spain, J. Geophys. Res, 110, 1-15.

Escudero, M., Stein, A.F., Draxler, R.R., Querol, X., Alastuey, A., Castillo, S., Avila, A., (2011), Source apportionment for African dust outbreaks over the Western Mediterranean using the HYSPLIT model, Atmos. Res., 99, 518-527.

Estellés, V., Utrillas, M. P., Martínez-Lozano, J. A., Alcántara, A., Alados-Arboledas, L., Olmo, F. J., Lorente, J., de Cabo, X., Cachorro, V., Horvath, H., Labajo, A., Sorribas, M., Díaz, J. P., Díaz, A. M., Silva, A. M., Elías, T., Pujadas, M., Rodrigues, J. A., Cañada, J., García, Y., (2006), Intercomparison of spectroradiometers and Sun photometers for the determination of the aerosol optical depth during the VELETA-2002 field campaign, J. Geophys. Res., 111, D17207, doi:10.1029/2005JD006047.

Estellés, V., Martinez-Lozano, J.A., Utrillas, M.A.P., (2007), Influence of air mass history on the columnar aerosol properties at Valencia, Spain, J. Geophys. Res, 112, D15211, doi:10.1029/2007JD008593.

Estellés, V., Campanelli, M., Utrillas, M. P., Expósito, F. and Martínez-Lozano, J. A., (2012), Comparison of AERONET and SKYRAD 4.2 inversion products retrieved from a Cimel CE318 sunphotometer, Atmos. Meas. Tech., 5, 569–579.

Falkovich, A. H., Gomez, E., Lewin, Z., Formenti, P., & Rudich,Y., (2001), Analysis of individual dust particles, J. Geophys. Res., 106(D16), 18029–18036.

Foster, P., Ramaswamy, V., Artaxo, P., Berntsen, T., Betts, R., Fahey, D. W., Haywood, J., Lean, J., Lowe, D. C., Myhre, G., Nganga, J., Prinn, R., Raga, G., Schulz, M., and Van Dorland, R., (2007), Changes in Atmospheric Constituents and in Radiative Forcing, in: Climate Change 2007: The Physical Science Basis, Contribution of Working Group I to the Fourth Assessment Report of the Intergovernmental Panel on

References

Climate Change, edited by: Solomon, S., Qin, D., Manning, M., Chen, Z., Marquis, M. , Averyt, K. B., Tignor, M., and Miller, H. L., Cambridge University Press, Cambridge, United Kingdom and New York, NY, USA.

Fu, Q., Zhuang, G., Li, J., Huang, K., Wang, Q., Zhang, R., Fu, J., Lu, T., Chen, M., Wang, Q., Chen, Y., Xu, C., Hou, B., (2010), Source, long-range transport, and characteristics of a heavy dust pollution event in Shanghai, J. Geophys. Res. 115, D00K29, 12 doi:10.1029/2009JD013208.

Gangoiti, G., Alonso, L., Navazo, M., García, J. A., and Millán, M. M., (2006), North African soil dust and European pollution transport to America during the warm season: Hidden links shown by a passive tracer simulation, J. Geophys. Res., 111, D10109, doi:10.1029/2005JD005941.

García, O. E., Díaz, A. M., Expósito, F. J., Díaz, J. P., Gröbner, J. and Fioletov, V. E., (2006), Cloudless aerosol forcing efficiency in the UV region from AERONET and WOUDC databases, Geophys. Res. Lett., 33, L23803, doi:10.1029/2006GL026794.

García, O. E., Díaz, A. M., Expósito, F. J. and Díaz, J. P., (2009), Aerosol radiative forcing and forcing efficiency in the UVB for regions affected by Saharan and Asian mineral dust, J. Atmos. Sc., 66, 1033-1040, doi: 10.1175/2008JAS2816.1.

Garcia, O.E., Exposito, F.J., Diaz, J.P., Diaz, A.M., (2011), Radiative forcing under mixed aerosol conditions, J. Geophys. Res., 116, D01201, doi:10. 1029/2009JD013625.

Gerasopoulos, E., Andreae, M.O., Zerefos, C.S., Andreae, T.W., Balis, D., Formenti, P., Merlet, P., Amiridis, V., Papastefanou, C., (2003), Climatological aspects of aerosol optical properties in Northern Greece, Atmos. Chem. Phys., 3, 2025–2041.

Gerasopoulos, E., Kouvarakis, G., Babasakalis, P., Vrekoussis, M., Putaud, J.P., Mihalopoulos, N., (2006), Origin and variability of particulate matter (PM10) mass concentrations over the Eastern Mediterranean, Atmos. Environ., 40, 4679-4690.

Gerasopoulos, E., Kokkalis, P., Amiridis, V., Liakakou, E., Perez, C., Haustein, K., Eleftheratos, K., Andreae, M.O., Andreae, T.W., Zerefos, C.S., (2009), Dust specific extinction cross-sections over the Eastern Mediterranean using the BSC-DREAM model

and sun photometer data: the case of urban environments, Annales Geophysicae 27, 2903-2912.

Giles, D. M., et al. (2011a), Aerosol properties over the Indo!Gangetic Plain: A mesoscale perspective from the TIGERZ experiment, J. Geophys. Res., 116, D18203, doi:10.1029/2011JD015809.

Giles, D. M., Holben, B. N., Eck, T. F., Sinyuk, A., Smirnov, A., Slutsker, I., Dickerson, R. R., Thompson, A. M., Schafer, J. S., (2012), An analysis of AERONET aerosol absorption properties and classifications representative of aerosol source regions, J. Geophys. Res., 117, D17203, doi:10.1029/2012JD018127.

Guerrero-Rascado, J.L., Ruiz, B., Alados-Arboledas, L., (2008), Multi-spectral Lidar characterization of the vertical structure of Saharan dust aerosol over southern Spain, Atmos. Environ., 42, 2668-2681.

Guerrero-Rascado, J.L., Olmo, F.J., Aviles-Rodriguez, I., Navas-Guzman, F., Perez-Ramirez, D., Lyamani, H., Alados Arboledas, L., (2009), Extreme Saharan dust event over the southern Iberian Peninsula in september 2007: active and passive remote sensing from surface and satellite, Atmos. Chem. Phys., 9, 8453-8469.

Gueymard, C.A., (2001), Parameterized transmittance model for direct beam and circumsolar, 2001,

spectral irradiance, Solar Energy, 71(5):325–346.

Gobbi, G.P., Kaufman, Y.J., Koren, I., Eck, T.F., (2007), Classification of aerosol properties derived from AERONET direct sun data, Atmos. Chem. Phys., 7, 453-458.

Gomez-Amo, J.L., Pinti, V., Di Iorio, T., di Sarra, A., Meloni, D., Becagli, S., Bellantone, V., Cacciani, M., Fua, D., Perrone, M.R., (2011), The June 2007 Saharan dust event in the central Mediterranean: Observations and radiative effects in marine, urban, and sub-urban environments, Atmos. Environ., 45, 5385-5393.

Goody, R.M., and Yung, Y.L., (1989), Atmospheric Radiation, 2nd ed, Theoretical Basis, Clarendon, Oxford.

Goudie, A. S. and Middleton, N. J., (2001), Saharan dust storms: nature and consequences, Earth-Science Reviews, 56(1-4), 179-204.

References

Grassl, H., (1971), Calculated circumsolar radiation as a function of aerosol type, field of view, wavelength, and optical depth, Appl. Opt. 10, 2542–2543.

Gu, Y., Liou, K.N., Chen, W., Liao, H., (2010), Direct climate effect of black carbon in China and its impact on dust storms, J. Geophys. Res., 115, D00K14, 12, doi:10.1029/2009JD013427.

Hand, V., Capes, G., Vaughan, D., Formenti, P., Jim M. Haywood, J. and Coe, H., (2010), Evidence of internal mixing of African dust and biomass burning particles by individual particle analysis using electron beam techniques, J. Geophys., Res 115, D13301, doi:10.1029/2009JD012938.

Harrison, L.J., Michalsky, J., (1994), Automated multi-filter rotating shadow-band radiometer: An instrument for optical depth and radiation measurements, Applied Optics 33, 5118-5125.

Harrys, J., Draxler, R. R. and Oltmans, S. J., (2005), Trajectory model sensitivity to differences in input data and vertical transport method, J. Geophys. Res., 110, D14109, doi:10.1029/2004JD005750.

Haywood, J., Ramaswamy, V., and Soden, B., (1999), Tropospheric aerosol climate forcing in clear-sky satellite observation over the oceans, Science, 283, 1299–1303.

Hegg, D.A., Ferek, R.J., Hobbs, P.V., (1993), Aerosol size distribution in the boundary layer of the North Atlantic ocean, J. Geophys., Res., 98, 8841-8846.

Höller, R., Ito, K., Tohno, S., kasahara, M., (2003), Wavelength-dependent aerosol single-scattering albedo: measurements and model calculations for a coastal site near the Sea of Japan during ACE-Asia, J. Geophys., Res., 108 (D23), 8648.

Holben, B. N., Eck, T. F. and Fraser, R. S., (1991), Temporal and spatial variability of aerosol optical depth in the Sahel region in relation to vegetation remote sensing, Int. J. Remote Sens., 12(6), 1147–1163, doi:10.1080/ 01431169108929719.

Holben, B.N., Eck, T.F., Slutsker, I., Tanre, D., Buis, J.P., Setzer, A., Vermote, E., Reagan, J.A., Kaufman, Y.J., Nakajima, T., Lavenu, F., Jankowiak, I., Smirnov, A., (1998), AERONET - A federated instrument network and data archive for aerosol characterization, Remote Sens, Environ., 66, 1-16.

References

Holben, B. N., et al., (2001), An emerging ground!based aerosol climatology: Aerosol optical depth from AERONET, J. Geophys. Res., 106(D11), 12,067–12,097, doi:10.1029/2001JD900014.

Holben, B.N., Tanré, D., Smirnov, A., Eck, T.F., Slutsker, I., Abuhassan, N., Newcomb, W.W., Schafer, J., Chatenet, B., Lavenue, F., Kaufman, Y.J., Vande-Castle, J., Setzer, A., Markham, B., Clark, D., Frouin, R., Halthore, R., Karnieli, A., O'Neill, N.T., Pietras, C., Pinker, R.T., Voss, K. and Zibordi, G., (2001), An emerging ground-based aerosol climatology: Aerosol optical depth from AERONET, J. Geophys. Res., 106(D11):12067–12098, doi: 10.1029/2001JD900014.

Holben, B. N., Eck, T. F., Slutsker, I., Smirnov, A., Sinyuk, A., Schafer, J., Giles,D. and Dubovik, O., (2006), AERONET's Version 2.0 quality assurance criteria - art. no. 64080 Q. In Remote Sensing of the Atmosphere and Clouds (edited by Tsay, SC and Nakajima, T and Singh, RP and Sridharan, R), vol. 6408 of PROCEEDINGS OF THE SOCIETY OF PHOTO-OPTICAL INSTRUMENTATION ENGINEERS (SPIE), page Q4080. 2006. ISBN 978-0-8194-6515-3. ISSN 0277-786X, Conference on Remote Sensing of the Atmosphere and Clouds, Goa, INDIA, NOV 13-16.

Horvath, H., (1993), Atmospheric light absorption- a review, Atmos. Environ., 27, 293–317.

Huang, J., Fu, Q., Su, J., Tang, Q., Minnis, P., Hu, Y., Yi, Y., Zhao, Q., (2009), Taklimakan dust aerosol radiative heating derived from CALIPSO observations using the Fu-Liou radiation model with CERES constraints, Atmos. Chem. Phys., 9, 4011-4021.

Ialongo, I., Casale, G.R. and Siani, A.M., (2008), Comparison of total ozone and erythemal UV data from OMI with ground-based measurements at Rome station, Atmos. Chem. Phys., 8, 3283–3289, doi:10.5194/acp-8-3283-2008.

Iwasaka,Y., Shi, G.-Y.,Yamada, M., Matsuki, A., Trochkine, D., Kim,Y. S. et al., (2003), Importance of dust particles in the free troposphere over the Taklaman desert: Electron microscopic experiments of particles collected with a baloonborne particle impactor at Dunhunag, China, J. Geophys. Res., 108(D23), 8644.

References

Jaenicke, R., (1988), Aerosol Physics and Chemistry in Zahlenwerte und Funktionen aud naturwissenschaft und Technik, Landolt Börnstein Group 5 (Vol. 4, subvolume b), Physikalische und chemische Eigenschaften der Luft. Berlin, Germany: Springer.

Kaaden, N., Massling, A., Schladitz, A., M¨uller, T., Kandler, K. Schütz, L., Weinzierl, B., Petzold, A., Tesche, M., Leinert, S., Deutscher, C., Ebert, M., Weinbruch, S. and Wiedensohler, A., (2009), State of mixing, shape factor, number size distribution, and hygroscopic growth of the saharan anthropogenic and mineral dust aerosol at Tinfou, Morocco, Tellus 61B, doi:10.1111/j.1600-0889.2008.00388.x.

Kalashnikova, O.V., Mills, F.P., Eldering, A., and Anderson, D., (2007), Application of satellite and ground-based data to investigate the UV radiative effects of Australian aerosols, Remote Sensing of Environment, 107, 65–80.

Kalliskota, S., Kaurola, J., Taalas, P., Herman, J., Celarier, E. and Krotkov, N., (2000), Comparison of daily UV doses estimated from Nimbus 7/TOMS measurements and ground-based spectroradiometer data, J. Geophys. Res., 105, 4273–4277.

Kandler, K., Benker, N., Bundke, U., Cuevas, E., Ebert, M., Knippertz, P., Rodríguez, S., Schützd, L., Weinbruch, S., (2007), Chemical composition and complex refractive index of Saharan Mineral Dust at Izaña, Tenerife (Spain) derived by electron microscopy, Atmos. Environ., 41, 8058–8074.

Kaskaoutis D.G., Kosmopoulos P.G., Kambezidis H.D., Nastos P.T., (2010), Identification of the aerosol types over Athens, Greece: The influence of air-mass transport, Adv. Meteorol., 168346, DOI: 10.1155/2010/168346.

Kazadzis, S., Kouremeti, N., Bais, A., Kazantzidis, A. and Meleti, C., (2009), Aerosol forcing efficiency in the UVA region from spectral solar irradiance measurements at an urban environment, Ann. Geophys., 27, 2515–2522, doi:10.5194/angeo-27-2515-2009.

Kaufman, Y. J., Setzer, A., Ward, D., Tanre, D., Holben, B. N., Menzel, P., Pereira, M. C. and Rasmussen, R., (1992), Biomass Burning Airborne and Spaceborne Experiment in the Amazonas (BASE-A), J. Geophys. Res., 97(D13), 14,581–14,599, doi:10.1029/92JD00275.

Kaufman, Y.J., (1993), Aerosol optical thickness and atmospheric path radiance, J. Geophys. Res., 98, 2677-2692.

References

Kim, D.H., et al.,(2004), Aerosol optical properties over east Asia determined from ground-based sky radiation measurement. J. Geophys. Res.,109(D02209).

Kim, D. H., Sohn, B. J., Nakajima, T., and Takamura, T., (2005), Aerosol radiative forcing over east Asia determined from ground-based solar radiation measurements, J. Geophys. Res., 110, D10S22, doi:10.1029/ 2004JD004678.

Kim, D., Chin, M., Yu, H., Eck, T. F., Sinyuk, A., Smirnov, A. and Holben, B. N., (2011), Dust optical properties over North Africa and Arabian Peninsula derived from the AERONET dataset, Atmos. Chem. Phys., 11, 10,733–10,741, doi:10.5194/acp-11-10733-2011.

Kinne, S., (2009), Climatologies of cloud related aerosols: Part 1: Particle number and size, in Clouds in the Perturbed Climate System, edited by J. Heintzenberg & R. J. Charlson, chap. 3, pp. 37 – 58, MIT Press, Cambridge, Mass.

Kneizys FX, Shettle EP, Abreu LW, Chetwind JH, Anderson GP, Gallery WO, et al., (1988), Users guide to LOWTRAN7, Environmental research paper 1010. Bedford, MA: US Air Force Geophys. Lab.

Knippertz, P., A. Ansmann, et al., (2009), Dust mobilization and transport in the northern Sahara during SAMUM 2006 - A meteorological overview, Tellus Series B: Chemical and Physical Meteorology 61(1), 12-31.

Knippertz, P., Ansmann, A., Althausen, D., Müller, D., Tesche, M. and co-authors, (2009), Dust mobilization and transport in the Northern Sahara during SAMUM 2006—a meteorological overview, Tellus 61B, 12–31.

Koren, I., Ganor, E., Joseph, J.H., (2001), On the relation between size and shape of desert dust aerosol, J. Geophys. Res., 106, 18047-18054.

Kobayashi, E., Uchiyama, A., Yamazaki, A. and Kudo, R., (2010), Retrieval of Aerosol Optical Properties Based on the Spheroid Model, J. Meteor. Society of Japan, 88, 847-856.

Koepke, P., et al., (1998), Comparison of models used for UV index calculations, Photochem. Photobiol., 67, 657–662.

References

Kokhanovsky, A.A., Budak, V.P., Cornet, C., Duan, M., Emde, C., Katsev, I.L., Klyukov, D.A., Korkin, S.V., C-Labonnote, L., Mayer, B., Min, Q., Nakajima, T., Ota, Y., Prikhach, A.S., Rozanov, V., Yokota, T., Zege, E.P., (2010), Benchmark results in vector atmospheric radiative transfer, J. Quant. Spectrosc. Radiat. Transfer., 111 (12-13), 1931-1946.

Krotkov, N. A., P.K. Barthia, J.R. Herman, V. Fioletov, and Kerr, J., (1998), Satellite estimation of spectral surface UV irradiance in the presence of tropospheric aerosols, J. Geophys. Res., 103, 8779–8793.

Krotkov, N. A., J.R. Herman, P.K. Barthia, V. Fioletov, and Ahmad, Z., (2001), Satellite estimation of spectral surface UV irradiance 2, Effects of homogeneous clouds and snow, J. Geophys. Res., 106, 11743–11759.

Krotkov, N. A., Barthia, P.K., Herman, J.R., Slusser, J., Scott, G., Labow, G., Vasilkov, A.P., Eck, T.F., Dubovik, O. and Holben, B.N., (2005), Aerosol ultraviolet absorption experiment (2000 to 2004), part 2: Absorption optical thickness, refractive index, and single scattering albedo, Opt. Eng., 44(4), 041005, doi:10.1117/1.1886819.

Kubilay, N., Cokacar, T., Oguz, T., (2003), Optical properties of mineral dust outbreaks over the northeastern Mediterranean, J. Geophys. Res., 108, D21, 4666, doi:10.1029/2003JD003798.

Kudish, A., Wolf, D. and Machalv, Y., (1983), Solar radiation data for Beer Sheva, Israel, Sol. Energy, 30, 33–37.

Lack, D. A. and Cappa, C. D., (2010), Impact of brown and clear carbon on light absorption enhancement, single scatter albedo and absorption wavelength dependence of black carbon, Atmos. Chem. Phys., 10, 4207–4220.

Lewis, K., Arnott, W. P., Moosmüller, H., Wold, C. E., (2008), Strong spectral variation of biomass smoke light absorption and single scattering albedo observed with a novel dual-wavelength photoacoustic instrument, J. Geophys. Res., 113, D16203, doi:10.1029/2007JD009699.

Li, Z., Goloub, P., Devaux, C., Gu, X., Qiao, Y., Zhao, F., Chen, H., (2004), Aerosol polarized phase function and single scattering albedo retrieved from ground-based measurements, Atmos. Res., 71, 233-241.

References

Liou, K.N., (1992), An introduction to Atmospheric Radiation, Elsevier, New York, 583 pp.

Lucht, W., and Roujean, J. L., (2000), Consideration in parametric modeling of BRDF and albedo from multi-angular satellite sensors observations, Remote Sens. Rev., 18, 343– 379.

Lyamani, H., Olmo, F.J., Alados-Arboledas, L., (2005), Saharan dust outbreak over southeastern Spain as detected by sun photometer, Atmos. Environ., 39, 7276-7284.

Lyamani, H., Olmo, F. J., Alcántara, A. and Alados-Arboledas, L., (2006a), Atmospheric aerosols during the 2003 heat wave in southeastern Spain I: Spectral optical depth, Atmos, Environ., 40-33, 6453-6464.

Lyamani, H., Olmo, F. J., Alcántara, A. and Alados-Arboledas, L., (2006b), Atmospheric aerosols during the 2003 heat wave in southeastern Spain II: Microphysical columnar properties and radiative forcing, Atmos. Environ., 40, 6465-6476.

Lyamani, H., Olmo, F.J., Alados-Arboledas, L., (2010), Physical and optical properties of aerosols over an urban location in Spain: seasonal and diurnal variability, Atmos. Chem. Phys., 10, 239-254.

Madronich, S., (2007), Analytic formula for the clear-sky UV index, Photochem. Photobiol., 83(6), 1537–1538, doi:10.1111/j.1751-1097.2007.00200.x.

Mladenov, N., Alados-Arboledas, L., Olmo, F.J., Lyamani, H., Delgado, A., Molina, A., Reche, I., (2011), Applications of optical spectroscopy and stable isotope analyses to organic aerosol source discrimination in an urban area. Atmos. Environ., 45, 1960-1969.

Mattis, I., Janenisch, V., Müller, D., Franke, K. and Ansmann, A., (2000), Classification of particle extinction profiles derived within the framework of the German lidar network by the use of cluster analysis of back trajectories, in Lidar Remote Sensing of the Atmosphere, edited by A. Dabas, C. Loth, and J. Pelon, pp. 211–214, Ed. Ecole Polytech., Palaiseau, France.

McKinlay, A.F., and Diffey, B.L., (1987), A reference spectrum for ultraviolet induced erythema in human skin, CIE Journal, 6, 21-27.

References

Meloni, D., Marenco, F. and di Sarra, A., (2003), Ultraviolet radiation and aerosol monitoring at Lampedusa, Italy, Ann. Geophys., 46, 373–383.

Meloni, D., di Sarra, A., Di Iorio, T. and Fiocco G., (2005), Influence of the vertical profile of Saharan dust on the visible direct radiative forcing, J. Quant. Spectrosc. Radiat. Transfer, 93, 397–413.

Meloni, D., di Sarra, A., Pace, G., Monteleone, F., (2006), Aerosol optical properties at Lampedusa (Central Mediterranean): 2. Determination of single scattering albedo at two wavelengths for different aerosol types, Atmos. Chem. Phys., 6, 715-727.

Meloni, D., di Sarra, A., Monteleone, F., Pace, G., Piacentino, S., Sferlazzo, D.M., (2008), Seasonal transport patterns of intense Saharan dust events at the Mediterranean island of Lampedusa, Atmos. Res., 88, 134-148.

Mischalsky, J.J., (1988), The astronomical almanac's algorithm for approximate solar position (1950-2005), Solar Energy, 40(3), 227-235.

Mishchenko MI., (1993), Light scattering by size-shape distributions of randomly oriented axially symmetric particles of a size comparable to a wavelength, Appl. Opt., 32, 4652–4666.

Mishchenko MI, Travis LD, Kahn RA, West RA., (1997), Modeling phase functions for dust like tropospheric aerosols using a shape mixture of randomly oriented polydisperse spheroids, J. Geophys. Res., 102(D14), 16831–16848.

Moody, E.G., King, M. D., Platnick, S., Schaaf C.B., Gao F., (2005), Spatially complete global spectral surface albedos: value-added datasets derived from Terra MODIS land products, IEEE Transactions on Geosciences and Remote Sensing, 43, 144-158.

Myhre, G., (2009), Consistency Between Satellite-Derived and Modeled Estimates of the Direct Aerosol Effect, Science 325, 187–190.

Müller, T., Schladitz, A., Massling, A., Kaaden, N., Kandler, K. and coauthors, (2009), Spectral absorption coefficients and imaginary parts of refractive indices of Saharan dust during SAMUM-1,Tellus 61B, 78–95.

References

Muñoz, O., Volten, H., de Haan, J.F., Vassen, W., Hovenier, J.W., (2001), Experimental determination of scattering matrices of randomly oriented fly ash and clay particles at 442 and 633 nm, J. Geophys. Res., 106, 22833-22844.

Myhre, G., Grini, A., Haywood, J. M., Stordal, F., Chatenet, B., Tanre D., Sundet, J. K. and Isaksen, I. S. A., (2003), Modeling the radiative impact of mineral dust during the Saharan Dust Experiment (SHADE) campaign, J. Geophys. Res., 108, 8579, doi:10.1029/2002JD002566.

Nakajima, T., Tonna, G., Rao, R.Z., Boi, P., Kaufman, Y., Holben, B., (1996), Use of sky brightness measurements from ground for remote sensing of particulate polydispersions, Appl. Opt., 35, 2672-2686.

O'Dowd, C. D., Lowe, J. A., and Smith, M. H., (1999), Coupling sea-salt and sulphate interactions and its impact pn cloud droplet concentration predications, Geophys. Res. Lett., 26, 1311–1314, doi:10.1029/1999GL900231.

Olmo, F.J., Tovar, J., Alados-Arboledas, L., Okulov, O., An Ohvril, H.O., (1999), A comparison of ground level solar radiative effects of recent volcanic eruptions, Atmos. Environ., 33, 4589-4596.

Olmo, F.J., Quirantes, A., Alcantara, A., Lyamani, H., Alados-Arboledas, L., (2006), Preliminary results of a non-spherical aerosol method for the retrieval of the atmospheric aerosol optical properties, J. Quant. Spectrosc. Radiat. Transfer., 100, 305-314.

Olmo, F.J., Quirantes, A., Lara, V., Lyamani, H., Alados-Arboledas, L., (2008), Aerosol optical properties assessed by an inversion method using the solar principal plane for non-spherical particles, J. Quant. Spectrosc. Radiat. Transfer., 109, 1504-1516.

Otto, S., Bierwirth, E., Weinzierl, B., Kandler, K., Esselborn, M., Tesche, M., Schladitz, A., Wendisch, M. and Trautmann, T., (2009), Solar radiative effects of a Saharan dust plume observed during SAMUM assuming spheroidal model particles, Tellus 61B, 270–296.

Pace, G., di Sarra, A., Meloni, D., Piacentino, S., Chamard, P., (2006), Aerosol optical properties at Lampedusa (Central Mediterranean: 1. Influence of transport and identification of different aerosol types, Atmos. Chem. Phys., 6, 697-713.

References

Papayannis, A., Amiridis, V., Mona, L., Tsaknakis, G., Balis, D., Bösenberg, J., Chaikovski, A., De Tomasi, F., Grigorov, I., Mattis, I., Mitev, V., Müller, D., Nickovic, S., Pérez, C., Pietruczuk, A., Pisani, G., Ravetta, F., Rizi, V., Sicard, M., Trickl, T., Wiegner, M., Gerding, M., Mamouri, R.E., D'Amico, G., Pappalardo, G., (2008), Systematic lidar observations of Saharan dust over Europe in the frame of EARLINET (2000-2002), J. Geophys. Res.,113, D10204, doi:10.1029/2007JD009028.

Papayannis, A., Mamouri, R.E., Amiridis, V., Kazadzis, S., Perez, C., Tsaknakis, G., Kokkalis, P., Baldasano, J.M., (2009), Systematic lidar observations of Saharan dust layers over Athens, Greece in the frame of EARLINET project (2004-2006), Annales Geophysicae, 27, 3611-3620.

Papayannis, A., Mamouri, R.E., Amiridis, V., Remoundaki, E., Tsaknakis, G., Kokkalis, P., Veselovskii, I., Kolgotin, A., Nenes, A., Fountoukis, C., (2012), Optical-microphysical properties of Saharan dust aerosols and composition relationship using a multi-wavelength Raman lidar, in situ sensors and modelling: a case study analysis, Atmos. Chem. Phys., 12, 4011-4032.

Pavese, G., De Tomasi, F., Calvello, M., Esposito, F., Perrone, M.R., (2009), Detection of Sahara dust intrusions during mixed advection patterns over south-east Italy: A case study, Atmos. Res., 92, 489-504.

Pandithurai, G., Seethala, C., Murthy, B.S., Devara, P.C.S., (2008), Investigation of atmospheric boundary layer characteristics for different aerosol absorptions: Case studies using CAPS model, Atmos. Environ., 42, 4755-4768.

Pedrós, R., Martinez-Lozano, J. A., Utrillas, M. P., Gómez-Amo, J. L., Tena, F., (2003), Column-integrated aerosol optical properties from ground-based spectroradiometer measurements at Barrax (Spain) during the Digital Airborne Imaging Spectrometer Experiment (DAISEX) campaigns, J. Geophys. Res., 108, 4571, 10.1029/2002jd003331.

Penner, J.E., et al., (2001), Aerosols, their direct and indirect effects. In: Climate Change 2001: The Scientific Basis. Contribution of Working Group I to the Third Assessment Report of the Intergovernmental Panel on Climate Change [Houghton, J.T., et al. (eds.)], Cambridge University Press, Cambridge, United Kingdom and New York, NY, USA, pp. 289–348.

References

Perrone, M.R., Bergamo, A., (2011), Direct radiative forcing during Sahara dust intrusions at a site in the Central Mediterranean: Anthropogenic particle contribution, Atmos. Res. doi:10.1016/jatmosres.2011.05.011.

Pereira, S.N., Wagner, F., Silva, A.M., (2011), Seven years of measurements of aerosol scattering properties, near the surface, in the southwestern Iberia Peninsula, Atmos. Chem. Phys., 11, 17-29.

Petzold, A., Rasp, K., Weinzierl, B., Esselborn, M., Hamburger, T., Dörnbrack, A., Kandler, K., Schütz, L., Knippertz, P., Fiebig, M. and Virkkula A., (2009), Saharan dust absorption and refractive index from aircraft-based observations during SAMUM 2006, Tellus 61B, doi: 10.1111/j.1600-0889.2008.00383.x.

Phillips, D., (1962), A technique for numerical solution of certain integral equations of first kind, Journal of the ACM, 9(1), 84-97.

Pierluissi J. H., Maragoudakis C. E. and Tehrani-Movahed R., (1989), New LOWTRAN band model for water vapor, Appl. Opt. 28, 3792–3795.

Pilinis, C. and Li, X., (1998), Particle shape and internal inhomogeneity effects in the optical properties of tropospheric aerosols of relevance to climate forcing, J. Geophys. Res., 103(D4), 3789–3800.

Pinker, R.T., Liu, H., Osborne, S.R., Akoshile, C., (2010), Radiative effects of aerosols in sub-Sahel Africa: Dust and biomass burning, J. Geophys. Res., 115, D15205, doi:10.1029/2009JD013335.

Prasad, A.K., Singh, S., Chauhan, S.S., Srivastava, M.K., Singh, R.P., Singh, R., (2007), Aerosol radiative forcing over the Indo-Gangetic plains during major dust storms, Atmos. Environ., 41, 6289-6301.

Prats, N., Cachorro, V.E., Sorribas, M., Mogo, S., Berjon, A., Toledano, C., De Frutos, A.M., de la Rosa, J., Laulainen, N., de la Morena, B.A., (2008), Columnar aerosol optical properties during "El Arenosillo 2004 summer campaign", Atmos. Environ., 42, 2643-2653.

References

Prospero, J.M., Carlson, T.N., (1972), Vertical and aereal distribution of Saharan dust over the Western Ecuatorial North Atlantic Ocean, J. Geophys. Res., 77(27), 5255-5265.

Prospero, J.M., Ginoux, P., Torres, O., Nicholson, S.E., Gill, T.E., (2002), Environmental characterization of global sources of atmospheric soil dust identified with the Nimbus 7 Total Ozone Mapping Spectrometer (TOMS) absorbing aerosol product, Rev. Geophys, 40 (1), 1002. doi:10.1029/20000GR000095.

Querol X., Alastuey, A., Rodriguez, S., Plana, F., Mantilla, E. and Ruiz, C.R., (2001), Monitoring of PM10 and PM2.5 around primary particulate anthropogenic emission sources, Atmos. Environ., 35, 845-858.

Querol, X., Pandolfi, M., Pey, J., Alastuey, A., Cusack, M., Pérez, N., Amato, F., Moreno, T., Viana, M. and Mihalopoulos, N., (2009), African dust contribution to mean ambient PM10 mass- level across the Mediterranean Basin, Atmos. Environ., 43, 4266-4277.

Ricchiazzi, P., S. Yang, C. Gautier, and D. Sowle., (1998), SBDART: A research and teaching software tool for plane-parallel radiative transfer in the Earth's atmosphere, Bull. Am. Meteorol. Soc., 79, 2101– 2114.

Rodríguez, S., Alastuey, A., Alonso-Perez, S., Querol, X., Cuevas, E., Abreu-Afonso, J., Viana, M., Pandolfi, M., and J. de la Rosa., (2011), Transport of desert dust mixed with North African industrial pollutants in the subtropical Saharan Air Layer, Atmos. Chem. Phys., 11, 6663–6685.

Romero, R., Sumner, G., Ramis, C., Genovés, A., (1999), A classification of the atmospheric circulation patterns producing significant daily rainfall in the Spanish Mediterranean area, International Journal of Climatology, 19, 765-785.

Rothman L. S. et al., (1992), The HITRAN molecular database: editions of 1991 and 1992, J. Quant. Spectrosc. Radiat., 48.

Rozwadowska, A., Zielinski, T., Petelski, T., Sobolewski, P., (2010), Cluster analysis of the impact of air back-trajectories on aerosol optical properties at Hornsund, Spitsbergen, Atmos. Chem. Phys., 10, 877-893.

References

Russell, P. B., Livingston, J. M., Dutton, E. G., Pueschel, R. F., Reagan, J. A., Defoor, T. E., Box, M. A., Allen, D., Pilewski, P., Herman, B. M., Kinne, S. A. and Hoffmann, D. J., (1993), Pinatubo and pre-Pinatubo optical depth spectra: Mauna Loa measurements, comparisons, inferred particle size distributions, radiative effects, and relationship to lidar data, J. Geophys. Res., 98, D12, 22967–22985.

Russell, P.B., Bergstrom, R.W., Shinozuka, Y., Clarke, A.D., DeCarlo, P.F., Jimenez, J.L., Livingston, J.M., Redemann, J., Dubovik, O., Strawa, A., (2010), Absorption Angstrom Exponent in AERONET and related data as an indicator of aerosol composition, Atmos. Chem. Phys., 10, 1155-1169.

Santos, D., Costa, M. J., and Silva, A. M., (2008), Direct SW aerosol radiative forcing over Portugal, Atmos. Chem. Phys., 8, 5771–5786.

Saha, A., Mallet, M., Roger, J.C., Dubuisson, P., Piazzola, J., Despiau, S., (2008), One year measurements of aerosol optical properties over an urban coastal site: Effect on local direct radiative forcing, Atmos. Res., 90, 195-202.

Schoeberl, M. R., A.R. Douglass, E. Hilsenrath, et al., (2006), Overview of the EOS Aura Mission, IEEE T. Geosci. Remote, 4, 1066–1074.

Schladitz, A., Müller, T., Kaaden, N., Massling, A., Kandler, K., Ebert, M., Weinbruch, S., Deutscher, C., Wiedensohler, A., (2009), In situ measurements of optical properties at Tinfou (Morocco) during the Saharan Mineral Dust Experiment SAMUM 2006, Tellus 61B, 64-78.

Seinfeld, J. H. and Pandis, S. N., (2006), Atmospheric chemistry and physics: from air pollution to climate change, Wiley-Interscience, New York, USA, 2nd edn.

Seckmeyer, G., A.F. Bais, G. Bernhard, M. Blumthaler, C.R. Booth, R.L. Lantz, R.L., McKenzie, P. Disterhoft, Webb, A., (1997), Instruments to Measure Solar Ultraviolet Radiation. Part 2: Broadband Instruments Measuring Erythemally Weighted Solar Irradiance, WMO, GAW 164. World Meteorological Organization, Geneva.

Silva, A. M., Bugalho, M. L., Costa, M. J., von Hoyningen-Huene, W., Schmidt, T., Heintzenberg, J., and Henning, S., (2002), Aerosol optical properties from columnar data during the second Aerosol Characterization Experiment on the south coast of Portugal, J. Geophys. Res., 107(D22), 4642, doi:10.1029/2002JD002196.

References

Shifrin, K. S., (1995), Simple relationships for the Angström parameter of disperse systems, Applied Optics, 34, 4480–4485.

Slusser, J., Gibson, J., Bigelow, D., Kolinski, D., Disterhoft, P., Lantz, K., Beaubien, A., (2000), Langley metbod of calibrating UV filter radiometers, J. Geophys. Res., 105, D4, 4841-4849.

Smirnov, A., Holben, B.N., Slutsker, I., Welton, E.J., Formenti, P., (1998), Optical properties of Saharan dust during ACE 2, J. Geophys. Res., 103, 28079-28092.

Smirnov, A., Holben, B.N., Eck, T.F., Dubovik, O., Slutsker, I., (2000), Cloud-screening and quality control algorithms for the AERONET database, Remote Sens. Rev., 73, 337-349.

Solomon, S., Qin, D., Manning, M., Alley, R., Berntsen, T., Bindoff, N., Chen, Z., Chidthaisong, A., Gregory, J., Hegerl, G., Heimann, M., Hewitson, B., Hoskins, B., Joos, F., Jouzel, J., Kattsov, V., Lohmann, U., Matsuno, T., Molina, M., Nicholls, N., Overpeck, J., Raga, G., Ramaswamy, V., Ren, J., Rusticucci, M., Somerville, R., Stocker, T., Whetton, P., Wood, R. and Wratt, D., (2007) Cambridge University Press, New York, USA, chapter Technical Summary Contribution of Working Group 1 to the 4th Assessment Report of the Intergovernmental Panel on Climate Change, p. 2187.

Sokolik, I.N., Toon, O.B., (1999), Incorporation of mineralogical composition into models of the radiative properties of mineral aerosol from UV to IR wavelengths, J. Geophys. Res., 104, 9423-9444.

Soni, K., Singh, S., Bano, T., Tanwar, R.S., Nath, S., Arya, B.C., (2010), Variations in single scattering albedo and Angstrom absorption exponent during different seasons at Delhi, India, Atmos. Environ., 44, 4355-4363.

Stamnes, K. and Dale, H., (1981), A new look at the discrete ordinate method for radiative-transfer calculations in anisotropically scattering atmospheres. II: intensity computations, J. Atmos. Scien., 38(12), 2696-2706.

Stamnes, K., C. Tsay, W. Wiscombe, and Jayaweera, K., (1988), Numerically stable algorithm for discrete-ordinate-method radiative transfer in multiple scattering and emitting layered media, Appl. Opt., 27, 2502–2509.

References

Stohl, A., (1998), Computation, accuracy and applications of trajectories: A review and bibliography, Atmos. Environ., 32, 947–966.

Su, L., Toon, O.B., (2011), Saharan and Asian dust: similarities and differences determined by CALIPSO, AERONET, and a coupled climate-aerosol microphysical model, Atmos. Chem. Phys., 11, 3263-3280.

Sumner, G., Homar, V., Ramis, C., (2001), Precipitation seasonality in eastern and southern coastal Spain, International Journal of Climatology, 21, 219-247.

Tafuro, A.M., Barnaba, F., De Tomasi, F., Perrone, M.R., Gobbi, G.P., (2006), Saharan dust particle properties over the central Mediterranean, Atmos. Res., 81, 67-93.

Tanskanen, A., N.A. Krotkov, J.R. Herman, and Arola, A., (2006), Surface Ultraviolet Irradiance From OMI, IEEE T. Geosci. Remote, 44, 1267–1271, doi:10.1109/TGRS.2005.862203.

Tanskanen, A., A. Lindfors, A. Maatta, N. Krotkov, J. Herman, J. Kaurola, et al., (2007), Validation of daily erythemal doses from OMI with ground-based UV measurement data, J. Geophys. Res., 112, D24S44, doi:10.1029/2007JD008830.

Tegen, I., Hollrig, P., Chin, M., Fung, I., Jacob, D., Penner, J., (1997), Contribution of different aerosol species to the global aerosol extinction optical thickness: Estimates from model results, J. Geophys. Res., 102, 23895-23915.

Tesche, M., Ansmann, A., Müller, D., Althausen, D., Mattis, I., Heese, B., Freudenthaler, V., Wiegner, M., Esselborn, M., Pisani, G., Knippertz, P., (2009), Vertical profiling of Saharan dust with Raman lidars and airborne HSRL in southern Morocco during SAMUM, Tellus 61B, 144-164.

G.E. Thomas and Stamnes, K., (1999), Radiative Transfer in the Atmosphere and Ocean, Cambridge University Press, Cambridge (Reino Unido).

Toledano, C V. E. Cachorro, A. M. de Frutos, M. Sorribas, N. Prats, and B. A. de la Morena., (2007a), Inventory of African desert dust events over the southwestern Iberian Peninsula in 2000–2005 with an AERONET Cimel Sun photometer, J. Geophys. Res., 112, D21201, doi:10.1029/2006JD008307.

References

Toledano, C V. E. Cachorro, A. M. de Frutos, M. Sorribas, N. Prats, and B. A. de la Morena, (2007b), Inventory of African desert dust events over the southwestern Iberian Peninsula in 2000–2005 with an AERONET Cimel Sun photometer, J. Geophys. Res., 112, D21201, doi:10.1029/2006JD008307.

Toledano, C., Cachorro, V.E., de Frutos, A.M., Torres, B., Berjon, A., Sorribas, M., Stone, R.S., (2009), Airmass Classification and Analysis of Aerosol Types at El Arenosillo (Spain), J. Appl. Meteorol. Climatol., 48, 962-981.

Toledano, C., Wiegner, M., Gross, S., Freudenthaler, V., Gasteiger, J., Mueller, D., Mueller, T., Schladitz, A., Weinzierl, B., Torres, B., O'Neill, N.T., (2011), Optical properties of aerosol mixtures derived from sun-sky radiometry during SAMUM-2, Tellus 63B, 635-648.

Torres, B., (2012), Study on the influence of different error sources on sky radiance measurements and inversion-derived aerosol products in the frame of AERONET, Ph. D. Atmospheric Optics Group, University of Valladolid, April.

Torres, B., Dubovik, O., Toledano, C., Berjon, A., Cachorro, V. E., Lapyonok, T., and Goloub, P., (2013), Sensitivity of aerosol retrieval to geometrical configuration of ground-based sun/sky-radiometer observations, Atmos. Chem. Phys. Discuss., 13, 6851-6921, doi:10.5194/acpd-13-6851-2013.

Udo, S. (2000), Sky conditions at Ilorin as characterized by clearness index and relative sunshine, Sol. Energy, 69, 45– 53.

Valenzuela, A., Olmo, F.J., Lyamani, H., Antón, M., Quirantes, A., Alados-Arboledas, L., (2012a), Analysis of the desert dust radiative properties over Granada using principal plane sky radiances and spheroids retrieval procedure, Atmos. Res., 104-105, 292–301.

Valenzuela, A., Olmo, F.J., Lyamani, H., Antón, M., Quirantes, A., Alados-Arboledas, L., (2012b), Classification of aerosol radiative properties during African desert dust intrusions over southeastern Spain by sector origins and cluster analysis, J. Geophys. Res., 117, D06214, doi:10.1029/2011JD016885.

References

Valenzuela, A., Olmo, F.J., Lyamani, H., Antón, M., Quirantes, A., Alados-Arboledas, L., (2012c), Aerosol radiative forcing during African desert dust events (2005-2010) over Southeastern, Atmos. Chem. Phys., 12, 10331–10351.

Van de Hulst, H.C., (1957), Light scattering by small particles, Wiley, New York.

Vermeulen A., Devaux, C., and Herman M., (2000), Retrieval of the scattering and microphysical properties of aerosols from ground based optical measurements including polarization. I. Method, Appl. Opt., 39, 6207-6220.

Vilaplana, J.M., A. Serrano, M. Antón, et al., (2009), Report of the El Arenosillo/INTA-COST calibration an intercomparison campaign of UVER broadband radiometers. In: "El Arenosillo", Huelva, Spain, August September 2007. COST Office, ISBN 978-84-692-2640-7, p. 64.

Wagner, F., D. Bortoli, S. Pereira, M. J. Costa, A. M. Silva, B. Weinzierl, M. Esselborn, A., Petzold, K., Rasp, B., Heinold, and Tegen, I., (2009), Properties of dust aerosol particles transported to Portugal from the Sahara desert, Tellus 61B, 297–306.

Warneck, P., (1988), Chemistry of the natural atmosphere, International Geophysics Series. Wiley & Sons, 41. Academy Press, 757 pp.

Waterman PC., (1971), Symmetry, unitarity, and geometry in electromagnetic scattering, Phys. Rev, D3:825–839.

Webb, A., J. Gröbner, Blumthaler, M., (2006), A Practical Guide to Operating Broadband Instruments Measuring Erythemally Weighted Irradiance, Office for Official Publications of the European Communities, ISBN 92-898-0032-1, 21 pp.

Weihs, P., M. Blumthaler, H.E. Rieder, et al., (2008), Measurements of UV irradiance within the area of one satellite pixel, Atmos. Chem. Phys., 8, 5615–5626, doi:10.5194/acp- 8-5615-2008, 2008.

Wiscombe, W., (1977), Delta-M Method – Rapid yet accurate radiative flux calculations for strongly asymmetric phase functions, J. Atmos. Scien., 34 (9), 1408-1422.

References

Whitby, K. T., and Cantrell, B., (1976), Fine particles. In International Conference on Environmental Sensing and Assessment, Las Vegas, NV, Institute of Electrical and Electronic Engineers.

Won, J.-G., Yoon, S.-C., Kim, S.-W., Jefferson, A., Dutton, E.G., Holben, B.N., (2004), Estimations of direct radiative forcing of Asian dust aerosols with sun/sky radiometer ans lidar measurements at Gosan, Korea, J. Meteor. Society of Japan, 82, 115-130.

Xingna Yu, Bin Zhu, Yan Yin, Jun Yang, Yanwei Li, Xiaoli Bu, (20119, A comparative analysis of aerosol properties in dust and haze-fog days in a Chinese urban region, Atmos. Res., 99, 241-247.

Yang, P., and Liou, K. N., (1996), Geometric-optics-integral-equation method for light scattering by nonspherical ice crystals, Appl. Opt., 35, 6568–6584.

Yang, P., Feng, Q., Hong, G., Kattawar, G.W., Wiscombe, W.J., Mishchenko, M.I., Dubovik, O., Laszlo, I., Sokolik, I.N., (2007), Modeling of the scattering and radiative properties of nonspherical dust particles, J. of Aerosol Sci., 38, 995–1014.

Yang, M., Howell, S. G., Zhuang, J., and Huebert, B. J., (2009), Attribution of aerosol light absorption to black carbon, brown carbon, and dust in China – interpretations of atmospheric measurements during EAST-AIRE, Atmos. Chem. Phys., 9, 2035–2050, doi:10.5194/acp-9-2035-2009.

References

List of symbols

Symbol	Definition
A	Area
A	Surface albedo
AAE	Absorption Angström Exponent
AI	Aerosol Index
AU	Astronomic unit
ARF_{TOA}	Aerosol radiative forcing in the top of the atmosphere
$ARF_{Surface}$	Aerosol radiative forcing in the surface
$ARF_{Atmosphere}$	Aerosol radiative forcing in the atmosphere
β	Turbidity parameter
β	Differential scattering coefficient
C_p	Specific heat of dry air
C	Cross section
E	Radiant energy
g	Asymmetry parameter
G	Gravitational aceleration
F	Radiant flux density
FMF	Fine mode fraction
f	Radiant flux

List of Symbols

I	Radiant intensity
J	Source function
k	Imaginary refractive index
L	Radiance
LER	Lambertian Equivalent Reflectivity
mr	Relative optic mass
m	Complex refractive index
N	Number of particles per volume unit
n	Real refractive index
n	Size numeric distribution
σ_e	Extinction coefficient
σ_s	Scattering coefficient
σ_a	Absorption coefficient
Q_e	Extinction efficiency factor
Q_s	Scattering efficiency factor
Q_a	Absorption efficiency factor
x	Size parameter
ε	Shape factor
Θ	Scattering angle
B	Planck function
P	Phase function
P	Pressure
r	Earth-Sun distance
r_o	Earth-Sun mean distance
r	Radius of particle
r_{eff}	Effective radius of particles
R	Normalized radiance

List of Symbols

RMSE	Root mean square error
SAE	Scattering Angström Exponent
s	Size surface distribution
sr	Steradiant
T	Temperature
T	Transmitance
TOC	Total ozone column
UVER	Ultraviolet erythemally weighted irradiance
V	Size volume distribution
V	Signal measured by the sun photometer
ω	Single scattering angle
α	Angström exponent
θ	Zenith angle
ϕ	Azimuthal angle
λ	Wavelength
r	Earth-Sun distance
Ω	Solid angle
σ	Standard deviation
μ	Cosine zenith angle
τ^{*}	Optical thickness
τ	Total optical depth
τ_{a}	Aerosol optical depth
τ_{aabs}	Absorption aerosol optical depth
η	Fine mode fraction

List of Symbols

List of publications

Publications in Journals:

Valenzuela, A., Olmo, F.J., Lyamani, H., Quirantes, A., Alados-Arboledas, L., (2011), Aerosol radiative properties retrieved during Saharan dust events in Southeastern Spain from 2005 to 2008, Optica Pura y Aplicada, 44 (4), 661-664.

Quirantes, A., Olmo, F.J., **Valenzuela, A.,** Lyamani, H., Alados-Arboledas, L., (2011), ALFA: A Database for light scattering simulations with atmospheric aerosol applications, Optica Pura y Aplicada, 44 (4), 641-645.

Quirantes, A., Olmo, F.J., **Valenzuela, A.,** Lyamani, H., Alados-Arboledas, L., (2011), Separation of fine and coarse aerosol contributions to the total aerosol light scattering: An Aeronet assessment, Atti della Accademia Peloritana dei Pericolanti, 89 (1), DOI: 10.1478/C1V89S1P078.

Anton, M., Gil, J., Fernández, J., Lyamani, H., **Valenzuela, A.,** Foyo, I., Olmo, F.J. and Alados-Arboledas, L., (2011), Evaluation of the aerosol forcing efficiency in the UV erythemal range at Granada, Spain, J. Geophys. Res., 116, D20214, doi:10.1029/2011JD016112.

Valenzuela, A., Olmo, F.J., Lyamani, H., Antón, M., Quirantes, A., Alados-Arboledas, L., (2012), Analysis of the desert dust radiative properties over Granada using principal plane sky radiances and spheroids retrieval procedure, Atmos. Res., 104-105, 292–301.

Valenzuela, A., Olmo, F.J., Lyamani, H., Antón, M., Quirantes, A., Alados-Arboledas, L., (2012), Classification of aerosol radiative properties during African desert dust

intrusions over southeastern Spain by sector origins and cluster analysis, J. Geophys. Res., 117, D06214, doi:10.1029/2011JD016885.

Valenzuela, A., Olmo, F.J., Lyamani, H., Antón, M., Quirantes, A., Alados-Arboledas, L., (2012), Aerosol radiative forcing during African desert dust events (2005-2010) over Southeastern, Atmos. Chem. Phys., 12, 10331–10351.

Antón, M., **Valenzuela, A.,** Román, R., Lyamani, H., Krotkov, N., Arola, A., Olmo, F. J. and Alados-Arboledas, L., (2012), Influence of desert dust intrusions on ground-based and satellitederived ultraviolet irradiance in southeastern Spain, J. Geophys. Res., 117, D19209, doi:10.1029/2012JD018056.

Antón, M., A. **Valenzuela, A.** Cazorla, J. E. Gil, J. Fernández-Gálvez, H. Lyamani, I. Foyo-Moreno, F. J. Olmo, and Alados-Arboledas, L., (2012), Global and diffuse shortwave irradiance during a strong desert dust episode at Granada (Spain), Atmos. Res., 118, 232–239, doi:10.1016/j.atmosres.2012.07.007.

Lyamani, H., Fernández-Gálvez, J., Pérez-Ramírez, D., **Valenzuela, A.,** Antón, M., Alados, I., Titos, G., Olmo, F.J. and Alados-Arboledas, L., (2012), Aerosol properties over two urban sites in South Spain during an extended stagnation episode in winter season, Atmos. Envir., 62, 424-432.

Quirantes, A., Olmo, F.J., Lyamani, H., **Valenzuela, A.,** Alados-Arboledas, L., (2012), Investigation of fine and coarse aerosol contributions to the total aerosol light scattering: Shape effects and concentration profiling by Raman lidar measurements, J. Q. S. Rad. Trans., 113, 2593–2600.

Román, R., Antón, M., **Valenzuela, A.,** Gil, J.E., Lyamani, H., De Miguel, A., Olmo, F. J., Bilbao, J. and Alados-Arboledas, L., (2013), Evaluation of the desert dust effects on global, direct and diffuse spectral ultraviolet irradiance, Tellus 63B, 19578, http://dx.doi.org/10.3402/tellusb.v65i0.19578.

Antón, M., Román, R., **Valenzuela, A.,** Lyamani, H., Olmo, F. J. and Alados-Arboledas, L., (2013), Direct-sun total ozone data from a spectroradiometer: methodology and comparison with satellite observations, Atmos. Meas. Tech., 6, 637–647.

Mateos, D., Antón, M., **Valenzuela, A.,** Cazorla, A., Olmo, F.J. and Alados-Arboledas, L., (2013), Shortwave radiative forcing for cloudy systems at a midlatitude site, under review.

Mateos, D., Antón, M., **Valenzuela, A.,** Cazorla, A., Olmo, F.J. and Alados-Arboledas, L., (2013), Efficiency of shortwave cloud forcing under overcast conditions at Granada (Spain), under review.

Antón, M., Matéos, D., Román, R., **Valenzuela, A.,** Olmo, F. J. and Alados-Arboledas, L., (2013), A method to determine the ozone radiative forcing in the ultraviolet range from experimental data, under review.

Valenzuela, A., Olmo, F.J., Lyamani, H., Granados Muñoz, M.J., Guerrero-Rascado, J.L., Antón, M., Alados-Arboledas, L., (2013), Air masses transport over Alborán Island: Anthropogenic aerosol characterization during desert dust events, to be submitted.

Valenzuela, A., Olmo, F.J., Antón, M., Lyamani, H., Titos, G., Cazorla, A., Alados-Arboledas, L., (2013), Aerosol scattering and absorption Angström exponent as indicators of dust and dust-free days over Granada (Spain), to be submitted.

Book chapters:

Valenzuela, A., Olmo, F.J., Lyamani, H., Quirantes, A., Alados-Arboledas, L., (2010), Aerosol retrieved from sky radiance at the principal plane for non-spherical particles, Book of extended abstracts of IV Reunión Española de Ciencia y Tecnología de Aerosoles, C14,1-6, ISBN: 978-84-693-4839-0.

Quirantes, A., Olmo, F.J., **Valenzuela, A.,** Lyamani, H., Alados-Arboledas, L., (2010), ALFA/BETA: A dual database for light scattering simulations on atmospheric aerosols, Book of extended abstracts of IV Reunión Española de Ciencia y Tecnología de Aerosoles, D4, 1-4, ISBN: 978-84-693-4839-0.

Alados-Arboledas, L., Olmo, F.J., Horvath, H., **Valenzuela, A.,** Lyamani, H., Quirantes, A., (2010), Designing a polar nephelometer for atmospheric aerosol characterization, E10, 1-6, ISBN: 978-84-693-4839-0.

Lyamani, H., Fernández-Gálvez, J., Pérez-Ramírez, D., **Valenzuela, A.,** Antón, M., Alados, I., Titos, G., Olmo, F.J. and Alados-Arboledas, L., (2011), Aerosol properties during an extended stagnation at two urban sites in South-eastern Spain, Book of extended abstracts of IV Reunión Española de Ciencia y Tecnología de Aerosoles, D2, 1-6, ISBN: 978-84-7834-662-2.

Anton, M., Gil, J., Fernández, J., Lyamani, H., **Valenzuela, A.,** Foyo, I., Olmo, F.J. and Alados-Arboledas, L., (2011), Evaluation of the aerosol forcing efficiency in the UV erythemal range at Granada, Spain, Book of extended abstracts of IV Reunión Española de Ciencia y Tecnología de Aerosoles, M4, 1-6, ISBN: 978-84-7834-662-2.

Valenzuela, A., Olmo, F.J., Lyamani, H., Antón, M., Quirantes, A., Alados-Arboledas, L., (2011), Aerosol radiative properties retrieved during desert dust events at Granada (2005-2010)-Air mass clasification, Book of extended abstracts of IV Reunión Española de Ciencia y Tecnología de Aerosoles, C1, 1-6, ISBN: 978-84-7834-662-2.

Participation in national and international conferences:

Quirantes, A., Olmo, F.J., **Valenzuela, A.,** Lyamani, H., Alados-Arboledas, L., (2010), Relationship between the fraction of backscattered light and the asymmetry parameter, IV Reunión Española de Ciencia y Tecnología de Aerosoles, Granada (Spain).

Valenzuela, A., Olmo, F.J., Lyamani, H., Quirantes, A., Alados-Arboledas, L., (2010), Aerosol radiative properties retrieved during the Saharan dust events in the Southeastern Spain from 2005 to 2008, 37rd Annual European Meeting on Atmospheric Studies by Optical Methods, Valladolid (Spain).

Quirantes, A., Olmo, F.J., **Valenzuela, A.,** Lyamani, H., Alados-Arboledas, L., (2010), A light scattering database for radiative-transfer simulations on atmospheric aerosols, 37rd Annual European Meeting on Atmospheric Studies by Optical Methods, Valladolid (Spain).

Alados-Arboledas, L., Navas-Guzmán, F., Bravo-Aranda, J.A., Lyamani, H., Pérez-Ramírez, J D. J., Guerrero-Rascado, L., Foyo, I., Alados, I., Granados, M.J., Titos, G., Fernández Gálvez, J., **Valenzuela, A.,** Antón, M., Quirantes, A. Querol, X., Alastuey,

A. and Olmo, F. J., (2011), Multi-instrumental characterization of the mixing of Eyjafjallajökull volcanic aerosols and boundary layer aerosols at Granada, Spain, European Aerosol Conference, Manchester (England).

Valenzuela, A., Olmo, F.J., Lyamani, H., Quirantes, Pérez-Ramirez, D., A., Alados-Arboledas, L., (2011), Aerosol properties during long-range transport of African dust air masses over Granada (Spain), European Aerosol Conference, Manchester (United Kingdom).

Quirantes, A., Olmo, F.J., **Valenzuela, A.,** Lyamani, H., Alados-Arboledas, L., (2011), Shape dependence of atmospheric aerosol light scattering parameters: ALFA simulations and comparison to AERONET, European Aerosol Conference, Manchester (United Kingdom).

Quirantes, A., Olmo, F.J., **Valenzuela, A.,** Lyamani, H., Alados-Arboledas, L., (2011), Separation of fine and coarse aerosol contributions to the total aerosol light scattering: an AERONET assessment, XIII Conference on Electromagnetic and Light Scattering, Taormina (Italy).

Anastasio, J.l., Foyo-Moreno, I., **Valenzuela, A.,** Antón, M., Olmo, F.J., Lyamani, H., A., Alados-Arboledas, L., (2012), Experimental study of the surface shortwave aerosol forcing efficiency, European Aerosol Conference, Granada (Spain).

Valenzuela, A., Olmo, F.J., Antón, M., Lyamani, H., Quirantes, A., Alados-Arboledas, L., (2012), Aerosol Scattering and Absorption Angström Exponents during desert dust events over Granada, European Aerosol Conference, Granada (Spain).

Antón, M., **Valenzuela, A.,** Román, R., Lyamani, H., Krotkov, N., Arola, A., Olmo, F. J. and Alados-Arboledas, L., (2012), Effects of desert dust aerosols on surface UV radiation from OMI satellite instrument at Granada (Spain), European Aerosol Conference, Granada (Spain).

Bravo-Aranda, J.A., Navas-Guzmán, F., Andrey, J., Granados-Muñoz, M.J., Guerrerro-Rascado, J.L, Gil, M., Lyamani, H., **Valenzuela, A.,** Titos-Vela, G., Fernández-Gálvez, J., Olmo, F.J. and Alados-Arboledas, L., (2012), CLIMARENO campaign 2011: Aerosol optical properties characterization from ground-based instrumentation, European Aerosol Conference, Granada (Spain).